THERMAL CONDUCTIVITY OF CARBON FIBRE FABRICS AND MULTI-SCALE COMPOSITES WITH HEAT TRANSFER SIMULATIONS FOR RFI MANUFACTURING

by

Yue Yang

A thesis submitted to the Faculty of Graduate and Postdoctoral Studies in partial fulfillment of the requirements for the degree of

MASTER OF APPLIED SCIENCE

in Mechanical Engineering

Ottawa-Carleton Institute for Mechanical and Aerospace Engineering
University of Ottawa
Ottawa, Canada

August 2013

Dedication

To my dear grandparents, BaoTing Luo and ShaoKun Zhang, for being my inspiration to pursue mechanical engineering.

Acknowledgements

I would like to express my sincere gratitude to Dr. François Robitaille for his encouragement and guidance throughout the past two years and for the opportunity to be part of this project. I would like to thank my colleague Simon Baril-Gosselin for his help in the lab and for putting up with all my questions. I would like to thank Aerospace Structures and Materials Performance-NRC and Simon Hind for their help and for granting me access to the THISYS and THASYS devices. I would like to thank Canadian Construction Materials Centre-NRC and Helen Yew for performing the DSC tests for the resin free of charge. I would like to thank Mohammed Yandouzi for his help with the SEM and sample polishing and all the shop technicians for their help.

I would like to thank NSERC, OGS, FQRNT, CRIAQ, Bombardier Aerospace and Axson for their funding.

Finally, I would like to thank my family for their patience throughout these two years and I would like to thank my fiancé for his love and support.

Abstract

Composites are increasingly used in aerospace applications where performance is the foremost priority of industry. Research on carbon nanotube (CNT)-reinforced polymers conducted in the past decade showed promising results for the improvement of mechanical, thermal and electrical properties of composites. This thesis was undertaken in the context of a larger project, the main goal of which is to develop a complete solution for the manufacturing of carbon fibre-epoxy composites using CNT-reinforced epoxies, referred to as multi-scale composites. This thesis focuses on the thermal aspect of this project under three topics: 1) thermal conductivity of dry carbon fibre fabrics for understanding heat diffusion in composites and similar fabric materials 2) thermal conductivity of CNT-reinforced polymers and composites for determining the effect of parameters including CNT addition, and 3) modelling of heat transfer during composite manufacturing for ensuring that their temperature distribution remains controlled.

In-plane k_{rip} and through-thickness k_{rtt} thermal conductivity data were measured for two dry carbon fibre fabrics as a function of fibre volume fraction V_f. Results showed that k_{rip} varies linearly with V_f whilst k_{rtt} varies in an exponential recovery trend with V_f. An existing analytical model was used successfully for predicting k_{rip} and simulations developed for predicting k_{rtt} values demonstrated that k_{rtt} depends on the evolution of heat conduction paths in the through-thickness direction as a result of improvements in the fibre contact network.

A procedure was developed for manufacturing composites using the RFI process. Thirty-two composites and multi-scale composite plates were manufactured and characterised for investigating the effects of eleven material and manufacturing parameters on fibre volume fraction, porosity, k_{rip} and k_{rtt}. Results showed that the effect of using multi-walled CNT-reinforced epoxy on thermal conductivity of composites is negligible at 0.3% CNT loading. However, this reduced the porosity of the composites significantly. Results also showed that using fabrics with higher surface densities led to a slight increase in k_{cip}.

A heat transfer model coupled with cure kinetics was developed for predicting temperature profiles of the laminate during RFI manufacturing. The model was validated experimentally and eleven simulation cases were run for investigating the effects of five material and manufacturing parameters on temperature profiles in the laminate. Results showed that the epoxy resins used in this project combined with the cure cycle recommended by the manufacturer are well-suited for manufacturing laminates with a typical thickness of approximately 5 mm as well as thick laminates of 15 mm to 20 mm.

Table of contents

List of tables

List of figures

Nomenclature

A_f cross section area of carbon fibre (m^2)

c_i contrast coefficient

C contrast

C_p specific heat (J/kgK)

d diameter of carbon nanotube (m)

d_f diameter of carbon fibre (m)

d_s distance between adjacent fibres (m)

E activation energy (J/mol)

h coefficient of heat transfer (W/m^2K)

k thermal conductivity (W/mK)

k_{fa} axial thermal conductivity of fibre (W/mK)

k_{ft} transverse thermal conductivity of fibre (W/mK)

k_{rip} in-plane thermal conductivity of fabric or reinforcement (W/mK)

k_{rtt} through-thickness thermal conductivity of fabric or reinforcement (W/mK)

k_{cip} in-plane thermal conductivity of carbon fibre-epoxy composite (W/mK)

k_{ctt} through-thickness thermal conductivity of carbon fibre-epoxy composite (W/mK)

k_1 thermal conductivity of unidirectional composite or laminate layer in axial direction (W/mK)

k_2 thermal conductivity of unidirectional composite or laminate layer in transverse direction (W/mK)

k_m thermal conductivity of matrix (W/mK)

k_{ya} axial thermal conductivity of yarn (W/mK)

k_v thermal conductivity of void (W/mK)

k_c thermal conductivity of carbon nanotube (W/mK)

$k_{11}^{\ c}$ thermal conductivity of carbon nanotube with interface layer in transverse direction (W/mK)

$k_{33}^{\ c}$ thermal conductivity of carbon nanotube with interface layer in longitudinal direction (W/mK)

k_{nc} thermal conductivity of nanocomposite (W/mK)

k_{ncv} thermal conductivity of nanocomposite accounting for voids (W/mK)

K_i constants in Arrhenius equation (1/s)

L length of carbon nanotube (m)

m_p mass of plate (kg)

m_r mass of resin (kg)

m_f mass of fibres (kg)

m_f mass of fibres (kg)

n_i observations per subgroup

N number of fabric plies

q'' heat flux (W/m^2)

$\dot{q}$ rate of internal heat generation per unit volume (W/m^3)

$\dot{Q}_R$ instantaneous heat of reaction due to curing exotherm (W)

Q_R cumulative heat of reaction (J)

Q_{RT} total heat of reaction (J)

r_k Kapitza radius (m)

R universal gas constant (J/molK)

R_k interfacial or Kapitza resistance (m^2K/W)

$SS(C)$ sum of squares

t_f thickness of fabric stack

t_r thickness of total resin required

T temperature (K)

T_s surface temperature (K)

T_∞ temperature of surrounding fluid (K)

V_f fibre volume fraction

V_{fy} yarn fibre volume fraction

V_v void volume fraction or porosity

α degree of cure

ρ_{sd} surface density of fabric (g/m^2)

ρ_r density of resin (kg/m^3)

ρ_f density of carbon fibre (kg/m^3)

$\forall_p$ volume of plate (m^3)

Abbreviations

CLT	classical lamination theory
CNF	carbon nanofibre
CNT	carbon nanotube
DSC	differential scanning calorimetry
DWCNT	double-walled carbon nanotubes
GF	fibreglass fabrics
HM	high modulus
HTS	high tensile strength
IM	intermediate modulus
MDSC	modulated differential scanning calorimetry
MWCNT	multi-wall carbon nanotube
NRC	National Research Council
PAN	polyacrylonitrile
PDVF	polyvinylidenefluoride
PEEK	polyetheretherketone
PMC	polymer matrix composite
PMMA	polymethylmethacrylate
RTM	resin transfer moulding
SWCNT	single-wall carbon nanotube
TEM	transmission electron microscopy
UDF	user-defined function

1 Introduction

1.1 Background

Composites are increasingly used in aerospace applications where performance is the foremost priority of industry [1]. Research on carbon nanotube (CNT)-reinforced polymers conducted in the past decade showed promising results for the improvement of mechanical, thermal and electrical properties. Studies have reported increases of up to 42%, 25% [2] and 60% [3] in the tensile modulus, tensile strength and hardness of polymers upon loading CNTs at 1% by weight. There is much scatter and debate found in the literature regarding improvements in thermal and electrical properties. Nevertheless, enhancements in thermal conductivities of up to 125% [4] and in electrical conductivities of up to several orders of magnitude [5] upon loading CNTs at 1% by weight have been reported.

This thesis was undertaken in the context of CRIAQ (Consortium for Research and Innovation in Aerospace in Quebec) COMP 510 project, entitled “Development of Nanochemicals Filled Epoxy Systems for Aerospace Applications”. The main goal of the project is to develop a complete solution for the manufacturing of carbon fibre-epoxy aerospace composites using CNT-reinforced epoxies, referred to as multi-scale composites. Out-of-autoclave resin film infusion (RFI) was selected and used for manufacturing composites plates, due to its low cost and simplicity compared to the conventional prepreg based process used typically for aerospace parts. Also, RFI yields parts with fibre volume

fractions (V_f) comparable with those of conventional liquid moulding processes such as resin transfer moulding (RTM) which require the complex design of a mould and involve higher capital cost. In a typical out-of-autoclave RFI process, films of partially cured resin are cut into plies, stacked and either placed under dry reinforcement fabric plies or intercalated with the dry fabric plies, and placed on a tool, Figure 1.1. The resin plies, fabric plies and manufacturing ancillaries are vacuum bagged and the assembly is heated in an oven under the application of vacuum; the viscosity of the resin is reduced to allow infusion into the fabric, followed by exothermal resin cure.

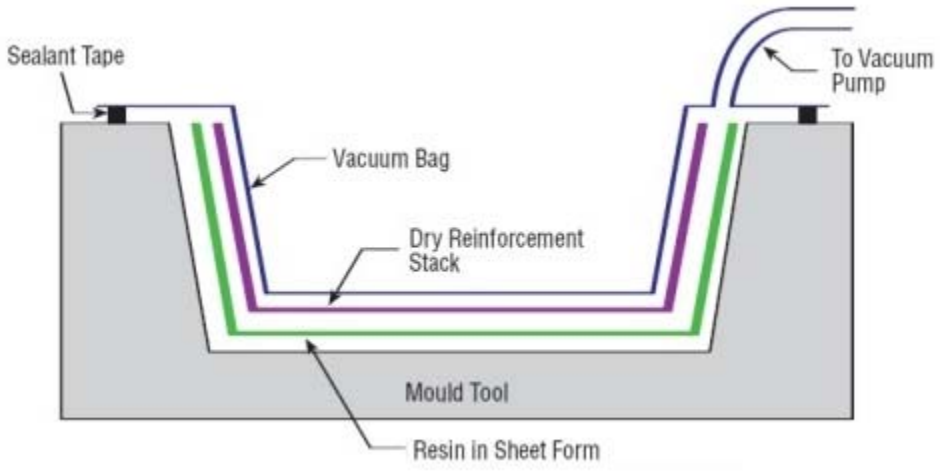

Figure 1.1- Resin film infusion (RFI) manufacturing process [6]

CRIAQ COMP 510 is an ongoing project which involves two universities, McGill and University of Ottawa as well as two industrial partners, Bombardier Aerospace and Axson. Bombardier Aerospace provides experience in aerospace composite structure design and manufacturing while Axson has expertise in developing CNT-reinforced polymers and supplies the resin materials used in this project.

Three PhD students and two MASc students study various aspects of this project: characterising CNT dispersion in the resins, modelling the infusion process and characterising the mechanical, thermal and electrical properties of the multi-scale composites. This thesis focuses on the thermal aspect of this project under three topics: 1) thermal conductivity of dry carbon fibre fabrics, 2) thermal conductivity of CNT-reinforced polymers and composites, and 3) modelling of heat transfer during composite manufacturing.

Carbon fibre fabrics are used extensively in the composite and aerospace industries. Knowledge of their thermal conductivity is important for understanding heat diffusion in composites. It would also benefit the understanding of heat diffusion in comparable technical fabric materials [7], with applications such as firefighter clothing design [8]. Also, it is an important parameter towards modelling heat transfer during composites manufacturing processes such as RFI where properties of the dry fabrics must be known prior to resin impregnation. However, there is almost no information or data available in the literature; only one paper was found reporting a preliminary investigation on the thermal conductivity of one dry carbon fibre fabric [9].

Thermal conductivities of up to 6600 W/mK have been reported for CNTs [10], hence they offer great potential as a reinforcement in polymers and composites for thermal conductivity enhancement. High thermal conductivity in composites is useful for high temperature applications such as parts used in proximity of an engine, or for temperature sensitive applications such as power electronics and optoelectronics where heat dissipation is a serious issue [11]. The effect of CNT addition on the thermal conductivity of polymers [12–23] has been investigated through several studies conducted in the past decade. Much scatter is present in data available from the literature; some studies reported thermal

conductivity enhancements of up to 125% upon loading CNTs at 1% by weight [4] while others reported decreases in thermal conductivity [17]. The effect of CNT addition on the thermal conductivity of composites [24]–[28] has also been investigated, and similar scatter is present in data available from the literature; some studies reported thermal conductivity enhancements of up to 105% upon loading CNTs at 1% by weight [29] while others reported no effect or decreases in thermal conductivity [28]. However, very little information is available in the literature where CNTs were loaded into a polymer, where this reinforced polymer was then used in manufacturing multi-scale composites. Hence no direct comparisons between the effect of CNT addition on the thermal conductivity of polymers and that of their fibre-reinforced composites can be made. Also, no studies investigated the effects of fabric material parameters on the in-plane and through-thickness thermal conductivities of multi-scale composites.

Thick laminates are increasingly used in aerospace, marine and civil applications [30]. Modelling heat transfer and cure kinetics is especially important towards ensuring that their temperature distribution remains controlled during manufacturing. The large curing exotherm in the resin caused by conventional cure cycles combined with the low thermal conductivity of the resin, limiting heat dissipation, can result in a temperature overshoot at the centre of the laminate and cause residual thermal stresses and degradation of the matrix in the most severe cases [31]. This can be minimised using knowledge gained from accurate heat transfer simulations which provide useful tools for optimisation of the cure cycle. Modelling heat transfer is also useful for studying resin infusion, where knowledge of resin viscosity which controls flow requires temperature profiles through the laminate during manufacturing. Heat transfer models of the RFI process coupled with cure kinetics were found in the literature

[22, 23]. However, some of these models were not validated experimentally [30] while others provide temperature predictions only at the top and bottom surfaces of the laminate but not at any location inside [32]. Also, none of these models investigated the effect of using a CNT-reinforced resin compared with its neat counterpart, or the effect of the laminate thermal conductivity on the temperature profiles in the laminate.

1.2 Objectives and Contributions

The overall goals of the thesis were to measure and model thermal conductivities of dry carbon fibre fabrics, CNT-reinforced epoxies and their multi-scale composites, and to model heat transfer in the laminate during manufacturing. Specific contributions resulting from the overall goals are listed as follows:

- Measuring in-plane k_{rip} and through-thickness k_{rtt} thermal conductivities of dry carbon fibre fabrics at various fibre volume fractions (V_f)
- Modelling k_{rip} and k_{rtt}
- Manufacturing neat and CNT-reinforced resin plates
- Determining whether CNT addition improves thermal conductivity of resin
- Developing a procedure for and manufacturing composite plates using the RFI process
- Investigating the effects of various manufacturing parameters on the V_f and void volume fraction (V_v) of composite plates

- Characterising the V_f, V_v, in-plane k_{cip} and through-thickness k_{ctt} thermal conductivities of composite plates
- Identifying influential material parameters including CNT addition on V_f, V_v, k_{cip} and k_{ctt} using a design of experiment methodology
- Developing simulations using FLUENT ANSYS to model heat transfer coupled with resin cure kinetics during manufacturing, and validate the model experimentally
- Investigating the effects of various parameters on the temperature profiles in the laminate

This thesis is organised in 6 chapters. Chapter 1 provides a background of the subject and project and states the objectives and contributions of this research.

Chapter 2 presents a thorough literature review on the three main topics of this thesis as mentioned previously. The review begins with thermal conductivity data for carbon fibres and dry carbon fibre fabrics available in the scientific literature and from commercial suppliers. Afterwards, measured data and analytical models for the thermal conductivity of polymer matrix composites (PMCs) are presented. Then thermal conductivity data for CNTs and CNT-reinforced polymers and PMCs are discussed. Finally, models for resin cure kinetics and heat transfer during composites manufacturing are presented.

Chapter 3 presents in-plane and through-thickness thermal conductivity data for two dry carbon fibre fabrics. The chapter begins by introducing dedicated devices for thermal conductivity measurements. Next, sample preparation and measurement procedures are presented followed by measured k_{rip} and k_{rtt} data for samples exposed to air and under

vacuum at various V_f values. Values measured for the dry fabrics are compared with those measured for carbon fibre-epoxy composites. Then analytical models and simulations in FLUENT ANSYS are used for predicting k_{rip} and k_{rtt}.

Chapter 4 investigates and compares the effect of CNT addition and other material parameters on the thermal conductivities of epoxy resins and composites. The chapter begins by presenting experimental procedures, thermal conductivity data and modelling for CNT-reinforced epoxy plates. Then materials, experimental procedures and equipment used for manufacturing and characterising composite plates are described. A set of 19 preliminary plates are manufactured for determining optimum manufacturing parameters and a set of 12 plates are manufactured using the Plackett-Burman design of experiment methodology to determine the effect of 4 material input parameters on measured parameters V_v, V_f, k_{cip} and k_{ctt} of the composite plates.

Chapter 5 presents the heat transfer model coupled with cure kinetics developed for predicting temperature profiles of the laminate during RFI manufacturing. The chapter begins with the model geometry, followed by material properties and input parameters. Then the simulation setup in FLUENT is presented followed by validation of the model through experimental means. Finally, comparisons are made between different simulation cases for investigating the effects of manufacturing and material parameters on temperature profiles of the laminate.

Chapter 6 presents a brief discussion and highlights the major findings of this thesis.

The most original contribution of this thesis is the thermal conductivity data measured for dry carbon fibre fabrics, and its preliminary modelling. As mentioned previously, such information or measured data is almost non-existent in the current scientific literature and commercial industry. This thesis does not only present measured data, but presents data collected systematically at various V_f values for different fabric architectures and compared with data measured for composites made from these fabrics. Models proposed in this thesis replicated experimental data successfully. This work enabled an understanding of heat diffusion in dry fabrics and composites. Results of this work were presented at the 19th International Conference on Composite Materials [33]. The novelty and impact of this work was recognized during the use of the thermal conductivity measurement devices at the Aerospace Structures and Materials Performance laboratory of the National Research Council (ASMP-NRC) and a continuation of this work is currently being pursued by the ASMP. More data collection is being performed with various fabrics, with the intent of providing a database of measured in-plane and through-thickness thermal conductivity data for dry reinforcement fabrics for use in the aerospace industry.

Another contribution is the measurement of thermal conductivities of CNT-reinforced epoxies as well as multi-scale composites made from these reinforced epoxies. This is the first available direct comparison between the effect of CNT addition on thermal conductivity of epoxy and the effect of CNT addition on thermal conductivity of carbon fibre-epoxy composites. This is also the first study investigating the effects of fabric architecture and surface density on the thermal conductivity of composites or multi-scale composites. Finally, this is the first study investigating the effect of using a CNT-reinforced resin compared with

its neat counterpart and the effect of the laminate thermal conductivity on the temperature profiles in laminates during RFI manufacturing.

2 Literature review

This review begins with a presentation of thermal conductivity data for carbon fibres and carbon fibre fabrics available from the scientific literature and commercial suppliers, Section 2.1. This is followed by a review of measured data and analytical models for the thermal conductivity of polymer matrix composites (PMCs), Section 2.2. Then, thermal conductivity data for carbon nanotubes (CNTs) are presented in Section 2.3, along with a discussion of their effect on the thermal conductivity of polymers and PMCs. The chapter ends with a presentation of basic models for resin cure kinetics, as well as models for heat transfer during composites manufacturing, Section 2.4.

2.1 Thermal conductivity of carbon fibres and carbon fibre fabrics

2.1.1 Carbon fibres

Carbon fibres have excellent tensile properties and low densities, resulting in their extensive use as structural reinforcements in composite materials. The global carbon fibre consumption has doubled in a decade from 16600 tons in 1999 to 34200 tons in 2010, with the aerospace sector accounting for a third of this consumption [34]. Carbon fibres derived from polyacrylonitrile (PAN) precursors became the predominant reinforcement in composites for aerospace applications in the 1960s. These PAN-based carbon fibres offer excellent tensile strength but have relatively low thermal conductivity. Bethwick [35] cited that typical tensile strengths for standard modulus PAN-based carbon fibres range from 3.5 GPa to 4.8 GPa and stiffnesses are approximately 250 GPa. Typical axial thermal

conductivity k_{fa} for these fibres ranges from 7 W/mK to 10 W/mK. The author also reported that ultra high modulus PAN-based carbon fibres are available, which have higher stiffnesses ranging from 440 GPa to 1000 GPa and also higher k_{fa} values ranging from 40 W/mK to 75 W/mK, but these fibres have lower tensile strengths ranging from 2.1 GPa to 3.2 GPa.

The development in the 1970s of mesoscale pitch-based carbon fibres derived from petroleum and coal tar offered improved stiffnesses and drastically increased thermal and electrical conductivities, at the expense of reduced tensile strength compared to PAN-based fibres. Typical thermally conductive pitch-based carbon fibres have stiffnesses of approximately 960 GPa and tensile strengths ranging from 1.7 GPa to 1.9 GPa while k_{fa} values can be as high as 1100 W/mK [35]–[37]. PAN-based fibres are less expensive than pitch-based fibres and the majority of all carbon fibres used today are PAN-based, as shown by production numbers for PAN-based carbon fibres relative to pitch-based fibres from major global producers, Table 2.1 [34].

Table 2.1 - Global production of PAN-based and pitch-based carbon fibres by major manufacturers [34]

	PAN (tons)	Pitch (tons)
Toray Industries	9100	
Toho Tenax	8200	
Mitsubishi	4700	
Zoltek	3500	
Hexcel	2300	
Formosa Plastics	1750	
Cytec Engineered Materials	1500	360
SGL Carbon Group	1500	
Mitsubishi Chemical		750
Nippon Graphite Fibre		120

A relatively recent technology is the synthesis of carbon fibres grown from the vapour of low molecular weight hydrocarbon compounds, referred to as vapour-grown carbon fibres (VGCFs). Unlike continuous PAN-based and pitch-based carbon fibres, VGCFs are produced in short lengths of 50 mm to 70 mm and in diameters as small as 0.1 μm [38]. Their commercialization in the 1990s placed more emphasis on enhancing specific properties such as electrical and thermal conductivities, where values up to 2000 W/mK were reported on a pilot scale [3, 7, 8]. Tensile strengths are comparable to those of PAN-based carbon fibres while stiffnesses are highly dependent on the diameter [41].

PAN-based carbon fibres are now discussed in more detail, as work conducted towards this thesis used fibres of this type, which are more common in industrial aerospace applications. Hou et al. [42] measured the thermal diffusivity of a single PAN-based fibre to be 1.15×10^{-7} m^2/s using optical heating and electrical thermal sensing techniques, resulting in a thermal conductivity of 0.17 W/mK which is lower than most reported values. Wei [43] reported k_{fa} values for T300 and another unspecified Chinese-made PAN-based fibre to be 4.9 W/mK and 4.4 W/mK respectively using the laser flash method, compared to 10.5 W/mK cited by Toray datasheets for T300 [44]. The effect of heat treatment temperature upon manufacturing was reported in the literature. Katzman et al. [45] reported k_{fa} values in the range of 2 W/mK to 14 W/mK for unspecified PAN-based fibres at different heat treatment temperatures, Figure 2.1. Qiu et al. [46] measured k_{fa} and obtained values in the range of 20 W/mK to 69 W/mK from an unspecified general purpose grade PAN-based fibre heat treated at temperatures from 1500°C to 2100°C.

Thermal conductivities measured at various temperatures were also investigated. Yamane et al. [47] calculated k_{fa} values between 300 K to 800 K of PAN-based fibres from their measured thermal diffusivities. The authors studied five MJ series high stiffness PAN-based fibres and two T series high strength PAN-based fibres from Toray. The k_{fa} values ranged from 5 W/mK to 180 W/mK as a function of temperature, Figure 2.2. The k_{fa} values for the high strength fibres were within the typical values for PAN-based fibres cited above while those for the high stiffness fibres were some of the highest reported for PAN-based fibres. Also, correlations were found relating thermal conductivity of carbon fibres to their stiffness, as stiffness and thermal conductivity are directly dependent on the microstructure, Figure 2.3 [36].

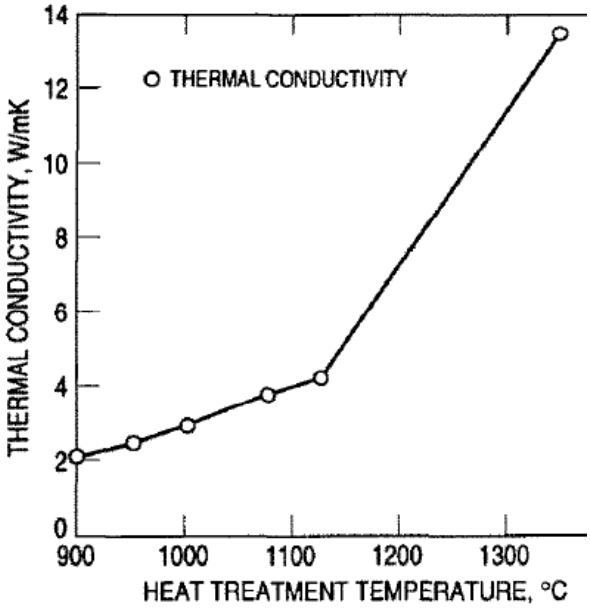

Figure 2.1 - Thermal conductivity of PAN-based carbon fibres as a function of heat treatment temperature [45]

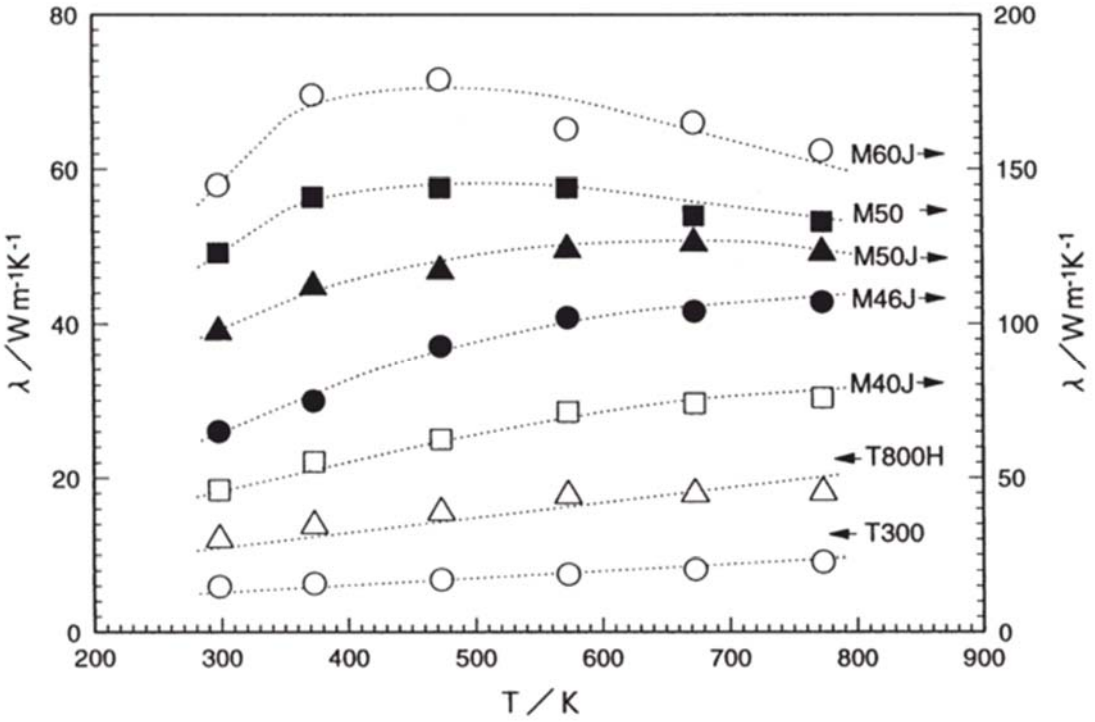

Figure 2.2 - Thermal conductivity of several high stiffness and high strength PAN-based carbon fibres as a function of temperature [47]

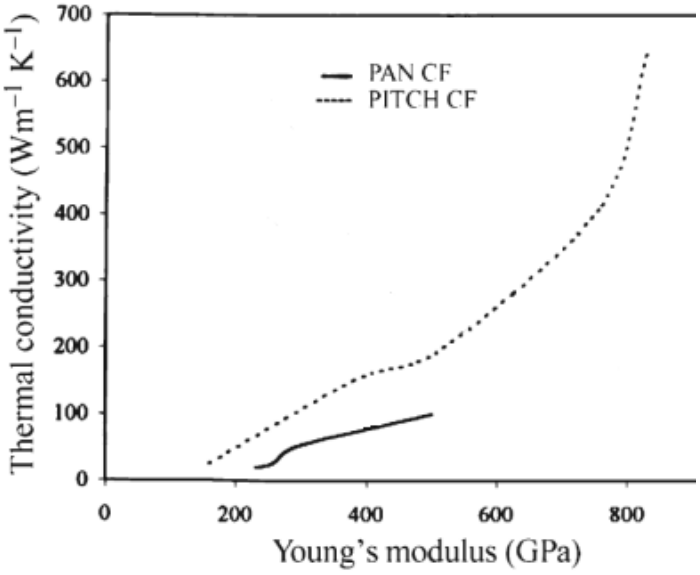

Figure 2.3 - Thermal conductivity of PAN-based and pitch-based carbon fibres as a function of stiffness [36]

Various datasheets for PAN-based carbon fibres are available from suppliers along with the literature cited above. k_{fa} values reported by Hexcel for fibres IM7, IM10 and AS4 are 5.4 W/mK, 6.1 W/mK and 6.8 W/mK, respectively [48]–[50]. Hind [51] cited values of 8.4 W/mK and 9.5±1.1 W/mK for AS4 fibres from two journal papers. Toho Tenax cited k_{fa} for both the HTS40 and HTS45 fibres to be 10 W/mK [52]. Toray cited 10.5 W/mK for the k_{fa} of fibre T300 [44] while BP Amoco cited 14 W/mK and 15 W/mK for fibres k_{fa} of the T650/35 and T650/42, respectively [53].

Data for the transverse fibre thermal conductivity k_{ft} is more difficult to find in the literature or from suppliers. k_{ft} of PAN-based carbon fibres is often estimated by the general rule of anisotropy ratios stating that k_{ft} is generally 5 to 10 times smaller than k_{fa} [54], or back-calculated from various analytical models using through-thickness thermal conductivity

k_{ctt} measurements made on composite plates of known V_f [55]. The only k_{ft} values cited by suppliers are 5 W/mK for both the T650/35 and T650/42 from BP Amoco [53].

Although most thermal conductivity values reported for PAN-based fibres are low, there are also some fibres with high thermal conductivities such as the MJ series reported above and the Thornel 50 which is cited to have k_{fa} of 70 W/mK by the supplier Cytec [56]; Lee et al. [57] measured 59 W/mK for the same fibre using the laser flash method. As a credible general estimate in accordance with the above datasheets, a present-day common grade commercial PAN-based carbon fibre can be expected to have a k_{fa} value in the range of 5 W/mK to 15 W/mK and a k_{ft} value 5 to 10 times smaller than the k_{fa}.

A summary of the room temperature thermal conductivity values for various PAN-based carbon fibres is shown in Table 2.2.

Table 2.2 - Summary of room temperature thermal conductivities of PAN-based carbon fibres

Direction	Type	Carbon fibre	Thermal conductivity (W/mK)	Authors
Axial	HTS	T300	4.9	Wei [43]
		T300	10.5	Toray [44]
		T300	7	Yamane et al. [47]
		unspecified	4.4	Wei [43]
		IM7	5.4	Hexcel [49]
		IM10	6.1	Hexcel [48]
		AS4	6.8	Hexcel [50]
		AS4	8.4	Hind [51]
		AS5	9.5	Hind [51]
		HTS40	10	Toho Tenax [52]
		HTS45	10	Toho Tenax [52]
		T800H	13	Yamane et al. [47]
		T650/35	14	BP Amoco [53]
		T650/42	15	BP Amoco [53]
	HM	M40J	18	Yamane et al. [47]
		M46J	26	Yamane et al. [47]
		M50J	39	Yamane et al. [47]
		M50	49	Yamane et al. [47]
		M60J	58	Yamane et al. [47]
Transverse	HTS	T650/35	5	BP Amoco [53]
		T650/42	5	BP Amoco [53]

2.1.2 Carbon fibre fabrics

Carbon fibre fabrics are used extensively in the aerospace industry as reinforcements for composites; in this work the term reinforcement is used interchangeably with fabric. Knowledge of their thermal conductivity is paramount in modelling heat transfer in processes such as in-autoclave and out-of-autoclave infusion, where the thermal properties of dry

fabrics must be known at various fibre volume fractions prior to impregnation. This knowledge would also benefit the understanding of heat conduction in comparable materials with applications to the high performance clothing industry. However, there is little published data regarding any type of thermal conductivity for these fabrics, despite their common usage and the fact that data for their constituent fibres are found readily in the published literature.

Most data found for the thermal conductivity of fabrics originate from the clothing industry, for applications such as fire-fighter clothing design or thermal insulation for winter jackets. Matusiak [58] studied the through-thickness thermal insulation properties of single and multi-layered textile materials including cotton fabrics, and concluded that porous non-woven materials have high thermal conductivity. Uzun [59] measured the through-thickness thermal conductivity of fabrics, also called reinforcements, k_{rtt} made of natural-based material such as linen, bamboo, cotton and wool. Onofrei et al. [60] conducted studies on the effect of the knitting structure on k_{rtt} of fabrics made of thermo-regulating yarns. Thermal conductivities were measured for nine different knitted structures, with certain knitting structures such as the locknit and double locknit found to have higher thermal conductivity than others. The authors stated that the thermal conductivity of the air medium is extremely important in contributing to the thermal conductivity of the fabrics made of fibres that are generally far less conductive than carbon fibres. Matusiak and Silkorski [61] studied the effect of fabric architecture in a broader sense by measuring k_{rtt} for cotton fabrics made of several types of weaves: plain, twill 1/3, twill 2/2, rep 1/1, rep 2/2 and hopsack 2/2, Figure 2.4. The plain weave fabric yielded the highest thermal conductivity which the authors

attributed to its higher density, followed by the twill 1/3 and the rep 2/2, while the hopsack 2/2 yielded the lowest thermal conductivity.

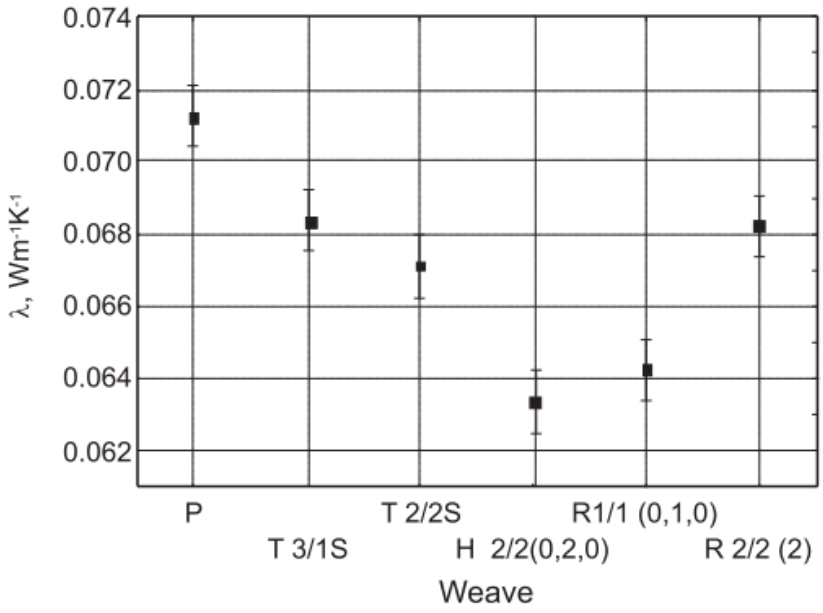

Figure 2.4- Effect of weave type on the thermal conductivity of woven cotton fabrics [61]

A few papers were found that studied the general heat transfer behaviour of woven fabrics. Li et al. [7] investigated heat conduction in PAN-based carbon fibre fabrics based on thermal radiation and infrared imaging technology. The authors obtained temperature-time curves for five different fabrics and concluded that infrared thermal imaging is a simple method of evaluating heat conduction performance in carbon fibre fabrics. Ziaei et al. [62] studied the thermal insulation properties of cotton and polyester spacer fabrics impregnated with ceramic powders, which effectively reduced the thermal conductivity of these fabrics. The authors stated that natural convection in porous materials with densities of 20 kg/m^3 or higher is negligible [30, 31]. Similar to Onofrei et al., Ziaei et al. also pointed out that as the

thermal conductivity of air is much lower than that of the fibres, air between the fibres plays an important role in determining the thermal properties of reinforcements.

Even fewer studies originated from the composites or aerospace industry and academia, studying the in-plane thermal conductivity k_{rip} or through-thickness thermal conductivity k_{rtt} of dry carbon fibre reinforcements. Yamashita et al. [9] measured k_{ft} of T300 carbon fibres, as well as k_{rtt} of plain woven fabrics made from the same fibre, and k_{ctt} of fibre-epoxy composite using the same fabric. Experiments were performed using the KES-F7 Thermo Labo apparatus; k_{ft} was measured to be 0.095 W/mK whilst k_{rtt} and k_{ctt} values are shown in Figure 2.5. The authors developed two models for the through-thickness thermal conductivity of the fabric and composite using an electric circuit analogy. Measurements and model predictions were evaluated between 20% to 50% V_f. For the fabric k_{rtt} values ranged from 0.05 W/mK to 0.08 W/mK, varying linearly with V_f. The authors attributed this increase to the higher fibre content as fibres have a higher thermal conductivity than the air medium, without providing further explanation on the linear trend nor experimental details on how the V_f values were obtained. For the composite, k_{ctt} ranged from 0.21 W/mK to 0.25 W/mK and remained constant with V_f, which is unusual for carbon fibre-epoxy composites as k_{ctt} is found to increase with V_f in literature as reported in Section 2.3.

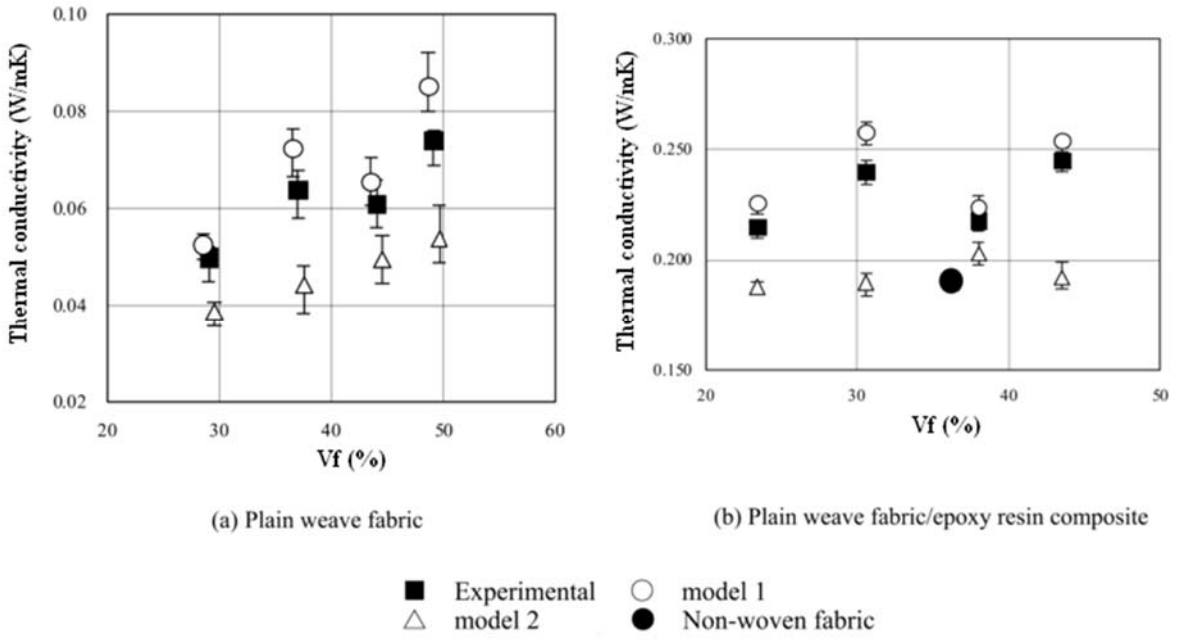

Figure 2.5 - Effect of fibre volume fraction V_f on through-thickness thermal conductivity of plain woven carbon fabric k_{rtt} and its fabric-epoxy composite k_{ctt} [9]

Bol'shakova et al. [64] measured the axial and transverse thermal conductivity of several carbon-graphite fibre stacks, Figure 2.6. Theirs is also the only published paper found to study the in-plane as well as the through-thickness thermal conductivity of several carbon-graphite fibre fabrics, Figure 2.6. Uglen and Evlon are viscose carbon fibres and VMN-4 is a carbon braid consisting of an unspecified PAN-based carbon fibre. Thermal conductivities were measured for each of these three fibres stacked into a cylindrical cell. Measurements were done over a temperature range of 0°C to 600°C in a medium of either air or oil, and different stacks were used for measuring the axial and the transverse thermal conductivities.

The densities of the Uglen and Evlon fibres are 1550 kg/m^3 and 1470 kg/m^3 respectively while that of the VMN-4 braid is unknown. The fibre volume fraction V_f values

of the Uglen and Evlon stacks used for axial measurements were calculated to be 25% and 50% respectively from the stack densities given in Figure 2.6 (a) while that of the VMN-4 is unknown. Similarly, V_f of the Evlon stack used for transverse measurements was calculated to be 34% from the stack density given in Figure 2.6 (b) while those of the Uglen and VMN-4 are unknown. Hence the axial thermal conductivity values are not directly comparable to the transverse values, as the fibre stacks used had different V_f values. However, the results do demonstrate room temperature anisotropy ratios of approximately 18 and 10 for the VMN-4 and Evlon fibres respectively which fall in line with the generally-accepted anisotropy ratios mentioned above. The effect of the medium on the axial thermal conductivity of a fibre stack can be seen through the significant increase for the Evlon stack measured in oil compared to the stack in air, while this effect is not seen in the transverse direction. For the VMN-4 PAN-based fibre, axial thermal conductivity values remain approximately constant with temperature while those in the transverse direction increase as a function of temperature following a generally linear trend.

k_{rip} values for graphite fibre fabric TGN-2M and k_{rtt} values for carbon fibre fabric Ural T-22 as a function of temperature in different mediums of air, nitrogen and vacuum were also measured, Figure 2.7. The authors did not state the V_f values associated with these measurements nor the fabric architectures. Thermal conductivity in air in both directions increased with temperature, where k_{rtt} values ranged from 0.6 W/mK to 1.4 W/mK following an exponential recovery trend. k_{rtt} values ranged from 0.22 W/mK to 0.28 W/mK following a linear trend. Comparing thermal conductivities in air in the in-plane and through-thickness directions yields an anisotropy ratio of 3; however these graphs cannot be

compared directly since the measurements result from fabrics of different densities using different carbon and graphite fibres with no specified fabric architecture. The authors already concluded from measurements presented in Section 2.1.1 that the transverse thermal conductivity of fibres is affected by the medium while this effect is not seen for the axial thermal conductivity. From Figure 2.7 (b) it is seen that the transverse thermal conductivity of fabrics is also affected significantly by the medium and this difference is especially prominent between results obtained in air and in vacuum.

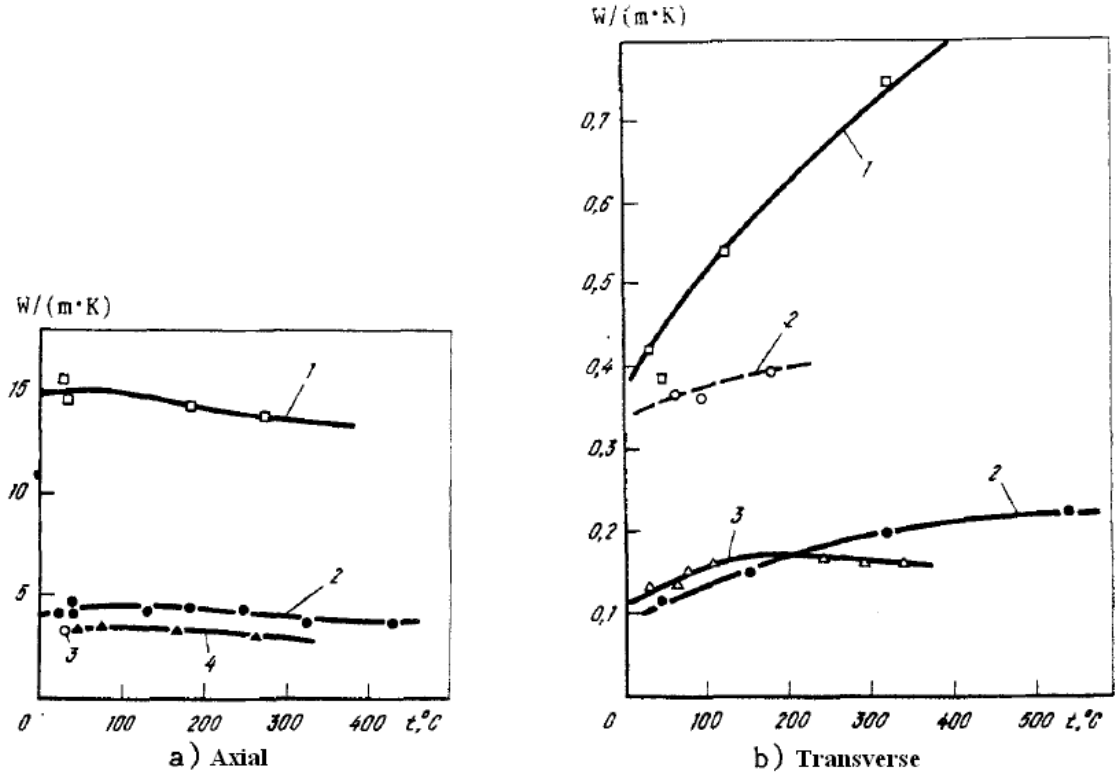

a) Thermal conductivity of carbon-graphite fiber materials in the longitudinal direction: 1) VMN-4, density 1094 kg/m³; 2, 3) Évlon, density 735 kg/m³; 4) Uglen, density 386 kg/m³ Medium: 1, 2, 4) air; 3) oil

b) The thermal conductivity of carbon-graphite materials in the transverse direction: 1) VMN-4, density 682 kg/m³; 2) Évlon, density 503 kg/m³; 3) Uglen in the form of braid with impregnation with oil mixed with commercial carbon
Medium: ——) air; ----) oil

Figure 2.6 - Axial k_{fa} and transverse k_{ft} thermal conductivities of several carbon fibres as a function of temperature [64]

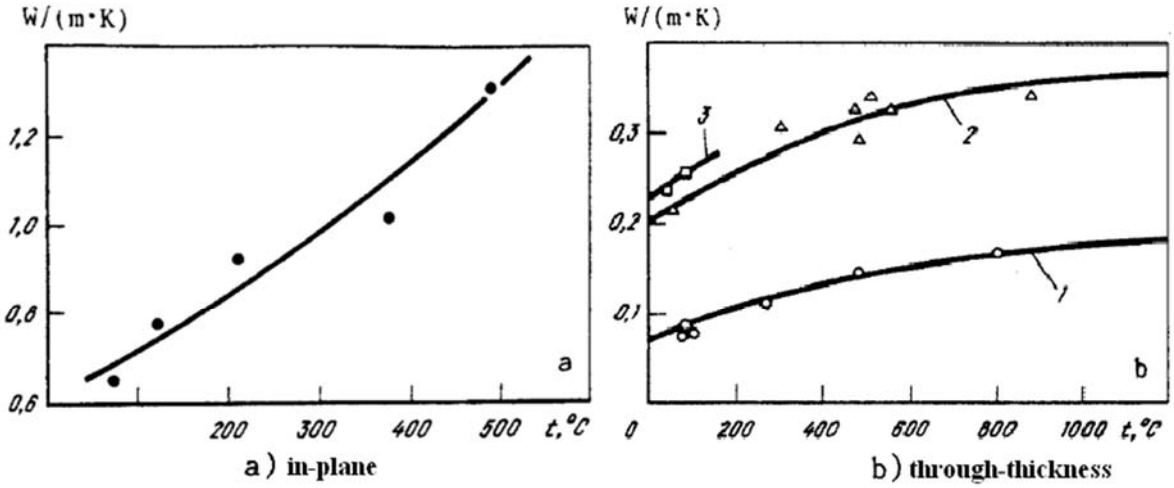

Thermal conductivity of carbon-graphite fabrics: a) TGN-2M, density 442 kg/m³, medium air; b) Ural T-22, density 687 kg/m³, medium: 1) vacuum; 2) nitrogen; 3) air.

Figure 2.7 - In-plane thermal conductivity k_{rip} of a carbon fibre fabric and through-thickness thermal conductivity k_{rtt} of a graphite fibre fabric as a function of temperature [64]

Regarding fabric thermal conductivity data obtained from suppliers, Cytec [65] cites a k_{rtt} value of 0.25 W/mK for Thornel VCB-20 carbon fibre cloth while stating that k_{fa} for the constituent carbon fibre is 15 W/mK.

A summary of room temperature thermal conductivities for carbon fibre fabrics available in the literature appears in Table 2.3.

Table 2.3 - Summary of room temperature thermal conductivities of carbon fibre fabrics

Carbon fabric	Direction	Architecture	Medium	V_f (%)	Thermal conductivity (W/mK)	Authors
T300 fibre fabric	through-thickness	plain weave	air	29	0.05	Yamashita et al. [9]
T300 fibre fabric	through-thickness	plain weave	air	37	0.06	Yamashita et al. [9]
T300 fibre fabric	through-thickness	plain weave	air	44	0.06	Yamashita et al. [9]
T300 fibre fabric	through-thickness	plain weave	air	49	0.75	Yamashita et al. [9]
TGN-2M	in-plane	unspecified	air	unspecified	0.95	Bol'shakova et al. [64]
Ural-T22	through-thickness	unspecified	air	unspecified	0.30	Bol'shakova et al. [64]
Ural-T22	through-thickness	unspecified	nitrogen	unspecified	0.28	Bol'shakova et al. [64]
Ural-T22	through-thickness	unspecified	vacuum	unspecified	0.11	Bol'shakova et al. [64]
Thornel VCB-20	through-thickness	unspecified	air	unspecified	0.25	Cytec [65]

This literature review reported on a number of studies where k_{fa} was measured and a few where k_{ft} was measured. There are also studies measuring the in-plane thermal conductivity k_{rip} and through-thickness thermal conductivity k_{rtt} of carbon fibre reinforcements with preliminary investigations on the effect of fabric architecture, medium and V_f. However, no paper has studied both k_{rip} and k_{rtt} of dry carbon fibre fabrics as a function of V_f systematically. Chapter 3 of this thesis reports work done on measuring k_{rip} as well as measuring and modelling k_{rtt} at various V_f values for the same fabrics. Thermal conductivities of the constituent fibres k_{fa} and k_{ft} are known or calculated from analytical models, and anisotropy ratios of the fabrics are compared to those of the fibres. The effects of vacuum and fabric architecture on k_{rip} and k_{rtt} are also studied.

2.2 Thermal conductivity of carbon fibre-epoxy composites

2.2.1 Unidirectional composites

The thermal conductivity of unidirectional composites in the axial or fibre direction k_1 can be calculated using the axial rule of mixture (ROM-A). This model is widely acknowledged and requires the thermal conductivity of the constituent fibres k_{fa}, thermal conductivity of the matrix k_m and the fibre volume fraction V_f:

$$k_1 = V_f \cdot k_{fa} + (1 - V_f) \cdot k_m \tag{2.1}$$

Many analytical models exist for predicting the thermal conductivity of unidirectional composites in the in-plane direction transverse to the fibres k_2, which is the same as the

through-thickness thermal conductivity k_{ctt} for unidirectional composites. The simplest model for predicting k_2 is the transverse rule of mixture (ROM-T):

$$k_2 = \frac{1}{\frac{V_f}{k_{ft}} + \frac{1-V_f}{k_m}} \tag{2.2}$$

This model does not account for fibre geometry and fibre packing arrangement in the matrix, and generally underestimates the thermal conductivity [66]. Springer and Tsai [67] identified the model as the lower bound for k_2 and the authors developed a semi-empirical model applicable to cylindrical or square filaments packed in a square array, based on a shear loading analogy for unidirectional composites. Model predictions agreed reasonably well with experimental data with a maximum error of 15% at 58% V_f. Equations for the case of cylindrical fibres are shown below:

$$\frac{k_2}{k_m} = \left(1 - 2\sqrt{\frac{V_f}{\pi}}\right) + \frac{1}{B}\left(\pi - \frac{4}{\sqrt{1 - B^2 \cdot V_f / \pi}} \tan^{-1} \frac{\sqrt{1 - B^2 \cdot V_f / \pi}}{1 + B^2 \cdot V_f / \pi}\right) \tag{2.3}$$

where

$$B = 2\left(\frac{k_m}{k_{ft}} - 1\right) \tag{2.4}$$

Clayton [68] developed a semi-empirical model validated by Dasgupta et al. [69] where thermal conductivity values vary following a power law trend as a function of V_f:

$$k_2 = \frac{k_m}{4}\left\{\sqrt{\left(1 - V_f\right)^2 \left(\frac{k_{ft}}{k_m} - 1\right)^2 + \frac{4k_{ft}}{k_m}} - \left(1 - V_f\right)\left(\frac{k_{ft}}{k_m}\right)\right\}^2 \tag{2.5}$$

Halpin and Tsai [70] developed a model accounting for the fibre geometry, which was validated by Antar et al. [12] showing a maximum deviation of 12% from experimental data. For cylindrical fibres:

$$k_2 = \frac{1+\eta \cdot V_f}{1-\eta \cdot V_f} \tag{2.6}$$

where

$$\eta = \frac{k_{ft}/k_m - 1}{k_{ft}/k_m + 1} \tag{2.7}$$

Lewis and Nielsen [70] proposed a model to further account for the shape and packing of the reinforcement which was validated by Pal [71] and Antar et al. [12]:

$$k_2 = k_m \left(\frac{1+A \cdot B \cdot V_f}{1-B \cdot \varphi \cdot V_f} \right) \tag{2.8}$$

where ϕ_m is the maximum volume fraction of the reinforcement achieved for a specified packing arrangement and parameter A is chosen based on the shape and orientation of the fibres from Table 2.4. Parameters B and φ are given by the following equations:

$$B = \frac{k_{ft}/k_m - 1}{k_{ft}/k_m + A} \tag{2.9}$$

$$\varphi = 1 + \left(\frac{1-\phi_m}{\phi_m{}^2} \right) V_f \tag{2.10}$$

Table 2.4 - Parameters for Lewis-Nielsen model

Type of dispersed phase	Direction of heat flow	A
Cubes	Any	2.0
Spheres	Any	1.50
Aggregates of spheres	Any	$\frac{2.50}{\phi_a} - 1$
Randomly oriented rods Aspect ratio = 2	Any	1.58
Randomly oriented rods Aspect ratio = 4	Any	2.08
Randomly oriented rods Aspect ratio = 6	Any	2.8
Randomly oriented rods Aspect ratio = 10	Any	4.93
Randomly oriented rods Aspect ratio = 15	Any	8.38
Uniaxially oriented fibers	Parallel to fibers	$2L/D$
Uniaxially oriented fibers	Perpendicular to fibers	0.5

Shape of Particle	Type of Packing	ϕ_m
Spheres	Hexagonal close	0.7405
Spheres	Face centered cubic	0.7405
Spheres	Body centered cubic	0.60
Spheres	Simple cubic	0.524
Spheres	Random close	0.637
Spheres	Random close	0.601
Rods or fibers	Uniaxial hexagonal close	0.907
Rods or fibers	Uniaxial simple cubic	0.785
Rods or fibers	Uniaxial random	0.82
Rods or fibers	Three dimensional random	0.52

Progelhof [70] identified the Lewis-Nielsen model as the most reliable for predicting k_2. However, for continuous fibre-reinforced composites, differences between between Clayton and Lewis-Nielsen model predictions are small [51]; hence the simpler Clayton model is used for calculating k_2 in this work.

Wetherhold et al. [55] reported that models developed for predicting k_2 such as the ones above are accurate as long as contacts between the fibres and the matrix are adequate and the composite is free of major cracks and delaminations, and as long as k_{ft} and k_m values stay in a comparable range. In this work, the HTS40 carbon fibres used have a calculated k_{ft} value of 1.36 W/mK as shown in Chapter 3, which is relatively close to k_m values of epoxy resins at approximately 0.2 W/mK; hence these models apply.

There are also various models available in the literature that account for the effect of voids on the through-thickness thermal conductivity, presented in Section 2.3.2. The effect of voids on k_2 and k_{ctt} are accounted for, first by using these void models to adjust the matrix thermal conductivity k_m then using this adjusted value in the above models for predicting k_2 .

Knowing the thermal conductivity of a unidirectional ply in the in-plane directions parallel or transverse to the fibres k_1 and k_2, the in-plane thermal conductivity of laminates composed of such plies in any direction can be calculated using the classical lamination theory (CLT) developed by Tsai and Hahn [72]. Values of k_1 are given by Equation 2.1 above and values of k_2 can be calculated using various analytical models as discussed above.

For the 0° direction, the thermal conductivity of the laminate is given by Equation 2.11 knowing the laminate thickness $2h$, orientation θ_i of the i^{th} ply, thickness t_i of the i^{th} ply and the number of plies N :

$$k_{0^\circ} = \frac{1}{2h}\sum_{i=1}^{N} t_i \left(k_1 \left(\cos\theta_i\right)^2 + k_2 \left(\sin\theta_i\right)^2 \right) \qquad (2.11)$$

It can be shown that laminates featuring groups of equal numbers of plies separated by equal angles of $\pi/2$ or less demonstrate in-plane isotropy for thermal conductivity, as opposed to an angle of $\pi/3$ or less required for in-plane isotropy of mechanical properties [51]. This means that laminates with layups such as $[0/90]_s$ will have the same thermal conductivity k_{cip} along any in-plane direction, known as the effective in-plane thermal conductivity k_{cip} while for a unidirectional laminate, the value of k_{cip} along any in-plane direction varies between k_1 and k_2.

Tsai and Hahn [51] state that the through-thickness thermal conductivity k_{ctt} of laminates consisting of unidirectional plies can be assumed to equal k_2 of a single unidirectional ply since the transverse conductivities for the plies are equal and independent of orientation; hence the analytical models presented above for k_2 are also applicable in predicting k_{ctt} of these composites.

Pilling et al. [73] measured the thermal conductivity of unidirectional and bidirectional carbon fibre-epoxy composites in various in-plane directions. At 270K, the reported k_1 value of unidirectional composites reinforced with PAN-based high modulus (HM) fibres with a V_f of 60.7% is 50.6 W/mK, compared with 9.33 W/mK for unidirectional composites reinforced with PAN-based high tensile strength (HTS) fibres at a similar V_f. This was also true for bidirectional composites; those reinforced with HM fibres had higher thermal conductivities than those reinforced with HTS fibres. For balanced bidirectional composites reinforced with HM fibres at 270K, in-plane thermal conductivity parallel to one set of fibres at a V_f of 55.7% is 22.6 W/mK, compared to 22.0 W/mK for the thermal

conductivity at the bisecting angle between the two sets of fibres at a similar V_f. These results agree with conclusions from the CLT mentioned above, as the in-plane thermal conductivity of balanced bidirectional composites should be isotropic. The authors also showed that the thermal conductivity increased linearly as a function of temperature, for both unidirectional and bidirectional composites. Values ranged from 1.9 W/mK to 9.33 W/mK for k_1 of HTS unidirectional composites and from 1.2 W/mK to 5.73 W/mK for k parallel to one set of fibres of HTS bidirectional composites, within a temperature range of 90 K to 270K.

Kregers et al. [74] reported 4.08 W/mK for k_1 for a unidirectional carbon-reinforced polymer at 61.3% V_f. Radcliffe et al. [75] reported measured values for HM and HTS unidirectional carbon fibre-epoxy composites at cryogenic temperatures from 2 K to 80K. The authors reported a k_1 value of 2 W/mK for the composites reinforced with the HTS fibres and 8 W/mK for the composites reinforced with the HTM fibres at 80K. Hind [51] reported room temperature k_1 values for two unidirectional laminates at 62% V_f to be 6.40 W/mK and 7.33 W/mK and room temperature k_2 values for the same laminates to be 0.70 W/mK and 0.85 W/mK, compared to room temperature k_{cip} values of the same laminates to be 3.07 W/mK and 3.28 W/mK. A $[0/90/0/90]_s$ laminate made from the same prepreg material at the same V_f was reported to have a k_{cip} value of 2.99 W/mK. Although many of the measurements found in the literature were performed on composites reinforced with PAN-based fibres, some authors also investigated the thermal conductivity of composites reinforced with pitch-based fibres, resulting in much higher in-plane thermal conductivity values such as 96.4 W/mK for a unidirectional composite reported by Nysten et al [76].

Piling et al. [73] reported values of 1.463 W/mK and 0.747 W/mK for k_2 of unidirectional carbon fibre-epoxy plates reinforced with HM and HTS fibres respectively at similar V_f values close to 60%. As mentioned above, k_2 of a unidirectional laminate is the same as k_{ctt}. The authors reported that k_2 increased linearly with temperature in the range of 175 K to 270K and increased exponentially as a function of V_f, which agrees with the trend predicted by the Clayton model. Kregers et al. [74] reported 0.39 W/mK for k_2 of a unidirectional carbon-reinforced polymer at 61.3% V_f. Radcliffe et al. [75] concluded that differences in k_2 due to the type of reinforcing fibres were small at these temperatures and reported a k_2 value of 0.3 W/mK at 80K for HTS and HTM fibre-epoxy composites. Hind [51] reported measured room temperature k_{ctt} values of two unidirectional prepreg laminates at 62% V_f to be 0.73 W/mK and 0.81 W/mK and that of a $[0/90/0/90]_s$ bidirectional laminate made of the same prepreg at a similar V_f to be 0.74 W/mK.

A summary of thermal conductivity values in various directions for PAN carbon fibre-reinforced non-woven composites is shown in Table 2.5.

Table 2.5 - Summary of thermal conductivities of PAN carbon fibre-reinforced composites

Type of carbon fibre	Lamination	Direction	Temperature (K)	V_f (%)	Thermal conductivity (W/mK)	Authors
HM-reinforced	unidirectional	parallel to fibres	80	48	8.0	Radcliffe et al. [75]
		parallel to fibres	270	61	50.6	Pilling et al. [73]
		perpendicular to fibres	80	50	0.3	Radcliffe et al. [75]
		perpendicular to fibres	270	58	1.5	Pilling et al. [73]
	balanced directional	parallel to one set of fibres	270	56	22.6	Pilling et al. [73]
		along bisecting angle between the two sets of fibres	270	56	22.0	Pilling et al. [73]
HTS-reinforced	unidirectional	parallel to fibres	80	51	2.0	Radcliffe et al. [75]
		parallel to fibres	270	58	9.3	Pilling et al. [73]
		parallel to fibres	298	62	6.4	Hind [51]
		parallel to fibres	298	62	7.3	Hind [51]
		perpendicular to fibres	80	50	0.3	Radcliffe et al. [75]
		perpendicular to fibres	270	59	0.7	Pilling et al. [73]
		perpendicular to fibres	298	62	0.7	Hind [51]
		perpendicular to fibres	298	62	0.9	Hind [51]
		effective in-plane	298	62	3.1	Hind [51]
		effective in-plane	298	62	3.3	Hind [51]
		through-thickness	298	62	0.7	Hind [51]
		through-thickness	298	62	0.8	Hind [51]
	balanced directional	parallel to one set of fibres	270	62	5.7	Pilling et al. [73]
		effective in-plane	298	62	3.0	Hind [51]
		through-thickness	298	62	0.7	Hind [51]
Unspecified	unidirectional	parallel to fibres	298	61	4.1	Kregers et al. [74]
		perpendicular to fibres	298	61	0.4	Kregers et al. [74]

2.2.2 Woven textile composites

Modelling the thermal conductivity of woven textile composites is more complicated than that of unidirectional composites, as the geometry of the reinforcement is more complex. Most models found in the literature are complex analytical models based on circuit analogies or computational models of conduction performed on textile composite unit cells to account for geometry characteristics. This type of modelling was done previously by Hind [51] in a thorough manner and is not the emphasis of the present work; a brief review will be given here.

Gowayed and Hwang [77] studied the through-thickness thermal conductivity of composites made from plain weaves. The authors concluded that the fabric geometry model developed by Kregers [78] yields thermal conductivity predictions close to experimental values, which varied from 0.29 W/mK to 0.45 W/mK for AS4 fibre-epoxy composites over a V_f range of 27% to 56%. Ning and Chou [79] constructed equivalent thermal resistance networks from the geometry of plain weave composites, twill weave composites and eight harness satin weave composites. The authors concluded that model predictions for k_{ctt} fall in line with experimental values for fibreglass-epoxy and Kevlar-epoxy composites. The authors reported predictions in the range of 0.29 W/mK to 0.31 W/mK for graphite-epoxy composites with a V_f of 36%, depending on the fabric architecture. Composites made from plain weave fabrics had a slightly higher thermal conductivity at 0.31 W/mK compared with those made from twill weave fabrics at 0.3 W/mK or eight harness satin weave fabrics at 0.29 W/mK. Similarly, the authors reported no significant effect of fabric architecture on k_{ctt} of fibreglass-epoxy and Kevlar-epoxy composites.

Dasgupta et al. [80] constructed unit cell models, Figure 2.8, to predict k_{cip} and k_{ctt} of composites featuring plain weave reinforcement architectures by solving microscale boundary value problems using finite element analysis, and reported that values agreed with experimental data for fiberglass-epoxy composites.

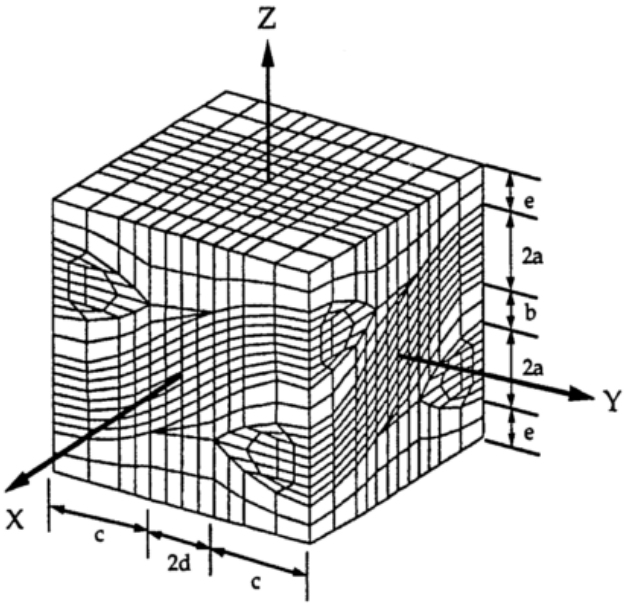

Figure 2.8 - Unit cell model, Dasgupta et al. [80]

Goo and Woo [81] measured k_{cip} and k_{ctt} for carbon fibre-epoxy composites made from reinforcements featuring a plain weave architecture, and predicted values using finite element analysis on a unit cell, Figure 2.9.

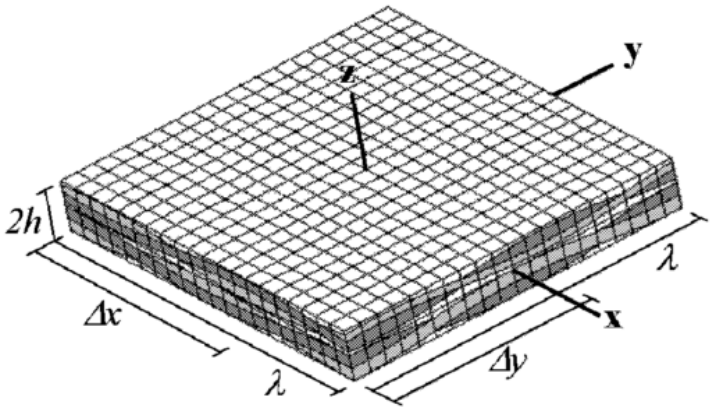

Figure 2.9 - Unit cell model, Goo and Woo [81]

Constituent fibres had k_{fa} and k_{ft} values of 8.4 W/mK and 0.84 W/mK respectively while the epoxy had a k_m value of 0.19 W/mK. The authors reported measured k_{cip} and k_{ctt} values of 1.73 W/mK and 0.33 W/mK respectively at a V_f of 70.7%, compared to model predictions of 2.12 W/mK and 0.35 W/mK. The authors also reported that both k_{cip} and k_{ctt} values increased linearly as a function of V_f, which is also supported by k_{ctt} results from unit cell simulations with plain weave architecture by Hind, Figure 2.10 [51].

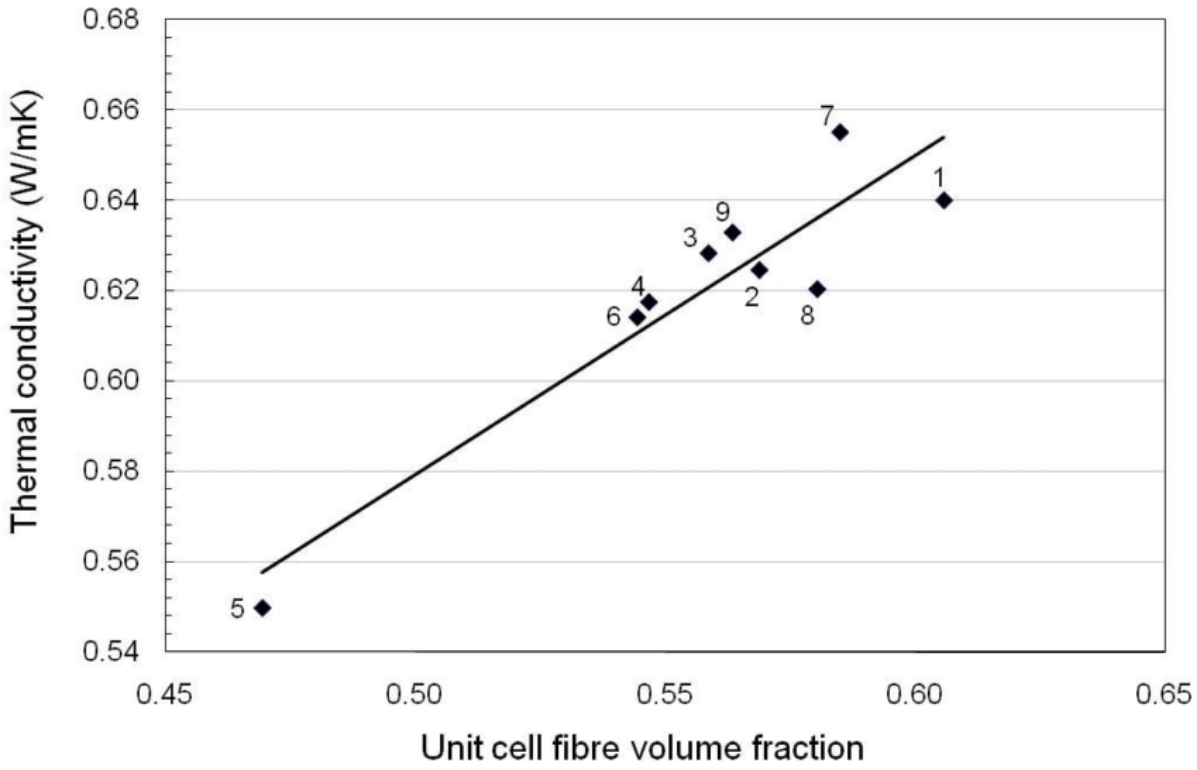

Figure 2.10 - Through-thickness thermal conductivity k_{rtt} as a function of fibre volume fraction V_f from woven unit cell simulations, Hind [51]

Hind [51] measured k_{cip} for two $[0/90]_8$ carbon fibre-epoxy plain weave prepreg laminates at a V_f of 61% at 2.56 W/mK, and k_{ctt} for the same laminates at 0.62 W/mK and 0.60 W/mK. Simulations of heat transfer through unit cells of the plain weave composite were developed, Figure 2.11; the author reported simulation results of 0.55 W/mK to 0.66 W/mK within a V_f range of 47% to 61%.

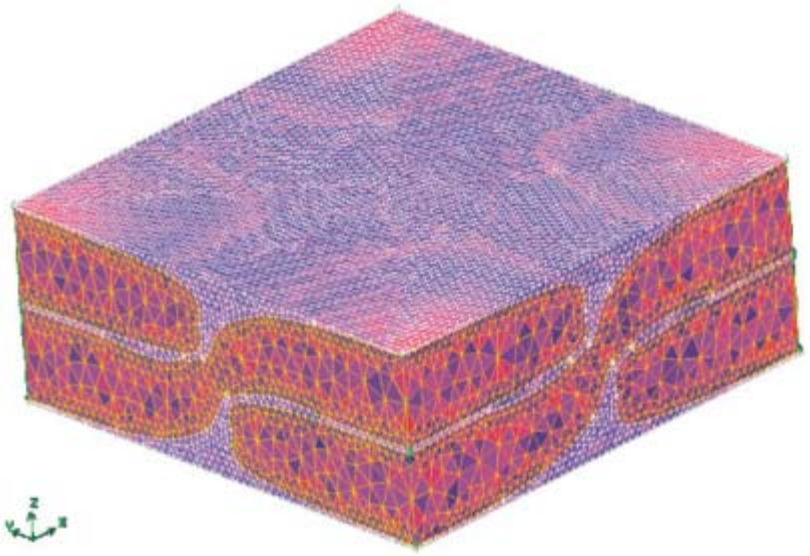

Figure 2.11 - Unit cell model, Hind [51]

A summary of the room temperature thermal conductivities of woven composites is shown in Table 2.6.

Table 2.6 - Summary of thermal conductivities of woven composites

	Fibre	Architecture	V_f (%)	Thermal conductivity (W/mK)	Authors
Effective in-plane	carbon-HTS	plain weave	71	1.73	Goo and Woo [81]
	carbon-HTS	plain weave	61	2.56	Hind [51]
	carbon-HTS	plain weave	61	0.62	Hind [51]
	carbon-HTS	plain weave	61	0.6	Hind [51]
Through-thickness	carbon-HTS	plain weave	56	0.45	Gowayed and Huang [77]
	graphite	plain weave	36	0.31	Ning and Chou [79]
	graphite	twill	36	0.3	Ning and Chou [79]
	graphite	eight harness satin	36	0.29	Ning and Chou [79]
	carbon-HTS	plain weave	71	0.33	Goo and Woo [81]

2.3 Addition of carbon nanotubes

2.3.1 Thermal conductivity of carbon nanotubes

Carbon nanotubes (CNTs) are increasingly being incorporated into composite materials to improve their mechanical, electrical and thermal properties [82]. Thermal conductivity data are available in the literature for CNTs, with values up to 6600 W/mK reported. However, thermal conductivity values vary widely depending on the morphology, diameter, length, purity, functionalisation and presence of any defects in the CNTs [66]. Functionalisation refers to the grafting of molecular chains onto to the CNTs by chemical reaction and is discussed in Section 2.3.2.

Li et al. [83] measured the room temperature thermal conductivity of an individual suspended single-wall carbon nanotube (SWCNT) 1.8 nm in diameter and 41 μm in length to be 2400 ± 400 W/mK by electrical heating in vacuum. Pop et al. [84] reported the room temperature thermal conductivity of a SWCNT 1.7 nm in diameter and 2.6 μm in length to be 3500 W/mK. Berber et al. [10] calculated the room temperature thermal conductivity of an individual SWCNT of unspecified diameter and length to be 6600 W/mK from molecular dynamics simulations. Gu et al. [85] calculated the room temperature thermal conductivity of an individual SWCNT of unspecified diameter and length to be 474 W/mK. Lukes and Zhong [86] conducted molecular dynamics simulations on SWCNTs of various lengths over a range from 5 nm to 40 nm and over a temperature range from 200 K to 500K, and reported that the thermal conductivity of SWCNTs increased with tube length; this trend was also reported by Cao et al [87].

Li et al. [83] measured the room temperature thermal conductivity of an individual multi-wall carbon nanotube (MWCNT) with an outer diameter of 8.2 nm, an unspecified

inner diameter and a length of 32 μm to be 1400 ± 250 W/mK. The lower thermal conductivity of the MWCNT compared to the SWCNT measured at 2400 ± 400 W/mK in the same study reported above was attributed to the higher density of defects and intertube scattering in MWCNTs. Kim et al. [88] measured the room temperature thermal conductivity of an individual MWCNT with an outer diameter of 14 nm, an unspecified inner diameter and a length of 2.5 μm with a micro suspension device to be greater than 3000 W/mK. The temperature dependence of thermal conductivity was also studied and a peak value of 3200 W/mK was seen at 320K.

Choi et al. [89] measured the room temperature thermal conductivity of an individual MWCNT with an outer diameter of 20 nm, an inner diameter of 10 nm and a length of 1.4 μm to be 300 ± 20 W/mK using the 3ω method. 3ω is a common measurement technique used for obtaining thermal conductivities of carbon nanotubes. A metal line is placed on the specimen to act as a heater. Applied alternating current excites the heater at a frequency ω and generates electrical resistance oscillations at a frequency of 2ω as well as a third harmonic at a frequency of 3ω. The thermal conductivity of the specimen can be obtained through analysis of the amplitude and phase of the third harmonic [90].

Fujii et al. [91] used a suspended T-type nano sensor for measuring the room temperature thermal conductivity of individual MWCNTs with different diameters and lengths. The authors reported a thermal conductivity of 2000 W/mK for a MWCNT with an outer diameter of 9.8 nm, an inner diameter of 5.1 nm and a length of 3.7 μm. A thermal conductivity of 1600 W/mK was found for a MWCNT with an outer diameter of 16.1 nm, an inner diameter of 4.9 nm and a length of 1.9 μm. Finally, a thermal conductivity of 500 W/mK was found for a MWCNT with an outer diameter of 28.2 nm, an inner diameter of 4.2

nm and a length of 3.6 μm. Thermal conductivities were found to decrease with increasing diameters, and were found to increase with temperature over a range from 100 K to 320K, Figure 2.12.

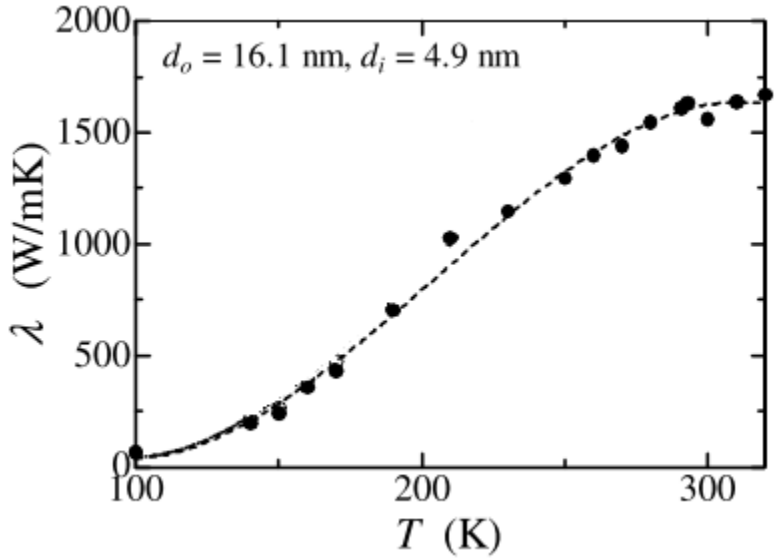

Figure 2.12 - Thermal conductivity of an individual MWCNT as a function of temperature [91]

The CNTs used in this thesis are Baytubes C150P from Bayer MaterialScience. These MWCNTs have an outer diameter of 13 nm, an inner diameter of 4 nm and a length of 1 μm. The thermal conductivity is reported to be 2000 W/mK from the product datasheet [92]. MWCNTs are easier to produce in large quantities [93] and hence they are sold at a much lower price by commercial suppliers. Table 2.7 shows prices for SWCNTs compared to MWCNTs, quoted from the catalogues of several large commercial CNT suppliers [94]–[97]. Room temperature thermal conductivity data for SWCNTs and MWCNTs as quoted above from the literature are summarized in Table 2.8.

Table 2.7 - Prices of CNTs from several commercial suppliers

SWCNTs		MWCNTs		Supplier
Purity	Price (US$/g)	Purity	Price (US$/g)	
99%	250	99%	25	Cheap Tubes Inc. [94]
unspecified	unknown	98.50%	24	Nanothinx [95]
>95%	200	>85%	12	Nanolab [96]
unspecified	210	unspecified	28 to 75	Helix Material Solutions [97]

Table 2.8 - Summary of room temperature thermal conductivities of SWCNTs and MWCNTs

	Length (μm)	Outer diameter (nm)	Inner diameter (nm)	Thermal conductivity (W/mK)	Authors
SWCNTs	2.6	1.7	N/A	3500	Pop et al. [84]
	41.0	1.8		2400 ± 400	Li et al. [83]
	unspecified	1.4		6600	Berber [10]
	unspecified	1.4		474	Gu et al. [85]
MWCNTs	1.0	13.0	4.0	2000	Bayer [92]
	1.4	20.0	10.0	300 ± 20	Choi et al. [89]
	1.9	16.1	4.9	1600	Fujii et al. [91]
	2.5	14.0	unspecified	3000	Kim et al. [88]
	3.6	28.2	4.2	500	Fujii et al. [91]
	3.7	9.8	5.1	2000	Fujii et al. [91]
	32.0	8.2	unspecified	1400 ± 250	Li et al. [83]

2.3.2 Effect of CNT addition on the thermal conductivity of polymers

CNT thermal conductivities as high as 6600 W/mK were reported as quoted in Section 2.3.1, hence they have been added into polymer matrices to enhance their thermal conductivity; such CNT-reinforced polymers are called nanocomposites. However, there is much scatter in experimental thermal conductivity data for nanocomposites k_{nc} reported in

the literature; some studies report large thermal conductivity increases of up to 300% upon loading 3% CNTs by weight in epoxy [14] while others mention decreases in thermal conductivity upon loading CNTs [68].

Han and Fina [66] conducted a review of the research done on the thermal conductivity of CNT-reinforced polymers. The authors reported several factors that affect the thermal conductivity of these nanocomposites: the interfacial resistance between the CNTs and the polymer, the dispersion of the CNTs in the polymer and the functionalisation of the CNTs. The authors reported that quantized modes of vibration occurring in a rigid crystal lattice, known as phonons, are the primary method of thermal conduction in CNT-reinforced polymers. High thermal interfacial resistance between CNTs and the polymer matrix comes from phonon vibration frequency mismatch at the interface, which causes phonon scattering and in turn decreases the thermal conductivity of the nanocomposite. Han and Fina cited this as the major reason why measured thermal conductivities of nanocomposites are much lower than what one may expect given the very high thermal conductivities of the CNTs themselves.

The authors stated that uniform dispersion of the CNTs also is important to enhance thermal conductivity successfully. When dispersion is poor, nanocomposites consisting of large CNT aggregates will be conductive locally while the surrounding polymer matrix shows low conductivity. It is difficult to disperse CNTs evenly throughout polymers because of the strong van der Waals forces that tend to hold them in bundles. However, if the nanoparticles were to be dispersed perfectly and form no physical network, heat would be forced to flow in series through many CNT-polymer interfaces, greatly impeding phonon transport and yielding a low thermal conductivity. Hence it is important that CNTs be

dispersed adequately to avoid large aggregates, but not overly so as to still form a network providing thermally conductive paths in the nanocomposite.

Functionalisation of CNTs also affects the thermal conductivity of nanocomposites. Clancy et al. [15] grafted linear hydrocarbon chains to the surfaces of SWCNTs through covalent chemical bonds. The authors reported that these bonds decreased the interfacial resistance and hence increased the thermal conductivity of the nanocomposite, Figure 2.13. Shenogin et al. [98] grafted octane molecules to SWCNTs and found that the interfacial resistance decreased by a factor of three. Functionalised CNTs also demonstrated better dispersion into the matrix with smaller clusters and less entanglements, which can lead to improvements in thermal conductivity. This was shown in transmission electron microscopy (TEM) images taken by Spitalsky et al. [99] of non-functionalized and functionalized MWCNTs loaded at 1% by weight into epoxy, Figure 2.14. However, Han and Fina [66] reported that chemical functionalisation of COOH groups is usually done by acid treatment which induces structural defects in the CNTs and hence decreases their thermal conductivity. This was shown by Shenogin et al. [98] who found that functionalisation of the CNTs decreased the thermal interfacial resistance as well as the thermal conductivities of the CNTs. In summary, functionalisation can change the thermal conductivity of the CNTs, their dispersion in the matrix and the thermal interface resistance between the CNTs and the matrix.

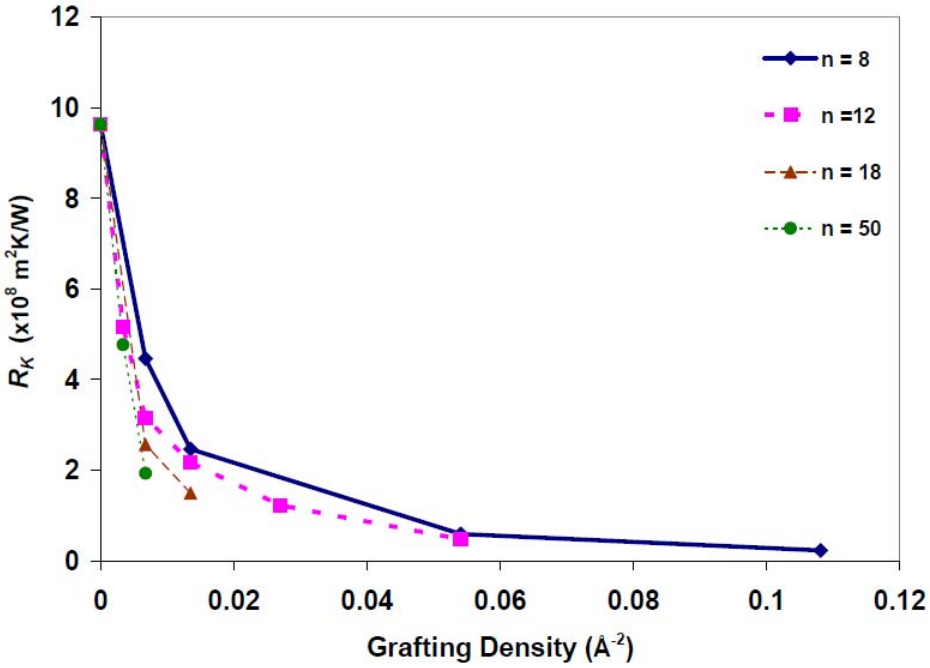

Figure 2.13 - Thermal interfacial resistance as a function of grafting density [15]

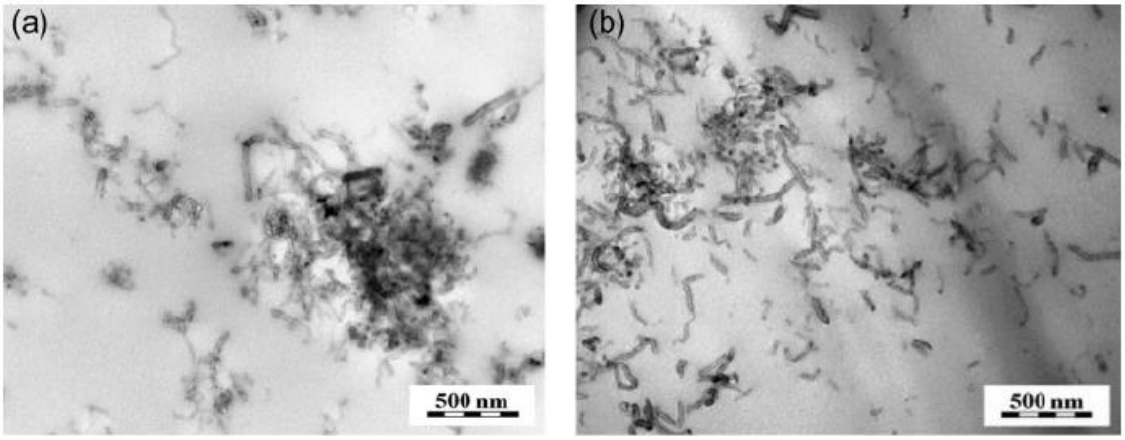

Figure 2.14 - TEM micrographs at 1% loading by weight of non-functionalised MWCNTs (left) and functionalised MWCNTs (right) in epoxy [99]

In this work, industrial partner Axson loaded unfunctionalised MWCNTs into epoxy resin and processed the nanocomposite into semi-solid films. MWCNTs were chosen due to their lower cost compared to SWCNTs as well as better dispersion in polymers compared to SWCNTs [17]. MWCNTs provide a more profitable method of enhancing the mechanical, thermal and electrical properties of polymers in industry.

Analytical models which take into account the geometry of the reinforcing CNTs can be used for predicting the thermal conductivity of these nanocomposites, such as the Lewis-Nielsen model presented in Section 2.2.1. However, such models do not account for the interfacial resistance between the CNTs and the matrix, otherwise known as the Kapitza resistance R_k. Studies have shown that the thermal conductivity of CNT-reinforced polymers is largely limited by the Kapitza resistance and that this resistance must be modelled to predict k_{nc} properly [67-68]. This provides an explanation for the large discrepancy between experimental data and Lewis-Nielsen predictions for the CNT-reinforced epoxy reported by Erkstrand et al. [16], Figure 2.15, as well as that reported by Xu et al [101].

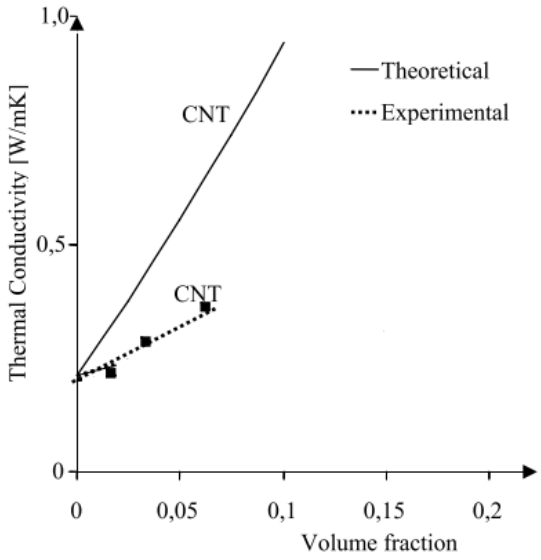

Figure 2.15 - Thermal conductivity of CNT-reinforced epoxy: experimental vs. Lewis-Nielsen model predictions [16]

Nan et al. [100] reported a Kapitza resistance of $8 \cdot 10^{-8}$ m^2K/W for MWCNTs in epoxy while Huxtable et al. [20] measured a value of $8.3 \cdot 10^{-8}$ m^2K/W for SWCNTs in epoxy. Clancy et al. [15] calculated Kaptiza resistances R_k for SWCNTs with varying degrees of functionalisation from simulations, reporting a value of $9 \cdot 10^{-8}$ m^2K/W for a non-functionalised SWCNT in an ethylene vinyl acetate matrix. As reported above, the authors found that thermal resistance decreased with an increased degree of functionalisation, Figure 2.13.

The Maxwell-Garnett [102] effective medium approach is an analytical model that does account for the Kapitza resistance. Nan et al. [67, 70] and Clancy et al. [15] validated this model for predicting thermal conductivities of CNT-reinforced polymers. The model is valid if CNTs in low loadings are dispersed randomly in the polymer matrix; it accounts for

the thermal conductivities of the CNTs and the polymer matrix, the geometry of the CNTs and the Kapitza resistance between the CNTs and the matrix. The Kapitza resistance R_k is modelled as an interface layer of the polymer matrix around each nanotube with a Kapitza radius r_k defined as:

$$r_k = R_k \cdot k_m \tag{2.12}$$

Then, the equivalent thermal conductivities of the nanotube surrounded by the interface layer in the transverse and longitudinal directions are given by ${k_{11}}^c$ and ${k_{33}}^c$ respectively:

$${k_{11}}^c = \frac{k_c}{1 + \frac{2r_k k_c}{dk_m}} \tag{2.13}$$

$${k_{33}}^c = \frac{k_c}{1 + \frac{2r_k k_c}{Lk_m}} \tag{2.14}$$

where k_c, d and L are the thermal conductivity, diameter and length of the nanotube, respectively. Finally, the thermal conductivity of the nanocomposite k_{nc} is given by:

$$\frac{k_{nc}}{k_m} = \frac{3 + V_{cnt}\left(B_x + B_z\right)}{3 - fB_x} \tag{2.15}$$

where parameters B_x, B_z and the volume fraction of the nanotubes V_{cnt} are given by:

$$B_x = \frac{2\left(k_{11}{}^c - k_m\right)}{k_{11}{}^c + k_m} \tag{2.16}$$

$$B_z = \frac{k_{33}{}^c}{k_m} - 1 \tag{2.17}$$

$$V_{cnt} = \frac{W_{cnt}}{W_{cnt} + \left(1 - W_{cnt}\right) \cdot \frac{\rho_{cnt}}{\rho_m}} \tag{2.18}$$

where W_{cnt} is the weight fraction of the CNTs; ρ_{cnt} and ρ_m are the densities of the CNTs and matrix, respectively.

The widely known Maxwell analytical model [70] can be used for predicting the thermal conductivity of a matrix with void content k_{mv}, given the thermal conductivity of the void-free matrix k_m and assuming that the voids are spherical and uniformly distributed in the matrix:

$$\frac{k_{mv}}{k_m} = \frac{2k_m + k_v - 2\left(k_m + k_v\right)V_v}{2k_m + k_v + \left(k_m - k_v\right)V_v} \tag{2.19}$$

where V_v and k_v are the volume fraction and thermal conductivity of the voids, respectively.

Ashrafi et al. [29] validated the Maxwell model to account for voids in the CNT-reinforced resin phase of fibreglass-reinforced polyetheretherketone (PEEK) composites. In this work, the thermal conductivities of void-free CNT-reinforced polymers are first

calculated using the effective medium approach shown in Equations 2.12 to 2.18. Then the resulting k_{nc} is substituted into Equation 2.19 as k_m to predict the thermal conductivity of CNT-reinforced polymers with void content. There is no directionality to thermal conductivities of CNT-reinforced polymers; isotropy is assumed.

Biercuk et al. [4] studied the thermal conductivity of SWCNT and vapour-grown carbon fibre (VGCF)-reinforced epoxy at room temperature. The SWCNTs measured 1.1 nm in diameter were aggregated into bundles 30 nm in diameter. Both the SWCNTs and VGCFs were loaded at 1% by weight into the epoxy. It was found that the thermal conductivity of the SWCNTs-epoxy was 125% higher than that of the neat epoxy whilst thermal conductivity of the VGCF-epoxy was 45% higher than that of the neat epoxy, Figure 2.16. The authors deduced that the thermal conductivity increase was larger for the SWCNTs than for the VGCFs at same loading because the SWCNTs formed a better network within the matrix, due to their smaller diameters and larger aspect ratios.

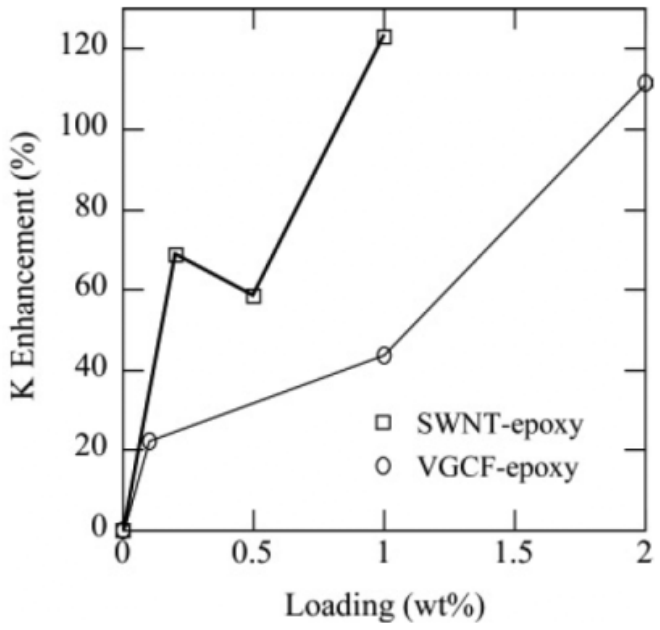

Figure 2.16 - Thermal conductivity enhancements of SWCNT-epoxy and VGCF-epoxy nanocomposites as a function of loading by weight [4]

Nihar [104] studied the thermal conductivity of SWCNT-reinforced polymethylmethacrylate (PMMA) over a temperature range from 300 K to 400K. The SWCNTs measured 1.3 nm in diameter and were loaded at five different percentages by weight. It was found that the thermal conductivity of SWCNT-PMMA increased with nanotube content, Figure 2.17.

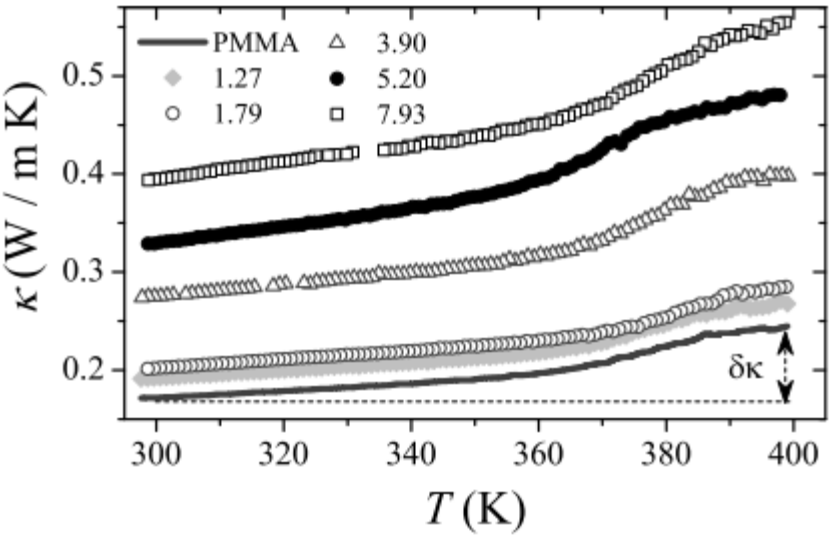

Figure 2.17 - Thermal conductivities of SWCNT-PMMA nanocomposites as a function of temperature at several loadings by weight [104]

Xu et al. [101] studied the thermal conductivity of SWCNT-reinforced polyvinylidenefluoride (PDVF). The SWCNTs measured 0.7 nm to 1.2 nm in diameter and 0.1 μm to 10 μm in length. Thermal conductivities at 5% and 10% loading by volume were measured at 0.278 W/mK and 0.314 W/mK respectively compared to that of the neat PDVF at 0.233 W/mK. Similarly to work by Erkstrand et al. [16] reported above, the authors attempted to use the Lewis-Nielsen model for predicting the thermal conductivity of the nanocomposites and found that predictions largely overestimated experimental values. The authors attributed this to the importance of modelling the interfacial resistance between the CNTs and polymer, this lacking capability in the Lewis-Nielsen model.

Ashrafi et al. [29] studied the thermal conductivity of SWCNT-reinforced PEEK. The nanotubes used were either laser-grown SWCNTs measuring 1.17 nm to 1.52 nm in diameter or arc-grown SWCNTs measuring 1.16 nm to 1.69 nm in diameter. They were loaded into

the PEEK matrix at 0.5% and 1% by weight. Both types of SWCNTs were available as-received or functionalised and all combinations enhanced the thermal conductivity of the PEEK polymer, Table 2.9.

Table 2.9 - Thermal conductivity values of neat and SWCNT-reinforced PEEK [29]

		Thermal conductivity (W/mK)
Neat resin	PEEK	0.23 ± 0.01
Nanocomposites	PEEK/arc SWCNTs (1wt%)	0.29 ± 0.02
	PEEK/laser SWCNTs (1wt%)	0.30 ± 0.02
	PEEK/arc SWCNTs-f (1wt%)	0.46 ± 0.03
	PEEK/laser SWCNTs-f (0.5wt%)	0.44 ± 0.02
	PEEK/laser SWCNTs-f (1wt%)	0.50 ± 0.04

Park et al. [105] studied the thermal conductivity of MWCNT-reinforced epoxy. Long MWCNTs of type I measured 50 nm to 100 nm in diameter and 5 mm in length while long MWCNTs of type II measured less than 10 nm in diameter and 100 μm in length. Short MWCNTs measured 10 nm to 20 nm in diameter and 1 μm in length. The long MWCNTs of types I and II were loaded at 2.00% and 6.38% by weight respectively as well as short MWCNTs at 10.00% by weight. Room temperature thermal conductivities of the type I long MWCNT-reinforced epoxy, type II long MWCNT-reinforced epoxy and short MWCNT-reinforced epoxy were measured at 0.9 W/mK, 2.6 W/mK and 0.4 W/mK respectively compared to that of the neat epoxy at 0.2 W/mK, Figure 2.18.

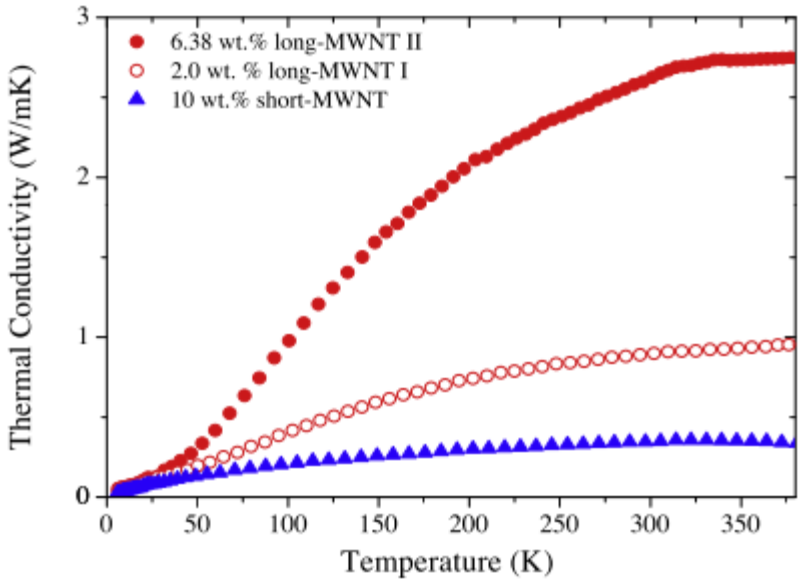

Figure 2.18 - Thermal conductivities of several MWCNT-epoxy nanocomposites as a function of temperature [105]

Sineai and Hoa [106] studied the thermal conductivity of MWCNT-reinforced epoxy. Thermal conductivities at 1%, 2%, 3% and 4% loading by weight were measured at 0.34 W/mK, 0.41 W/mK, 0.44 W/mK and 0.49 W/mK respectively compared to that of the neat epoxy at 0.18 W/mK. Gallego et al. [22] also studied the thermal conductivity of MWCNT-reinforced epoxy. The MWCNTs measured 1.2 nm to 1.5 nm in diameter and 2.5 μm in length. Thermal conductivities at 0.6% and 1% loadings by weight were 0.29 W/mK and 0.38 W/mK respectively compared to that of the neat epoxy at 0.22 W/mK.

Ekstrand et al. [16] studied the thermal conductivity of MWCNT-reinforced epoxy. The MWCNTs measured 10 nm to 30 nm in diameter and 1 μm in length. Thermal conductivity at 6.8% by volume was measured at 0.36 W/mK compared to that of the neat epoxy at 0.21 W/mK. Yang et al. [107] studied the thermal conductivity of non-

functionalised and functionalised MWCNT-reinforced epoxy. The MWCNTs measured 60 nm to 100 nm in diameter and 5 μm to 15 μm in length. Thermal conductivities at 1% and 2% loading by volume were measured to be 0.5 W/mK and 0.62 W/mK respectively compared to that of the neat epoxy at 0.35 W/mK. Thermal conductivities at the same loadings were measured to be 0.45 W/mK and 0.5 W/mK respectively compared to that of the neat epoxy at 0.35 W/mK.

Gojny et al. [17] studied the thermal conductivity of SWCNT-reinforced and MWCNT-reinforced epoxy. The SWCNTs measured less than 2 nm in diameter and up to 10 μm in length, while the MWCNTs measured 15 nm in outer diameter, 4 nm in inner diameter and up to 50 μm in length. Thermal conductivities for the SWCNT-reinforced epoxy at 0.1% and 0.3% by weight were measured at 0.241 W/mK and 0.243 W/mK respectively compared to that of the neat epoxy at 0.242 W/mK. Thermal conductivities of the MWCNT-reinforced epoxy at the same loadings were measured at 0.244 W/mK and 0.251 W/mK respectively compared to that of the neat epoxy at 0.242 W/mK. MWCNTs induced a slight increase in thermal conductivity while loading SWCNTs did not change the thermal conductivity. The authors attributed this to the smaller specific surface area of the MWCNTs compared to SWCNTs, which yielded lower interfacial resistances between the MWCNTs and matrix compared to the interfacial resistances between the SWCNTs and matrix.

Moisala et al. [23] studied the thermal conductivity of SWCNT-reinforced epoxy. SWCNTs aggregated into bundles consisted of tubes measuring 2 nm in diameter and several microns in length. There were also aligned MWCNT bundles which measured tens of nanometers in diameter and 80 μm in length. Thermal conductivities for the MWCNT bundle-reinforced epoxy at 0.1%, 0.3%, and 0.5% loading by weight were measured at 0.27

W/mK, 0.27 W/mK and 0.29 W/mK respectively compared to that of the neat epoxy at 0.26 W/mK. The authors found similar results as Gojny et al. reported above [17]; loading MWCNTs induced a slight increase in thermal conductivity while loading SWCNTs decreased the thermal conductivity slightly, Figure 2.19.

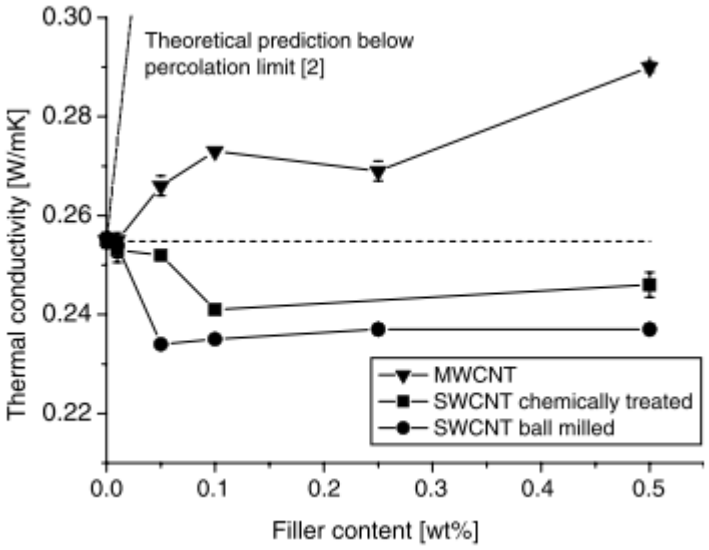

Figure 2.19 - Thermal conductivity of SWCNT-epoxy and MWCNT-epoxy nanocomposites as a function of loading by weight [23]

Changes in thermal conductivity of polymers upon loading CNTs are summarized in Table 2.10. All values are at room temperature and studies where loadings were presented by volume fraction were converted to weight fraction for comparison purposes using 1200 kg/m^3 and 1890 kg/m^3 [108] as density of the resin and CNTs respectively, Equation 2.18.

Table 2.10 - Summary of change in the thermal conductivity of polymers upon loading CNTs

	Loading (%wt)	Length (μm)	Outer diameter (nm)	Inner diameter (nm)	Polymer	Change in thermal conductivity (%)	Authors
SWCNT-reinforced	0.1	10	2.0	N/A	epoxy	-1	Gojny et al. [17]
	0.1	1 to 5	2.0		epoxy	-8	Moisala et al. [23]
	0.3	2 to 5	2.0		epoxy	-8	Moisala et al. [23]
	0.3	10	2.0		epoxy	1	Gojny et al. [17]
	0.5	3 to 5	2.0		epoxy	-8	Moisala et al. [23]
	1.0	unspecified	1.1		epoxy	125	Biercuk et al. [4]
	1.3	unspecified	1.3		PMMA	80	Nihar [104]
	1.8	unspecified	1.3		PMMA	100	Nihar [104]
	3.9	unspecified	1.3		PMMA	170	Nihar [104]
	5.2	unspecified	1.3		PMMA	230	Nihar [104]
	8.0	unspecified	1.3		PMMA	300	Nihar [104]
MWCNT-reinforced	0.1	50	15.0	4	epoxy	1	Gojny et al. [17]
	0.1	80	unspecified	unspecified	epoxy	7	Moisala et al. [23]
	0.3	50	15.0	4	epoxy	4	Gojny et al. [17]
	0.3	80	unspecified	unspecified	epoxy	6	Moisala et al. [23]
	0.5	80	unspecified	unspecified	epoxy	14	Moisala et al. [23]
	1.0	2.5	1.2 to 1.5	unspecified	epoxy	89	Sineai and Hoa [106]
	2.0	2.5	1.2 to 1.6	unspecified	epoxy	128	Sineai and Hoa [106]
	2.0	5000	100	50	epoxy	350	Park et al. [105]
	2.0	5 to 15	100 (functionalised)	60	epoxy	43	Yang et al. [107]
	2.0	6 to 15	100	60	epoxy	29	Yang et al. [107]
	3.0	2.5	1.2 to 1.7	unspecified	epoxy	144	Sineai and Hoa [106]
	4.0	2.5	1.2 to 1.8	unspecified	epoxy	172	Sineai and Hoa [106]
	4.0	7 to 15	100 (functionalised)	60	epoxy	77	Yang et al. [107]
	4.0	8 to 15	100	60	epoxy	43	Yang et al. [107]
	6.4	100	10.0	unspecified	epoxy	1100	Park et al. [105]
	10.0	1	20.0	10	epoxy	100	Park et al. [105]
	14.0	1	30.0	10	epoxy	71	Erkstrand et al. [16]

2.3.3 Effect of CNT addition on the thermal conductivity of composites

The high thermal conductivity of CNTs offers potential towards enhancing the thermal conductivity of fibre-reinforced composites. Thermal conductivity values are available in the literature for fibre-reinforced composites, where the polymer matrix has been loaded with CNTs; these are referred to as multi-scale composites, whereas fibre-reinforced composites with a neat polymer matrix are referred to as neat composites in this thesis. Loading percentages of CNTs refer to the loading by weight or volume into the polymer matrix. Similar to results summarized in Section 2.3.2 for nanocomposites, much scatter is present in the data; some studies reported thermal conductivity enhancements up to 150% upon loading CNTs [27] while others reported no effect or a decrease in thermal conductivity upon loading CNTs [28].

Han and Chung [24] studied the effect of loading SWCNTs on the thermal conductivity of carbon fibre-epoxy composites. SWCNTs measuring 1.1 nm in diameter were suspended in a solvent solution and applied on both surfaces of the prepreg sheets. The sheets were stacked after the solvent evaporated and the laminate was cured under compression moulding. Temperature and pressure were held at 177°C for two hours, at either 0.1 MPa or 0.2 MPa maximum cure pressure. The weight percentages of SWCNTs out of the total weight of the composite reported by the authors were equivalent to 0.55% and 0.70% loadings by weight into the epoxy. Through-thickness thermal conductivities were measured at 0.910 W/mK and 1.453 W/mK for the multi-scale composites cured at 0.1 MPa and 0.2 MPa respectively, compared to 0.729 W/mK and 1.091 W/mK for the neat composites cured in the same conditions. Through-thickness thermal conductivities were enhanced by both the presence of SWCNTs and the increase in cure pressure.

Ashrafi et al. [29] studied the effect of loading SWCNTs into a PEEK resin, as reported in Section 2.3.2, on the thermal conductivity of multi-scale composites manufactured with this loaded resin. Whilst most papers compare either the thermal conductivity of CNT-reinforced polymers to that of the neat polymer, or the thermal conductivity of CNT-reinforced composites to that of the neat fibre-reinforced composite, this work was the only one found where both comparisons are made based on the same CNTs and resin. The nanotubes used were either laser-grown SWCNTs measuring 1.17 nm to 1.52 nm in diameter or arc-grown SWCNTs measuring 1.16 nm to 1.69 nm in diameter loaded at 0.5% and 1.0% by weight into epoxy. Furthermore, both types of SWCNTs were available as-received or functionalised. Plain weave fibreglass fabrics (GF) were used for manufacturing the neat and multi-scale composites using a hot press technique.

Through-thickness thermal conductivities measured on nanocomposite plates featuring five combinations of SWCNT types, loadings and functionalisation were presented in Table 2.9. Corresponding values for the multi-scale composite plates appear in Table 2.11. Results show that loading any combination of SWCNTs enhanced the thermal conductivity compared to that of the neat PEEK. Loading SWCNTs into the matrix of fibre-reinforced composites also enhanced the thermal conductivity in all cases compared to the neat composites. All multi-scale composites had a V_f of 64%. Results also show that loading laser-grown SWCNTs yielded higher thermal conductivity compared to loading arc-grown SWCNTs, while functionalisation and higher loadings also increased the thermal conductivity. Interestingly, loading CNTs into the neat composites was also found to decrease the void content due to altered bleeding.

Table 2.11 - Through-thickness thermal conductivity of neat and SWCNT-reinforced composites [29]

		Thermal conductivity (W/mK)	Void content (%)
Neat fibre-reinforced composites	PEEK/GF	0.21 ± 0.01	5.3 ± 1.2
Multi-scale composites	GF/PEEK/arc SWCNTs (1wt%)	0.27 ± 0.01	3.4 ± 0.8
	GF/PEEK/laser SWCNTs (1wt%)	0.34 ± 0.02	2.2 ± 1.3
	GF/PEEK/arc SWCNTs-f (1wt%)	0.33 ± 0.01	1.3 ± 0.5
	GF/PEEK/laser SWCNTs-f (0.5wt%)	0.29 ± 0.01	1.6 ± 0.7
	GF/PEEK/laser SWCNTs-f (1wt%)	0.43 ± 0.01	0.3 ± 0.2

Zimmer et al. [28] studied the effect of loading MWCNTs into an epoxy resin on the thermal conductivity of multi-scale composites manufactured with this loaded resin. MWCNTs measuring 20 nm to 40 nm in diameter and 2 mm in length were loaded into epoxy matrix at 0.5%, 1%, 5% and 10% by weight. Neat and multi-scale composites were manufactured with IM7 carbon fibre fabrics using compression moulding. Through-thickness thermal conductivity values for the MWCNT-reinforced composite plates measured at 220°C showed that only the 10% loading enhanced the thermal conductivity to 1.4 W/mK compared to that of the neat plate at 1.25 W/mK while the 0.5%, 1% and 5% loadings either maintained or decreased the thermal conductivity to as low as 1.15 W/mK. The authors attributed this to a large thermal interfacial resistance between the MWCNTs and the matrix, and deduced that only the 10% loading enabled overcoming this resistance to increase the thermal conductivity.

Tzeng and Lin [26] studied the effect of loading MWCNTs and carbon nanofibres (CNFs) into a phenolic resin on the through-thickness thermal conductivity of multi-scale composites manufactured with this loaded resin. MWCNTs measuring 10 nm to 20 nm in

diameter were loaded into the resin at 0.1%, 0.5% and 1% by weight while CNFs were loaded at 0.05%, 0.1% and 0.5% by weight. Neat and multi-scale composites were manufactured using a hot press technique where carbon fibre fabrics were impregnated with the neat or loaded resin solution, respectively. Measurements showed that the thermal conductivity of both the MWCNT and CNF-reinforced composites was higher than that of the neat composite, Figure 2.20. Optimal loading for the MWCNTs was reported to be 0.5% by weight which yielded a thermal conductivity of 0.77 W/mK compared to 0.68 W/mK for the neat composite.

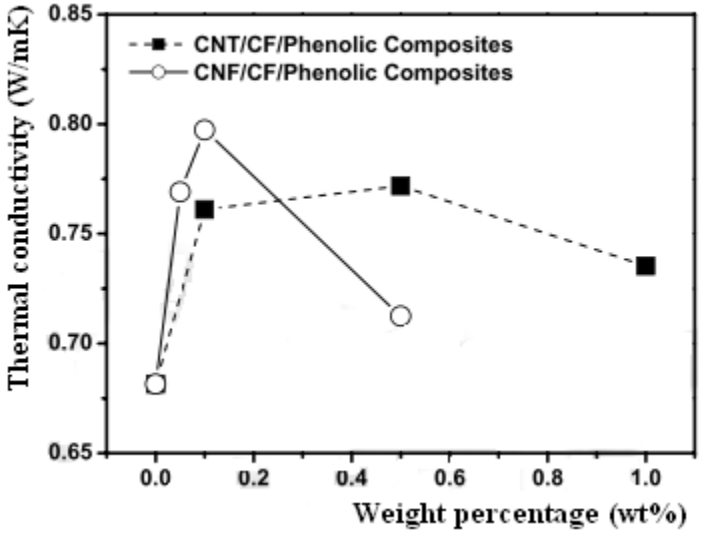

Figure 2.20 - Thermal conductivity of MWCNT and CNF-reinforced composites as a function of loading by weight [26]

Wang and Qiu [27] studied the effect of loading MWCNTs into a polyester resin on the through-thickness thermal conductivity of multi-scale composites manufactured with this loaded resin. MWCNTs measuring 8 nm in outer diameter and 3 μm in length were loaded

into the resin at 0.1% and 0.3% by volume. Neat and multi-scale composites were manufactured by infusing the neat or loaded resin into fibreglass textiles respectively using resin transfer moulding (RTM). Loading CNTs at 0.1% and 0.3% by volume enhanced the thermal conductivity to 0.3 W/mK and 0.45 W/mK respectively, compared to that of the neat composite at 0.18 W/mK.

Kim et al. [25] studied the effect of loading MWCNTs into a phenolic resin on the in-plane thermal conductivity of multi-scale composites manufactured with this loaded resin. As-received and highly crystalline MWCNTs measuring 80 nm in diameter and 10 nm to 20 nm in length were loaded into phenolic resins at 5%, 7% and 10% by weight. Crystallinity refers to the periodic repeating pattern of the bonds between the carbon atoms hence CNTs with high crystallinity have fewer defects in the atomic structure. Neat and multi-scale composites were manufactured using hot press moulding where pitch-based carbon fibres with a high thermal conductivity of 500 W/mK were impregnated with the neat or loaded resin solution, respectively. Measurements showed that the thermal conductivity of the multi-scale composites reinforced with as-received MWCNTs at 5% and 7% loadings were lower than that of the neat carbon fibre composite at 255 W/mK while thermal conductivity increased to 265 W/mK at 10% loading. Kim et al. attributed the lower values at 5% and 7% to structural defects in as-received MWCNTs. For highly crystalline MWCNTs, thermal conductivity was higher than that of the neat composite at all loadings, with a maximum of 400 W/mK at the optimal loading of 7% by weight. A drop in thermal conductivity was seen at 10% loading, similar to the drop seen in Figure 2.21 from Tzeng and Lin. The authors attributed this to the formation of aggregates and poor dispersion past the optimal loading.

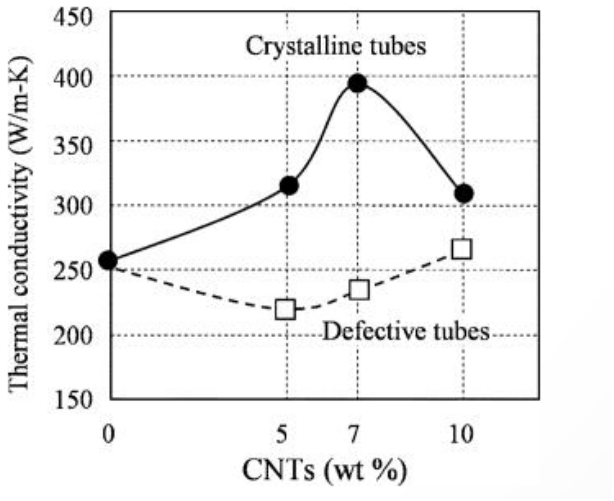

Figure 2.21 – In-plane thermal conductivities k_{cip} of as-received and highly crystalline MWCNT-reinforced composites as a function of loading [25]

Changes in thermal conductivity of carbon fibre-polymer composites upon loading CNTs in the polymer are summarized in Table 2.12. All values are at room temperature and studies where loadings were presented in volume fraction were converted to weight fraction for comparison purposes using 1200 kg/m^3 and 1890 kg/m^3 [108] as density of the resin and CNTs respectively, Equation 2.18. IP represents enhancements in the in-plane direction whilst TT represents enhancements in the through-thickness direction of the composite.

Table 2.12 - Summary of change in the thermal conductivity of fibre-reinforced composites upon loading CNTs

	Loading (%wt)	Length (μm)	Outer diameter (nm)	Inner diameter (nm)	Fibre	Polymer	Direction/thermal conductivity enhancement (%)	Authors
SWCNT-reinforced	0.4	unspecified	1.1	N/A	carbon	epoxy	k_{ctt} : 25 (0.1MPa)	Han and Chung [24]
	0.4	unspecified	1.1		carbon	epoxy	k_{ctt} : 33 (0.2MPa)	Han and Chung [24]
	0.5	unspecified	1.17 to 1.52 (laser,functionalised)		glass	PEEK	k_{ctt} : 38	Ashrafi et al. [29]
	1.0	unspecified	1.16 to 1.69 (arc)		glass	PEEK	k_{ctt} : 29	Ashrafi et al. [29]
	1.0	unspecified	1.17 to 1.52 (laser)		glass	PEEK	k_{ctt} : 62	Ashrafi et al. [29]
	1.0	unspecified	1.16 to 1.69 (arc,functionalised)		glass	PEEK	k_{ctt} : 57	Ashrafi et al. [29]
	1.0	unspecified	1.17 to 1.52 (laser,functionalised)		glass	PEEK	k_{ctt} : 105	Ashrafi et al. [29]
MWCNT-reinforced	0.1	unspecified	20	10	carbon	phenolic	k_{ctt} : 12	Tzeng and Lin [26]
	0.2	3	8	unspecified	glass	polyester	k_{ctt} : 67	Wang and Qiu [27]
	0.5	3	8	unspecified	glass	polyester	k_{ctt} : 150	Wang and Qiu [27]
	0.5	unspecified	20	10	carbon	phenolic	k_{ctt} : 13	Tzeng and Lin [26]
	0.5	2000	40	20	carbon	epoxy	k_{ctt} : -1	Zimmer et al. [28]
	1.0	2000	40	20	carbon	epoxy	k_{ctt} : -1	Zimmer et al. [28]
	1.0	unspecified	20	10	carbon	phenolic	k_{ctt} : 7	Tzeng and Lin [26]
	5.0	0.01 to 0.02	80 (as received)	unspecified	carbon	phenolic	k_{cip} : -14	Kim et al. [25]
	5.0	0.01 to 0.03	81 (highly crystalline)	unspecified	carbon	phenolic	k_{cip} : 24	Kim et al. [25]
	5.0	2000	40	20	carbon	epoxy	k_{ctt} : -8	Zimmer et al. [28]
	5.0	0.01 to 0.02	80 (as received)	unspecified	carbon	phenolic	k_{cip} : -14	Kim et al. [25]
	7.0	0.01 to 0.04	82 (as received)	unspecified	carbon	phenolic	k_{cip} : -8	Kim et al. [25]
	7.0	0.01 to 0.05	83 (highly crystalline)	unspecified	carbon	phenolic	k_{cip} : 57	Kim et al. [25]

	10.0	0.01 to 0.06	84 (as received)	unspecified	carbon	phenolic	k_{cip} : 4	Kim et al. [25]
	10.0	0.01 to 0.07	85 (highly crystalline)	unspecified	carbon	phenolic	k_{cip} : 22	Kim et al. [25]
	10.0	2000	40	20	carbon	epoxy	k_{cip} : 12	Zimmer et al. [28]

Modelling the thermal conductivity of multi-scale composites involves a combination of modelling the thermal conductivity of neat fibre-reinforced composites as presented in Section 2.2.1, and that of CNT-reinforced polymers as presented in Section 2.3.2 [35, 92]. For the in-plane direction, the thermal conductivity of the CNT-reinforced polymer matrix accounting for void content k_{ncv} is calculated from the effective medium approach combined with the Maxwell equation, Equations 2.12 to 2.19. This value is then substituted as the matrix thermal conductivity k_m into Equation 2.1 to predict the thermal conductivity of a unidirectional ply in the axial direction k_1, accounting for void content. Finally, this k_1 value is used in the classical lamination theory to predict the in-plane thermal conductivity of the multi-scale composite k_{mscip}.

For the through-thickness direction, the thermal conductivity of the CNT-reinforced polymer matrix accounting for void content k_{ncv} is also calculated from the effective medium approach combined with the Maxwell equation, Equations 2.12 to 2.19. This value is used as the matrix thermal conductivity k_m in the Clayton model to predict the through-thickness thermal conductivity of the multi-scale composites k_{msctt}, Equation 2.5. Ashrafi et al. [29] used measured values of void-free CNT-reinforced polymers k_{nc} combined with the Maxwell equation accounting for voids to obtain a k_m value which the authors substituted into the Clayton model to predict the through-thickness thermal conductivities of the multi-scale composites. Predictions matched experimental data with a maximum error of 7%. In this work, the thermal conductivity of nanocomposites accounting for voids k_{ncv} is modelled.

In summary, CNTs show high thermal conductivities up to 6600 W/mK and thus demonstrate a potential for enhancing the thermal conductivity of polymers and fibre-

reinforced composites. However, there is much scatter in thermal conductivity data for CNTs: values vary largely due to the morphology, functionalisation, purity, length and diameter of CNTs. Studies showed that there is also much scatter in thermal conductivity enhancements brought by loading CNTs into polymers and into the polymer matrices of fibre-reinforced composites depending on the CNTs used, their functionalisation and their dispersion into the polymer. Studies also showed that the thermal interfacial resistance is very important in predicting the thermal conductivity of a CNT-reinforced polymer.

Studies can be found in the literature where the thermal conductivity of a CNT-reinforced polymer is measured and compared to that of the neat polymer. Studies can also be found where the thermal conductivity of a CNT-reinforced composite is measured and compared to that of the neat fibre-reinforced composite. However, there have been no publications where both comparisons were done in the same study based on the same materials except for the work of Ashrafi et al. [29], in which the authors loaded SWCNTs into PEEK resin and fibreglass-reinforced PEEK composites. In the present work, MWCNTs were loaded into epoxy resin used in manufacturing nanocomposite plates (Section 4.1) and the same MWCNTs were loaded into the epoxy matrix of carbon fibre-reinforced composites used in manufacturing multi-scale composite plates (Section 4.2). The effects of MWCNTs on the thermal conductivities of epoxy and carbon fibre-epoxy composites were seen. Statistical design of experiments was performed to investigate systematically the effect of select resin and fabric parameters, including the addition of CNTs, on the thermal conductivities, fibre volume fractions and void content of the neat and multi-scale composite plates.

2.4 Modelling heat transfer during composites manufacturing

2.4.1 Resin cure kinetics

Differential scanning calorimetry (DSC) is one of the most common techniques for thermal analysis. The sample and reference are both maintained at a temperature predetermined by the temperature program. The heat flow which must be supplied to or withdrawn from the sample to maintain zero temperature difference between the sample and the reference is used for determining phase changes in the material such as glass transition and crystallization. DSC can also be used for measuring the specific heat of the material as a function of temperature, and for studying the cure kinetics of a resin. The output data from a DSC experiment consist of graphs of the total heat flow supplied to the sample $\dot{Q}_{DSC}$ as a function of time or temperature, which is the sum of the heat flow contributions due to the curing exotherm $\dot{Q}_R$ and that associated with any change in heat capacity C_p with temperature [109]:

$$\dot{Q}_{DSC} = \dot{Q}_R + C_p \frac{dT}{dt} \tag{2.20}$$

The curing exotherm and the specific heat are both functions of temperature and degree of cure; Equation 2.20 can be stated more accurately as:

$$\dot{Q}_{DSC} = \dot{Q}_R(\alpha, T) + C_p(\alpha, \mathrm{T}) \frac{dT}{dt} \tag{2.21}$$

For materials that do not cure or which are already fully cured, $\dot{Q}_R$ is zero and the DSC data can be used directly for calculating C_p as a function of temperature knowing the constant heating rate dT/dt. For materials which are cured upon DSC heating, the heat flow contribution due to the change in specific heat $C_p dT/dt$ is zero if the DSC measurement is performed as an isotherm; in that case the heat flow is entirely due to the curing exotherm.

However, epoxy curing cycles used in manufacturing composites are rarely isothermal; they usually consist of a heat ramp, a dwell for cure, another heat ramp and a second dwell for postcure. A typical cure cycle used in the aerospace industry is shown in Figure 2.22:

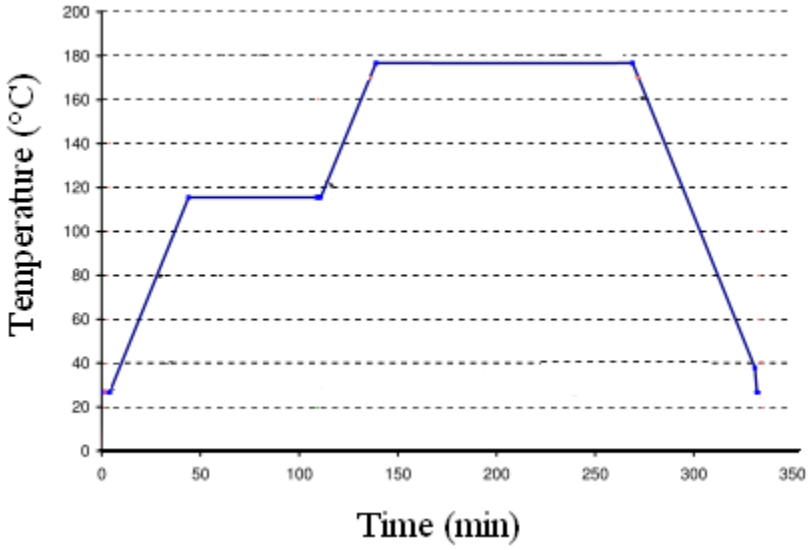

Figure 2.22 - Typical carbon fibre-epoxy composite cure cycle used in aerospace industry [96]

DSC can only measure the total heat flow $\dot{Q}_{DSC}$ in or out of the sample; the contribution to heat flow due to the curing exotherm needs to be separated from that due to changes in specific heat, shown in Figure 2.23:

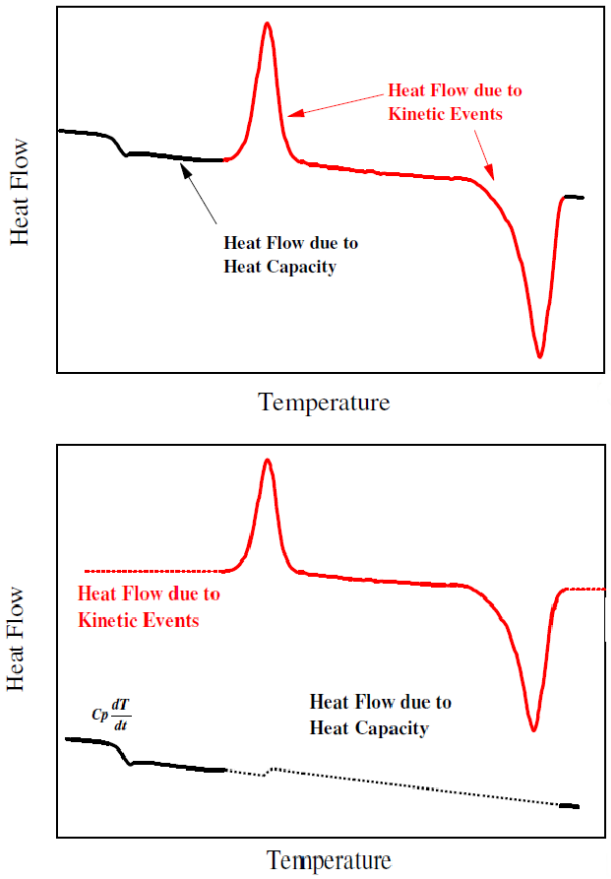

Figure 2.23 - Separation of heat flow due to curing exotherm and to changes in specific heat changes [95]

The instantaneous heat flow due to the curing exotherm can be calculated from various cure kinetics models available in the literature. Then the specific heat can be calculated from Equation 2.21. The most widely used cure kinetics model for epoxy resins is the Kamal-Sourour model; it is a semi-empirical equation that relates the rate of cure $d\alpha / dt$ to the degree of cure α. Kamal and Sourour [110] first presented the model in the form of Equation 2.22 during earlier stages of their work:

$$\frac{d\alpha}{dt} = K\alpha^m(1-\alpha)^n \tag{2.22}$$

where m and n are constants and K is a temperature dependent constant given by the Arrhenius Equation 2.23:

$$K_i = A_i e^{\left(-E_i/RT\right)} \tag{2.23}$$

for $i = 1, 2$, where A_i and E_i are the fitted constant and activation energy and R is the universal gas constant. Some researchers have applied this model and found that adding temperature dependency to the constants m and n in the form of an exponential function leads to a better fit with experimental data [31], [111]–[113], Equations 2.24 and 2.25:

$$m = C_1 e^{(-C_2 T)} \tag{2.24}$$

$$n = C_3 e^{(-C_4 T)} \tag{2.25}$$

Kamal also observed that epoxy DSC data fit experimental data more closely with an additional constant K added to Equation 2.22. The modified Kamal-Sourour equation [114] is given in Equation 2.26:

$$\frac{d\alpha}{dt} = (\mathrm{K}_1 + K_2\alpha^m)(1-\alpha)^n \tag{2.26}$$

where K_1 and K_2 are constants given by the Arrhenius equation.

The degree of cure α is given by the ratio of the cumulative heat of reaction Q_R divided by the total heat of reaction Q_{RT} of the sample, where the total heat of reaction can be obtained by integration of the area under the DSC curve:

$$\alpha = \frac{Q_R}{Q_{RT}} \tag{2.27}$$

Hence, the rate of cure is given by:

$$\frac{d\alpha}{dt} = \frac{\dot{Q}_R}{Q_{RT}} \tag{2.28}$$

A DSC test can consist of an isothermal temperature hold, a constant heating rate or a series of both, such as the temperature profile shown by Figure 2.22. The basis of the Kamal-Sourour model is that the constant heating rate phase during a DSC test can be approximated as many small isothermal steps. Isothermal DSC tests where the total heat flow measured is only due to the curing exotherm are run at multiple temperatures. The rate of cure and degree of cure for each isothermal test can be plotted as a function of time, Figure 2.24.

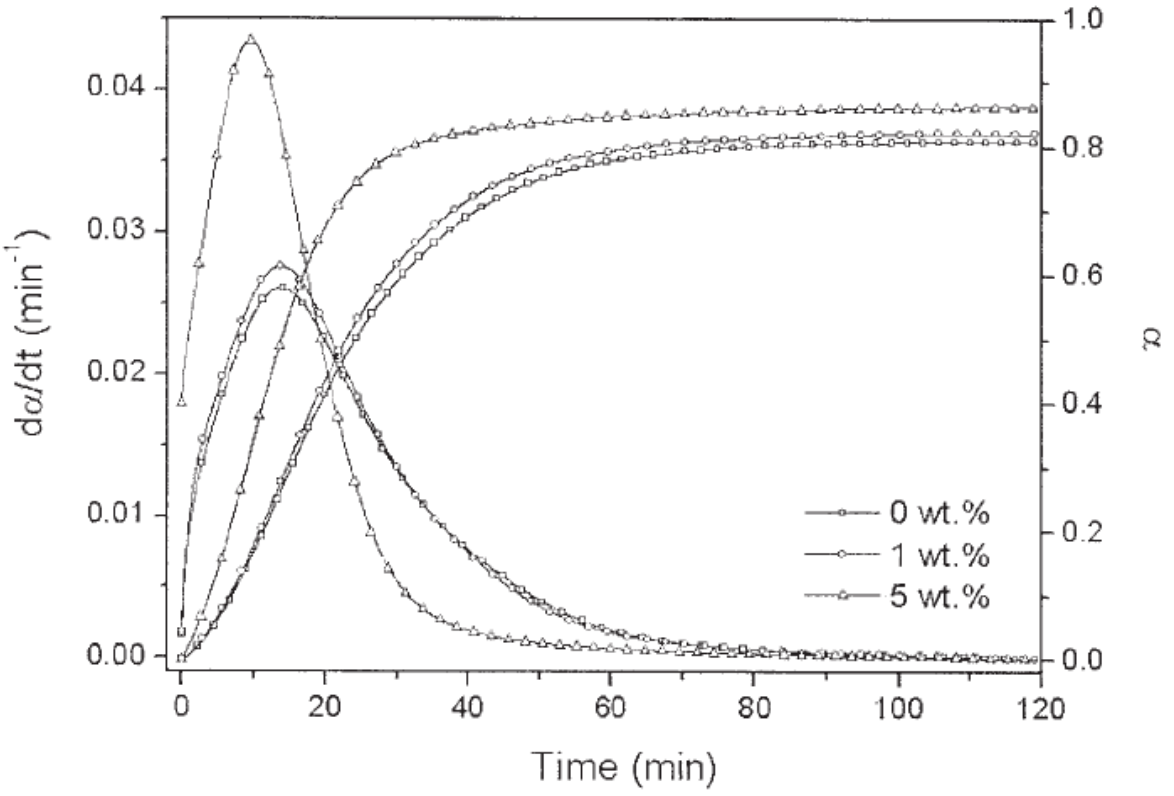

Figure 2.24 - Rate of cure and degree of cure as a function of time at 180°C [113]

From this, the rate of cure can be plotted as a function of the degree of cure at that temperature, and constants in Equation 2.26 can be fitted for that temperature. Then the constants for the different isothermal tests can be fitted to Equations 2.23 to 2.25 for temperature dependency.

Xie et al. [112] observed that the Kamal-Sourour model fitted the experimental data accurately up to a degree of cure of 0.7 while above this level the authors observed large deviations between the model and experimental data. The authors reported that cure is initially chemically controlled then becomes controlled by heat diffusion, which must be accounted for. Cole [115] introduced an empirically correlated diffusion factor into Equation 2.26 of the Kamal-Sourour model:

$$\frac{d\alpha}{dt} = K_1 \alpha^{m_1} (1-\alpha)^{n_1} + \frac{K_2 \alpha^{m_2} (1-\alpha)^{n_2}}{1+e^{\left(a\left[\alpha-(b+cT)\right]\right)}} \tag{2.29}$$

where is a , b and c are fitted constants.

Modulated DSC (MDSC) is an experimental alternative to separate heat flows due to the curing exotherm and to the change in specific heat due to temperature. The same temperature program as for standard DSC tests is run with an added temperature modulation. A typical MDSC test conducted for an epoxy resin is shown in Figure 2.25, where the temperature modulation added to the constant heat ramp is shown in red, the heat ramp with the added temperature modulation is shown in blue and the total heat flow is shown in green.

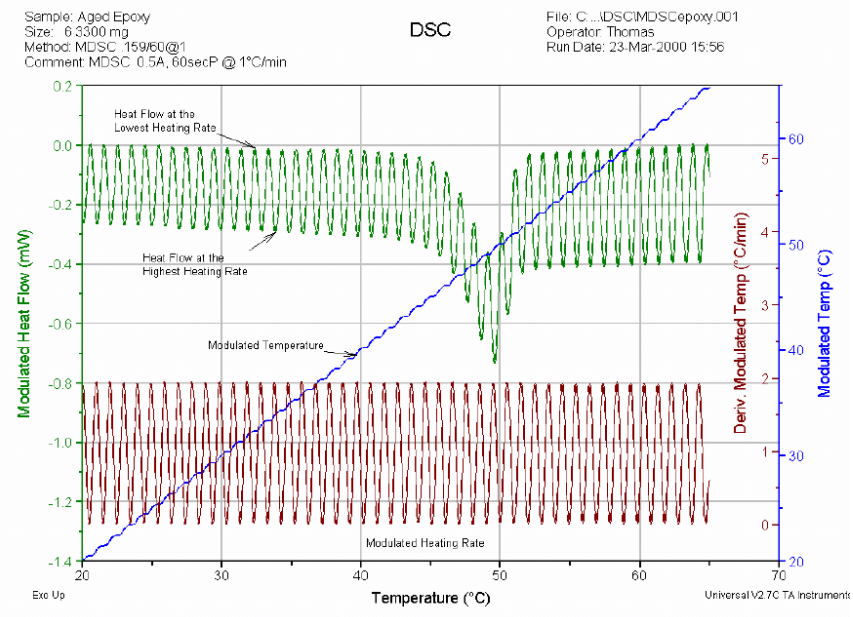

Figure 2.25 - Typical MDSC test parameters and data for epoxy [95]

The ratio of the amplitude of the total heat flow to the amplitude of the temperature modulation at any instant gives information about the specific heat while the shape of the total heat flow curve gives information about the curing exotherm. Hence the total heat flow can be de-convoluted and separated into the specific heat and curing exotherm curves. However, this experimental method can only achieve data collection for a specimen under the specified temperature program and cannot be used for developing a general model for the cure kinetics as a function of degree of cure and temperature, as done with the Kamal-Sourour model [109].

Xie et al. [113] fitted isothermal DSC data of a neat epoxy resin to the Kamal-Sourour model. The authors repeated the procedure for epoxy loaded with MWCNTs at 1% and 5% by weight. The MWCNTs were found to have an accelerating effect on cure kinetics during the initial stages; the initial reaction rates increased with the nanocomposites, the time taken to reach the maximum reaction rate decreased and the activation energies were lower than those of the neat epoxy. This can be seen in curves of the rate of cure and degree of cure as a function of time for an isothermal test at 180°C, Figure 2.25. Chapartegui et al. [116] also found that adding 0.1% and 1.0% MWCNTs by weight into epoxy resin accelerated the curing.

Sawi et al. [117] studied the effect of loading 0.4% double-walled carbon nanotubes (DWCNTs) by weight on the cure kinetics of epoxy resin. Similar to Xie et al. [113], the authors found an acceleration effect on the cure, and observed that the time to reach the maximum cure rate was shorter. Allouia et al. [118] conducted a literature survey and also reported the same trend, which the authors proposed could be caused by catalyst particles in the unprocessed CNTs.

2.4.2 Heat transfer models

The governing equations for heat transfer are presented briefly below. Fourier's law of heat conduction states that the heat flux q'' is linearly proportional to the thermal conductivity k and temperature gradient dT/dx [119]:

$$q'' = -k\frac{dT}{dx} \tag{2.30}$$

Newton's law of cooling states that the surface heat flux due to convection q_s'' is proportional to the coefficient of heat transfer h and to the difference between the surface temperature T_s and the temperature of the surrounding fluid T_∞:

$$q_s'' = h\left(T_s - T_\infty\right) \tag{2.31}$$

The heat equation is the general form of the heat conduction law and a special form of the law of conservation of energy:

$$\frac{\partial}{\partial x}\left(k\frac{\partial T}{\partial x}\right)+\frac{\partial}{\partial y}\left(k\frac{\partial T}{\partial y}\right)+\frac{\partial}{\partial z}\left(k\frac{\partial T}{\partial z}\right)+\dot{q}=\rho C_p\frac{\partial T}{\partial t} \tag{2.32}$$

where ρ and C_p are the density and specific heat of the material respectively, and the rate of internal heat generation $\dot{q}$ comes from the exotherm released during resin curing as presented in Section 2.4.1.

Modelling heat transfer and cure kinetics is important in studying the thermal behaviour of a laminate during composites manufacturing. It is especially important for thick

laminates, where the large curing exotherm caused by conventional cure cycles combined with the low thermal conductivity of the resin, limiting heat dissipation, results in a temperature overshoot at the centre of the laminate which can leave residual thermal stresses and cause degradation of the matrix in the worst cases. Heat transfer simulations enable the optimisation of the cure cycle and thermal behaviour during manufacturing.

In the RFI process, modelling heat transfer and cure kinetics cannot be separated from modelling resin flow. The three phenomena are coupled: the flow model requires viscosity which is influenced by temperatures obtained from the heat transfer model; the cure model requires temperatures from the heat transfer model; and the heat transfer model requires heat generation data from the cure model as well as changes in domain geometry from the flow model. However, the work reported in this thesis constitutes one component of the CRIAQ COMP 510 project, where the focus is on the thermal aspects of composite materials manufacturing and process modelling. Hence only the heat transfer and cure kinetics are modelled here; the model developed in this work does not account for resin flow and flow models are not discussed in detail in this literature survey.

Guo et al. [111] developed finite element formulations for solving one-dimensional transient heat transfer problems coupled with cure kinetics. The authors modelled a 20 mm thick T300/HD03 unidirectional carbon fibre-epoxy prepreg laminate subjected to a conventional autoclave temperature cycle. They assumed that the convective heat transfer caused by resin flow during cure was negligible and that the resin and fibres can be considered as a single macroscopically homogeneous material for the purposes of heat transfer. The authors also assumed that in the prepreg-based process, most of the consolidation is completed during the early stages of cure when the resin is at its minimum

viscosity; hence, the thickness is assumed to stay constant throughout the simulations and is taken as the final laminate thickness. Finite element formulations were derived from the heat Equation 2.32, where the internal heat generation $\dot{q}$ results from the exotherm released during resin cure. Cure kinetics were fitted to the Kamal-Sourour model, Equations 2.23 to 2.28 presented in Section 2.4.1. Isothermal DSC tests were performed on the carbon fibre-epoxy prepreg for fitting constants. Thermal properties of the prepreg were calculated using rule of mixtures except for its transverse thermal conductivity which was calculated using the Halpin-Tsai model, Equations 2.6 and 2.7 presented in Section 2.2.1. The authors performed simulations of a stack consisting of the carbon fibre-epoxy laminate with tooling and bagging materials, Figure 2.26. The locations of thermocouples are shown to be at the top, centre and bottom of the laminate centre.

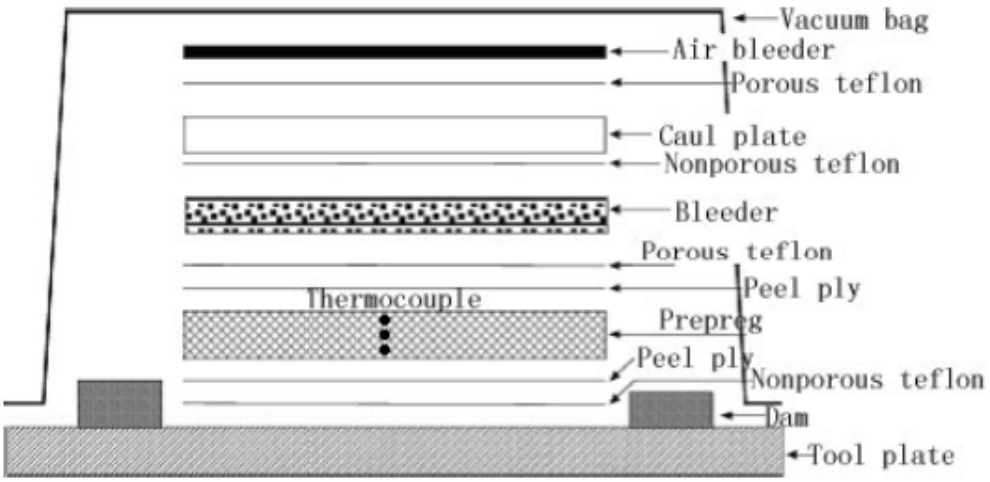

Figure 2.26 - Layup of laminate, tooling and bagging materials, Guo et al. [111]

The laminate was subjected to the autoclave temperature cycle recommended by the manufacturer (MRC), Figure 2.27. Convective boundary conditions were set with a heat transfer coefficient h of 70 W/m^{2}K between autoclave air and bagging materials.

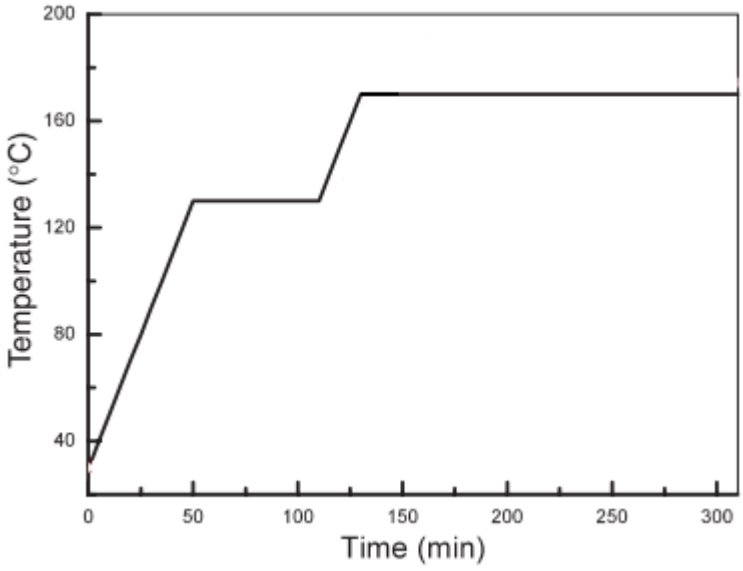

Figure 2.27 – Autoclave temperature cycle, Guo et al. [111]

The model yielded accurate predictions for temperature profiles at the top, mid-height and bottom of the laminate centre compared to experimental measurements along with the manufacturer recommended cure cycle (MRC), Figure 2.28:

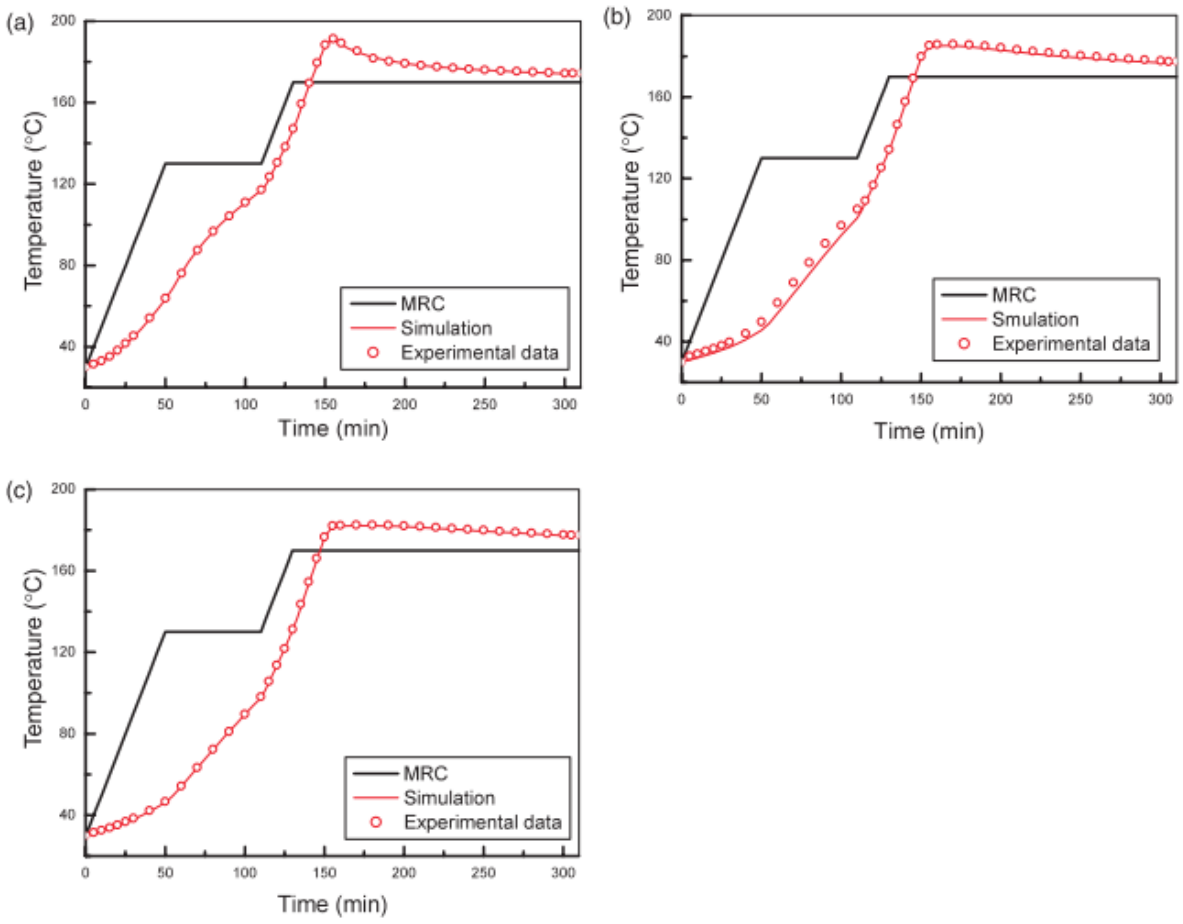

Figure 2.28 - Experimental and simulation results for temperature profiles at (a) top (b) middle (c) bottom of the laminate centre, Guo et al. [111]

Three-dimensional models were also found in the literature. Joshi et al. [120] used general purpose finite element software LUSAS to perform transient heat transfer simulations coupled with cure kinetics. The authors modelled a 23.1 mm thick AS4/3501 graphite-epoxy prepreg laminate subjected to a conventional autoclave temperature cycle. The authors made the same assumptions as Guo et al. [111] regarding constant thickness and

negligible convective heat transfer caused by resin flow as well as considering the resin and fibres as one macroscopically homogeneous material for the purposes of heat transfer.

The model consisted of the heat Equation 2.32 where the cure kinetics for internal heat generation $\dot{q}$ were fitted to the Arrhenius model as opposed to the Kamal-Sourour model. Isothermal DSC tests were performed on the graphite-epoxy prepreg for fitting constants. Thermal properties of the prepreg were calculated using rule of mixtures at 64% V_f. The authors performed simulations for a stack consisting of the carbon fibre-epoxy laminate with tooling and bagging materials, Figure 2.29.

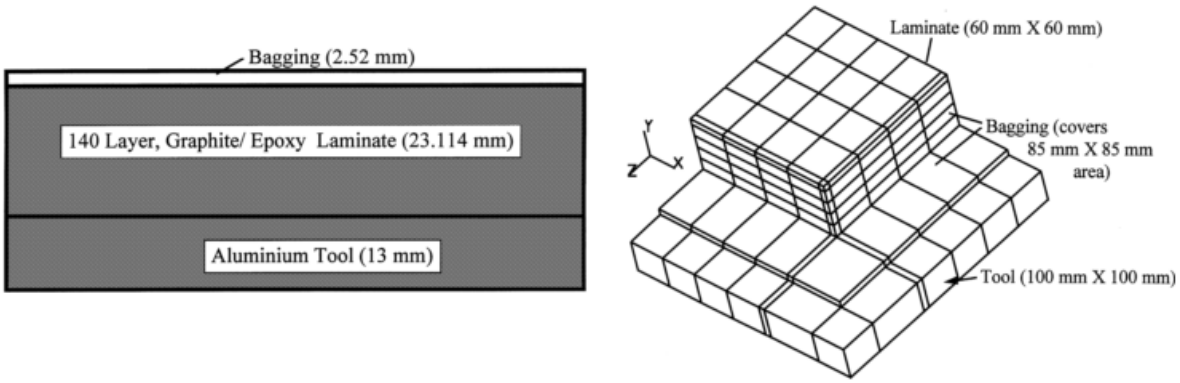

Figure 2.29 - Three-dimensional model, Joshi et al. [107]

The laminate was subjected to the conventional autoclave temperature cycle for the AS4/3501 prepreg, shown in Figure 2.30. Convective boundary conditions between autoclave air and the top of the bagging materials as well as the bottom of the tool were set using a heat transfer coefficient h of 85 W/m^{2}K.

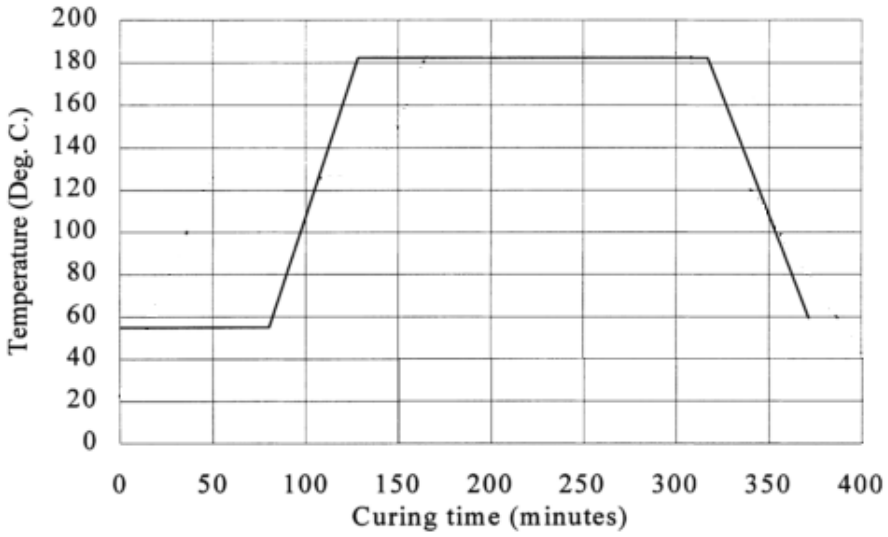

Figure 2.30 – Autoclave temperature cycle, Joshi et al. [107]

The model yielded accurate predictions for the temperature profile at mid-height of the laminate centre compared with experimental measurements, Figure 2.31:

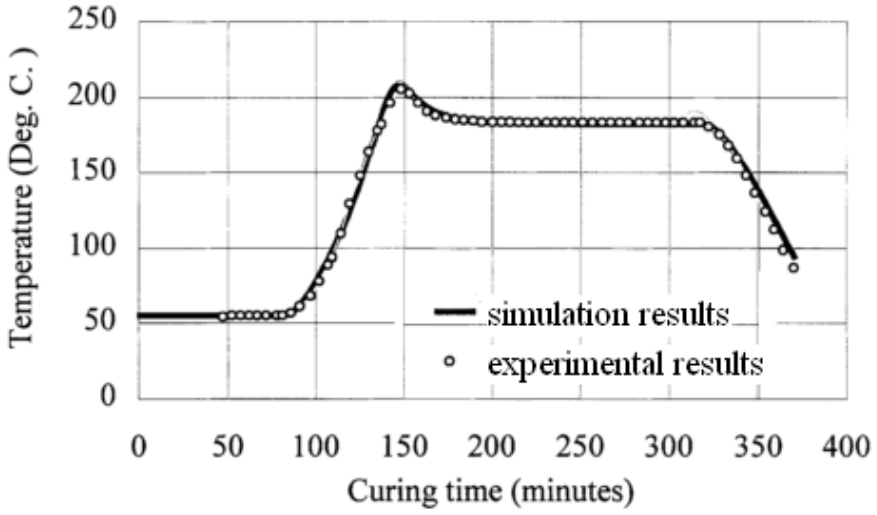

Figure 2.31 - Experimental and simulation results for temperature profile at mid-height of laminate centre, Joshi et al. [107]

The authors also investigated the effect of cure by comparing the experimental temperature curve to that from simulations where the cure kinetics functions were switched off, Figure 2.32. The temperature curve without cure does not overshoot and follows the autoclave temperature cycle closely.

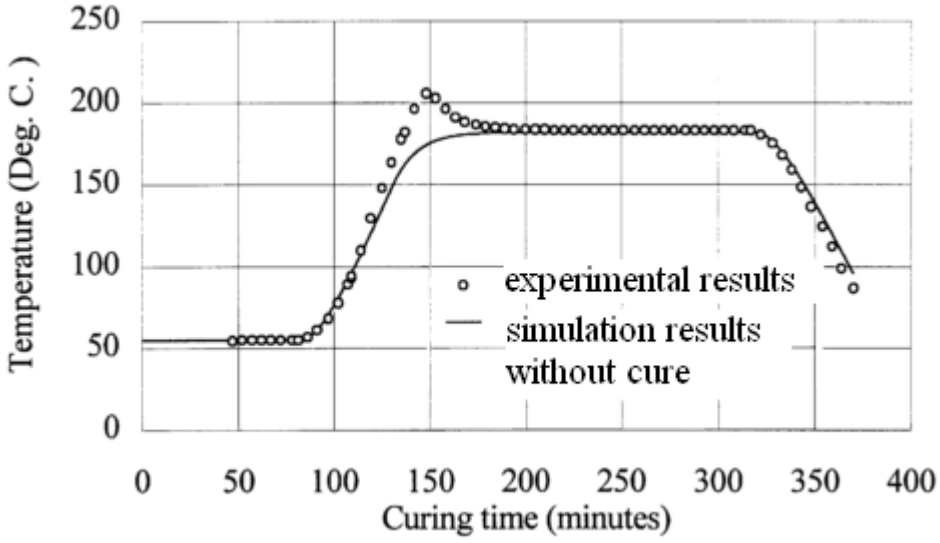

Figure 2.32 - Effect of cure kinetics on temperature profile at mid-height of laminate centre, Joshi et al. [107]

Oh and Lee [31] used ANSYS for performing three-dimensional resin flow simulations coupled with transient heat transfer and cure kinetics. The authors modelled a 20 mm thick UGN150 unidirectional fibreglass-epoxy prepreg laminate subjected to a conventional autoclave temperature cycle. The authors made the same assumptions as Guo et al. [111] and Joshi et al. [120] regarding negligible convective heat transfer caused by resin flow, and considered the resin and fibres as a single macroscopically homogeneous material for heat transfer.

The model consisted of momentum and viscosity equations for resin flow and the heat conduction Equation 2.32 for heat transfer and cure, where the cure kinetics for the internal heat generation $\dot{q}$ was fitted to the Kamal-Sourour model, Equations 2.23 to 2.28 presented in Section 2.4.1. Isothermal DSC tests were performed on the graphite-epoxy prepreg for fitting constants. Thermal properties of the prepreg were calculated using rule of mixtures except for its transverse thermal conductivity which was calculated using the Springer-Tsai model, Equations 2.3 and 2.4 presented in Section 2.2.1. The authors performed simulations of a stack consisting of the carbon fibre-epoxy laminate with tooling and bagging materials, Figure 2.33. The locations of thermocouples are shown to be at the top, centre and bottom of the laminate centre.

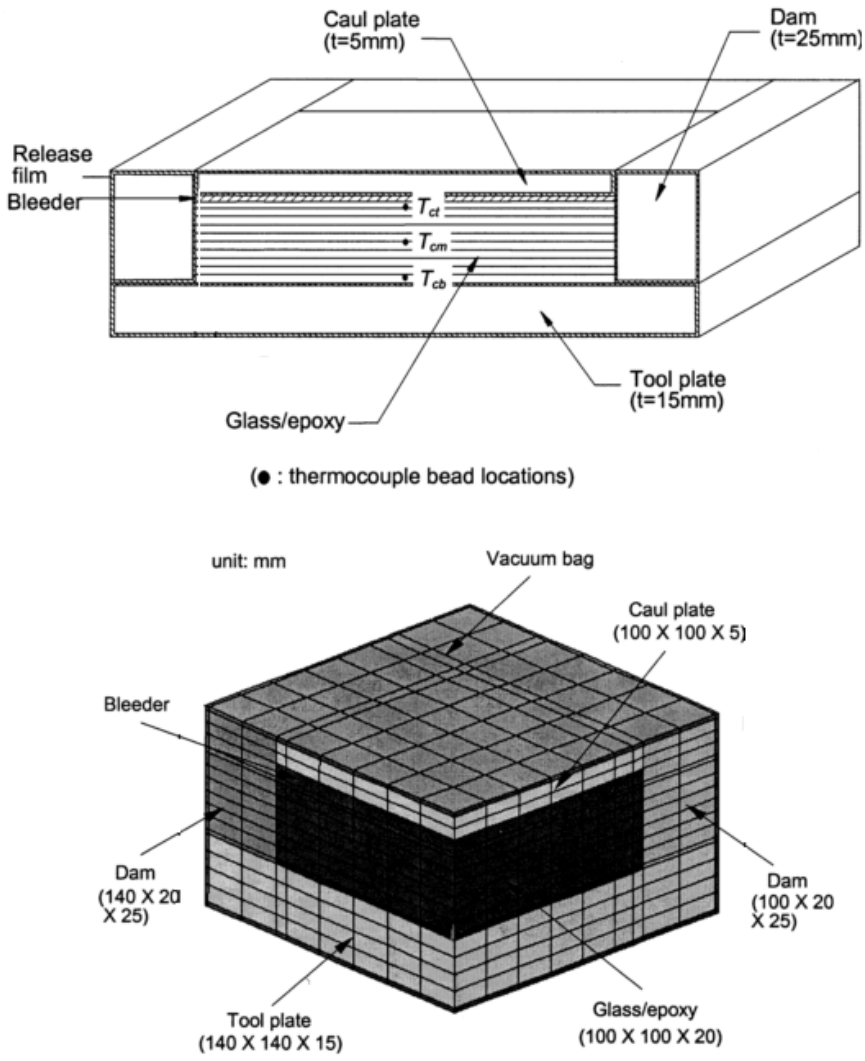

Figure 2.33 - Three-dimensional model, Oh and Lee [97]

The laminate was subjected to the conventional autoclave temperature cycle for the UGN150 prepreg, shown in Figure 2.34. Convective boundary conditions between autoclave air and bagging materials were set using a heat transfer coefficient h of 85 W/m^{2}K.

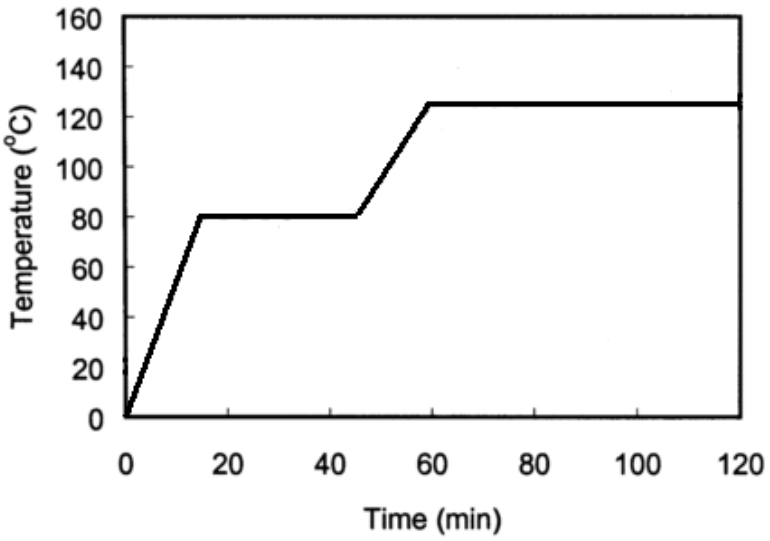

Figure 2.34 – Autoclave temperature cycle, Oh and Lee [97]

The model yielded accurate predictions for temperature profiles at the top, mid-height and bottom of the laminate centre location compared to experimental measurements, Figure 2.35:

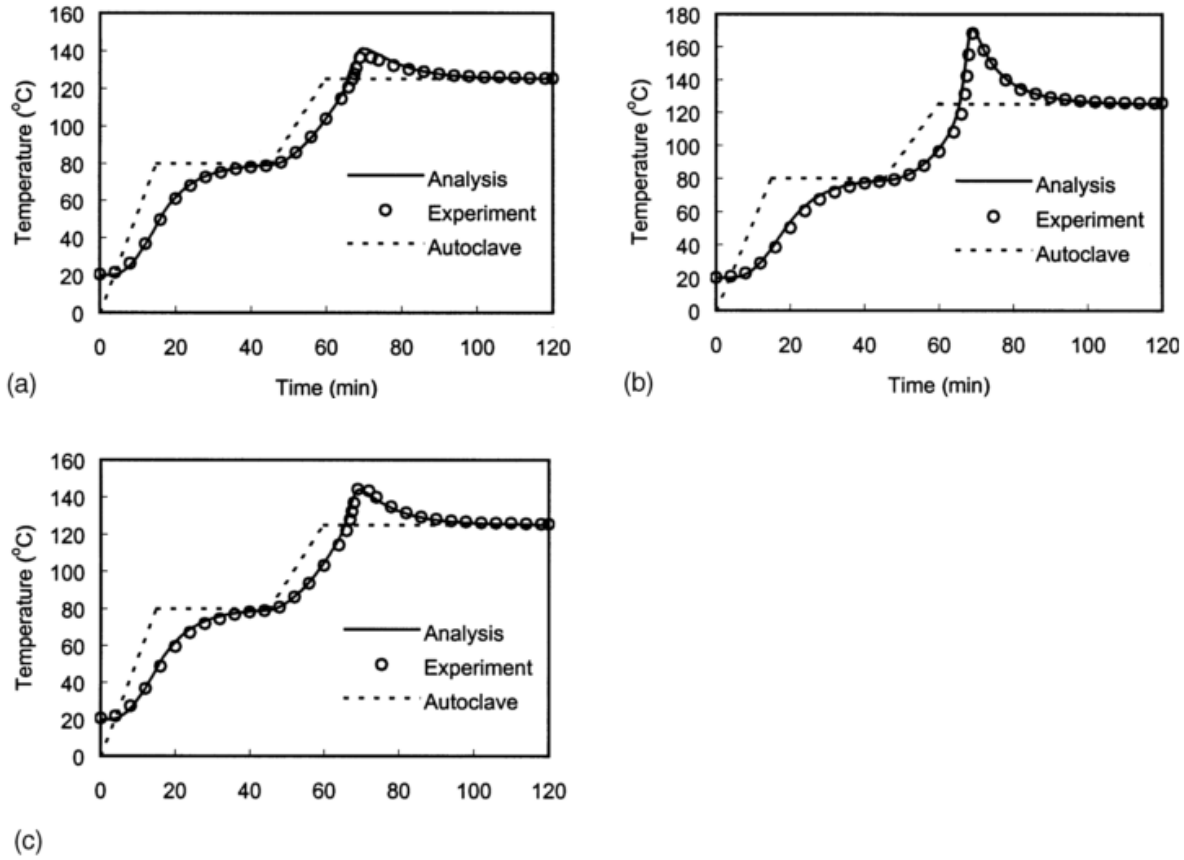

Figure 2.35 – Experimental and simulation results for temperature profiles at the (a) top (b) mid-height (c) bottom of the laminate centre, Oh and Lee [97]

The authors investigated the effect of the convective boundary condition on the temperature profile at mid-height of the laminate centre and found that a larger coefficient of heat transfer h increased the temperatures significantly, Figure 2.36:

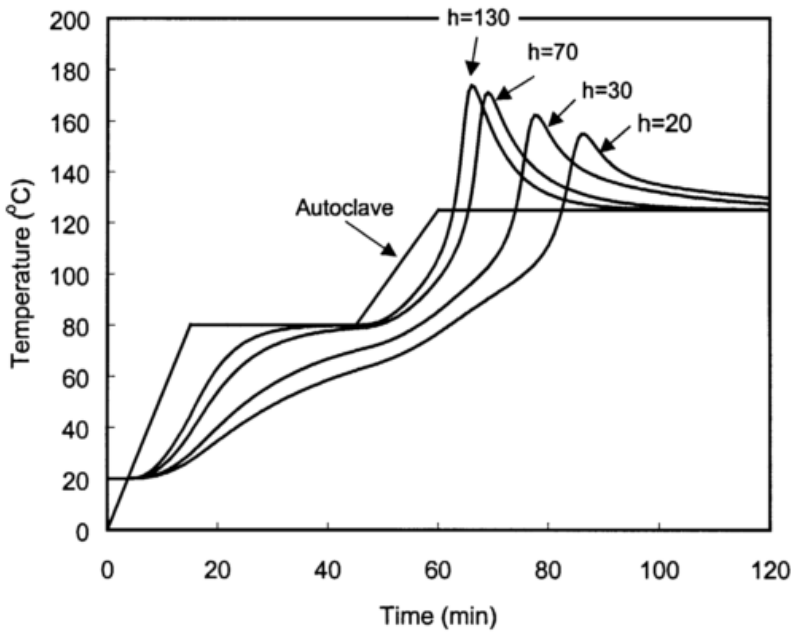

Figure 2.36 - Effect of heat transfer coefficient on temperature profile at laminate mid-height, Oh and Lee [97]

The authors also investigated the effect of bleeder thickness on the temperature profiles at the top and mid-height of the laminate centre, and found that a thicker bleeder decreased the temperatures significantly, Figure 2.37. This effect was especially prominent at the peak temperature caused by the curing exotherm where heat was trapped by the bleeder and dissipated less readily.

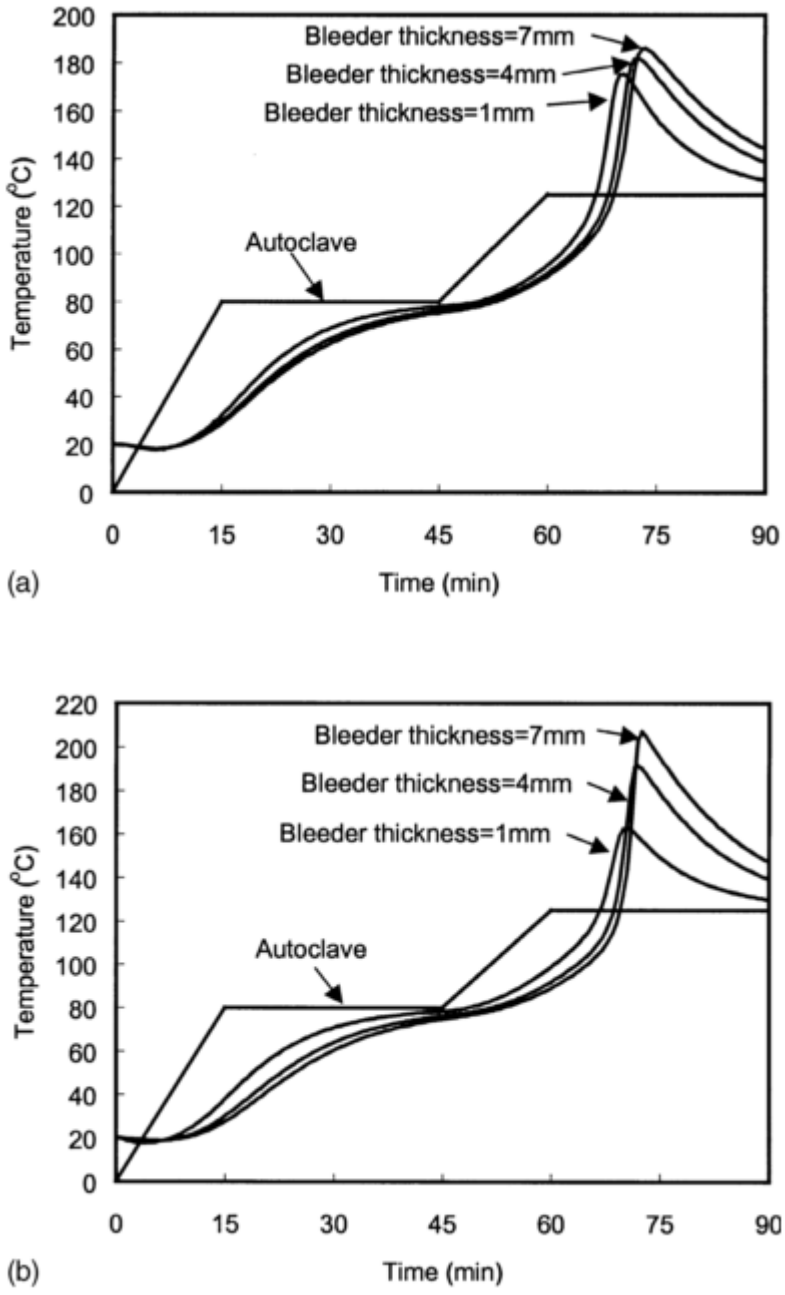

Figure 2.37 - Effect of bleeder thickness on temperature profiles at the (a) mid-height and (b) top of laminate centre, Oh and Lee [97]

The authors also investigated the effects of the tool plate, caul plate and dam thicknesses on the temperature profiles at the top, mid-height and bottom of the laminate

centre and found little difference in results generated for thicknesses ranging from 5 mm to 20 mm. This was to be expected as the tool plate, caul plate and dam are made of aluminium with a high thermal conductivity of 220 W/mK.

Studies were also found in the literature where heat transfer, cure kinetics and resin flow of laminates were modelled specifically for the RFI process. Blest et al. [30] developed a two-dimensional numerical model for resin flow coupled with transient heat transfer and cure kinetics. The authors modelled a carbon fibre-Hercules 3501-6 epoxy laminate during RFI manufacturing; the exact nature of the carbon fibres was not specified. The laminate was represented by a multi-ply stack consisting of three zone types: dry fabric plies, resin films and plies of fabric impregnated with resin, referred to as wetted fibres, Figure 2.38:

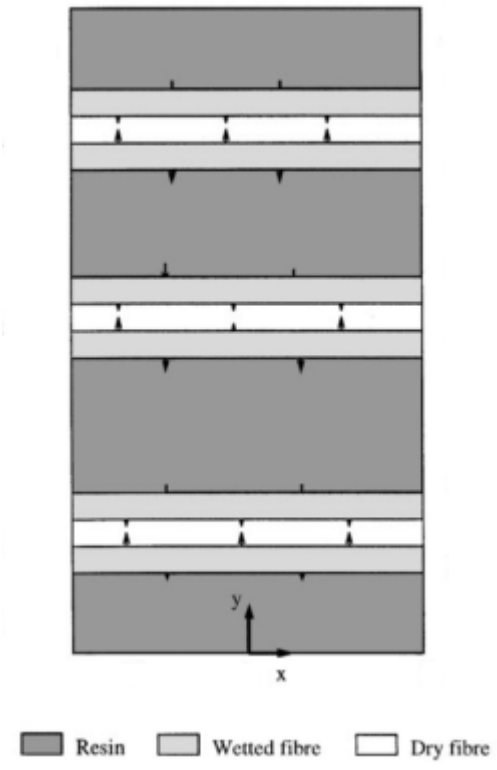

Figure 2.38 - Two-dimensional model, Blest et al. [108]

The model consisted of momentum and viscosity equations for resin flow and the heat Equation 2.32 for heat transfer. For cure, in the dry fibre zones the internal heat generation term $\dot{q}$ was zero while in the resin and wetted fibre zones the cure kinetics were fitted to the model from Lee et al. [121]. In the wetted fibres zones, density ρ and specific heat C_p were calculated using the rule of mixtures; calculation for thermal conductivity was not specified.

Adiabatic boundary conditions were set for the left and right sides of the model in Figure 2.38 while the autoclave temperature cycle shown in Figure 2.39 was imposed at the top and the bottom surfaces of the laminate as boundary conditions.

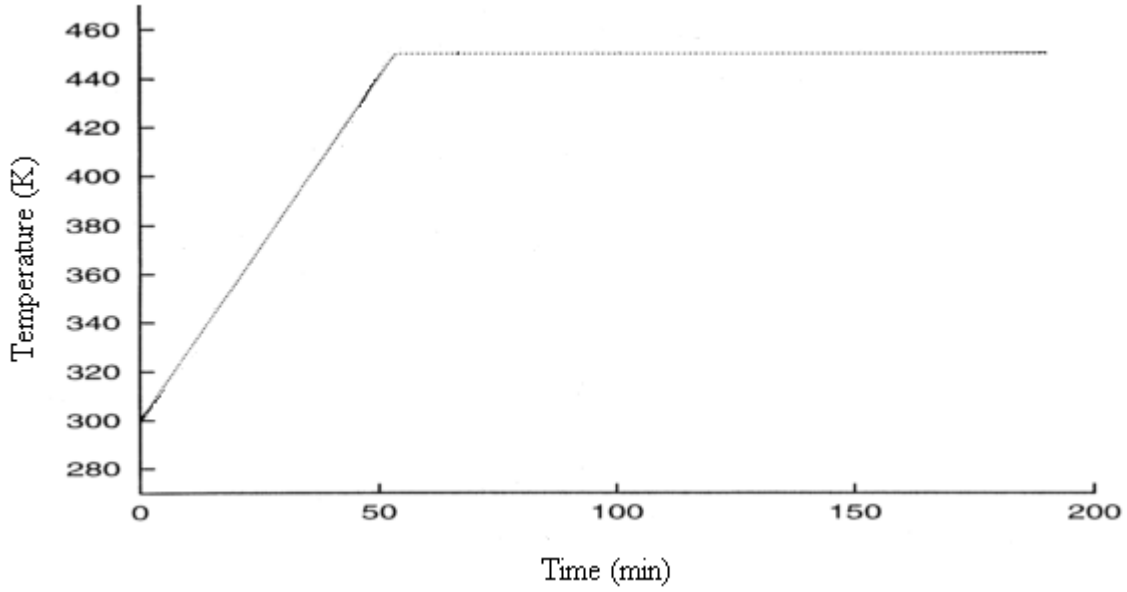

Figure 2.39 – Autoclave temperature cycle, Blest et al. [108]

Temperature profiles were obtained at laminate mid-height for laminates consisting of 16, 32 or 52 plies of fabric under both heating rates of 2.8 °C/min and 11.1°C/min, Figure

2.40. Exotherms were seen for all thicknesses under both heating rates, with the magnitude of the exotherm increasing for thicker laminates.

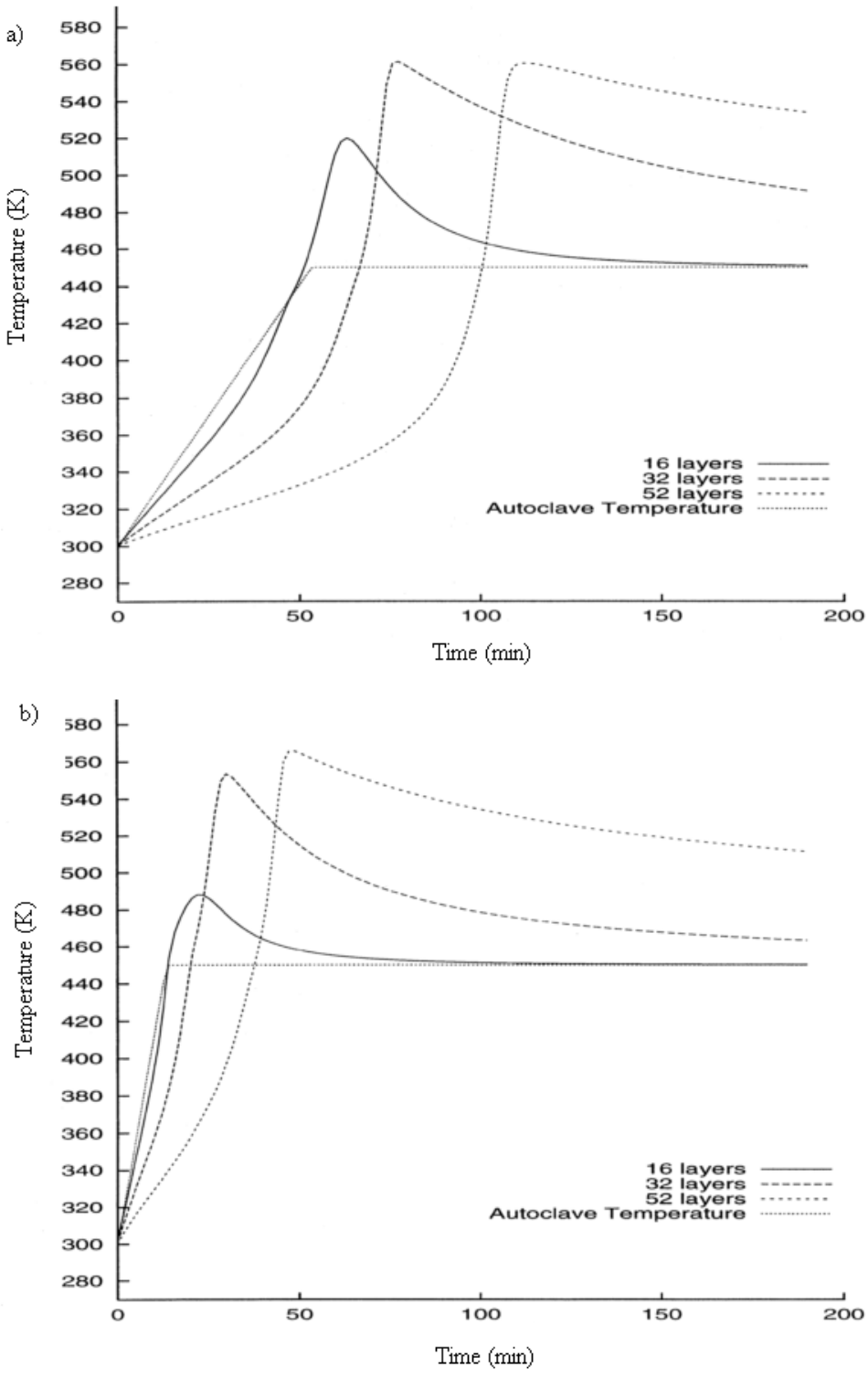

Figure 2.40 - Temperature profiles at mid-height of laminate centre obtained from model for various thicknesses under heating rates of (a) 2.8°C/min (b) 11.1°C/min, Blest et al. [108]

Comparison between the temperature profiles at the mid-height of a 16-ply laminate under heating rates of 2.8 °C/min and 11.1°C/min shows that a higher heating rate yields higher exotherms, Figure 2.41:

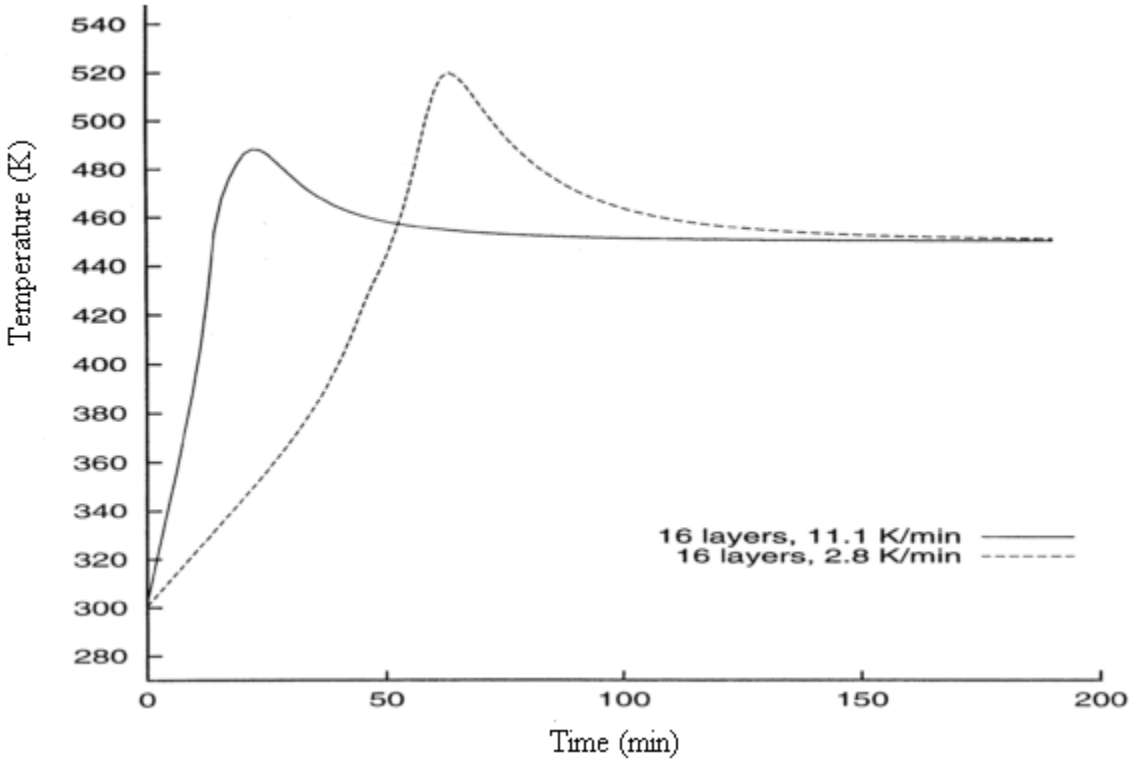

Figure 2.41 - Temperature profiles at mid-height of a 16-ply laminate obtained from model under different heating rates, Blest et al. [108]

Caba et al. [32] developed a three-dimensional numerical model for resin flow coupled with transient heat transfer and cure kinetics. The authors modelled a carbon fibre-Hercules 3501-6 epoxy laminate undergoing RFI manufacturing; the exact nature of the carbon fibres was not specified. Similar to work done by Blest et al. [30], the model featured the three zone types mentioned above where properties for the wetted fibre zone were

calculated according to the rule of mixtures except for the through-thickness thermal conductivity, which was calculated based on the Chamin model [122]. The geometry of the part modelled is shown along with the location of the thermocouples, Figure 2.42. Locations 1 and 7 were on the top and bottom surfaces of the part while all other thermocouples were in the autoclave air 5 cm away from the surface of the part at the locations indicated.

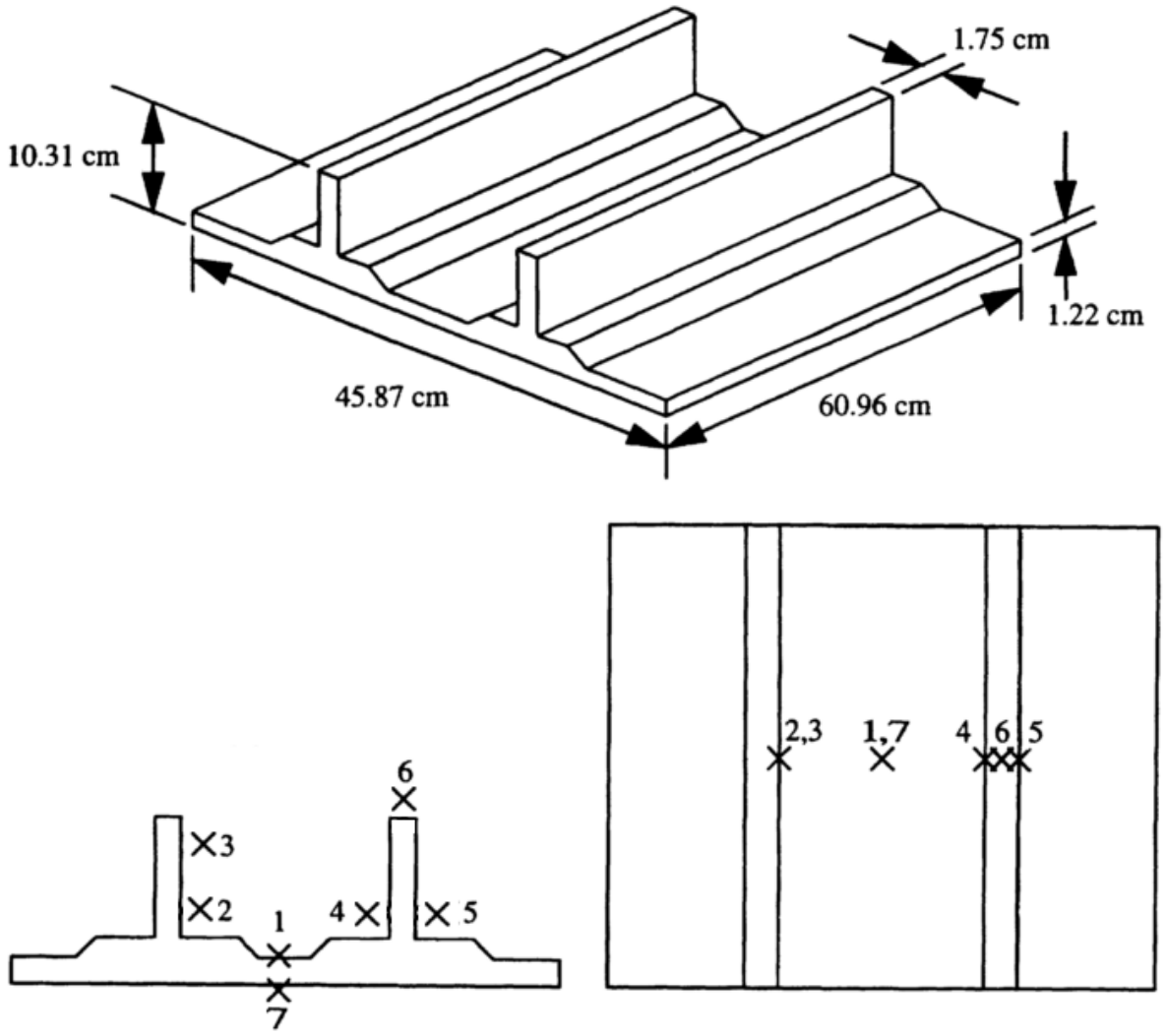

Figure 2.42 - Geometry of part, Caba et al. [110]

The model featured momentum and viscosity equations for resin flow and heat Equation 2.32 for heat transfer and cure. For the wetted fibre zones, the internal heat generation $\dot{q}$ was fitted to the Kamal-Sourour model. The autoclave temperature profile was measured, Figure 2.43 and imposed as boundary condition on all surfaces of the part.

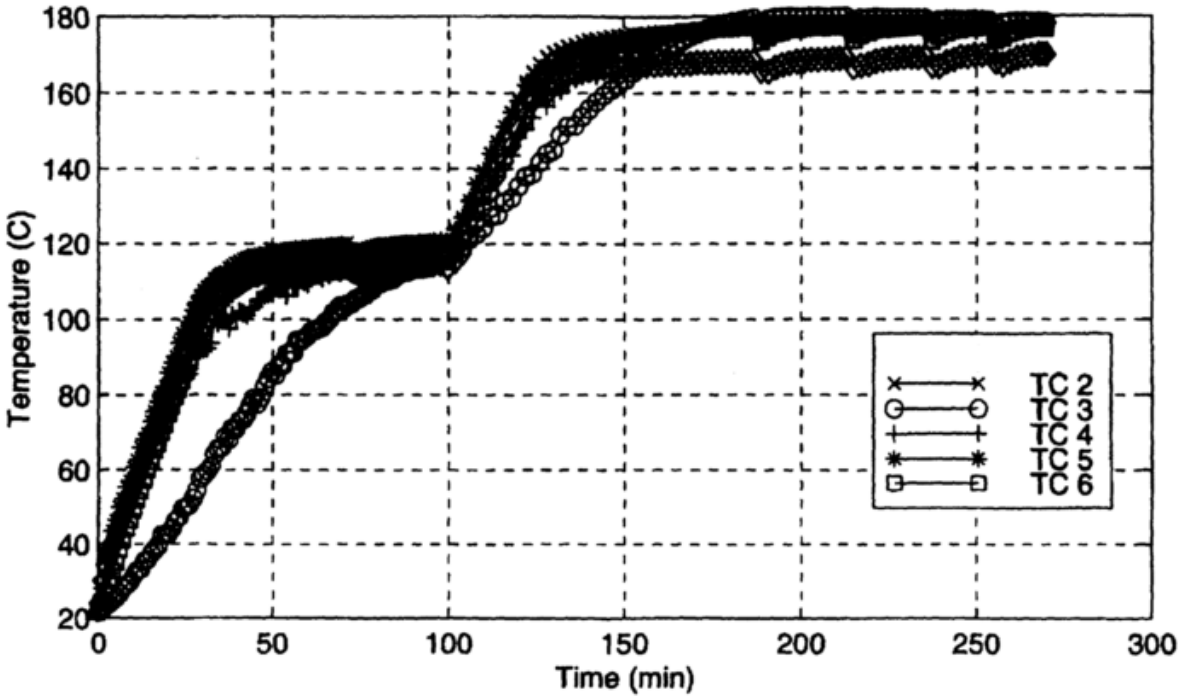

Figure 2.43 - Autoclave temperature cycle, Caba et al. [110]

Temperature profiles at locations 1 and 7 were obtained from the model and are in good agreement with experimental measurements, Figure 2.44:

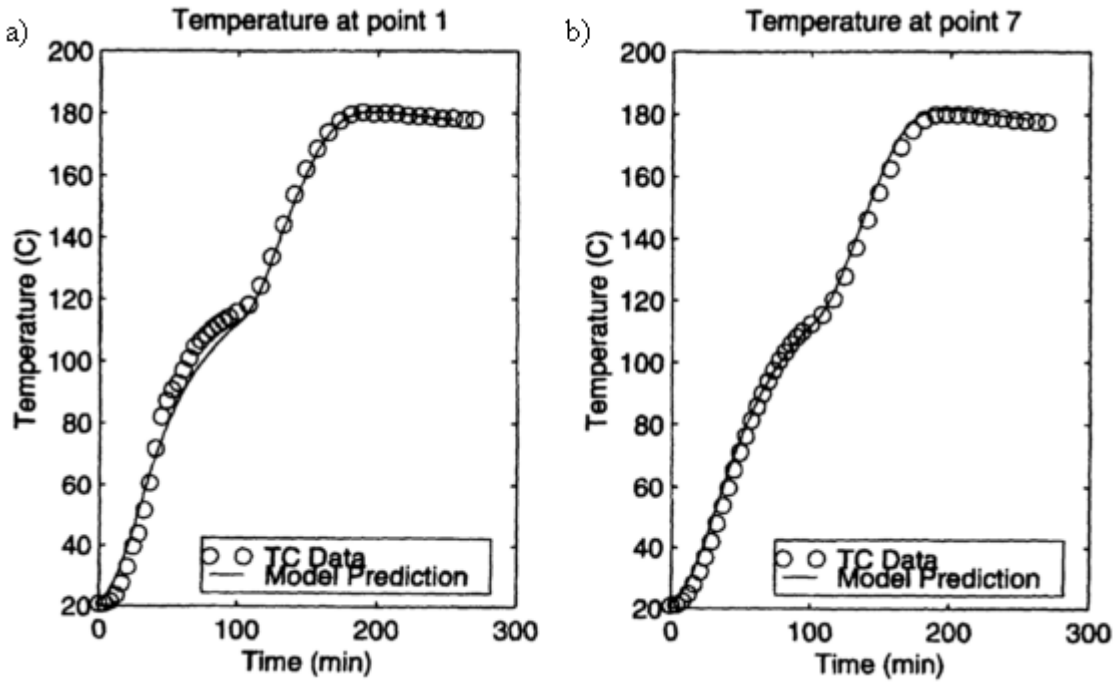

Figure 2.44 - Temperature profiles at locations (a) 1 and (b) 7 obtained from model, Caba et al. [110]

In summary, heat transfer models of the RFI process coupled with cure kinetics were found in the literature. Blest et al. [30] modelled the temperature profiles at the laminate centre; however, temperature profiles at the top and bottom of the laminate as well as the temperature distribution in the laminate thickness were not studied. Also, no comparisons or validations of the model against experimental temperature profiles were shown. Caba et al. [32] validated experimentally the temperature profiles on the top and bottom surfaces of a part with complex geometry but did not measure or model temperatures at any location inside the laminate. Oh and Lee [31] and Blest et al. [30] studied the effects of manufacturing parameters such as the heating rate and bleeder thickness on the temperature profiles of the

laminate; however, none of the models found in the literature investigated the effect of the laminate thermal conductivity or the effect of using a CNT-reinforced resin compared with its neat counterpart.

In Chapter 5 of this thesis, a three-dimensional transient heat transfer model coupled with cure kinetics developed in FLUENT ANSYS is presented, aiming at simulating temperature profiles at the top, mid-height and bottom of the laminate. The model was validated against experimental temperature profiles. Resin flow was not modelled; however, the effects of cure, heat transfer coefficient, laminate thermal conductivity, laminate thickness and CNT addition into the resin were investigated systematically.

3 Thermal conductivity of dry carbon fibre fabrics

Carbon fibre fabrics are used extensively in the aerospace industry as reinforcements for composites. The thermal conductivity of these fabrics, otherwise referred to as reinforcements, is an important parameter for understanding heat diffusion in composites and similar fabric materials, and for controlling and modelling heat transfer during composite manufacturing processes such as RFI and VARTM where the properties of dry fabrics must be known prior to resin impregnation. However, there are very few published results and data in the literature.

In this work, in-plane k_{rip} and through-thickness k_{rtt} thermal conductivities of two carbon fibre fabrics exposed to air and under vacuum were measured at various fibre volume fraction V_f values, where subscript r identifies the reinforcement. Measurement devices THISYS and THASYS are presented in Section 3.1 followed by sample preparation and measurement procedures in Section 3.2. Then k_{rip} and k_{rtt} values measured at various V_f values for the samples exposed to air are presented in Section 3.3 and compared with the in-plane k_{cip} and through-thickness k_{ctt} thermal conductivities of carbon fibre-epoxy composites made from the same fabrics, identified by subscript c. k_{cip} and k_{ctt} measurements performed on the composites and presented in this chapter were done for comparison purposes against measurements performed on the dry fabrics and they are not the main focus of this chapter; resin materials, experimental procedures as well as characterisation of the composite plates are presented in detail in Chapter 4. Two of the dry fabric samples were also measured under vacuum and results were compared with those obtained for the samples

exposed to air. Results from an analytical model and simulations attempting to predict k_{rtt} are presented in Section 3.4. The chapter ends with a discussion of major findings and their implications, Section 3.5.

3.1 Measurement devices

Dedicated thermal conductivity measurement devices THISYS and THASYS manufactured by Hukseflux were used for experimental data collection at Aerospace Structures and Materials Performance laboratory, National Research Council (NRC), Ottawa. THISYS measures the in-plane thermal conductivity while THASYS measures the through-thickness thermal conductivity, Figure 3.1. THISYS requires one flat sample measuring 70 mm by 110 mm with a thickness ranging from 0.1 mm to 6 mm, Figure 3.1 (a) while THASYS requires two such identical samples, Figure 3.1 (b).

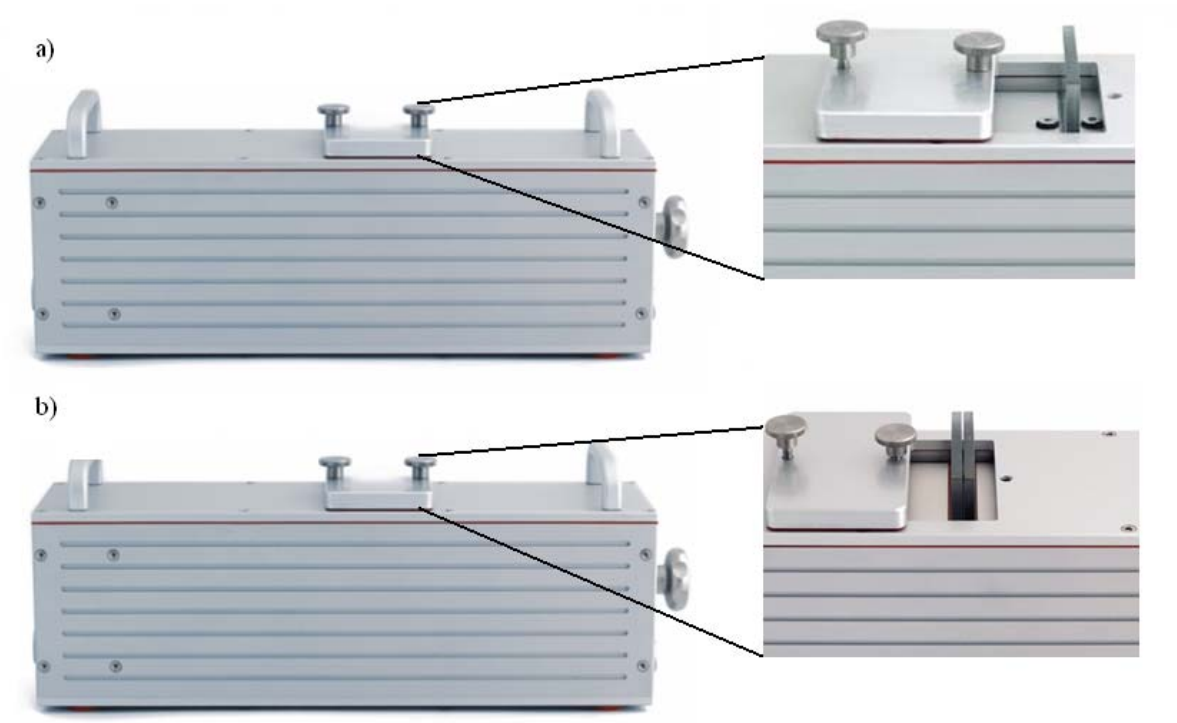

Figure 3.1 - Thermal conductivity measurement devices (a) THISYS: in-plane (b) THASYS: through-thickness [123]

The components and configuration of THISYS are shown in Figure 3.2. A single sample is mounted into the device between two thin heaters and manually tightened via a spring. There is a heat sink as well as an air-filled insulation cavity beside each heater for reducing lateral heat losses from the heaters to a negligible level. The sample, heaters and heat sinks are immersed in a glycerol bath for minimizing thermal contact resistance. A heating cycle is applied during one hour where heat flows from the heaters into the heat sinks through the sample along its plane. The heating cycle has three stages, each lasting 20 minutes: the heaters begin to supply heat during the first stage, steady state is reached during

the second stage and the sample is cooled during the third stage. Once steady-state is reached the in-plane thermal conductivity of the sample can be calculated from the heat flux, which is known from heater power and the in-plane temperature gradient using Fourier's law, Equation 2.30. A more detailed description of the device can be found in previous work by Hind [51]. Variability of the THISYS device for measurements taken at 20°C is quoted to be ±2% by the manufacturer and measurements performed on reference samples with known thermal conductivities showed an accuracy of ±6% [124].

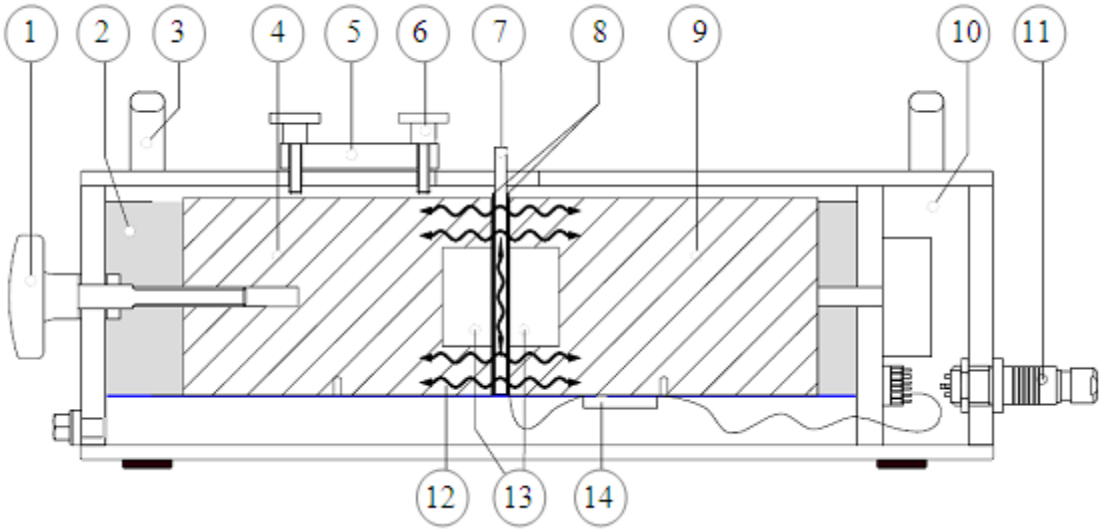

1) Adjustment for moving heat sink
2) Glycerol bath
3) Handle
4) Movable heat sink
5) Cover plate
6) Cover plate screw
7) Sample
8) Heaters (2)
9) Fixed heat sink
10) Empty compartment for cable connectors
11) Connector for power and DAQ
12) Direction of heat flux
13) Air filled insulation cavities
14) Thermopile connector

Figure 3.2 - Components and configuration of THISYS device for in-plane thermal conductivity measurements [124]

The components and configuration of THASYS are shown in Figure 3.3. Two identical samples are mounted into the device on either side of a single thin heater and

tightened manually via a spring. There is a heat sink beside each sample. Similar to THISYS, the samples, heater and heat sinks are immersed in a glycerol bath for minimizing thermal contact resistance. A heating cycle is applied during one hour where heat flows from the heater into the heat sinks across the thickness of the samples. Similar to THISYS, the heating cycle has the same three stages, each lasting 20 minutes. Once steady-state is reached the through-thickness thermal conductivity of the samples can be calculated from the heat flux which is known from heater power and the through-thickness temperature gradient using Fourier's law. A more detailed description of the device can be found in previous work by Hind [51]. Variability of the THASYS device for measurements taken at 20°C is quoted at ±1% by the manufacturer [125].

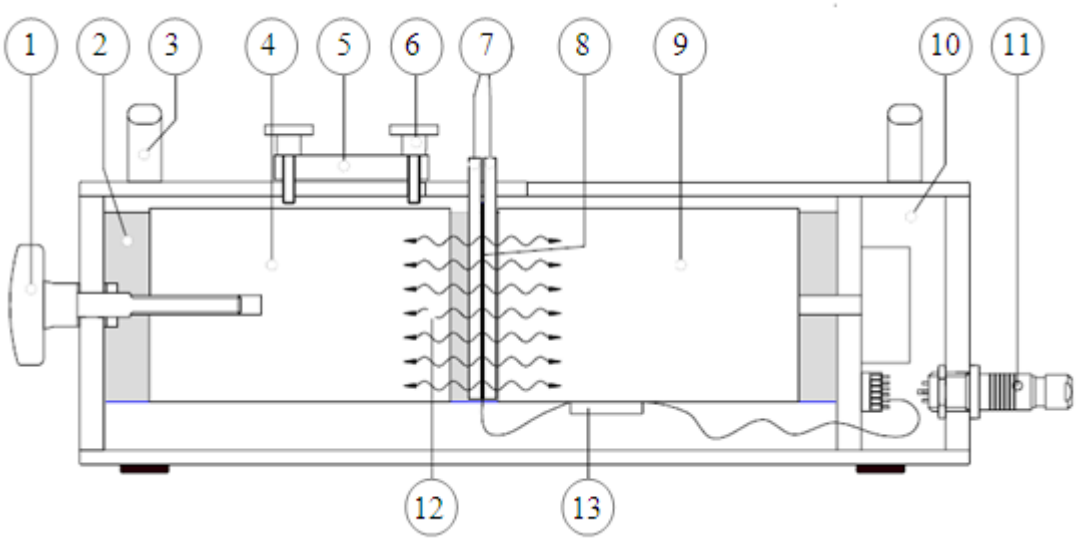

1) Adjustment for moving heat sink
2) Glycerol bath
3) Handle
4) Movable heat sink
5) Cover plate
6) Cover plate screw
7) Samples (2)
8) Heater and thermopile
9) Fixed heat sink
10) Empty compartment for cable connectors
11) Connector for power and DAQ
12) Direction of heat flux
13) Thermopile connector

Figure 3.3 - Components and configuration of THASYS device for through-thickness thermal conductivity measurements [51]

THISYS and THASYS are typically used for measuring the in-plane k_{cip} and through-thickness k_{ctt} thermal conductivities of composites and other solid materials such as plastics.

In this thesis the devices were also used for measuring the in-plane k_{rip} and through-thickness k_{rtt} thermal conductivities of dry carbon fibre fabrics exposed to air and under vacuum.

3.2 Sample preparation and measurement procedure

Thermal conductivities of two carbon fibre fabrics were measured: a non-crimp stitched bidirectional fabric and a 2x2 twill woven fabric, both consisting of HTS40 carbon fibres from Toho Tenax, Table 3.1. The fabrics were cut into 70 mm by 110 mm plies, stacked together and sealed into a film material described below.

Table 3.1 - Carbon fibre fabrics

Fabric architecture	Product code	Supplier	Surface density (g/m^2)	Filaments per yarn
Bidirectional ±45°	S32CX00K-00534-01270-264000	Saertex	534	12K
2x2 Twill	TC06T50F	JB Martin	215	3K

For composites, both k_{cip} and k_{ctt} increase with V_f and can be calculated as a function of V_f, Equations 2.1 to 2.10. Hence, it is important to measure k_{rip} and k_{rtt} as a function of V_f and to use the thermal conductivity of the dry fabric at the appropriate V_f when modelling heat transfer during manufacturing. The V_f values of interest for thermal conductivity measurements range from that of the as-received fabrics at approximately 30% to that of typical composites manufactured using the RFI process, ranging between 50% and 60%. Hence, the number of plies used in the samples for each fabric was chosen as to yield a

V_f range between 30% and 60% whilst yielding reasonable stack thicknesses between 3 mm and 5 mm for measurements in THISYS and THASYS. The numbers of plies for each sample of the non-crimp fabric and the twill fabric were 6 and 16 respectively, calculated using Equation 3.1 which relates the fabric stack thickness t_f to V_f :

$$t_f = \frac{N\rho_{sd}}{\rho_f V_f} \tag{3.1}$$

where N is the number of plies of the fabric, ρ_{sd} is the surface density of the fabric and ρ_f is the density of the carbon fibres.

The film material was 50 μm thick Dahlar® release film 125 from Airtech; this is made of polypropylene [126] and typically used as vacuum bagging and release film material in composite layups. Each sealed sample was tested in water for 10 minutes to ensure that no leakage was present. This procedure was used so as to avoid penetration of glycerol from the devices into the dry fabric samples. Most samples were sealed on three sides, leaving the top side open to enable progressive compaction of the samples in the devices, Figure 3.4 while the two samples run under vacuum were sealed on all sides and equipped with a port sealed inside the film material for connection to the vacuum pump, Figure 3.5.

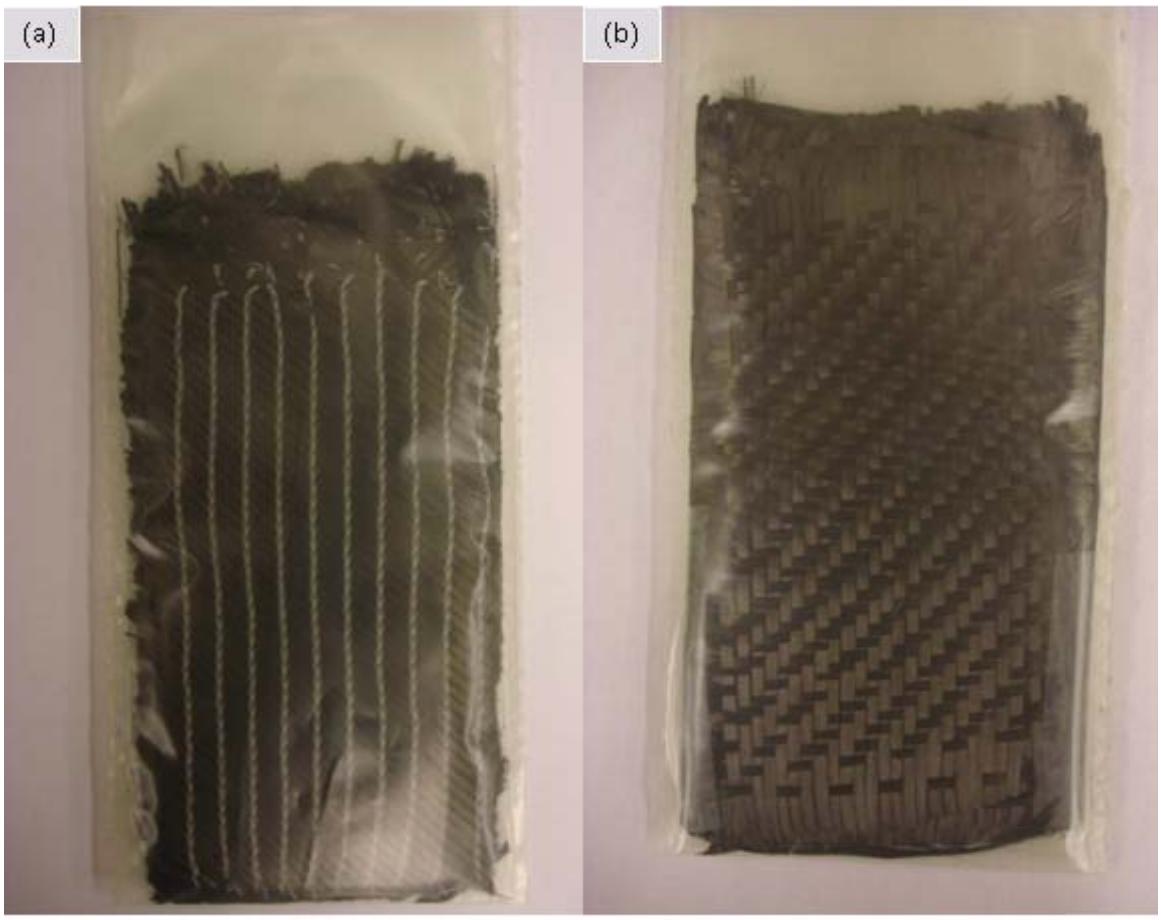

Figure 3.4 - Samples for thermal conductivity measurements of the (a) non-crimp and (b) 2 by 2 twill carbon fibre fabric

Figure 3.5 - Vacuumed samples for (a) in-plane and (b) through-thickness thermal conductivity measurements of the non-crimp fabric

Increases in V_f were achieved by compaction in THISYS and THASYS; the samples were tightened using the adjustment for the moving heat sink as shown in Figures 3.2 and 3.3, hence reducing the gap width of the devices. Plexiglass inserts milled to accurate thicknesses were used for controlling the gap width of the devices. The inserts had thicknesses ranging from 3.39 mm to 4.76 mm, leading to V_f ranges for each fabric close to the targeted V_f range from 30% to 60% as previously mentioned, Table 3.2. Thickness of the

release film used for sample preparation is very small compared to that of the samples; hence its effect on thermal conductivity results is neglected.

Table 3.2 - Insert thicknesses and corresponding dry fabric V_f

Insert	Thickness (mm)	V_f (%) of non-crimp fabric	V_f (%) of twill fabric
I1	4.76	37.5	40.1
I2	4.48	39.8	42.9
I3	4.20	42.5	45.6
I4	3.90	45.7	49.1
I5	3.39	52.6	56.4

The effect of subjecting the samples to multiple compaction cycles is also of interest, as the fibres can potentially reorganise after each compaction cycle which may affect the thermal conductivity of the fabric. Multiple compaction cycles occur during the debulking procedure employed in industry, where the laminate is compacted under vacuum and moderate heat multiple times during layup for removal of volatiles and air. In this thesis, thermal conductivity measurements on each sample were taken during three cycles of compaction and unloading.

During each compaction cycle, measurements were taken at discrete V_f values in ascending order corresponding to I1 to I5. The samples and inserts I1 were mounted into THISYS and THASYS devices and tightened manually, Figure 3.6. Upon end of the measurement, the samples were loosened in the device during which inserts I1 were taken out and replaced with inserts I2. Then, the samples and inserts I2 were tightened and the conductivity measurement at the corresponding V_f was taken. This procedure was repeated until all desired measurements were taken during the first compaction cycle. The sample was

then unloaded and taken out of the device, and afterwards the second and third compaction cycles were performed in the same manner with measurements taken at the same V_f values for each fabric as during the first cycle.

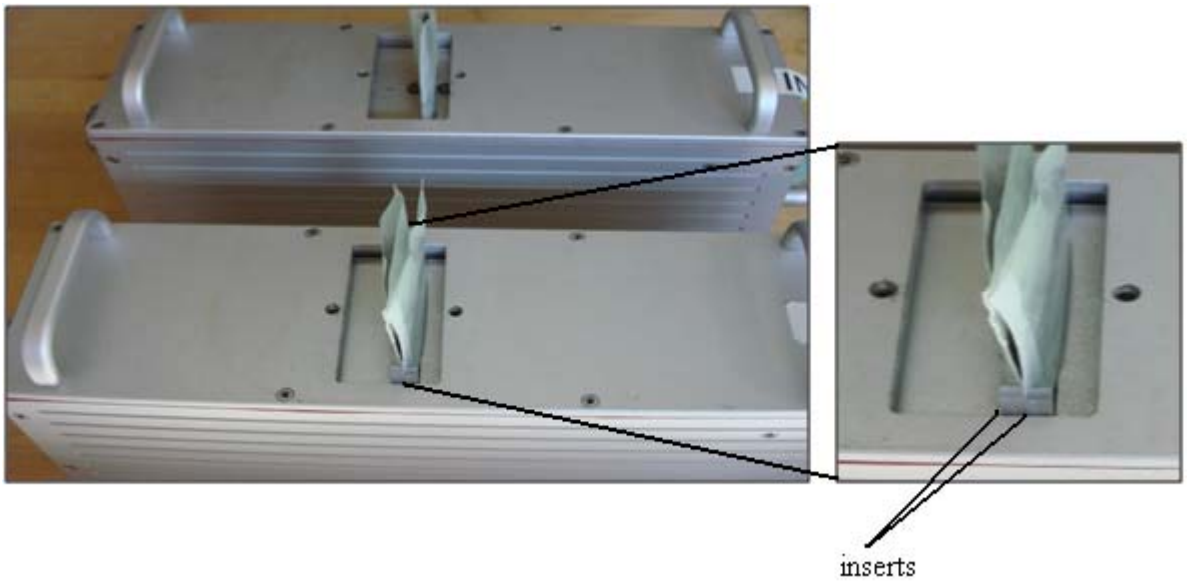

Figure 3.6 - Samples and inserts mounted in THASYS (front) and THISYS (back) during measurement

For the last set of measurements performed on both fabrics where V_f is controlled by inserts I5, compaction of the samples to the thickness of the inserts could not be achieved solely by manual tightening of the devices. Therefore, external compaction of the samples was performed beforehand using an Instron 4482 universal testing frame. Each sample was placed upon the bottom fixture, Figure 3.7 (a) and a clean and flat metal platen was placed on top of the sample for applying uniform pressure, Figure 3.7 (b). The samples were subjected

to four successive compaction cycles under 1 MPa pressure at a rate of 4mm/min, and then mounted into THISYS and THASYS for measurements using inserts I5.

Figure 3.7 - Compaction setup on Instron 4482 universal testing frame: (a) sample placed on bottom fixture (b) aluminium platen placed on top of sample

The vacuumed samples seen in Figure 3.5 were mounted into THISYS and THASYS and measurements were taken under vacuum; a DAA-V715A vacuum pump from Gast, Figure 3.8, was connected to the port sealed in the samples and run at 0.02 bars or 98% vacuum for the entire duration of the measurements. Figure 3.9 shows through-thickness thermal conductivity measurements performed on the vacuumed non-crimp fabric sample using THASYS.

Figure 3.8 - Vacuum pump DAA-V715A from Gast

Figure 3.9 - Through-thickness thermal conductivity measurement of non-crimp fabric sample in THASYS

Two types of variability for both the in-plane and through-thickness thermal conductivity measurements were quantified at selected data points: variability of the THISYS and THASYS devices, and total variability of the data. Each device variability value was calculated based on two or three measurements: the original data value and either one or two repeat measurements performed on the same sample and at the same V_f, taken one after another without removing the sample from the device. Each data variability value was calculated based on four measurements: the original data value measured using the original sample and three more data values, each measured using a different sample at the same V_f. Hence this variability includes variability of the device, variability due to differences in mounting the samples and inserts as well as variability due to differences in preparation of the four samples.

Two composite plates were manufactured using the RFI process, one based on the non-crimp fabric and the other based on the twill fabric mentioned above, and two samples measuring 70 mm by 110 mm were cut from each plate for measurement using THISYS and THASYS. As mentioned previously, the resin materials and experimental procedures used for manufacturing these composite plates as well as their V_f characterisation are presented in detail in Chapter 4. The aim of presenting results of the composite plates in this chapter is to provide direct comparisons between thermal conductivity of the dry fabrics and thermal conductivity of composites manufactured using the same fabrics for a better understanding of heat transfer in these materials.

3.3 Results

Results obtained from thermal conductivity measurements performed on the two dry fabrics are shown in Figures 3.10 to 3.13. In the in-plane direction, Figures 3.10 to 3.11 show that k_{rip} for both fabrics varies linearly as a function of V_f. The non-crimp and twill fabrics showed conductivities in comparable ranges; values ranged from 1.303 W/mK to 2.249 W/mK for the non-crimp fabric and from 1.367 W/mK to 2.092 W/mK for the twill fabric. k_{rip} values for the non-crimp fabric were slightly higher compared with values of the twill fabric at the same V_f; k_{rip} values of 1.597 W/mK and 1.462 W/mK were measured for the non-crimp fabric and the twill fabric at of 43% V_f respectively and 1.880 W/mK and 1.562 W/mK were measured for the non-crimp fabric and the twill fabric at of 46% V_f, respectively. For both fabrics, the effect of successive compaction cycles can be seen, where values measured at the same V_f increased slightly after each compaction cycle. The vacuumed non-crimp sample returned a value of 2.188 W/mK at 52.6% V_f; 2.4% lower than that of its non-vacuumed counterpart.

In the through-thickness direction, Figures 3.12 and 3.13 show that k_{rtt} for both fabrics follows an exponential recovery trend as a function of V_f. The non-crimp and twill fabrics showed conductivities in comparable ranges: values ranged from 0.112 W/mK to 0.209 W/mK for the non-crimp fabric and from 0.145 W/mK to 0.219 W/mK for the twill fabric. k_{rtt} values for the non-crimp fabric were also very similar compared with values of the twill fabric at the same V_f: k_{rtt} values of 0.187 W/mK and 0.181 W/mK were measured for the

non-crimp fabric and the twill fabric at of 43% V_f respectively and 0.189 W/mK and 0.197 W/mK were measured for the non-crimp fabric and the twill fabric at of 46% V_f, respectively. Similar to the in-plane direction, the effect of successive compaction cycles can be seen with both fabrics. The vacuumed non-crimp sample returned a value of 0.182 W/mK at 52.6% V_f; 7.4% lower than that of the non-vacuumed counterpart. All thermal conductivities were measured at room temperature and inputted into the simulation model in Chapter 5 as constant values; thermal conductivities for PAN-based fibres increase little with temperature, as shown by T300 and T800H curves in Figure 2.2.

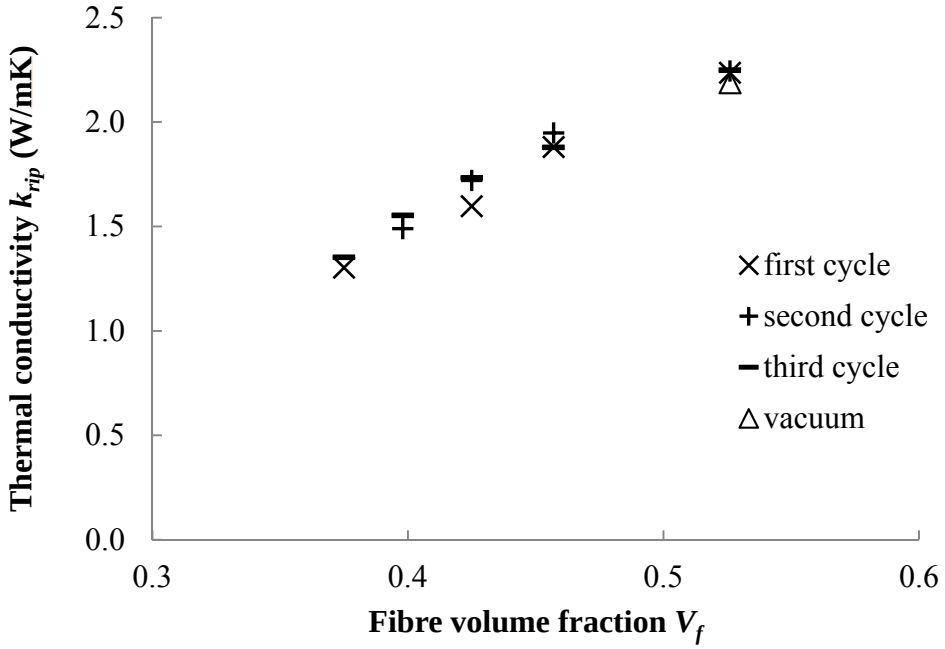

Figure 3.10 – In-plane thermal conductivity k_{rip} data, non-crimp fabric

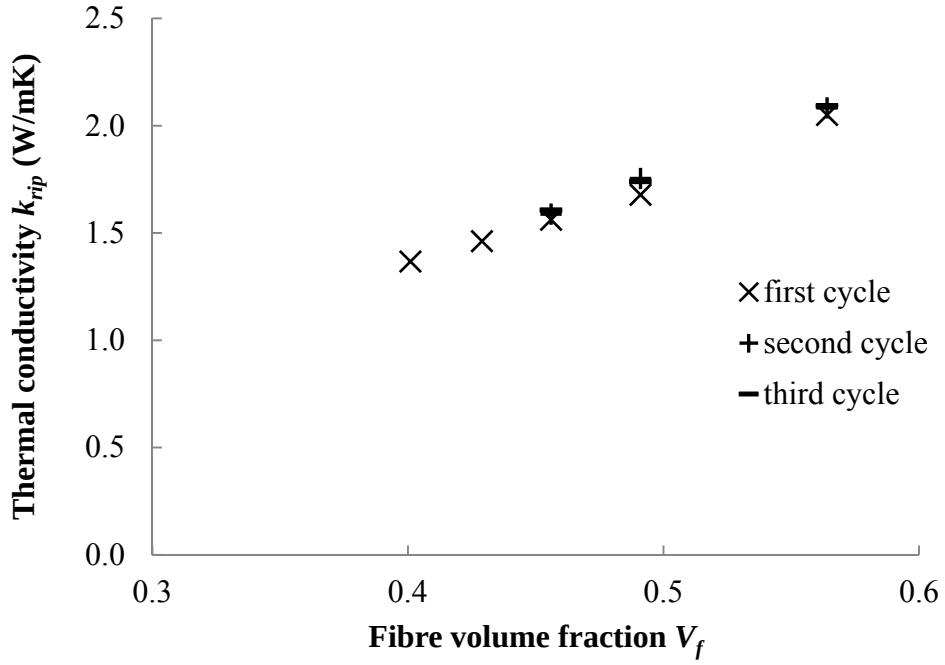

Figure 3.11 – In-plane thermal conductivity k_{rip} data, twill fabric

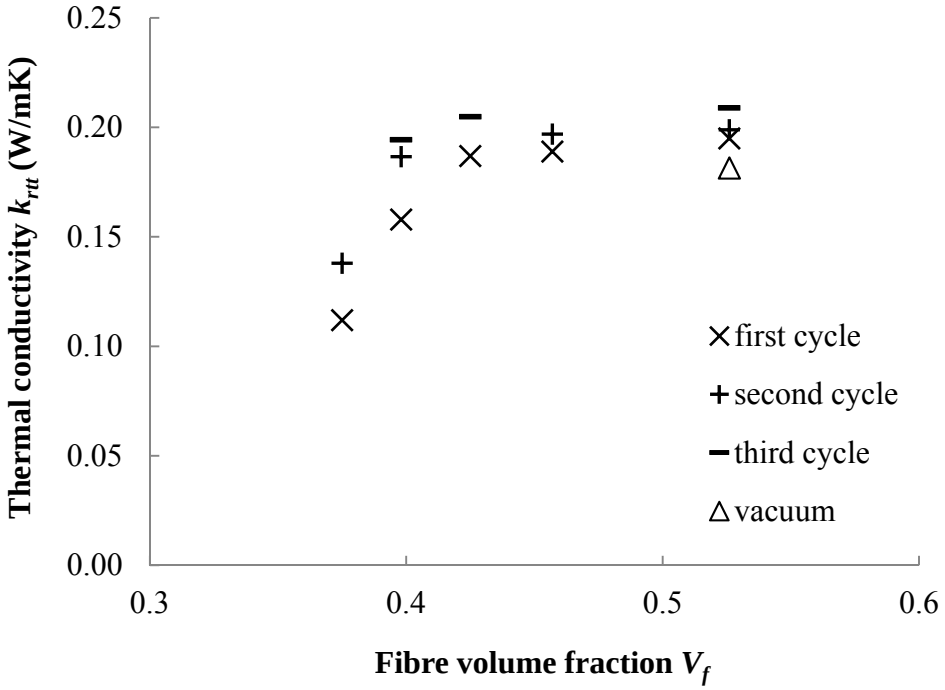

Figure 3.12 – Through-thickness thermal conductivity k_{rtt} , non-crimp fabric

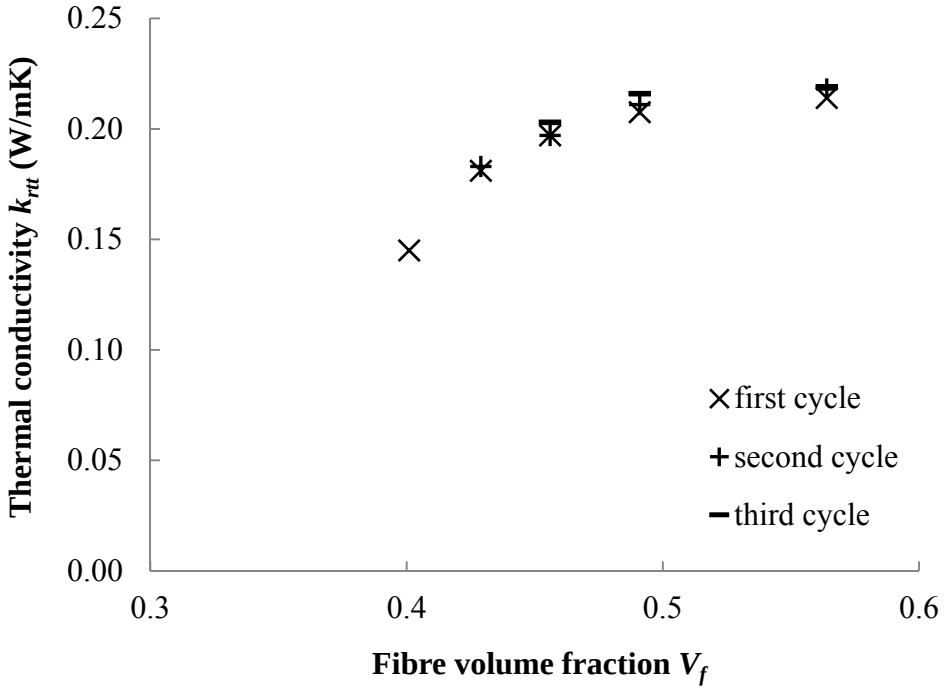

Figure 3.13 - Through-thickness thermal conductivity k_{rtt} , twill fabric

Variability values are shown in Tables 3.3 to 3.6, calculated based on the difference between the maximum and minimum data points relative to the minimum one. For the device variability, values are generally less than 1% except for that of the vacuumed sample at 2.8%. Values confirm the 2% and 1% variability data reported for THISYS and THASYS by the manufacturer, indicating that the devices operated satisfactorily with the dry fabric samples tested. Total variability of the data ranged from 6.7 % to 11.2%.

Table 3.3 - Variability of THISYS device

Fabric	V_f (%)	k_{rip} (W/mK)	Variability (%)
Twill	40.1	1.371 1.369 1.362	0.7
Twill	56.4	2.089 2.077	0.6

Table 3.4 - Variability of THASYS device

Fabric	V_f (%)	k_{rtt} (W/mK)	Variability (%)
Non-crimp	39.8	0.187 0.187 0.186	0.5
Non-crimp	39.8	0.195 0.194	0.5
Non-crimp	52.6 vacuum	0.184 0.179	2.8
Twill	49.1	0.208 0.207	0.5

Table 3.5 - Total variability of in-plane thermal conductivity k_{rip} data

Fabric	Sample	V_f (%)	k_{rip} (W/mK)	Variability (%)
Twill	1 2 3 4	45.6	1.562 1.59 1.597 1.666	6.7
Non-crimp	1 2 3 4	42.5	1.597 1.668 1.744 1.663	9.2

Table 3.6 - Total variability of through-thickness thermal conductivity k_{rtt} data

Fabric	Sample	V_f (%)	k_{rip} (W/mK)	Variability (%)
Twill	1 2 3 4	49.1	0.208 0.193 0.188 0.187	11.2
Non-crimp	1 2 3 4	45.7	0.189 0.190 0.196 0.182	7.7

Thermal conductivity data for the two composites were compared with those of the two dry fabrics in the in-plane and through-thickness directions, as shown in Figures 3.14 and 3.15 respectively. The composite plates made using the non-crimp fabric and the twill fabric had V_f values of 57.5% and 53.5% respectively while V_f values for the dry non-crimp and the twill fabric used for comparison were 52.6% and 56.4% respectively. In the in-plane direction, k_{cip} and k_{rip} of composites based on the non-crimp fabric are 2.499 W/mK and 2.236 W/mK respectively while values for the twill fabric are 2.513 W/mK and 2.050 W/mK, respectively.

The same comparisons made for the through-thickness data show more significant differences: k_{ctt} and k_{rtt} for the non-crimp fabric are 0.547 W/mK and 0.195 W/mK respectively while values for the twill fabric are 0.505 W/mK and 0.214 W/mK respectively. The in-plane to through-thickness thermal conductivity ratio is approximately five for the carbon fibre-epoxy composites compared to approximately ten for the dry carbon fibre fabrics.

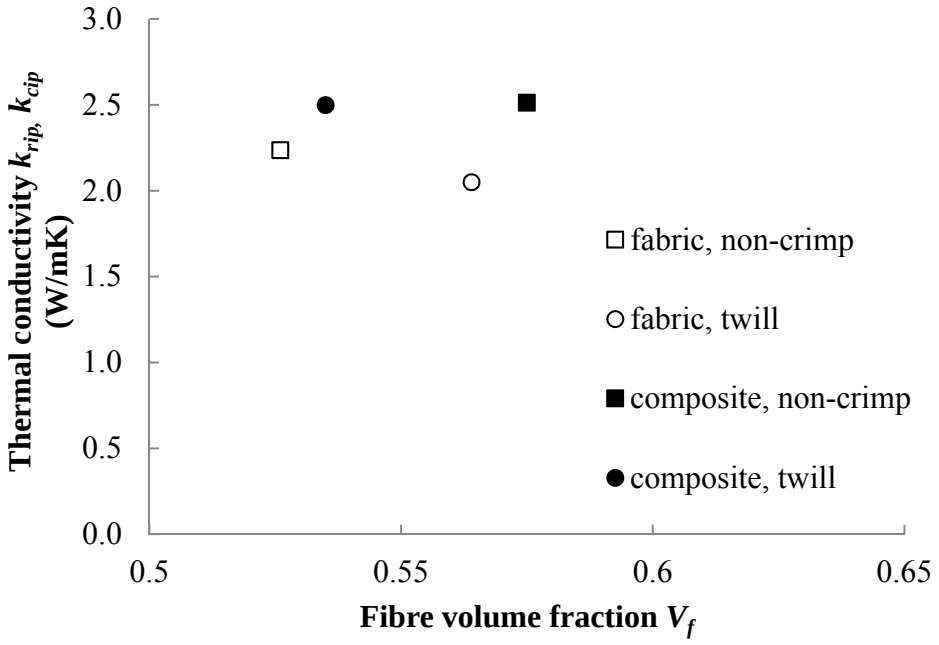

Figure 3.14 - In-plane thermal conductivity measurements of composites k_{cip} vs. dry fabrics k_{rip}

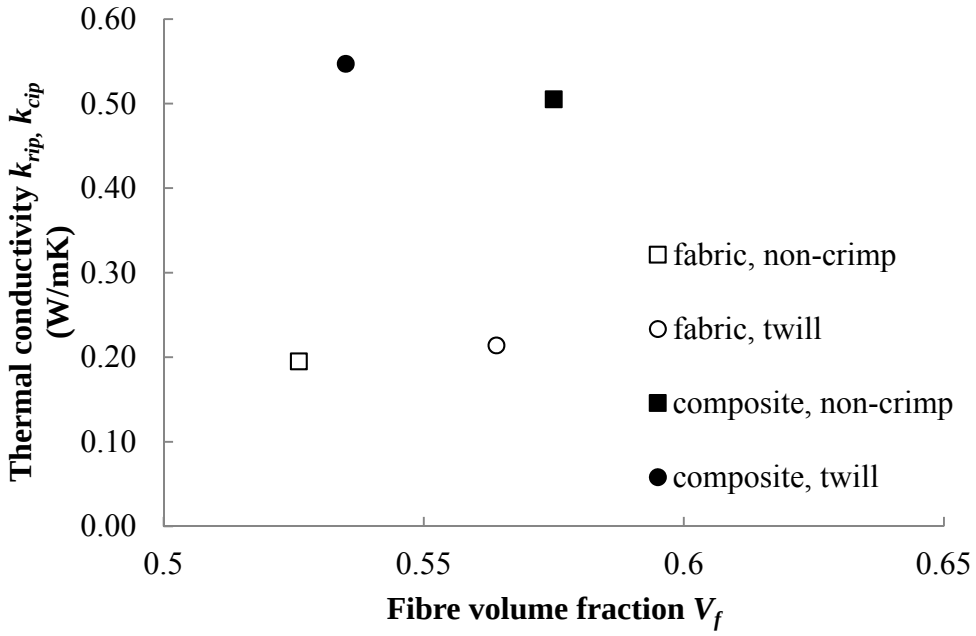

Figure 3.15 - Through-thickness thermal conductivity measurements of composites k_{ctt} vs. dry fabrics k_{rtt}

3.4 Modelling

This section discusses analytical models and heat transfer simulations used for predicting k_{rip} and k_{rtt} of dry fabrics. The Classical Lamination Theory (CLT), Equations 2.1 and 2.11 and the Clayton analytical model, Equation 2.5 were used in attempting to predict k_{rip} and k_{rtt}. CLT yielded k_{rip} predictions which generally agreed with the measured data and replicated the linear trend of k_{rip} as a function of V_f observed with the measured data successfully. Conversely, the Clayton model yielded k_{rtt} predictions which not only largely underestimated the measured data, but was also not able to replicate the exponential

recovery trend of k_{rtt} as a function of V_f observed with the measured data. Hence simulations were developed in attempting to replicate the trend shown by the measured data for k_{rtt}. All simulations predicting k_{rtt} were two-dimensional and did not account for fabric architecture based on the scant difference in measured data for k_{rtt} between the two fabrics, Figures 3.12 and 3.13. Modelling results were compared with measured data for the non-crimp fabric only. Heat transfer in dry fabrics was assumed to occur primarily through conduction; natural convection of the air in the samples was assumed to be negligible.

CLT, which provided accurate predictions for k_{cip} and the Clayton model for heat transfer of reinforcing cylinders in a matrix, which provided accurate predictions for k_{ctt}, were used in attempting to predict k_{rip} and k_{rtt} of the non-crimp dry carbon fibre fabric respectively at the V_f values corresponding to those of the measured data. CLT requires the axial thermal conductivity of the constituent fibre k_{fa} while the Clayton model requires the transverse thermal conductivity of the constituent fibre k_{ft}. k_{fa} of the constituent HTS40 carbon fibre was quoted as 10 W/mK by the manufacturer while no k_{ft} value was given in the datasheet [52]. However, carbon fibre manufacturers provide a rough estimate of k_{fa} only and not a measured value. Hence k_{fa} and k_{ft} of the HTS40 fibre were first back-calculated from measured k_{cip} and k_{ctt} values of a composite plate manufactured using the same non-crimp fabric, using CLT and the Clayton model combined with the Maxwell analytical model, Equation 2.19, respectively. Details of the manufacturing and characterisation procedures and equipment can be found in Section 4.2. Thermal conductivity of the matrix k_m in both models was used as that of air at room temperature and pressure, 0.026 W/mK

[127]. Measured k_{cip}, k_{ctt}, V_f and V_v values for the composite were 2.848 W/mK, 0.602 W/mK, 63% and 4.3% respectively which yielded k_{fa} and k_{ft} values of 7.95 W/mK and 1.36 W/mK from the models, respectively.

CLT predictions compared with measurements from the first compaction cycle of the non-crimp fabric are shown in Figure 3.16. CLT yielded fair predictions for k_{rip} and successfully replicated the experimental trend; experimental values range from 1.303 W/mK to 2.236 W/mK and show a linear trend as a function of V_f while model predictions range from 1.527 W/mK to 2.143 W/mK and show a linear trend as a function of V_f. Possible sources of error include deviations in alignment of the fabric plies due to cutting or stacking during sample preparation.

Clayton model predictions and measured data obtained from the first compaction cycle of the non-crimp fabric are shown in Figure 3.17. Not only does the model not yield accurate predictions for k_{rtt} of dry fabrics, but it cannot replicate the experimental trend: experimental values range from 0.112 W/mK to 0.209 W/mK and show an exponential recovery trend as a function of V_f while model predictions range from 0.072 W/mK to 0.117 W/mK and show an exponential trend as a function of V_f.

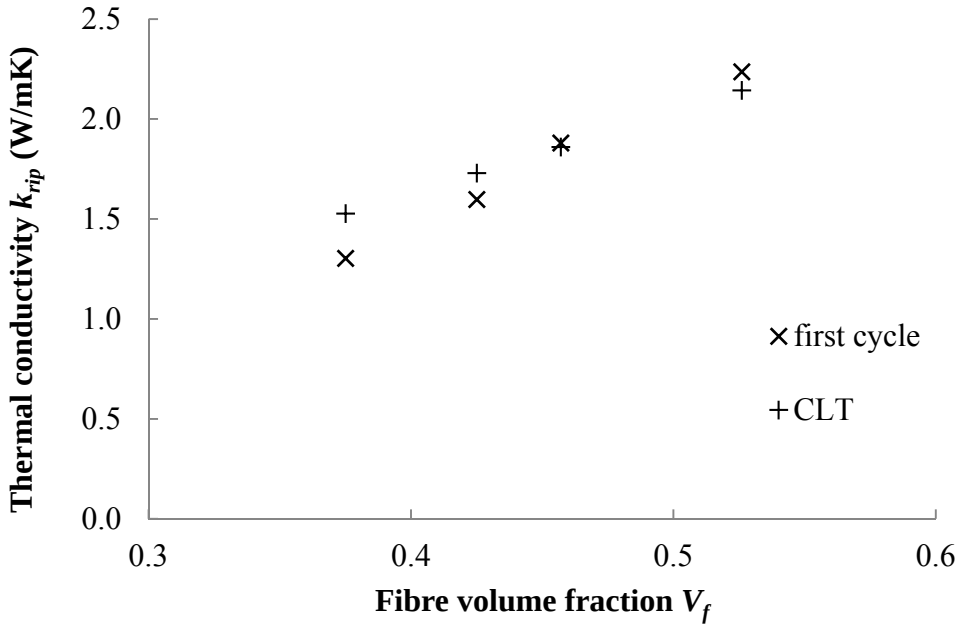

Figure 3.16 – CLT predictions compared with measured data for in-plane thermal conductivity k_{rip} of the non-crimp fabric

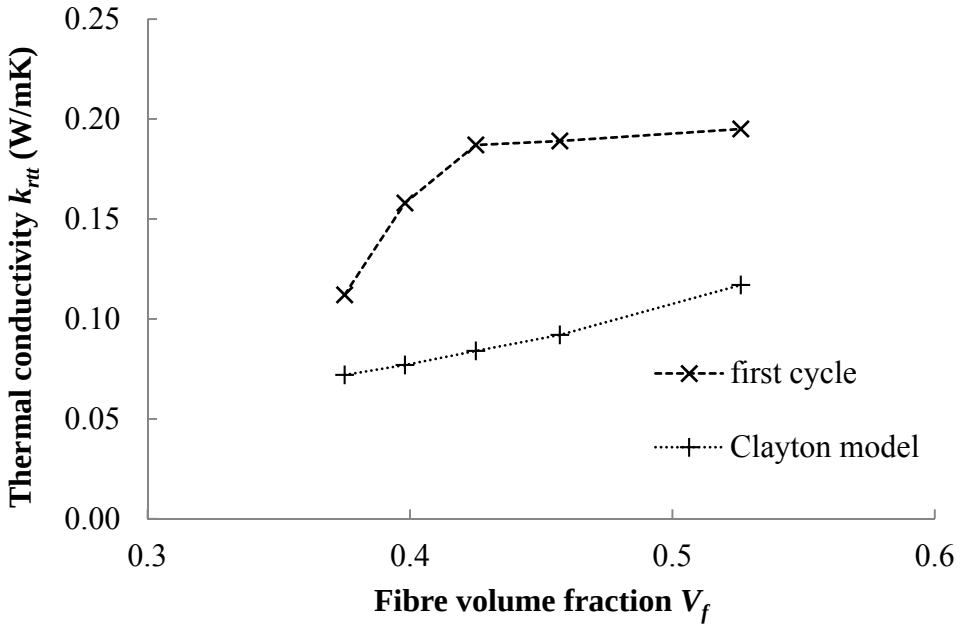

Figure 3.17 - Clayton model predictions compared with measured data for through-thickness thermal conductivity k_{rtt} of the non-crimp fabric

Two-dimensional steady-state simulations were then performed using FLUENT ANSYS 13.0 in attempting to replicate k_{rtt} values of the dry fabrics and explain the exponential recovery trend. A first group of simulations that do not model contacts between fibres are referred to as SimNC. Equally spaced and regularly aligned fibres of circular cross-sections surrounded by air were represented by square unit cells, Figure 3.18. Eight unit cells were used for the simulation model as shown in Figure 3.19 to loosely portray the width to thickness ratio of the dry fabric samples. This aspect ratio is greater than 2 in reality; however, as the simulations are used in attempting to predict k_{rtt} and modeling the in-plane heat transfer is of no interest, the number of repeating unit cells along the width can be

reduced to simplify the model geometry. Four cases were run for V_f values ranging from 38.0% to 53.0%, which correspond to values of the experimental data. Diameter of the fibres d_f was set to 7 μm based on specifications from the carbon fibre datasheet [52]; V_f was increased by reducing the height and width a of each unit cell, hence reducing the distance d_s between adjacent fibres; geometry of the unit cell in Figure 3.18 and simulation model are described in Equations 3.2 and 3.3.

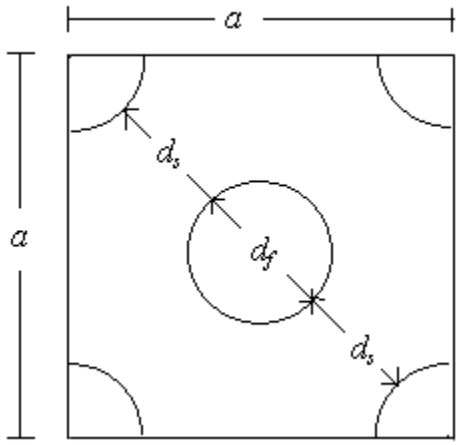

Figure 3.18 - Unit cell in simulation model

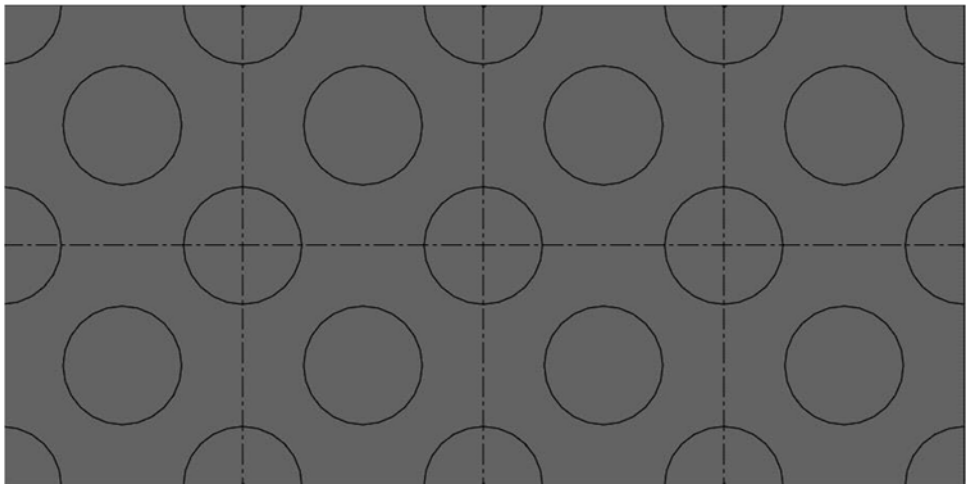

Figure 3.19 – Model for SimNC simulations

$$V_f = \frac{2A_f}{A_{unitcell}} = \frac{2\pi\left(d_f/2\right)^2}{a^2} \tag{3.2}$$

$$\sqrt{2a^2} = 2d_f + 2d_s \tag{3.3}$$

Constant temperatures were imposed on the top and bottom walls of the domain in Figure 3.19 while the side walls were set as adiabatic. The through-thickness thermal conductivity k_{rtt} was calculated using Fourier's law, Equation 2.30, based on the average of the resulting heat flux measured at the top and bottom boundaries which were consistent within 5%. Material properties of the carbon fibres [52] and air [127] are found in Table 3.7. Four simulation cases SimNC1 to SimNC4 were run with the geometry parameters shown in Table 3.8. Convergence was checked by refining the mesh generated for each case twice as shown by a typical set of meshes for the simulation cases, Figure 3.20; values were consistent within 5% between the most coarse and most fine mesh. The numbers of elements of the finest mesh of the simulation cases are shown in Table 3.8.

Table 3.7 - Material properties used in simulations

Property	HTS40 fibres	Air
Density (kg/m^3)	1770	1.205
Specific heat (J/kgK)	710	1005
Thermal conductivity (W/mK)	1.36	0.026

Table 3.8 - Geometry parameters for simulations SimNC

Case	V_f (%)	Width (μm)	Height (μm)	Cell width (μm)	Distance between fibres (μm)	No. of elements
SimNC1	38.0	56.9	28.5	14.2	3.1	12636
SimNC2	43.0	53.5	26.8	13.4	2.5	11311
SimNC3	46.0	51.7	25.9	12.9	2.1	10690
SimNC4	53.0	48.2	24.1	12.1	1.5	9327

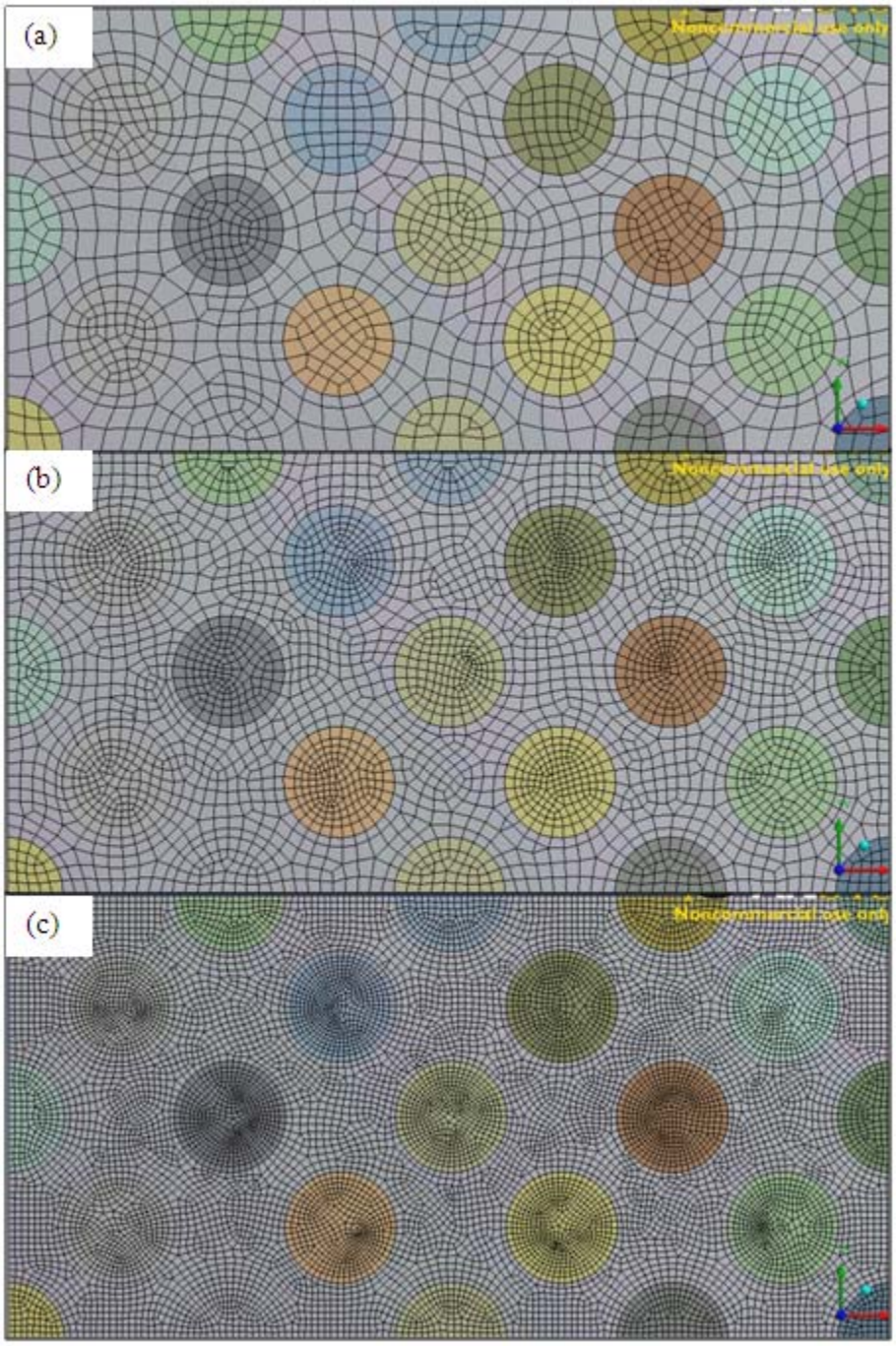

Figure 3.20 - Geometry and mesh refinements of model for SimNC2

Simulation results appear in Figure 3.21, along with measured data and predictions from the Clayton model, the latter two specifically for the non-crimp fabric. Simulations, based on models such as the one shown in Figure 3.19 did not yield accurate predictions for k_{rtt} of dry fabrics, and could not replicate the experimental trend; experimental values ranged from 0.112 W/mK to 0.209 W/mK and showed an exponential recovery trend as a function of V_f while simulation results were very similar to values predicted by Clayton's model, which ranged from 0.058 W/mK to 0.095 W/mK and showed an exponential trend as a function of V_f .

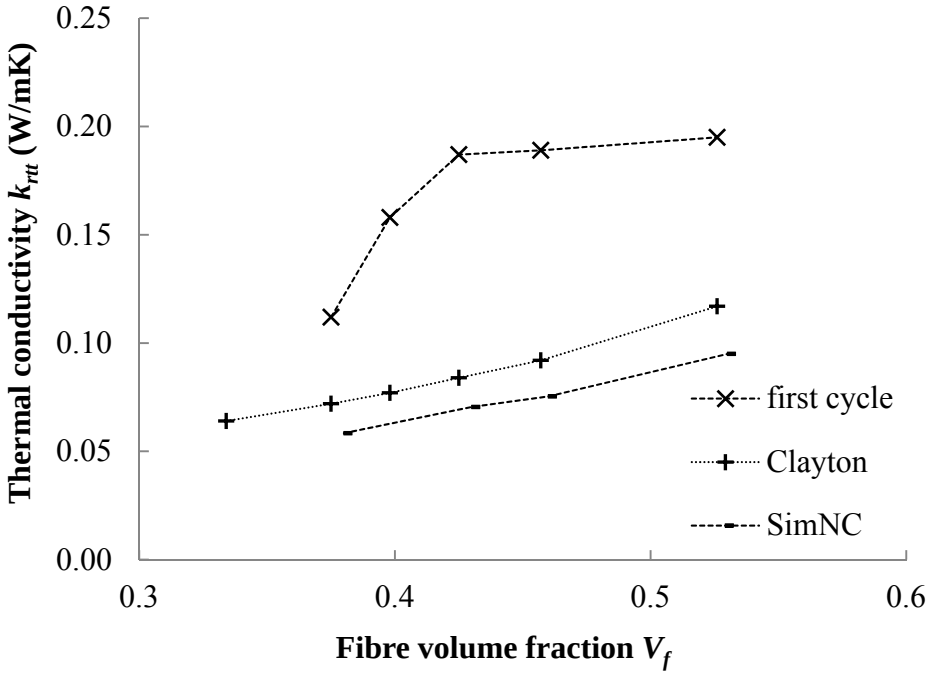

Figure 3.21 –Through-thickness thermal conductivity k_{rtt} predictions for the non-crimp fabric using SimNC simulations

It was suspected that the SimNC simulations largely underestimated k_{rtt} values due to the lack of modelling of fibre-fibre contacts which can provide conductive paths for heat flow; hence fibre-fibre contacts were incorporated into simulations. A second group of additional two-dimensional steady-state simulations were performed in FLUENT using the same boundary conditions and material properties, Table 3.7, as used in the SimNC simulations. However, the following simulations featured fibre cross-sections represented by 24-sided polygons to yield small contact lines between adjacent fibres with a base circle measuring 7 μm in diameter, representing fibre-fibre contacts; this new series of simulations accounting for contacts are referred to as SimC simulations.

Five cases SimC1 to SimC5 were run for V_f values ranging from 33.4% to 65.8%, Figure 3.22 where the cases show progressive changes in contacts between adjacent fibres developed during a compaction cycle. SimC1 represents an initial state at the onset of compaction where contact between adjacent fibres is limited. Additional contacts begin to develop in SimC2 and SimC3, where direct paths for the conduction of heat through fibres in the through-thickness direction appear and heat transfer through air can be avoided. Fibres start to shift in SimC4 as a result of further compaction, connecting additional heat paths along different directions; this 2D contact network is further enhanced in SimC5. Height was decreased during compaction while width remained constant. k_{rtt} was calculated using Fourier's law, a linear first order equation based on imposed temperatures and the average resulting heat flux, hence it should not be affected by the aspect ratio of the domain. Whilst the 5 cases represent only a few simple configurations taken for illustration among a very wide array of possible fibre arrangements, these cases represent incremental changes in fibre-fibre contacts and configuration along with corresponding increases in V_f .

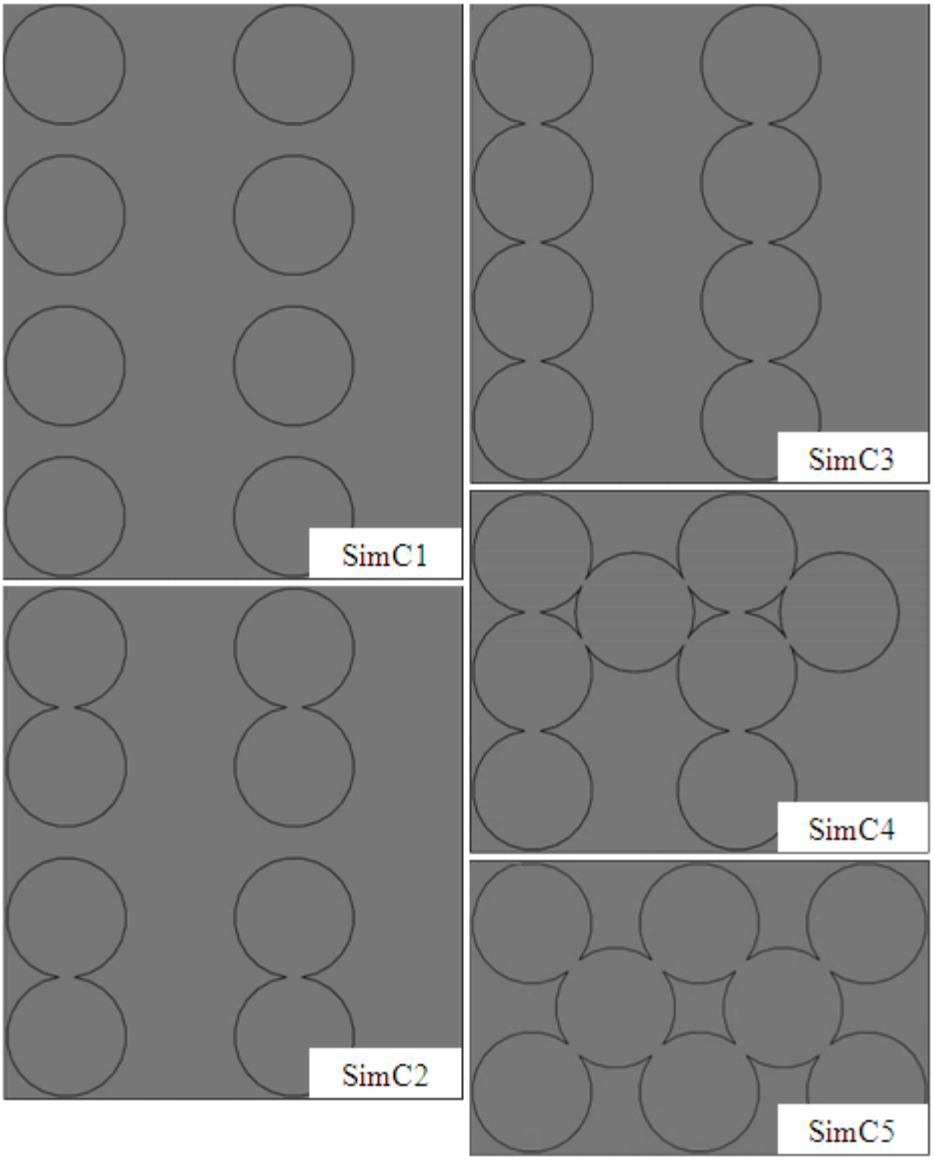

Figure 3.22 - Simulation model accounting for fibre-fibre contact: SimC1 to SimC5

Simulations were run with the geometry parameters shown in Table 3.9. SimC simulations feature similar domains and meshes compared with those of the SimNC simulations; resulting thermal conductivities converged for the SimNC simulations presented above and were consistent within 5% between the most coarse and most fine mesh, hence

mesh refinement was not probed again for the SimC simulations. A typical mesh generated for the model is shown in Figure 3.23 for SimC3.

Table 3.9 - Geometry parameters for SimC simulations accounting for contact points

Cases	V_f (%)	Width (μm)	Height (μm)	No. of elements
SimC1	33.4	27.2	34.1	6978
SimC2	37.6	27.2	30.3	6154
SimC3	40.0	27.2	28.4	5835
SimC4	53.2	27.2	21.4	4529
SimC5	65.8	27.2	17.3	3857

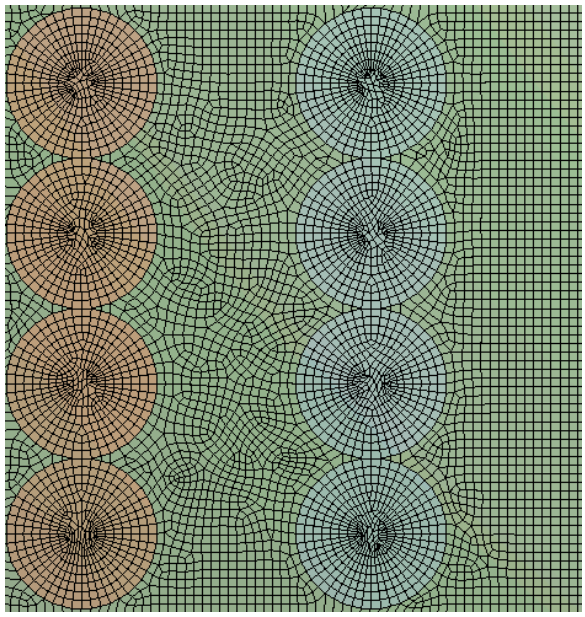

Figure 3.23 - Geometry and mesh of simulation model accounting for contact points: SimC3

Simulation results accounting for fibre-fibre contacts appear in Figure 3.24 along with experimental data, Clayton model predictions and results from the SimNC simulations for the non-crimp fabric. The SimC simulations featuring contact yielded reasonable predictions for

k_{rtt} of dry fabrics and replicated the exponential recovery trend seen with the measured data [33]. Plots showing the temperature distributions can be seen in Figures 3.25 to 3.29.

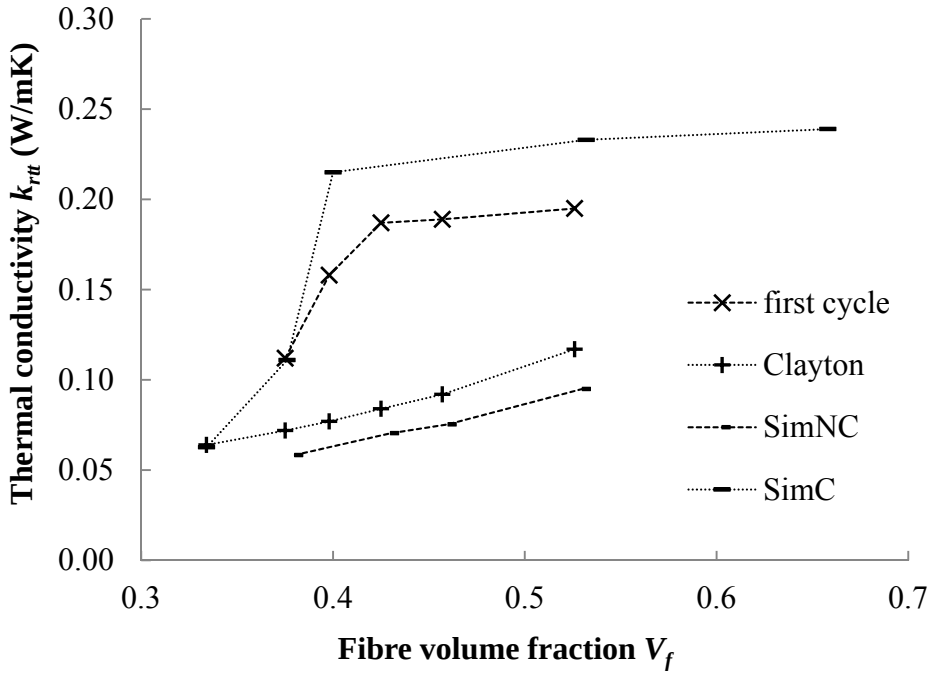

Figure 3.24 - Through-thickness thermal conductivity k_{rtt} predictions for the non-crimp fabric using SimC simulations

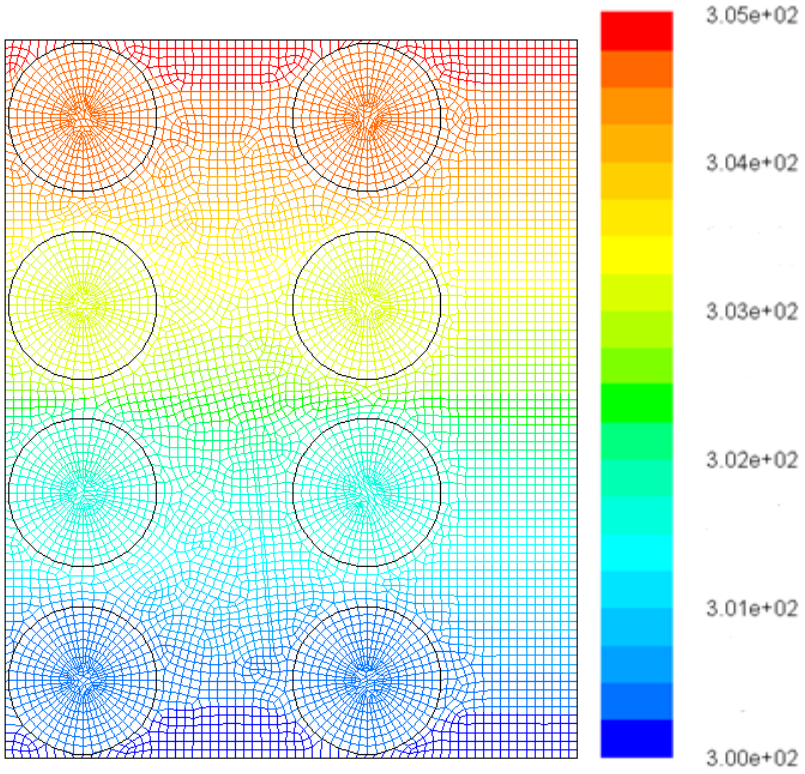

Figure 3.25 - Temperature plot: SimC1 (K)

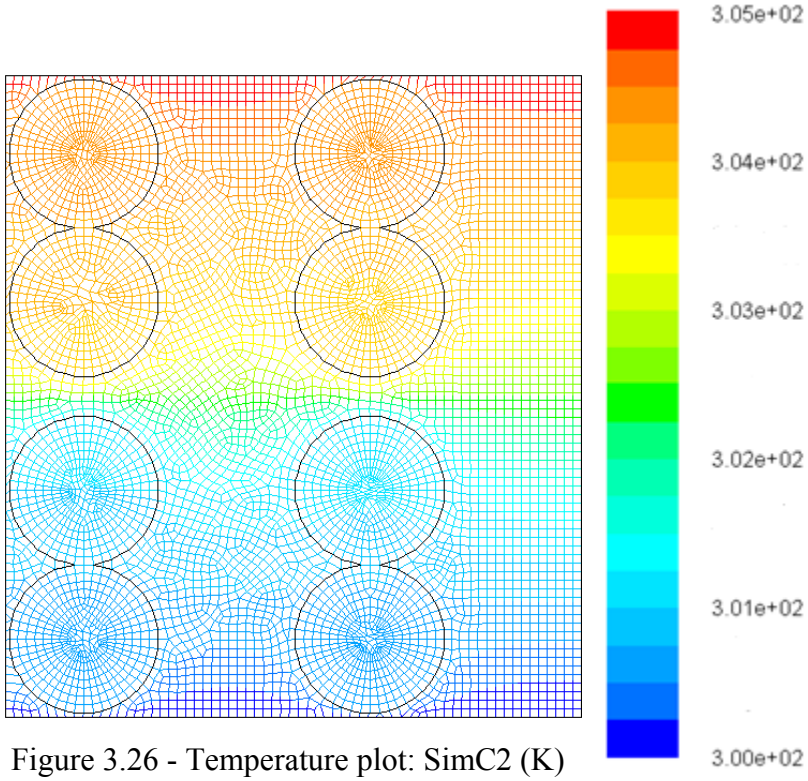

Figure 3.26 - Temperature plot: SimC2 (K)

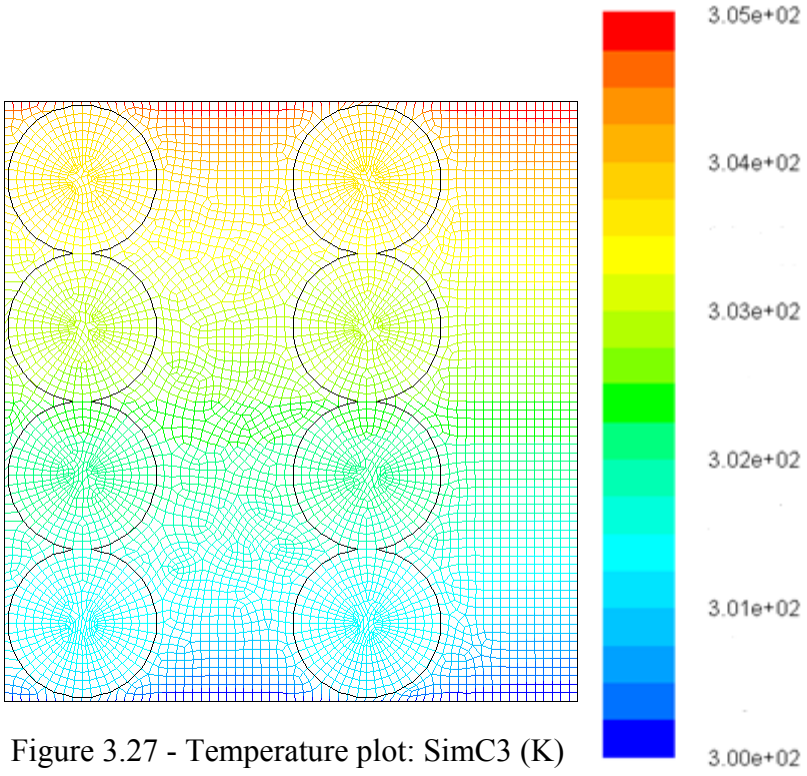

Figure 3.27 - Temperature plot: SimC3 (K)

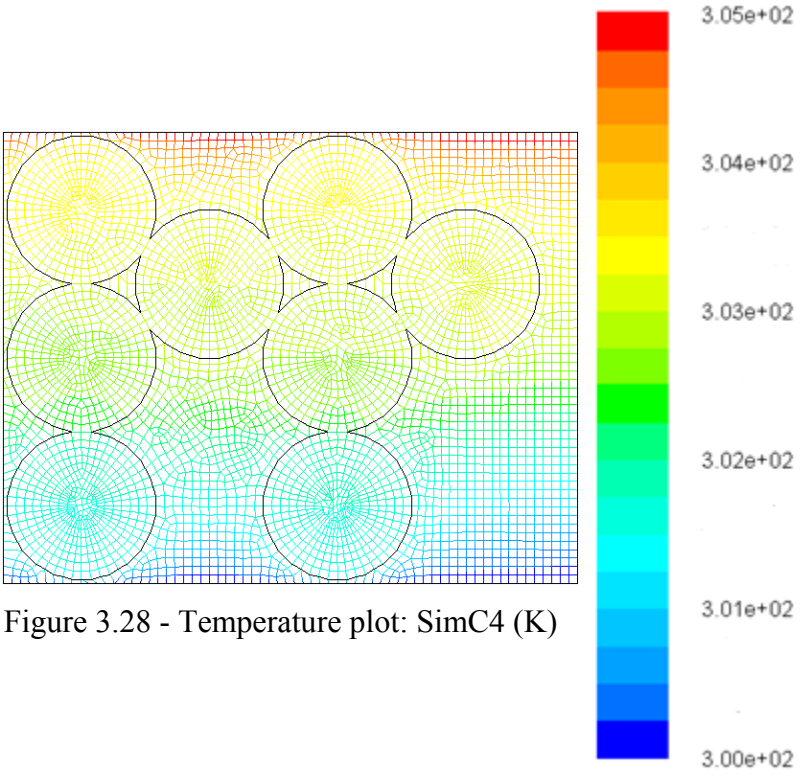

Figure 3.28 - Temperature plot: SimC4 (K)

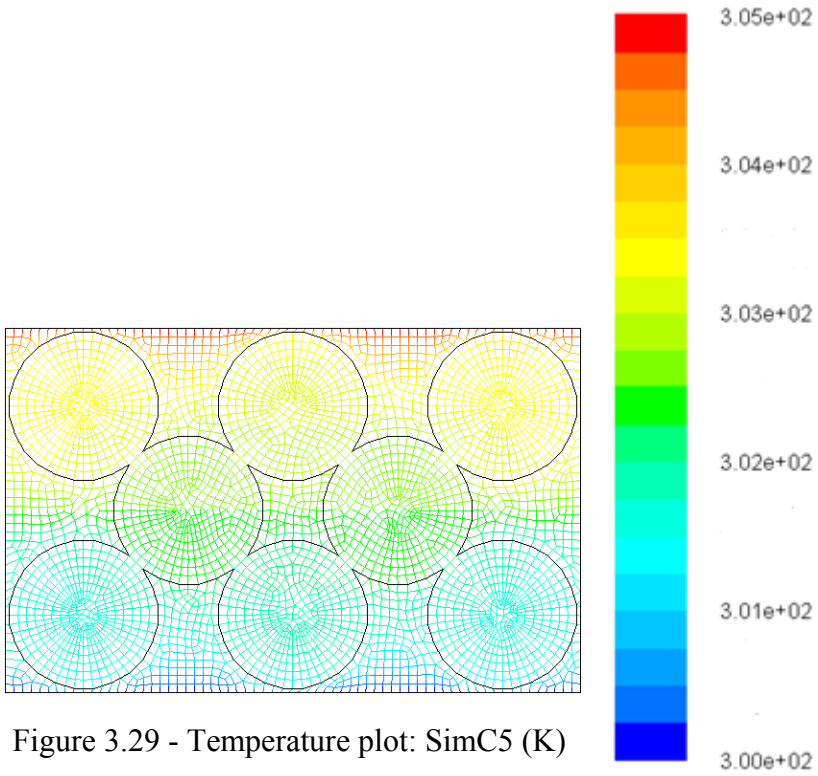

Figure 3.29 - Temperature plot: SimC5 (K)

3.5 Discussion

In the in-plane direction, measured k_{rip} values do not differ significantly from k_{cip} values, Figure 3.14. Furthermore, Figure 3.10 shows a difference of only 2.4% between samples exposed to air and samples from which air was removed by applying vacuum. This demonstrates that in-plane heat transfer occurs primarily along the carbon fibres and is driven by the axial fibre thermal conductivity k_{fa}. Hence k_{rip} varies linearly as a function of V_f and can be modelled by the CLT; thermal conductivity increases proportionally to the amount of fibres present. k_{rip} values of the non-crimp fabric were slightly higher than those of the twill fabric at the same V_f, Figures 3.10 and 3.11. As both fabrics consist of the same HTS40

carbon fibre, this may be explained by the crimp present in the fibres of the twill fabric due to weaving which is not present in the non-crimp fabric; heat must travel along the crimped fibres in the twill fabric as opposed to travelling directly along the straight fibres in the non-crimp fabric, hence reducing heat conduction in the in-plane direction.

In the through-thickness direction, measured k_{rtt} values are two to three times smaller than k_{ctt} values, Figures 3.15. Furthermore, Figure 3.12 shows a 7.4% decrease in the thermal conductivity of the samples from which air was removed by applying vacuum compared to that of the samples exposed to air. This demonstrates that thermal conductivity in the through-thickness direction is affected significantly by that of the surrounding material, whether it is air for dry fabrics or resin for composites. The non-crimp and the twill fabrics showed similar k_{rtt} values, suggesting that k_{rtt} is independent of fabric architecture. The effect of cycling on both k_{rip} and k_{rtt}, shown by the slightly higher thermal conductivity values measured after each successive cycle in Figures 3.10 to 3.13, indicates that the fibre network improves upon each compaction.

For predicting k_{rtt}, the Clayton model and SimNC simulations devoid of fibre-fibre contacts showed comparable values and demonstrated the same exponential trend as a function of V_f, Figure 3.21. The Clayton model predicts thermal conductivity in a manner equivalent to SimNC simulations by increasing V_f through a reduction of distances between adjacent, non-contacting fibres. However, neither the Clayton model nor SimNC simulations could provide accurate predictions for k_{rtt}; neither accounted for the fibre-fibre contacts present in the dry fabric samples which are crucial for predicting k_{rtt} accurately. The Clayton model can be used for predicting k_{ctt} as shown by studies reported in the literature, as

contacts between the fibres in composites are impeded by the presence of resin. It can also be used for predicting k_{rtt} at low V_f values where few fibre-fibre contacts are present, as shown by the close agreement between predictions from the Clayton model and k_{rtt} values obtained from case SimC1 accounting for contacts, Figure 3.24. However, it cannot be used for predicting k_{rtt} where many contacts are present, Figure 3.17.

Predicting k_{rtt} values when contacts are present must be achieved by accounting for fibre-fibre contacts during compaction and the evolution of heat paths along with increases in V_f, as shown by simulation cases SimC1 to SimC5, Figure 3.22. From cases SimC1 to SimC3, there is a significant improvement in heat paths in the through-thickness direction due to contacts developed during compaction. In SimC1, there were no direct heat paths connecting the top and bottom surfaces of the domain and heat was forced to travel through fibres and air in series. This can be seen by the uniform temperature inside each fibre and the uniform temperature gradient in the through-thickness direction, Figure 3.25. In SimC2, some paths were developed for the heat to flow through contacting fibres, as shown by the temperature gradients in the through-thickness direction which are no longer uniform; gradients are small where fibres are in contact due to their high thermal conductivity while gradients in the surrounding air separating these contacting fibres are large, Figure 3.26. By SimC3, the formation of paths for heat flow in the through-thickness direction is complete, as shown by the temperature gradients which are once again uniform in the through-thickness direction, Figures 3.27. At this stage of the compaction, there are direct heat paths connecting the two boundaries of the domain; heat can fast-track through the thermally conductive fibres.

From cases SimC3 to SimC5, although there is an enhanced two-dimensional network present which improves conduction in the direction along the model width, this does not improve heat flow in the through-thickness direction significantly, as shown by the similar temperature plots for SimC3 to SimC5, Figures 3.27 to 3.29. Hence k_{rtt} varies in an exponential recovery trend as a function of V_f, Figures 3.12 and 3.13, and values begin to level off after case SimC3, indicating that improvements in the through-thickness heat paths are significantly less for V_f values above 50%. These results provide an illustration of the fibre-fibre contacts developed during compaction, which will be investigated more formally in future work.

Simulations accounting for fibre-fibre contacts yielded reasonable predictions for k_{rtt}, Figure 3.24. Results from the last three cases are higher than measured values due to the better heat transfer capability of the small contact lines modelled between adjacent 24-sided polygons as opposed to contact points between adjacent circles in reality. The simulations clearly simplify reality, but nevertheless they are credible and manage to replicate and explain the trend seen in the experimental results successfully, which cannot be achieved by any published model.

4 Thermal conductivity of consolidated plates

This chapter is divided into two parts: Section 4.1 presents experimental and modelling aspects pertaining to MWCNT-reinforced nanocomposites while Section 4.2 features similar information for MWCNT-reinforced multi-scale composites. The effects of MWCNT addition on the thermal conductivities of neat epoxy and neat composites were investigated and compared.

4.1 Neat resin and nanocomposite plates

The materials and experimental procedures for manufacturing neat resin and nanocomposite plates are described in Section 4.1.1. This is followed by the presentation of methods for thermal and void content characterisation of the plates, Section 4.1.2. Then, analytical modelling and results are presented in Section 4.1.3 aiming at predicting thermal conductivities of nanocomposites plates, followed by a discussion of the effect of MWCNT addition on thermal conductivity of neat epoxy, Section 4.1.4.

4.1.1 Materials and manufacturing

Two epoxy base systems, 237x and 239x supplied by Axson were used for manufacturing neat resin and MWCNT-reinforced nanocomposite plates. The epoxies 237x and 239x can be neat, designated 2376 and 2396 respectively, or loaded with 0.3% MWCNTs by weight, designated 2377 and 2397 respectively, Table 4.1. Each of the four epoxies can be either in the form of bulk resin supplied in a can and designated by the letters AKD or in the form of 120 μm thick rolled film, designated as LEO. Bulk resins are shown

in Figure 4.1 and cut plies of the resin films are shown in Figure 4.2, except for that of the 2397 resin film which Axson was not able to supply. All of the resins are B-stage epoxies where the cure reaction is halted at an early stage by storage in a freezer. The cure cycle recommended by the manufacturer [128] for all resins is a 2°C/min heating ramp up to 130°C followed by a two hour dwell, then another 2°C/min heating ramp up to 200°C followed by a second two hour dwell for post-cure. Datasheets for the resins are found in Appendix B.

Table 4.1 - Epoxy resins

Resin	Base epoxy	0.3% MWCNTs
AKD/LEO 2376	237x	yes
AKD/LEO 2377	237x	no
AKD/LEO 2396	239x	yes
AKD/LEO 2397	239x	no

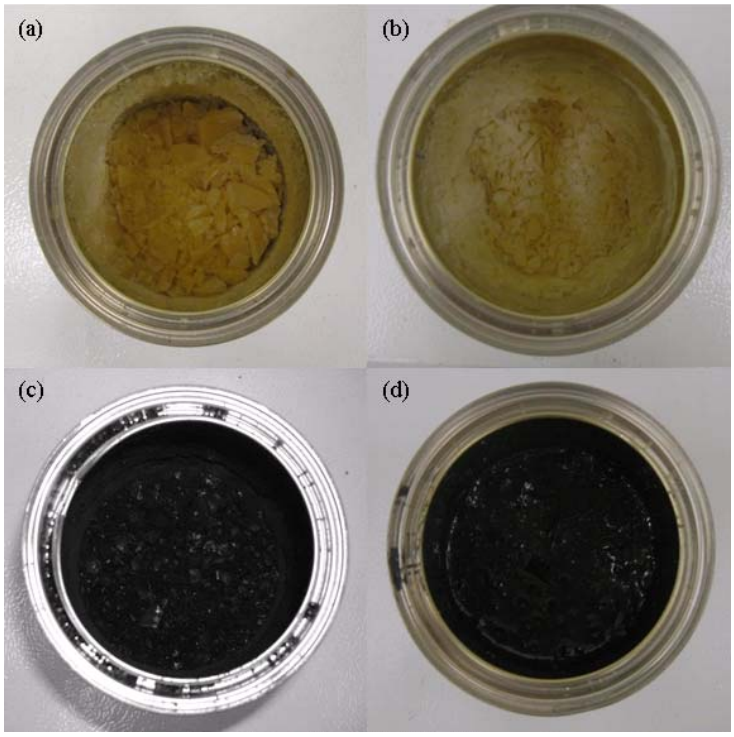

Figure 4.1 - Bulk resins: (a) AKD 2376 (b) AKD 2396 (c) AKD 2377 and (d) AKD 2397

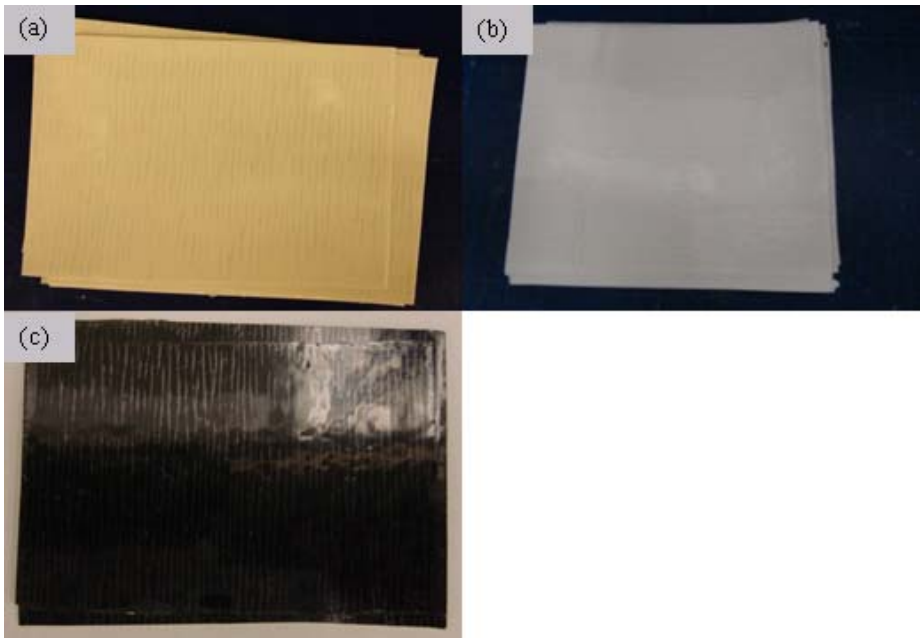

Figure 4.2 – Resin films: (a) LEO 2376 (b) LEO 2396 and (c) LEO 2377

For producing the 2377 and 2397 resins, Axson loaded Baytubes® C150P MWCNTs from Bayer Materials Science into their respective base epoxies 2376 and 2396. The production process is specified by the manufacturer and the dispersion of the MWCNTs in the epoxy is being studied by Mostafa Yourdkhani, a candidate for the PhD at McGill University working on this CRIAQ COMP 510 project. The MWCNT outer and inner diameters were 13 nm and 4 nm respectively as reported by the manufacturer [129]. Tube lengths greater than 1 μm before dispersion into a polymer matrix and 0.2 μm to 1 μm after dispersion were also reported. Nadler et al. [108] conducted TEM analysis of the Baytubes dispersed into an epoxy matrix and measured an average tube length of 0.48 μm. The authors also reported a true density of 1850 kg/m^3 to 1930 kg/m^3 for the Baytubes, which generally agrees with the true density of 2100 kg/m^3 reported by other major MWCNT suppliers [130].

The manufacturer reported a bulk density of 130 kg/m^3 to 150 kg/m^3. True density refers to the density of a single nanotube whereas bulk density refers to that of a bundle of nanotubes. Specifications for Baytubes® C150P obtained from the manufacturer and studies available in the literature are summarized in Table 4.2 and found in Appendix B.

Table 4.2 - Specifications of MWCNTs Baytubes® C150P

Outer diameter (nm)	13
Inner diameter (nm)	4
Length before dispersion (μm)	>1
Length after dispersion (μm)	0.48
Bulk density (kg/m^3)	130-150
True density (kg/m^3)	1850-1930

Six resin plates R1 to R6 were manufactured; plates R1, R4, R5 and R6 were made from AKD bulk resins whilst plates R2 and R3 were made from LEO resin films. The manufacturing procedure for plates made with the bulk resins consisted in thawing the resin at room temperature for 10 minutes after taking it out of the freezer, then breaking the resin into 10 to 15 chunks by gently tapping with a hammer, Figure 4.3 (a). A sheet metal container 140 by 110 mm was used for heating the resin; the size was chosen in order to obtain two 70 mm by 110 mm samples for thermal conductivity measurements using the THISYS and THASYS devices. The mass of resin required for obtaining a sample thickness of approximately 3 mm was weighed. Five layers of Chemlease70-90 mould release agent were applied to the inner sides of the container and the resin chunks were distributed evenly into the container, Figure 4.3 (b). The resin was then heated at 2°C/min up to 100°C in a PF120 Carbolite convection oven and the liquid resin, Figure 4.3 (c) was taken out of the oven and degassed for 10 minutes, Figure 4.5 (d). The resin was then placed back into the oven, heated according to the cure cycle recommended by the manufacturer, and left to cool

overnight. The plate was then cut into two samples 70 mm by 110 mm using a Walker-Turner 3331 band saw.

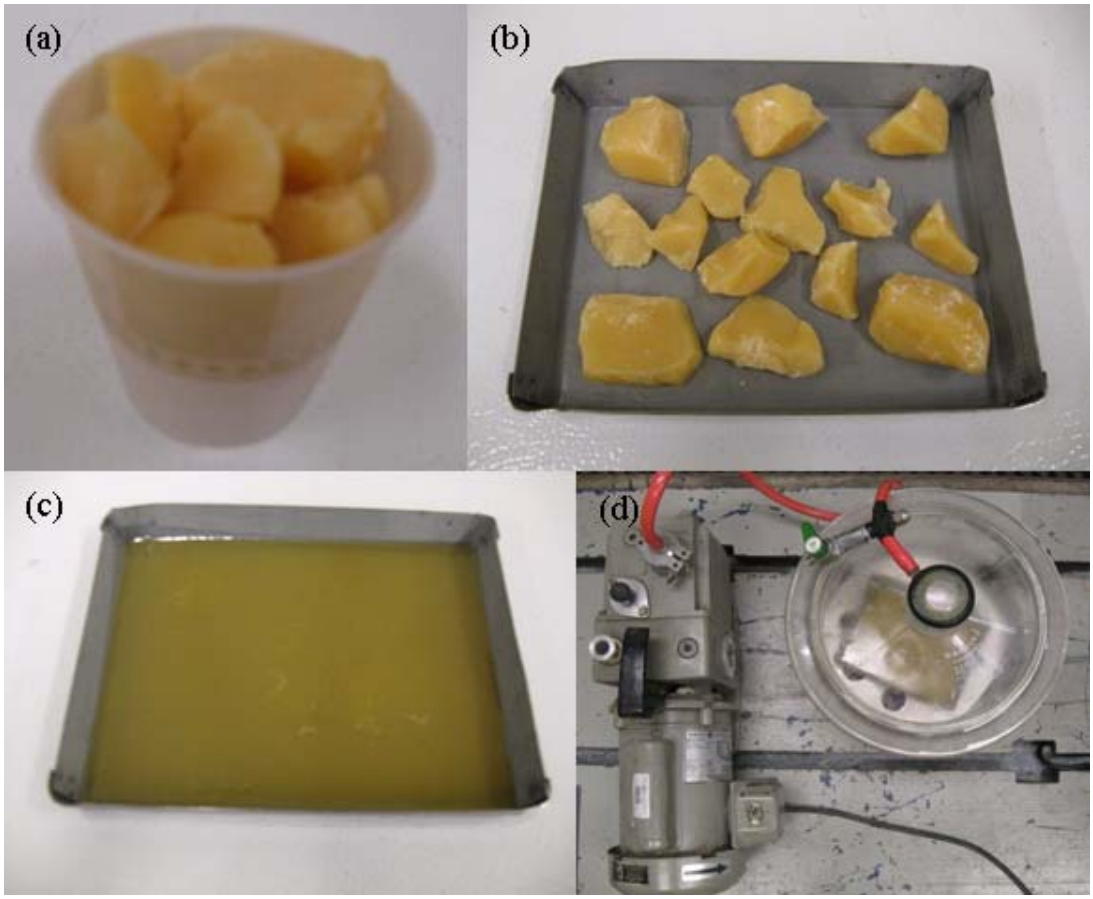

Figure 4.3 - Manufacturing procedure for resin plates made from AKD bulk resins: (a) frozen resin broken into chunks (b) resin chunks distributed evenly in container (c) resin after heating and (d) degassing

The procedure for plates made from resin films is described below. The roll of resin film was taken out of the freezer and left to thaw for 10 minutes at room temperature. Twenty plies 70 mm by 110 mm were cut from the roll using a utility knife, and stacked. The stack

was then rolled manually to reduce the void content. A machined aluminium mould and cover featuring a 75 mm by 115 mm, 6 mm deep cavity was used, Figure 4.4. The surfaces of the cavity and cover were polished to a smooth surface finish and the cover contained a degassing port.

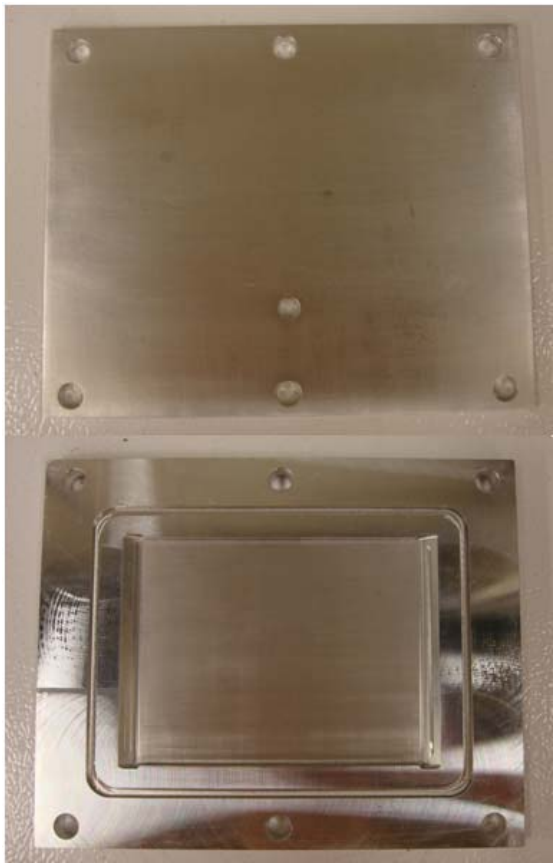

Figure 4.4 - Aluminium mould and cover for making neat resin plates from LEO resin films

The resin stack was placed into the mould, Figure 4.5 (a) and an Airtech vacuum bag sealant tape was pressed around the perimeter of the cavity. Airtech bleeders and the vacuum port were placed on top of the cover near the degassing port, and sealed with the vacuum bag using further vacuum bag sealant tape, Figure 4.5 (b). The cover was then pressed and sealed

onto the top of the mould, Figure 4.5 (c). The assembly was placed into the Carbolite convection oven and heated according to the cure cycle recommended by the manufacturer. A DAA-V715A Gast vacuum pump operating at 0.02 bars or 98% vacuum was connected for degassing during a portion of the heating cycle from 90°C to 130°C. The assembly was left in the oven to cool overnight after the cure cycle was complete.

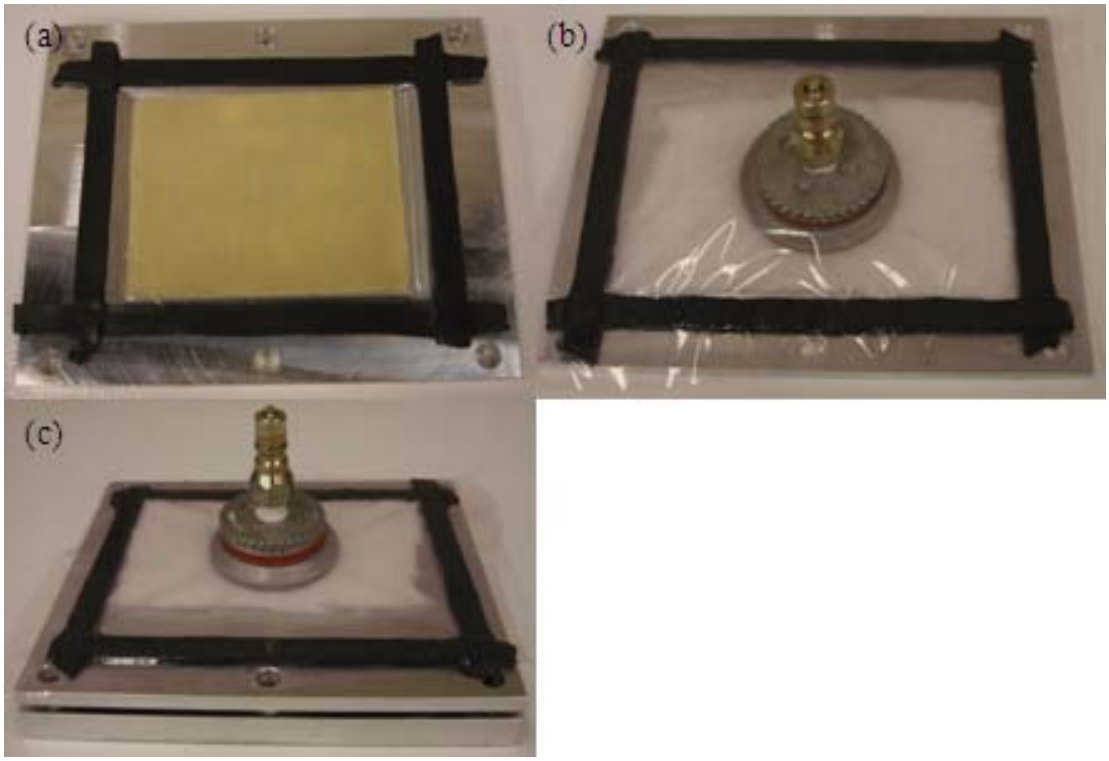

Figure 4.5 - Manufacturing procedure for resin plates made from LEO resin films: (a) resin plies placed into mould cavity (b) bleeders and vacuum port vacuum bagged onto cover and (c) cover sealed onto mould

Six resin plates were manufactured, Figure 4.6. Plates R1, R2 and R3 are neat resin plates and showed negligible voids upon visual inspection while plates R4, R5 and R6 are

nanocomposite plates reinforced with Baytubes® C150P MWCNTs and showed visible void content. Plates R1 and R2 were manufactured with AKD 2376 and LEO 2396. Plate R3 was also manufactured with LEO 2396 but the resin was left to cure overnight in the oven at 200°C after completion of the standard cure cycle; a change in colour compared with plate R2 was observed. Plates R4 and R5 were manufactured with AKD 2377 and AKD 2397. Plate R6 was a repeat of plate R5 with a thicker resin stack, which resulted in a higher void content. The dimensional measurements of length, width and thickness of the resin plates are found in Appendix A.

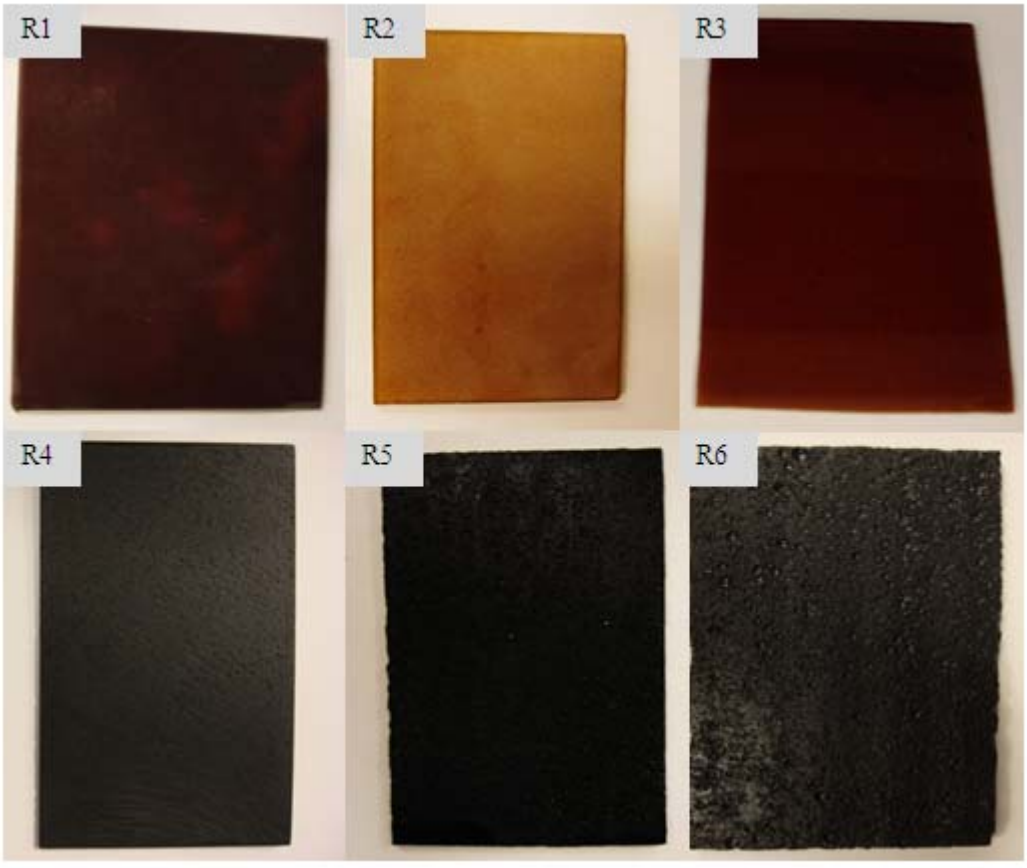

Figure 4.6 - Resin plates: (1) 2376 (2) 2396 (3) 2396 overnight cure (4) 2377 (5) 2397 and (6) 2397 repeat

4.1.2 Characterisation

Densities of the 2376 and 2396 resins were measured in the form of raw films and consolidated resin plates, Table 4. LEO 2376 and LEO 2396 films were cut and densities were calculated based on the measured masses and thicknesses; mass and thickness measurements were performed by Simon Baril-Gosselin, a candidate for the PhD studying fluid flow as part of the CRIAQ COMP 510 project. The thickness of the resin films averaged approximately 120 μm with slight variations in thickness at different locations. Each ply was rolled by hand and many plies were stacked together for mass and thickness measurements to reduce the effect of small variations in thickness. Resin plates R1 and R2 with negligible void content were used for calculating the densities of the plates. Both base systems showed higher densities in the form of consolidated plates compared with the raw films. This is likely accounted for by the shrinkage of epoxy resins during cure. Values presented are in agreement with the density range of 1100 kg/m^3 to 1200 kg/m^3 reported by the manufacturer [131]. Densities of the 2377 and 2397 resins were assumed to be the same as those of the 2376 and 2396 resin respectively, as MWCNTs were only loaded at 0.3% by weight.

Table 4.3 - Densities of 2376 and 2396 resins

Resin	Density (kg/m^3)
Raw 2376 film	1110
Raw 2396 film	1150
Consolidated 2376 plate	1242
Consolidated 2396 plate	1266

Void volume fractions are also presented, caused by trapped gases and volatiles released during the resin cure. The voids are spherical, approximately 1 mm in diameter and evenly distributed. Plates R1, R2 and R3 showed negligible void content upon visual inspection whereas the void volume fractions of plates R4, R5 and R6 were calculated based on the volumes and measured masses of the rectangular plates. Volumes of the plates were calculated based on average measured lengths, widths and thicknesses of the plates. Plate mass and the appropriate resin density from Table 4.3 were used for calculating the volume taken up by the resin. Then the void volume fraction or porosity was calculated from the remainder of the plate volume taken up by air. Thermal conductivities of the six resin plates were measured using THISYS and THASYS devices, Table 4.4. The through-thickness and in-plane thermal conductivities for plates R3 and R6 were not measured upon observations that resin plates R1, R2, R4 and R5 demonstrated thermal isotropy. Hence, these one-hour measurements were not performed; plates R3 and R6 were also assumed be thermally isotropic.

Table 4.4 - Thermal conductivities and void volume fraction of resin plates

Containing MWCNTs	Resin plate	Description	Void volume fraction (%)	In-plane thermal conductivity (W/mK)	Through-thickness thermal conductivity (W/mK)
No	R1	AKD 2376	0	0.204	0.204
No	R2	LEO 2396	0	0.211	0.211
No	R3	LEO 2396	0	0.209	not measured
Yes	R4	AKD 2377	16.4	0.166	0.169
Yes	R5	AKD 2397	16.9	0.180	0.176
Yes	R6	AKD 2397	22.6	not measured	0.159

4.1.3 Modelling

The effective medium approach combined with the Maxwell analytical model presented in Section 2.3.2 was used for predicting the thermal conductivities of the CNT-reinforced nanocomposites containing voids k_{ncv}. The effective medium approach, Equations 2.12 to 2.18, was first used for predicting thermal conductivity for a void-free nanocomposite k_{nc} using a Kapitza resistance of $8 \cdot 10^{-8}$ m^2K/W found in the literature, Section 2.3.2. Physical resin and MWCNT properties used in the calculations were taken from Tables 4.3 and Table 4.2 respectively, and thermal conductivities of the neat resins k_m were taken from Table 4.4. Results for k_{nc} are shown in Table 4.5 for various MWCNT loadings. Thermal conductivities varied from 0.204 W/mK to 0.259 W/mK for MWCNT loadings between 0 and 10% by weight.

Then void content was accounted for through the use of the Maxwell model, Equation 2.19 presented in Section 2.3.2, to predict k_{ncv}. Void volume fraction V_v and resin thermal conductivity k_m were taken from Table 4.4 and air thermal conductivity was taken to be 0.026 W/mK at room temperature and pressure [127]. Results are shown in Table 4.6 where void volume fractions correspond to those of plates R4 to R6 at 0.3% loading. Predictions are compared with the average of in-plane and through-thickness measurements reported in Table 4.4. The model yielded accurate predictions compared with experimental values with a maximum error of -3.4%.

Table 4.5 - Thermal conductivity predictions for void-free MWCNT-reinforced nanocomposites

MWCNT loading (%)	Thermal conductivity of resin 2377 (W/mK)	Thermal conductivity of resin 2397 (W/mK)
0.0	0.204	0.211
0.3	0.206	0.213
0.6	0.207	0.214
1.0	0.209	0.216
2.0	0.214	0.220
5.0	0.228	0.235
10.0	0.253	0.259

Table 4.6 - Thermal conductivity predictions for MWCNT-reinforced nanocomposites accounting for void content at 0.3% loading

Resin plate	Resin	Void volume fraction (%)	Predicted thermal conductivity (W/mK)	Error (%)
R4	2377	16.4	0.168	0.0
R5	2397	16.9	0.172	-3.4
R6	2397	22.6	0.160	0.1

4.1.4 Discussion

As expected, results from Table 4.4 show scant differences in the in-plane and through-thickness thermal conductivities for all plates; neat epoxy and epoxy loaded with MWCNTs dispersed at random demonstrate thermal isotropy. Results also show that thermal conductivity of the 239x base system was slightly higher than that of the 237x base system. For the neat resins, thermal conductivity of resin 2396 was 0.211 W/mK compared with that

of resin 2376 at 0.204 W/mK; for the loaded resins at approximately the same void content, thermal conductivity of resin 2397 was 0.176 W/mK compared with that of resin 2377 at 0.169 W/mK.

Neither the effect of MWCNTs nor the effect of void content could be deduced solely from Table 4.4. Hence the effective medium approach combined with the Maxwell Equation was used for modelling thermal conductivities of CNT-reinforced polymers, so as to determine the effect of MWCNTs and void content separately. The model provided accurate predictions as shown by the close agreement of model predictions compared with experimental values, Table 4.6. Thermal conductivity predictions for void-free nanocomposites showed that loading MWCNTs at 0.3%, 0.6%, 1.0% and 2.0% does not improve the thermal conductivity significantly. Thermal conductivity values were predicted to be 0.214 W/mK and 0.220 W/mK for resins 2377 and 2397 respectively at 2% loading compared with 0.204 W/mK and 0.211 W/mK respectively for the neat resins.

Loading carbon nanotubes above 2% would not be feasible practically in the context of composite manufacturing processes such as RTM and RFI, as the addition of CNTs would increase the viscosity to such a level as to render resin flow extremely difficult, leading to processing issues [132]. Also, a cost-to-benefit analysis would have to be conducted to determine whether loading the CNTs at such high percentages can be justified by improvements in the mechanical, thermal and electrical properties of the parts. However, for the sake of determining the effect of MWCNT addition on k_{nc}, thermal conductivities were also predicted at loadings of 5% and 10% by weight. At 10% loading, predictions of 0.253 W/mK and 0.259 W/mK for resins 2377 and 2397 increased by 24% and 23% respectively compared with those of the neat resins at 0.204 W/mK and 0.211 W/mK, respectively.

Results in Table 4.5 show that loading MWCNTs into epoxy at 0.3% by weight increased the thermal conductivity by 1% for both 2377 and 2397 resins compared with the respective neat epoxies. This generally agrees with results from the literature regarding the addition of MWCNTs with similar physical properties as the ones used in this project at similar loadings. Gojny et al. [17] and Moisala et al. [23] loaded MWCNTs at 0.3% by weight into epoxy and obtained 4% and 6% increases in thermal conductivity respectively compared with the respective neat epoxies, Table 2.10. The MWCNTs used by Gojny et al. measured 15 nm and 4 nm in outer and inner diameters respectively and are comparable to the Baytubes® C150P used in this project, which measured 13 nm and 4 nm in outer and inner diameters, respectively. MWCNTs used by Moisala et al. [23] had unspecified diameters. However, the MWCNTs measured 80 μm in length for both studies from the literature, compared with 1 μm for the MWCNTs used in this work. The larger increases in thermal conductivity reported in the two studies compared with the present work can thus be explained by the longer MWCNTs used, which provide better local paths and less thermal resistances for heat flow to travel. However, the 1% increase is also within the variability values in Tables 3.3 to 3.6 and hence may be statistically insignificant.

Comparison of results with 0.3% loading presented in Tables 4.5 and 4.6 shows that the void volume fraction affected the thermal conductivity of CNT-reinforced nanocomposites significantly. Thermal conductivity of resin 2377 at 0.3% loading decreased by 18% from 0.206 W/mK for a void-free plate to 0.168 W/mK for a plate with 16.4% V_v. Thermal conductivity of resin 2397 at 0.3% loading decreased by 19% and 25% respectively from 0.213 W/mK for a void-free plate to 0.172 W/mK and 0.160 W/mK respectively for plates with 16.9% and 22.6% V_v.

4.2 Neat and multi-scale composite plates

The materials used for manufacturing neat and multi-scale composite plates are detailed in Section 4.2.1. The procedures and equipment used for manufacturing composite plates are described in Section 4.2.2, followed by procedures and equipment used for characterising the porosity or void volume fraction V_v and fibre volume fraction V_f of the plates, Section 4.2.3. A set of 19 preliminary plates P1 to P19 were manufactured for developing proficiency with the RFI process and determining optimum manufacturing parameters with various fabrics and resins, Section 4.2.4. Then a set of 12 plates PB1 to PB12 were manufactured using the Plackett-Burman design of experiment method for determining the effect of 4 input parameters on the V_v, V_f, in-plane k_{cip} and through-thickness k_{ctt} thermal conductivities of the plates, Section 4.2.5. It should be noted that a thick composite plate VD was also manufactured for validating temperature profiles established in heat transfer simulations as discussed in detail in Chapter 5. Chapter 4 ends with a discussion of the effects of several input factors including MWCNT addition on the V_v, V_f, k_{cip} and k_{ctt} of the composite plates, Section 4.2.6.

All plates presented in Sections 4.2.4 and 4.2.5 were manufactured in collaboration with PhD candidate Simon Baril-Gosselin, who studies fluid flow aspects in the same project. The V_v and V_f characterisation of all composite plates was performed by Simon while the thermal characterisation of all plates was performed by the author. As mentioned in Chapter 2, fibre-reinforced composites with a neat polymer matrix are referred to as neat

composites in this work whereas fibre-reinforced composites where the polymer matrix has been loaded with CNTs are referred to as multi-scale composites.

4.2.1 Materials

Six carbon fibre fabrics and four epoxy resin films were used for manufacturing 32 composite plates in this work. Three of the resin films used were LEO 2376, LEO 2377 and LEO 2396, described in detail in Section 4.1.1. An additional resin, Gurit SA70 150 μm thick epoxy film was also used for manufacturing the preliminary set of plates used in developing proficiency with the RFI process while waiting for supply of LEO resin films from Axson in the early stages of the project. Specifications for the resins can be found in Appendix B.

The six carbon fibre fabrics all featured the same HTS40 carbon fibres from Toho Tenax [52] but varied in architecture and surface density ρ_{sd}, Table 4.7. The non-crimp bidirectional and twill fabrics used for measuring thermal conductivities of dry fabrics in Chapter 3 of this thesis were fabrics F2 and F6, respectively. F1 was used for manufacturing the first few preliminary plates for developing proficiency with the RFI process while waiting for the rest of the fabric supplies. Fabrics F2 and F3 were chosen such that F2 shared the same non-crimp architecture as F3 whilst having approximately double its surface density. Fabrics F5 and F6 were chosen with approximately the same surface densities as F2 and F3 respectively whilst sharing the same twill architecture. These 4 fabrics were used for manufacturing the Plackett-Burman set of plates PB1 to PB12; the objective was to have a fully crossed design of fabrics for investigating the effects of fabric architecture and surface density as well as any interaction effects between these two parameters. Fabric F4 was added for manufacturing composite plates using a further variety of fabrics.

Table 4.7 - Carbon fibre fabrics

Fabric	Manufacturer	Product code	Architecture	Surface density (g/m^2)	Filaments per yarn
F1	Saertex	unknown	non-crimp bidirectional (with powder binder)	534	12K
F2	Saertex	S32CX00K-00534-01270-264000	non-crimp bidirectional	534	12K
F3	Saertex	S37CX00K-00250-01380-606000	non-crimp bidirectional	250	12K
F4	JB Martin	TC06P50C taffetas	plain weave	197	3K
F5	JB Martin	TC12T50B	twill 2x2	429	6K
F6	JB Martin	TC06T50F	twill 2x2	215	3K

The ancillaries used for composite layup and vacuum bagging are summarized in Table 4.8. More than one type of vacuum bag and release film were used because the composite plates manufactured with the Gurit resin required materials that withstand a temperature of 120°C during the cure cycle whilst LEO resins from Axson required materials to withstand a temperature of 200°C during the cure cycle. Hence less costly Dahlar ancillaries [133] were used for plates manufactured with the Gurit resin while Securlon [134] and WL5200 [135] materials, kindly supplied by Bombardier, were used for plates manufactured with the LEO resins. The Dahlar 125 release film was also used as a vacuum bag material.

Table 4.8 - Vacuum bagging ancillaries

Ancillary	Product code	Maximum temperature (°C)	Thickness (μm)	Density (kg/m^3)
Dahlar 125 release film/vacuum bag	Dahlar 125	140	50	unspecified
Dahlar 125 perforated release film	Dahlar 125-P3	140	50	unspecified
Bleeder	UltraWeave 606	232	650*	260
Vacuum bag	Securlon-L1000-002	202	50	1130
Release film	WL5200B-P3	260	25	1730
Perforated release film	WL5200B-001	260	25	1730

*Bleeder thickness after compression measured under vacuum pressure of 0.02 bars

4.2.2 Procedures and equipment for manufacturing

The general procedures along with the equipment used for manufacturing composite plates are described in this section. As mentioned above, 19 preliminary plates and 12 Plackett-Burman plates were manufactured. The fabric and resin used for manufacturing a plate were cut into square plies of the same size; the sizes of the plies were different for the various preliminary plates as shown in Table 4.9 in Section 4.2.4, while plies measuring 200 mm by 200 mm were cut for plates PB1 to PB12.

The total thickness of resin required was calculated based on a targeted V_f of 55%, Equation 4.1, and this thickness was converted into the number of resin plies required knowing the thickness of each resin ply to be 120 μm. This project involved manufacturing composites using the MWCNT-reinforced resin LEO 2377; hence resin plies were stacked, intercalated and distributed as evenly as possible among the fabric plies for minimising the effect of filtering of the MWCNTs during infusion. The effect of filtering for different layup sequences is discussed in detail in Section 4.2.4.9. Each resin stack consisted of several resin plies which were rolled prior to layup to reduce voids inside. The layup was rolled by hand with the addition of each fabric ply to reduce voids. A typical layup sequence is shown in

Figures 4.7 and 4.8, where Figure 4.8 (a) shows a layup with neat resin LEO 2396 which is white and Figure 4.8 (b) shows a layup with the MWCNT-reinforced resin LEO 2377 which is black due to the added MWCNTs.

$$t_r = \frac{(1 - Vf)\rho_{sd}}{V_f \rho_f} \tag{4.1}$$

Figure 4.7 - Typical layup sequence for composite plates

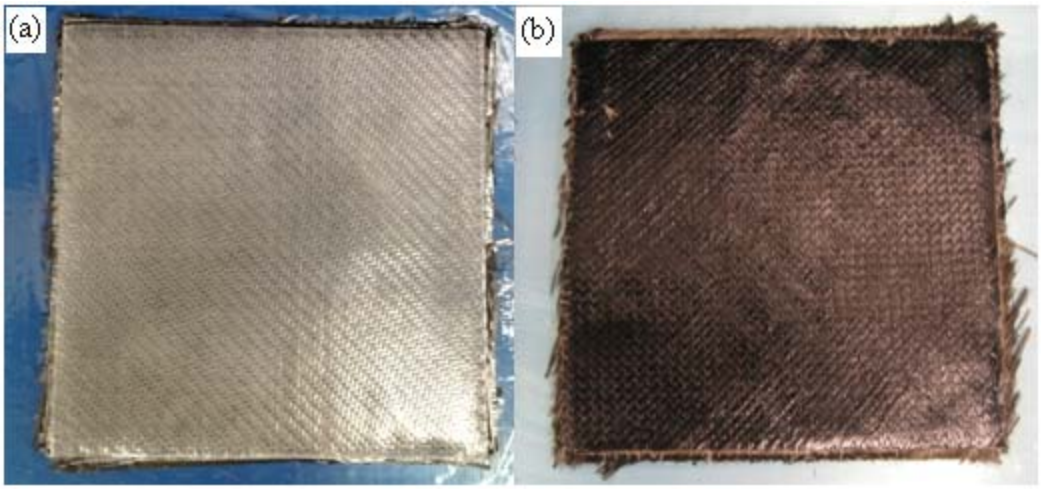

Figure 4.8 - Typical layup during composites manufacturing: (a) fabric F2 with resin LEO 2396 and (b) fabric F2 with resin LEO 2377

A polished 400 mm by 400 mm aluminium plate 6.35 mm thick was used as the tool plate and a layer of release film 330 mm by 330 mm was placed onto the centre of the tool. The composite stack was then placed on top of the release film. For preliminary plates P2 to P5, an aluminium frame was placed around the layup to prevent excessive edge bleeding, Figure 4.9. However, some resin escaped under the frame; hence for plates P6 to P19 as well as PB1 to PB12, vacuum bag sealant tape wrapped with fibreglass was taped around the layup, Figure 4.10. Some preliminary plates such as P10 in Table 4.9 consisted of multiple 100 mm by 100 mm plates, manufactured using different fabrics or resins with the same process parameters, Figure 4.11. These plates are designated by the plate series and plate number followed by letters, such as P10 (a) to (d) in the above case.

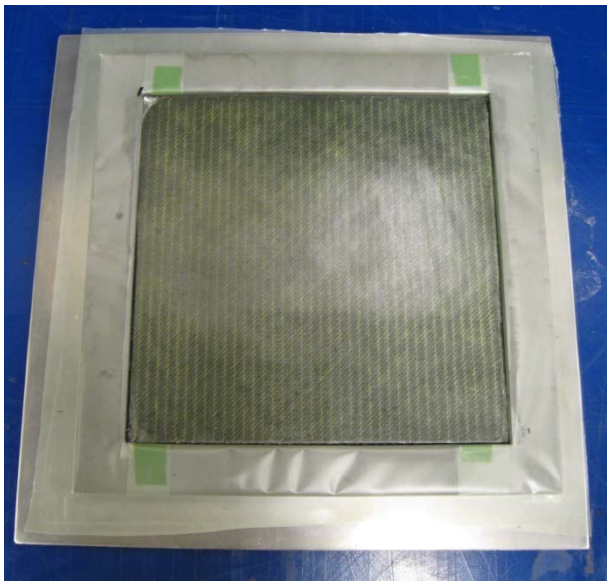

Figure 4.9 - Aluminium frame around layup: plate P2

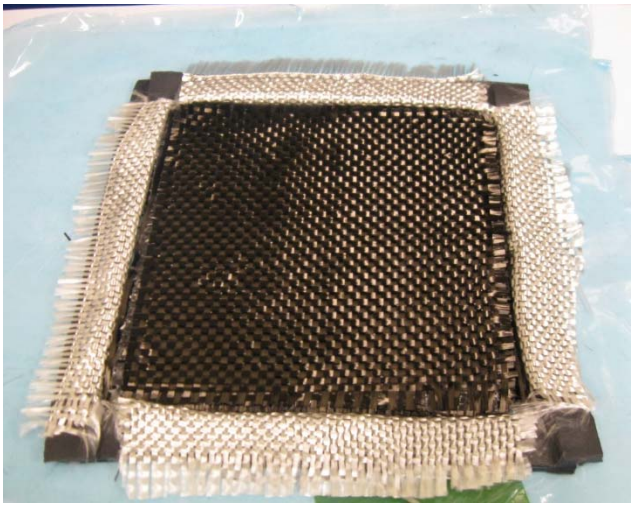

Figure 4.10 - Vacuum bag sealant tape wrapped with fibreglass around layup: plate P10 (d)

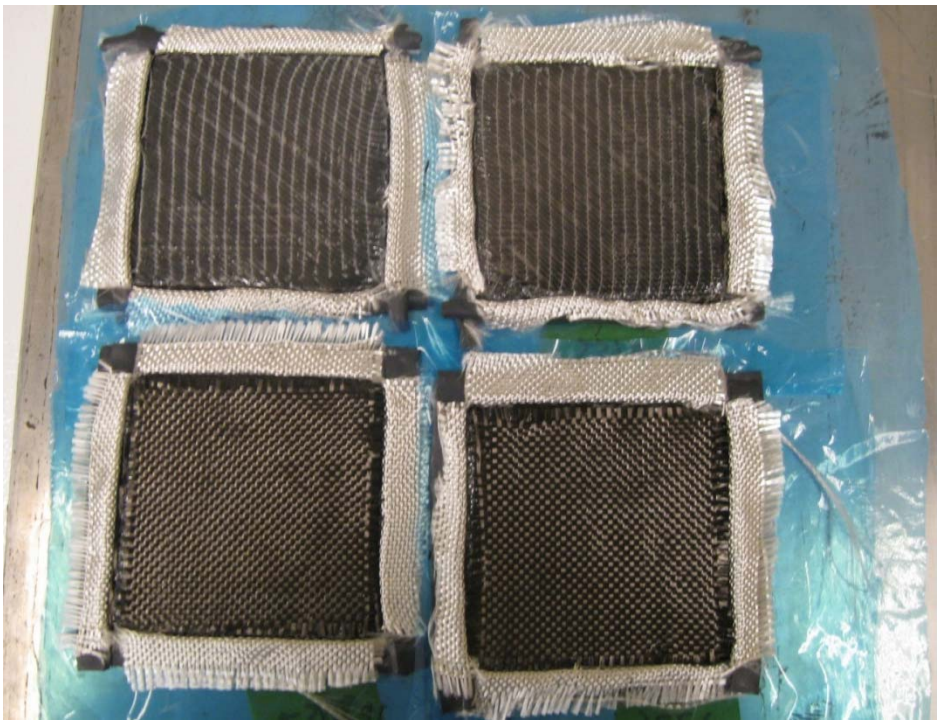

Figure 4.11 - Preliminary plates: P10 (a) to (d), clockwise from top left

Then the layup was vacuum bagged according to one of the two configurations described below; the configuration used is specified in Table 4.9. The first type is referred to as the standard configuration, Figures 4.12 (a) and 4.13 (a), while the second type is referred to as the bleed control configuration, Figures 4.12 (b) and 4.13 (b). For the standard configuration, a layer of perforated release film was placed on top of the layup and a layer of bleeder was placed on top of the perforated release film to absorb resin bleed. Then a polished aluminium caul plate wrapped in release film was placed on top of the bleeder to provide even pressure distribution during cure and ensure a smooth surface for the composite plate. Another layer of bleeder was placed on top of the caul plate to act as a breather for the vacuum and the vacuum port was then placed on top of that bleeder. Finally, the vacuum bag

was placed on top of the entire assembly and sealed with vacuum bag sealant tape along all the edges.

For the bleed control configuration, an aluminium piece was placed on the fibreglass around the layup to provide an air pathway for the application of vacuum. This configuration is seen in Figure 4.13 (b) with the bleeders and perforated release films cut to show the rest of the assembly. This piece was either an aluminium bar for preliminary plates, Figure 4.14 (a), or an aluminium spacer for Plackett-Burman plates, Figure 4.14 (b). Then a layer of release film was placed on top of the layup and taped with the layer of release film placed on the tool around all the edges to prevent resin bleed at the top surface of the layup, leaving only a small opening to place the aluminium piece, Figure 4.14 (b). The opening was sealed using vacuum bag sealant tape and an aluminium caul plate wrapped in release film was placed on top of the layup. A piece of perforated release film was placed on top of the release film followed by bleeders and the vacuum port. Finally, the vacuum bag was placed on top of the entire assembly and sealed with vacuum bag sealant tape along all the edges.

The difference between the two configurations is that the standard configuration allows for both surface bleeding through the top of the layup as well as edge bleeding whereas only edge bleeding is permitted in the bleed control configuration. Certain preliminary plates were manufactured using the standard configuration and others using the bleed control configuration while all of the Plackett-Burman plates were manufactured using the bleed control configuration. Thermocouples were placed inside the layup of several composite plates to record temperature profiles during manufacturing for experimental validation of the heat transfer model; details on this are found in Chapter 5.

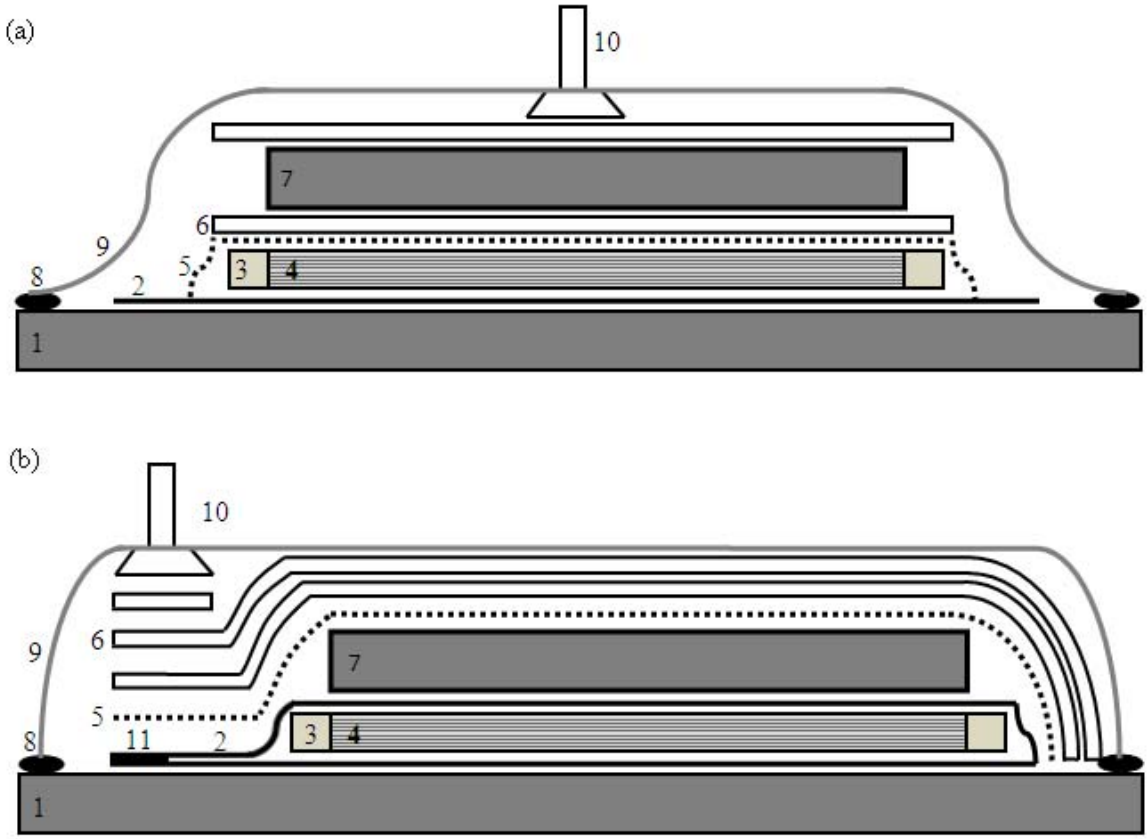

2) Tool plate

2) Release film

3) Aluminium frame or fibreglass wrapped around vacuum bag sealant tape

4) Fabric and resin layup

5) Perforated release film

6) Bleeder

7) Caul plate wrapped with release film

8) Vacuum bag sealant tape

9) Vacuum bag

10) Vacuum port

11) Aluminium piece

Figure 4.12 - Schematics of vacuum bag configurations: (a) standard and (b) bleed control

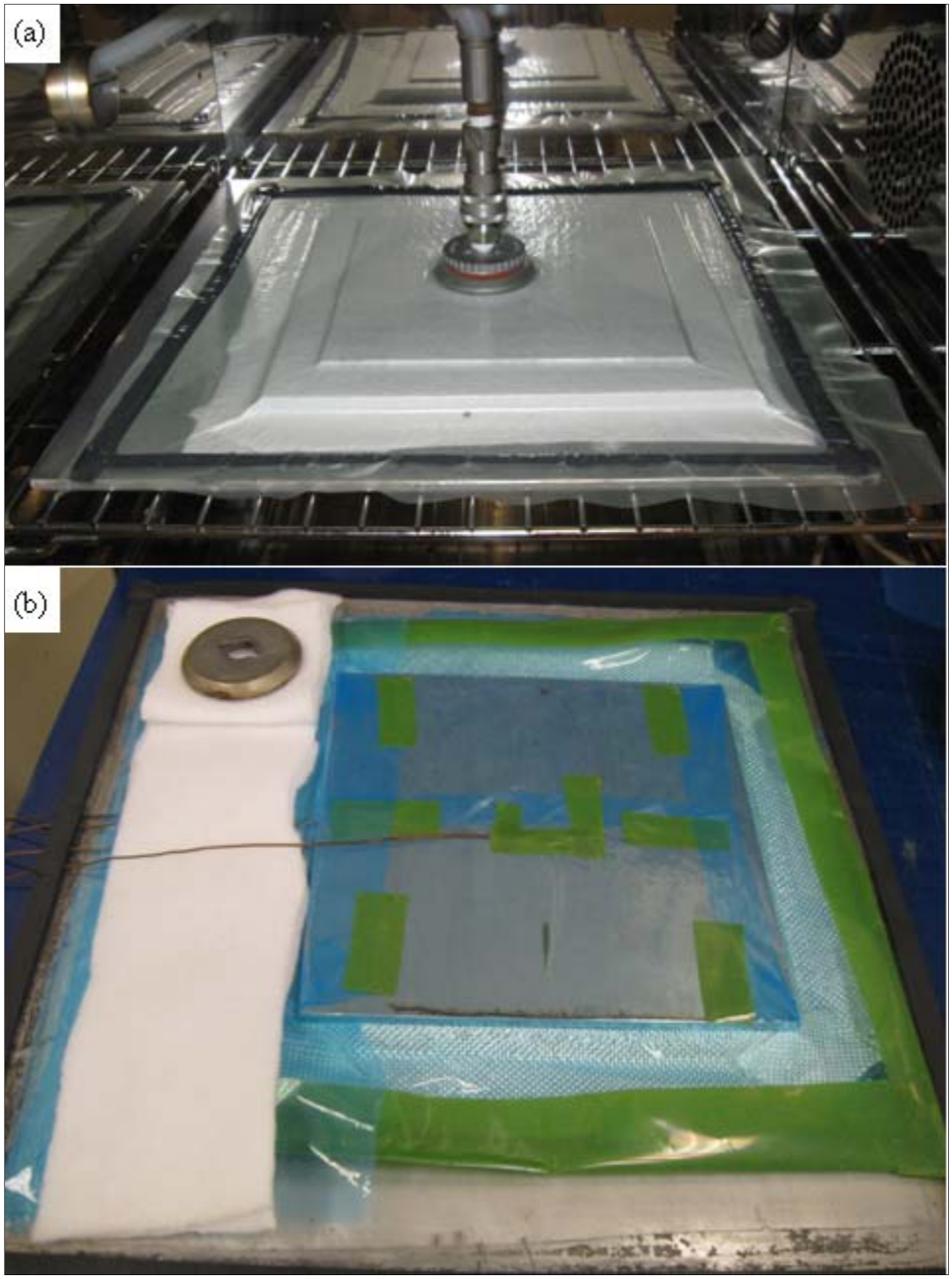

Figure 4.13 - Vacuum bag configurations: (a) standard and (b) bleed control

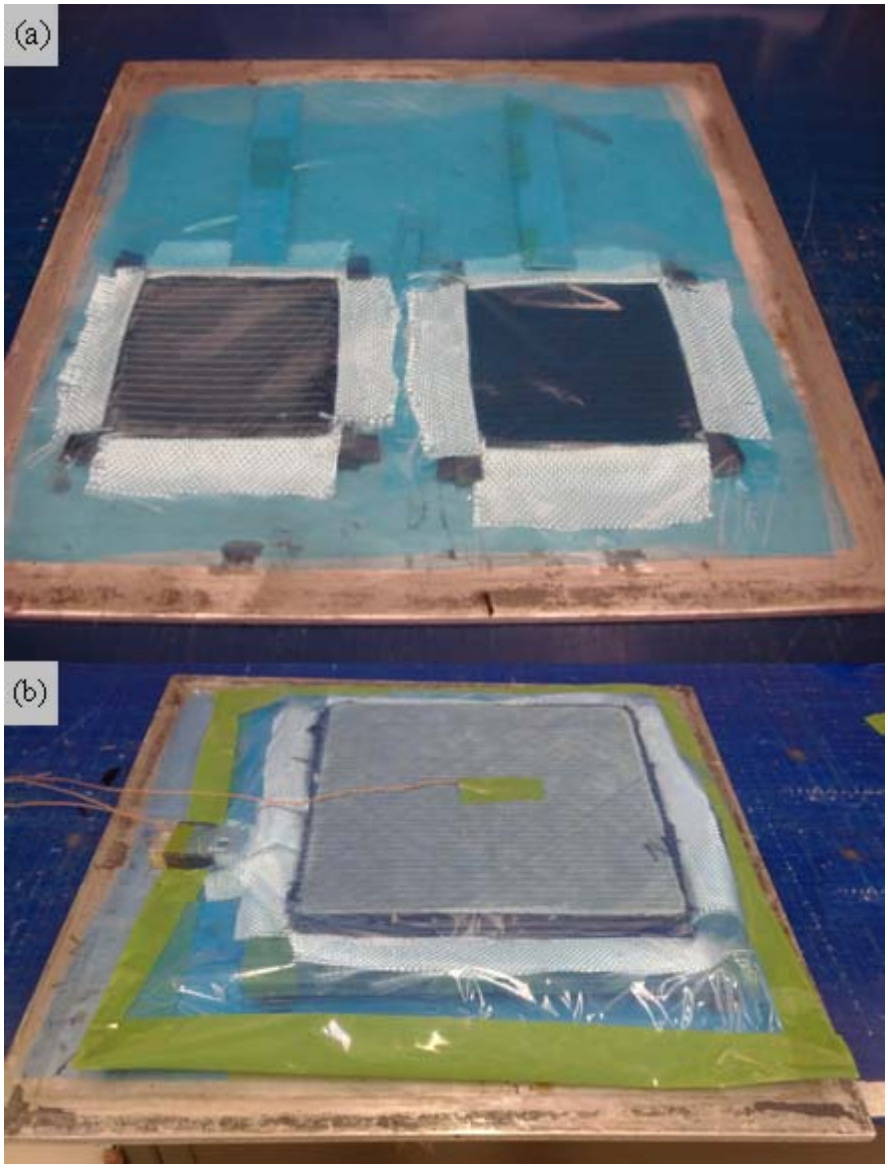

Figure 4.14 - Aluminium (a) bar and (b) spacer used in the bleed control configuration

The assembly was then placed into the PF120 Carbolite convection oven and vacuum was provided by the DAA-V715A Gast pump, Figure 3.8 at 0.02 bars or 98% vacuum for the entire duration of the cure cycle used. The cure cycles employed depended on the resin used. Plates manufactured with the SA70 resin were set to the standard Gurit cure cycle described below while all three LEO resins were set to the standard Axson cure cycle unless otherwise

specified in Table 4.9. The standard Gurit cure cycle consisted of a 2°C/min heating of up to 120°C followed by a half-hour dwell, while the standard Axson cure cycle consisted of a 2°C/min heating ramp up to 130°C followed by a two hour dwell, then another 2°C/min heating ramp up to 200°C followed by a two hour dwell. Vacuum was applied at 0.02 bars or 98% during both standard cure cycles unless otherwise specified in Table 4.9. The plate was cooled overnight in the oven after completion of the cure cycle.

4.2.3 Procedures and equipment for characterisation

The plate was taken out of the assembly, Figure 4.15 (a) and cut into six pieces as shown in Figure 4.15 (b) using a Walker-Turner 3331 band saw, towards V_v, V_f and thermal characterisation. The preliminary plates were of various sizes as presented in Table 4.9. All Plackett-Burman plates were 200 mm by 200 mm in size; one piece measuring 70 mm by 100 mm was cut from each corner of the plate and k_{cip} and k_{ctt} were measured using the THISYS and THASYS devices. Then one of the two 30 mm by 100 mm pieces left from the centre strip of the plate was used for characterising V_v and V_f, Figure 4.15 (b).

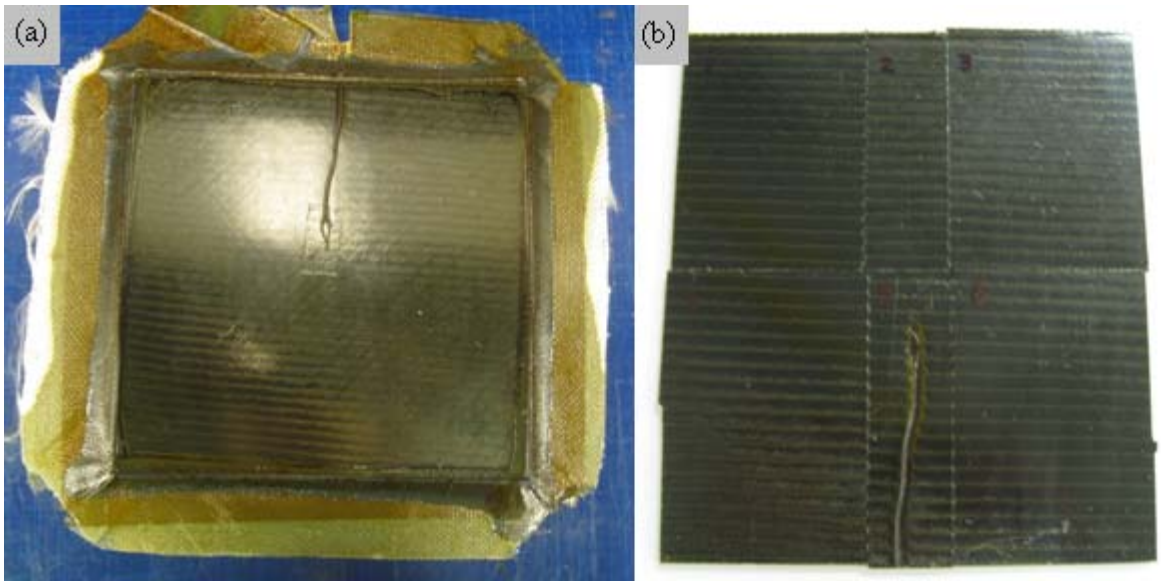

Figure 4.15 - Consolidated plate: (a) in original form and (b) cut for characterisation

Four strips approximately 15 mm long and 5 mm wide were precision cut from the 30 mm by 100 mm piece at different locations using a Struers Secotom-10 cutter with a diamond blade, Figure 4.16. One strip was cut from the edge of the piece facing the plate centre, one strip was cut from the opposite edge of the piece facing the plate edge and two strips were cut from the mid-length of the piece. This was done for obtaining representative V_v and V_f values for the plate, averaging from different locations, as variability between centre and edge locations was large. The strips were then placed into mounting cups and cold cast using Anamet liquid epoxy mixed with a hardener. The cast sample, Figure 4.17 was left to cure for 48 hours then polished using the Struers TegraPol-31 system, Figure 4.18. Five polishing disks were used in sequence, Figure 4.19. The detailed polishing procedure can be found in Appendix C.

Figure 4.16 - Struers Secotom-10 precision cutter

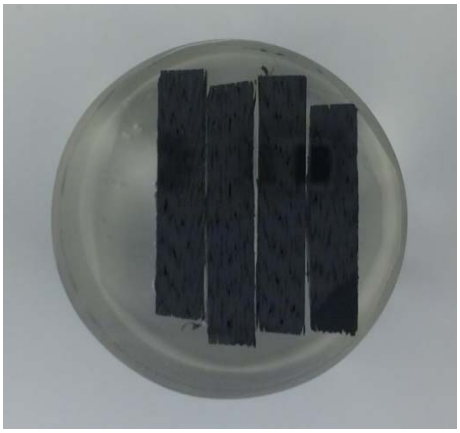

Figure 4.17 - Cast samples for V_v and V_f characterisation

Figure 4.18 - TegraPol-31 polishing system

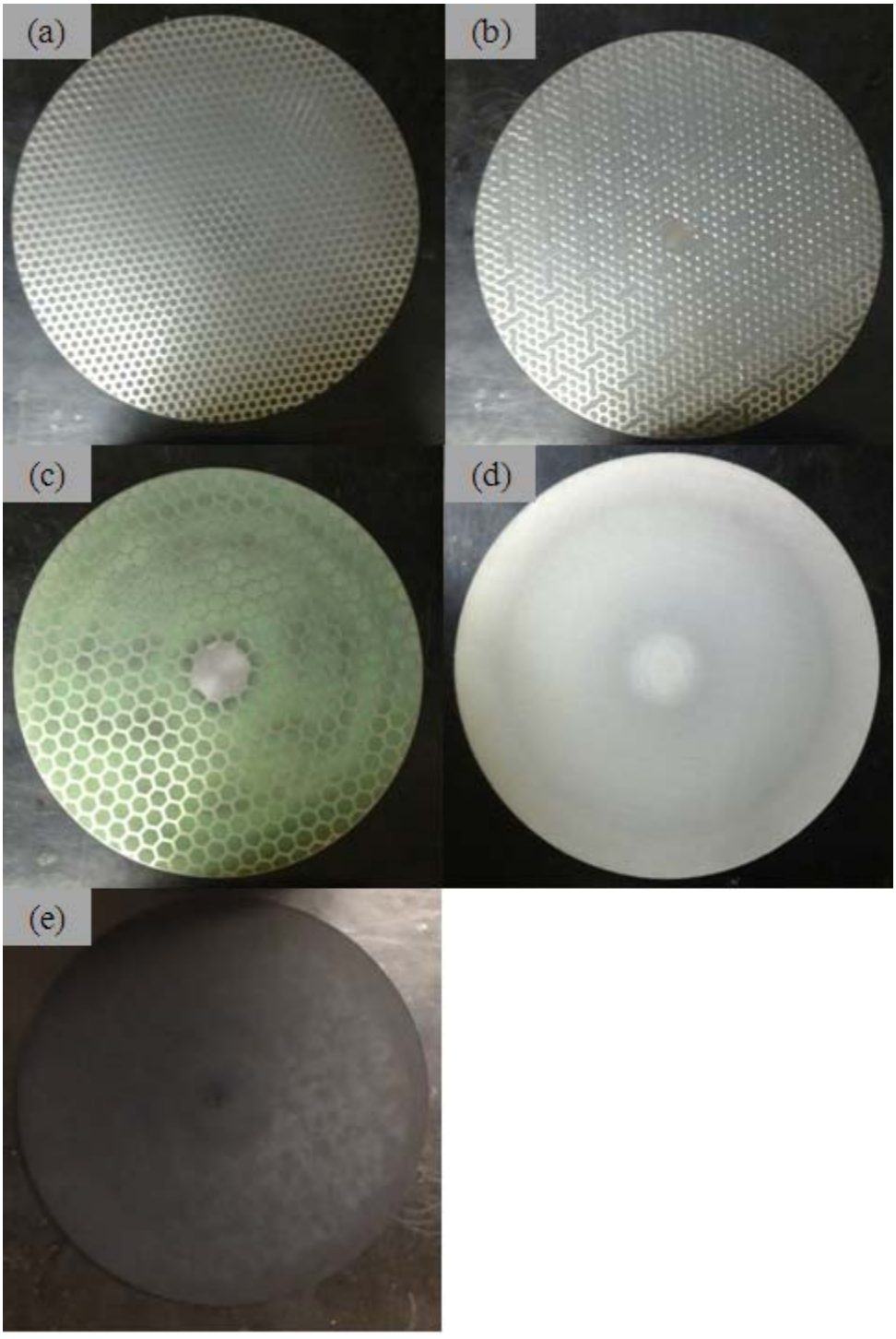

Figure 4.19 - Polishing disks: (a) PIANO 110 (b) PIANO 220 (c) LARGO (d) MOL and (e) CHEM

An Ancansco stereo microscope at x5 magnification was used for taking images of uncast samples for examining the infusion of the plates, Figure 4.20 (a). A Nikon metallographic optical microscope with 5x, 10x, 20x, 50x, and 100x magnifications was used with software Clemex for performing image analysis of cast and polished samples to obtain V_v and V_f values, Figure 4.20 (b).

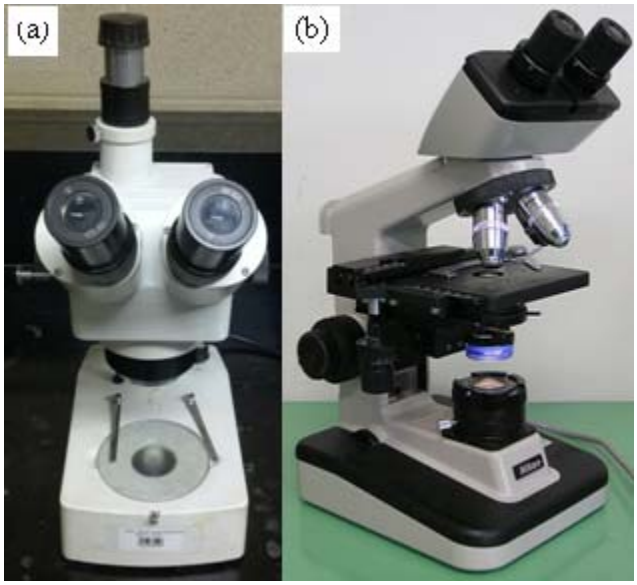

Figure 4.20 – Microscopes: (a) Ancansco stereo and (b) Nikon metallographic optical

Over 200 images were taken and used for calculating the V_v and V_f of each plate. This process is time-consuming, hence, image analysis was only used for plates PB1 to PB12. V_v and V_f values of the preliminary plates were calculated based on volumes and measured masses of the plates as well as densities of the resins presented in Table 4.3 and of the carbon fibres as specified by the manufacturer [52], using Equations 4.2 to 4.5. Plate

volume was calculated based on average measured lengths, widths and thicknesses of the plate.

$$m_f = N\rho_{sd}A_r \tag{4.2}$$

$$m_r = m_p - m_f \tag{4.3}$$

$$V_f = \frac{m_f}{\rho_f \forall_p} \tag{4.4}$$

$$V_v = 1 - \frac{m_f}{\rho_f \forall_p} - \frac{m_r}{\rho_r \forall_p} \tag{4.5}$$

where A_r is the surface area of the fabric or reinforcement ply, ρ_{sd} is the surface density of the fabric taken from Table 4.7, ρ_f is the density of the carbon fibres specified by the HTS40 fibre datasheet [52], ρ_r is the resin density taken from Table 4.3, m_p and $\forall_p$ are the measured mass and volume of the composite plate respectively, and m_f and m_r are the masses of the fibres and resin, respectively.

The backscattered electron mode of a Zeiss EVO-MA 10 Scanning Electron Microscope (SEM) with a resolution of 4.5 nm at 30 kV was used for taking images for preliminary plate P1, Figure 4.21. The objective was to take high resolution images of cross-sections of the composite plates. However, the high voltage of the SEM tended to burn the samples cast in epoxy and the SEM was complex to operate; hence images on the rest of the

composites plates manufactured were taken using the optical and stereo microscopes, which showed the distribution of the carbon fibres and voids equally effectively.

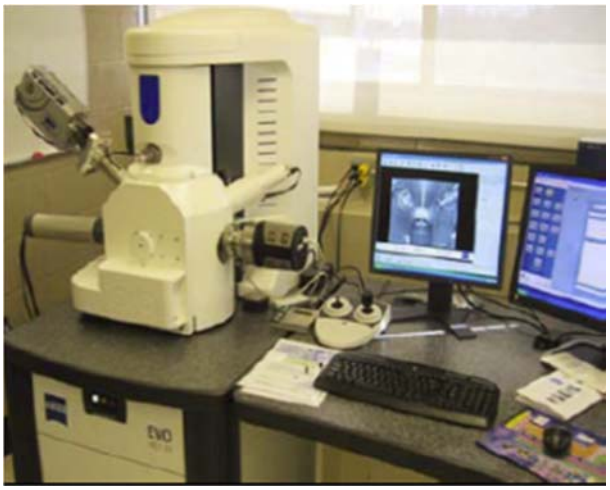

Figure 4.21 - Scanning Electron Microscope: Zeiss EVO-MA 10

4.2.4 Preliminary plates: results

Nineteen preliminary plates were manufactured using the RFI process with different fabric and resin materials under various experimental conditions, Table 4.9. Three types of preliminary plates were manufactured: 1) the first plates to be made using a certain resin for benchmarking purposes (plates #1, 6, 10, 18); 2) those manufactured for comparison against plates of the former type to determine the effect of various manufacturing parameters (plates #2, 5, 8, 9, 11, 12, 13, 14, 16, 17, 19); and 3) those manufactured to study infusion (plates #3, 4 and 7). The manufacturing parameters investigated are the side bleeding, curing temperature, degassing, resin and fabric materials, vacuum bag configuration, vacuum, pre-compaction and layup sequence. Plates manufactured for studying infusion as well as

observations related to resin flow are presented but not discussed in detail, as the emphasis of this thesis is the thermal characterization and not fluid flow.

Table 4.9 - Summary of preliminary plates

Plate	Size (mm)	Resin	Fabric	Stacking sequence	Vacuum bag Configuration	Cure cycle	Purpose	V_v (%)	V_f (%)
P1	150x150	SA70	F1	intercalated	standard	Gurit	first plate using RFI	NC	NC
P2	200x200	SA70	F1	intercalated	standard	Gurit	add frame	NC	47
P3	200x200	SA70	F1	resin at bottom	standard	Gurit	SA70 infusion	NC	NC
P4	200x200	SA70	F1	resin at mid-plane	standard	Gurit	SA70 infusion	NC	NC
P5	200x200	SA70	F1	resin at bottom	standard	Gurit with 4 hour dwell at 90°C	effect of cure cycle	NC	NC
P6	200x200	2396	F1	intercalated	standard	Axson	first plate using 2396	NC	NC
P7	200x200	2396	F1	resin at mid-plane	standard	Axson	2396 infusion	NC	NC
P8	200x200	2396	F1	intercalated	standard	Axson without vacuum	effect of vacuum	NC	NC
P9	200x200	2396	F1	resin at mid-plane	standard	Axson without vacuum	effect of vacuum	NC	NC
P10(a)	100x100	2376	F2	intercalated	standard	Axson	first plate using F2, F4 and 2376	4.0	62
P10(b)	100x100	2396	F2					4.4	62
P10(c)	100x100	2376	F4					5.4	64
P10(d)	100x100	2396	F4					5.5	63
P11(a)	100x100	2396	F2	intercalated	bleed control	Axson	effect of various vacuum bagging parameters	5.4	63
P11(b)	100x100	2396	F2					5.2	63
P11(c)	100x100	2396	F4					7.6	62
P11(d)	100x100	2396	F4					3.8	62
P12(a)	100x100	2376	F2	intercalated	standard	Axson with additional 6 hour dwell at 60°C	effect of degassing	1.9	60
P12(b)	100x100	2396	F2					2.0	61
P12(c)	100x100	2376	F4					0.8	63
P12(d)	100x100	2396	F4					4.1	60
P13(a)	100x100	2376	F2	intercalated	standard	Axson with heating ramp of 4°C/min and first dwell at 160°C	effect of cure cycle	2.9	61
P13(b)	100x100	2396	F2					4.7	60
P13(c)	100x100	2376	F4					4.3	62
P13(d)	100x100	2396	F4					4.1	60

P14(a) P14(b) P14(c) P14(d)	100x100 100x100 100x100 100x100	2396 2396 2396 2396	F1 F1 F1 F1	intercalated	bleed control	Axson	effect of bleed control	5.5 4.2 2.8 3.2	53 60 60 59
P15	200x200	2376	F2	intercalated	standard	Axson with additional 6 hour dwell at 60°C	repeat of 12 (d)	4.3	63
P16	100x100	2396	F2	intercalated	bleed control	Axson	effect of bleed control	2.5	58
P17(a) P17(b)	100x100 100x100	2396 2396	F2 F2	intercalated	bleed control	Axson	effect of pre-compaction	1.4 2.3	59 59
P18	100x100	2377	F2 F4	intercalated	bleed control	Axson	first plate with 2377	1.2 0.0	61 62
P19	100x100	2377	F2 F4	resin at bottom	bleed control	Axson	effect of placing 2377 at bottom	NC	NC

*NC – not calculated

4.2.4.1 Plate P1: first composite plate manufactured

Plate P1 was manufactured using the non-crimp bidirectional fabric F1 intercalated with Gurit resin films, vacuum bagged in the standard configuration without any frame or fibreglass around the edges, Table 4.9. Plate P1 was cured according to the standard Gurit cycle and excess bleed was observed around the edges, which causes voids through loss of resin. Optical microscope and SEM images of cast samples showed that the edge of the plate had large intra-tow voids while the centre of the plate had negligible voids, Figure 4.22.

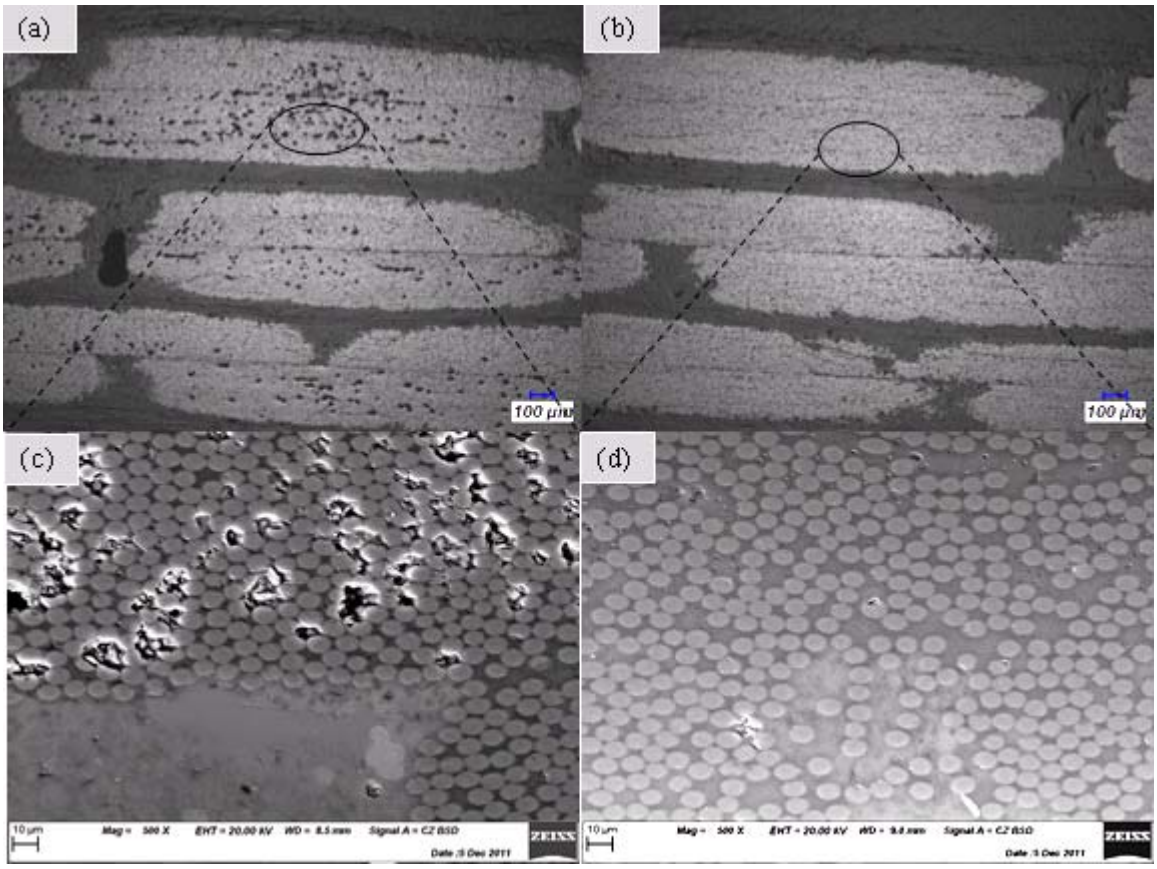

Figure 4.22 – Images of plate P1: (a) optical images of edge (b) optical images of centre (c) SEM images of edge and (d) SEM images of centre

4.2.4.2 Plates P2 to P6: reducing excess side bleed

An aluminium frame was placed around the edges of the layups for plates P2 to P6 as shown in Figure 4.9 to reduce the excessive edge bleeding observed with plate P1. Plate P2 showed less edge bleeding and microscope images showed that similar to plate P1, the edge of the plate had high intra-tow void content while the centre of the plate had negligible void content, Figure 4.23. The optical images of P1 and P2 indicate that the Gurit resin flows along the path of least resistance in between the fibre tows, filling the inter-tow spacing and leaving dry spots in the tows. Resin escaped under the aluminium frame for plate P6 manufactured with resin LEO 2396; hence fibreglass wrapped around vacuum bag sealant tape was placed around the edges of the layup for plates P7 to P19, Figure 4.10.

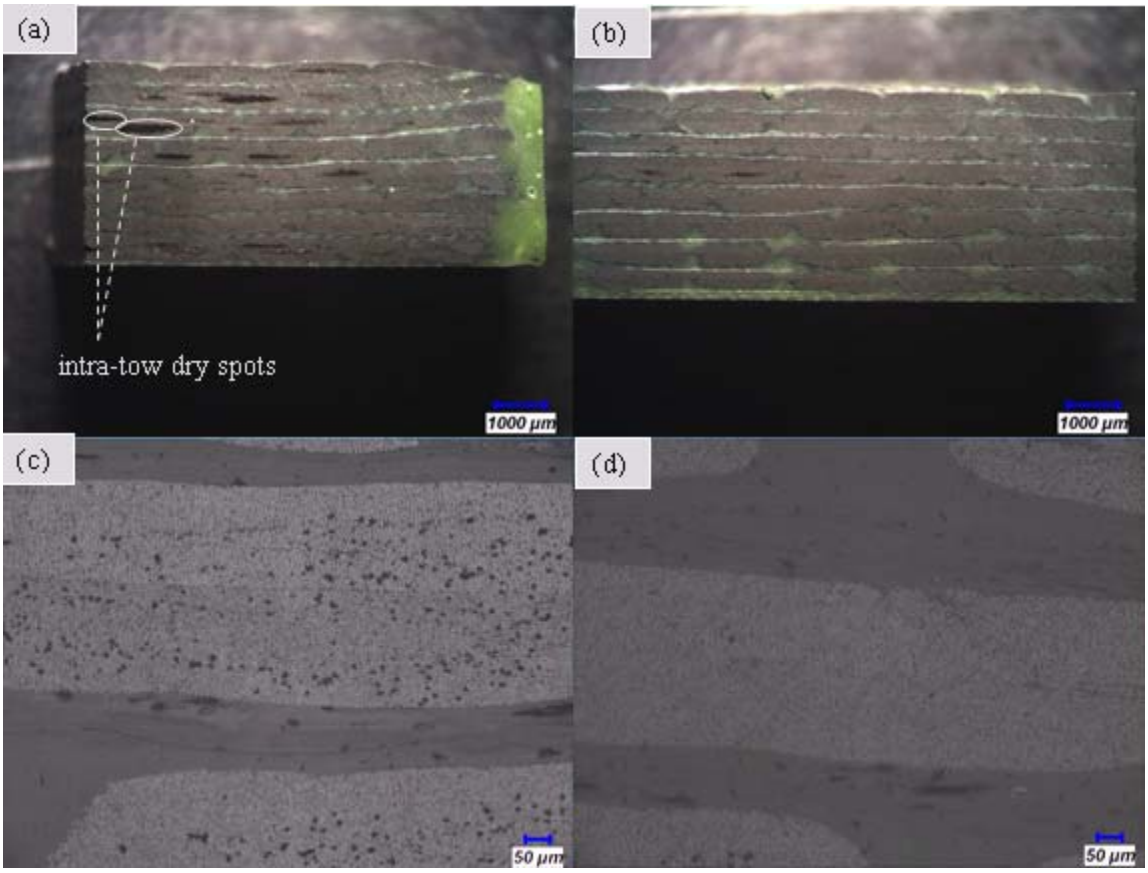

Figure 4.23 – Images of plate P2: (a) stereo images of edge (b) stereo images of centre (c) optical images of edge and (d) optical images of centre

4.2.4.3 Plates P6, P10 and P18: first plates made with LEO resins

Plates P6, P10 and P18 are the first plates manufactured using resins LEO 2396, LEO 2376 and LEO 2377, respectively. The stereo images of these plates showed that the LEO resins had different flow behaviour compared with the Gurit: the resin impregnated the fibre tows but left regions of the inter-tow gaps dry. This is shown in stereo microscope images of plates P10 (a) to (d), Figure 4.24. P10 uses neat LEO 2376 while P18 uses MWCNT-reinforced resin LEO 2377. In terms of other manufacturing parameters, plates P10 (a) and

P18 (a) as well as plates P10 (c) and P18 (b) are directly comparable. V_f values for plates P18 (a) and (b) were comparable with those for plates P10 (a) and (c) respectively while V_v values for plates P18 (a) and (b) were much lower at 1.2% and 0.0% respectively compared with those for plates P10 (a) and (c) at 4.0% and 5.4% respectively, Table 4.9. This is seen by comparing Figures 4.24 (a) and (c) to Figures 4.26 (a) and (b), respectively. The effect of loading MWCNTs into resin films was further investigated as reported in Section 4.2.5 using the Plackett-Burman design of experiments.

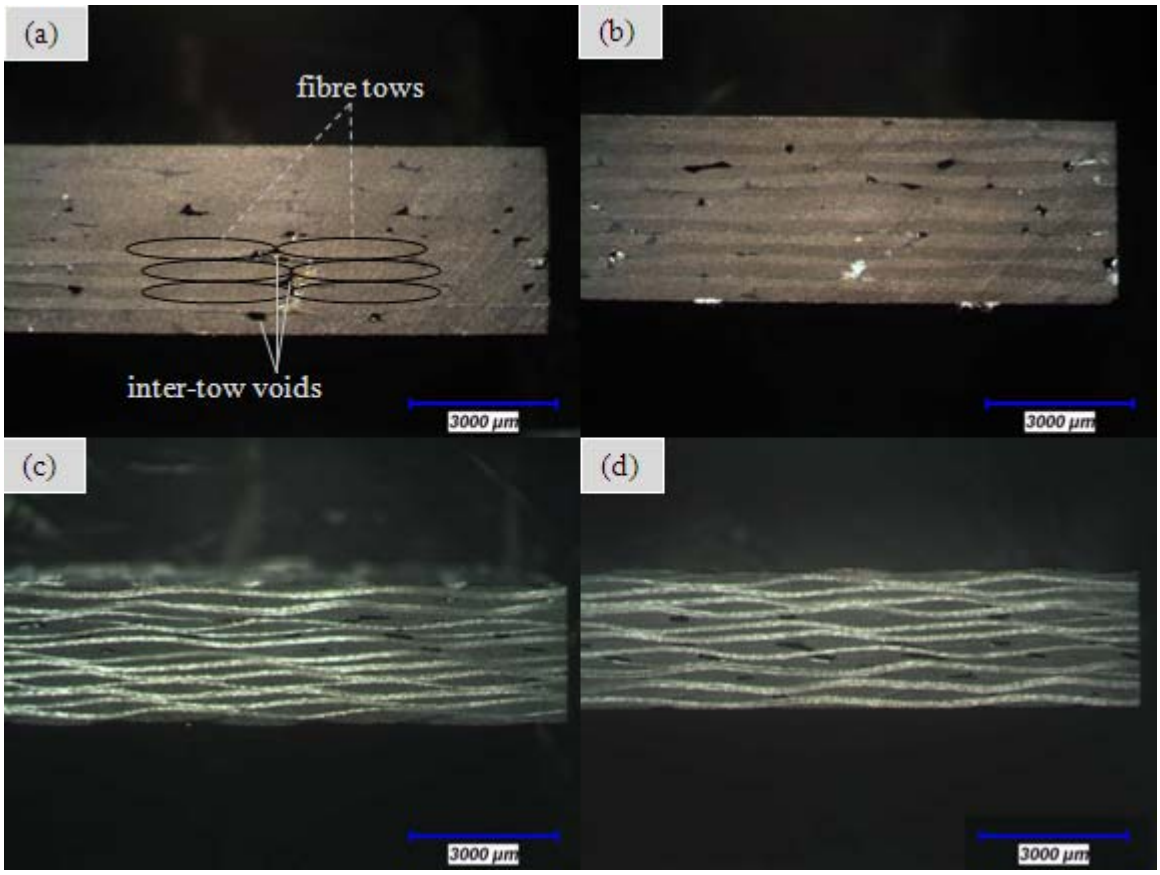

Figure 4.24 - Stereo microscope images of plate P10: (a) F2 with resin LEO 2376 (b) F2 with resin LEO 2396 (c) F4 with resin LEO 2376 and (d) F4 with resin LEO 2396

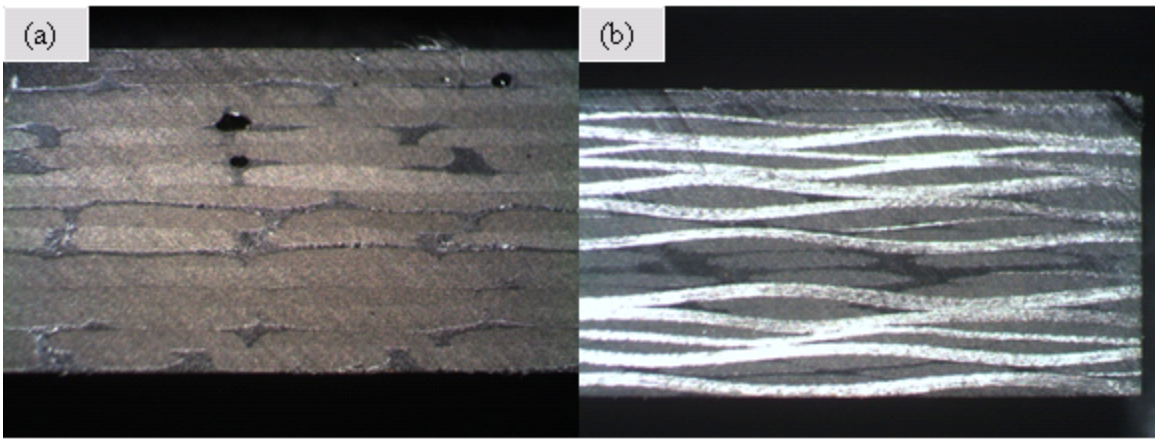

Figure 4.25 - Stereo microscope images of plate P18: (a) F2 with resin LEO 2377 and (b) F4 with resin LEO 2377

4.2.4.4 Plates P10, P12 and P13: effect of changes in cure cycle

The effect of a higher curing temperature is shown by comparing plates P10 and P13. Plate P13 had a curing temperature of 160°C compared with 130°C for plate P10. V_f values for plate P13 were comparable to those for plate P10 while V_v values for plate P13 (a) to (d), ranging from 2.9% to 4.7%, were significantly lower than those for plates P10 (a) to (d), ranging from 4.0% to 5.5%, Table 4.9. The effect of degassing on the porosity can be seen by comparing plates P10 and P12, where an additional dwell at 60°C for six hours was incorporated into the standard Axson cure cycle for plate P12. V_v values for plates P12 (a) to (d), ranging from 0.8% to 4.1%, were lower than those for plates P10 (a) to (d), ranging from 4.0% to 5.5%, Table 4.9. However, this would not be feasible practically for production in industry as the time required to manufacture each plate would be more than doubled. Thus the standard cure cycle was used for the remaining plates.

4.2.4.5 Plates P12 and P13: effect of materials

The effect of fabric architecture and resin can be observed by comparing plates P12 (a) to (d) and P13 (a) to (d) mentioned above in Section 4.2.4.4. V_v varied between plates manufactured using the non-crimp fabric F2 and the plain weave fabric F4 as well as between plates manufactured using LEO 2376 and LEO 2396 resins, Table 4.9. The effects of materials were investigated further as reported in Section 4.2.5, using the Plackett-Burman design of experiments.

4.2.4.6 Plates P10 and P16: effect of vacuum bag configuration

The effect of the vacuum bag configuration can be seen by comparing plate P10 (b) to P16. Plate P16 uses the bleed control configuration while plate P10 uses the standard configuration. In terms of other manufacturing parameters, plates P10 (b) and P16 are directly comparable. Porosity of the composites was reduced by approximately half by employing the bleed control configuration as opposed to the standard configuration; V_v value of plate P10 (b) is 4.4% while that of plate P16 is 2.5%, Table 4.9. Hence the bleed control configuration was used for the Plackett-Burman plates for minimising V_v. However, the V_f value of plate P16 is lower at 58% compared with that of plate P10 (b) at 62%. This is because the bleed control configuration effectively eliminates surface bleeding and allows only edge bleeding into the fibreglass, thus reducing total resin bleed as well as porosity; but in doing so more resin is left in the layup to cure, leading to a thicker laminate with a slightly lower V_f.

4.2.4.7 Plates P6 and P8: effect of vacuum

The effect of vacuum during manufacturing can be seen by comparing plates P6 and P8; the cure cycle for plate P6 included the application of 0.02 bars or 98% vacuum while that for plate P8 had no application of vacuum. Plate P8 was visibly thicker than plate P6 and showed more, larger voids upon visual inspection; hence vacuum was applied during the manufacturing of the Plackett-Burman plates for both maximising V_f and minimising V_v.

4.2.4.8 Plates P16 and P17: effect of pre-compaction

The effect of pre-compaction can be seen by comparing plates P16 and P17 (b) to P17 (a); P17 (b) was a repeat of P16 while P17 (a) was vacuum bagged and compacted for three cycles under 1 MPa on the Instron 4482 under 98% vacuum, Figure 4.26. Plate P17 (b) had similar V_f and V_v values of 59% and 1.3% respectively compared with those of plate P16 at 58% and 2.5%, respectively. Plate P17 (a) had a similar V_f of 59% and a lower V_v of 1.4%: pre-compaction reduced the porosity of the plate without sacrificing V_f.

Figure 4.26 - Pre-compaction: plate P17 (a)

4.2.4.9 Plates P18 and P19: effect of layup sequence

Fabric plies and resin film layers were intercalated in the layup for plate P18 whilst all of the resin was placed at the bottom of the layup for plate P19. Plate P18 (a) and (b) showed porosities of 1.2% and 0.0% respectively compared with negligible void content for plates P19 (a) and (b). However, plates P19 (a) and (b) were observed to be of a lighter shade on the top surface compared with the bottom surface: there was filtering of the MWCNTs. Hence the intercalated layup sequence was used for manufacturing the Plackett-Burman plates to ensure adequate dispersion of the MWCNTs in the composite plates.

4.2.5 Plackett-Burman plates: results

The manufacturing parameters used for the Plackett-Burman plates were selected based on the results presented in Sections 4.2.4.1 to 4.2.4.9, Table 4.10.

Table 4.10 - Manufacturing parameters for Plackett-Burman plates

Cure cycle	standard Axson
Vacuum bag configuration	bleed control
Vacuum	yes
Edge bleeding	fibreglass
Pre-compaction	no
Layup sequence	intercalated

Plackett-Burman statistical design of experiment [136] was used for investigating the effect of various input factors (Table 4.11) on the V_v, V_f, k_{cip} and k_{ctt} of the Plackett-Burman PB composite plates. The full factorial of the screening design is shown in Table 4.12 along with the fabric and LEO resin used for manufacturing each plate. However, only the first 12 plates were manufactured as LEO 2397 could not be supplied by Axson. PB2 and PB3 are the composites plates mentioned in Chapter 3 for comparison of their thermal conductivity to that of the dry fabrics.

Table 4.11 - Input factors for design of experiments

	A Resin base	B MWCNTs	C Fabric architecture	D Fabric surface density
-	LEO 2376	no	2x2 twill	215 (twill)/ 250 (non-crimp)
+	LEO 2396	yes	non-crimp bidirectional	429 (twill)/ 534 (non-crimp)

Table 4.12 - Screening design

	Input factors				Resin	Fabric
Plate	A	B	C	D		
PB1	-	-	-	+	LEO 2376	F6
PB2	-	-	-	-	LEO 2376	F5
PB3	-	-	+	+	LEO 2376	F2
PB4	-	-	+	-	LEO 2376	F3
PB5	-	+	-	+	LEO 2377	F6
PB6	-	+	-	-	LEO 2377	F5
PB7	-	+	+	+	LEO 2377	F2
PB8	-	+	+	-	LEO 2377	F3
PB9	+	-	-	+	LEO 2396	F6
PB10	+	-	-	-	LEO 2396	F5
PB11	+	-	+	+	LEO 2396	F2
PB12	+	-	+	-	LEO 2396	F3
PB13	+	+	-	+	LEO 2397	F6
PB14	+	+	-	-	LEO 2397	F5
PB15	+	+	+	+	LEO 2397	F2
PB16	+	+	+	-	LEO 2397	F3

In statistical design of experiments, a contrast is a way of making a comparison; it compares two values or two groups of values by quantifying their difference with zero. Given a set of j values $\mu_1, \mu_2, ...\mu_j$ to be compared, a contrast C is defined for this set of values by a set of j contrast coefficients $c_1, c_2, ...c_j$ which sum to zero, Equation 4.6; in this thesis $j = 12$ for the 12 PB plates shown in Table 4.12. The $c_1, c_2, ...c_j$ values are shown in Table 4.13 and $\mu_1, \mu_2, ...\mu_j$ values are shown in Table 4.14.

$$\sum_{i=1}^{j} c_i = 0 \tag{4.6}$$

The algebraic expression for a contrast is:

$$C = \sum_{i=1}^{j} c_i \mu_i \tag{4.7}$$

Nine contrasts were defined for plates PB1 to PB12: four representing main effects of input factors A to D on the response factors V_v, V_f, k_{cip} and k_{ctt} and five representing interaction effects between input factors on the response factors, above and beyond the main effects. For example, contrast A represents the effect of the resin base and contrast AB represents the joint effect of resin base and MWCNT, above the effect of each input factor A and B separately. Values $\mu_1, \mu_2, ...\mu_j$ assigned with a contrast coefficient of zero are excluded from the comparison whilst the comparison of values assigned with a non-zero contrast coefficient is defined by the signs of the coefficients. Coefficients were assigned for each contrast, Table 4.13. Cast samples of the plates were characterised as described in Section 4.2.3. Results for the response factors V_v, V_f, k_{cip} and k_{ctt} are shown in Table 4.14.

Table 4.13 - Contrast table

	Contrasts								
Plate	A	B	C	D	AC	AD	BC	BD	CD
PB1	-1	-1	-1	1	1	-1	1	-1	-1
PB2	-1	-1	-1	-1	1	1	1	1	1
PB3	-1	-1	1	1	-1	-1	-1	-1	1
PB4	-1	-1	1	-1	-1	1	-1	1	-1
PB5	0	1	-1	1	0	0	-1	1	-1
PB6	0	1	-1	-1	0	0	-1	-1	1
PB7	0	1	1	1	0	0	1	1	1
PB8	0	1	1	-1	0	0	1	-1	-1
PB9	1	0	-1	1	-1	1	0	0	-1
PB10	1	0	-1	-1	-1	-1	0	0	1
PB11	1	0	1	1	1	1	0	0	1
PB12	1	0	1	-1	1	-1	0	0	-1

Table 4.14 - Results for response factors

Plate	Void volume fraction V_v (%)	Standard deviation	Fibre volume fraction V_f (%)	Standard deviation	In-plane thermal conductivity k_{cip} (W/mK)	Through-thickness thermal conductivity k_{ctt} (W/mK)
PB1	4.0	3.8	53.8	5.6	2.729	0.568
PB2	0.7	0.9	53.5	5.5	2.499	0.547
PB3	1.5	1.8	57.5	6.1	2.513	0.505
PB4	1.8	1.7	57.7	6.0	2.481	0.511
PB5	0.5	0.9	57.5	6.7	2.638	0.583
PB6	0.1	0.6	55.6	5.6	2.392	0.550
PB7	0.7	0.9	55.5	7.1	2.673	0.525
PB8	1.3	1.2	55.7	5.5	2.594	0.551
PB9	1.8	1.9	58.4	5.5	2.588	0.567
PB10	1.7	1.9	55.4	5.5	2.634	0.560
PB11	2.8	2.3	57.0	6.0	2.752	0.582
PB12	2.2	1.6	53.4	5.7	2.522	0.536

Contrasts were calculated using Equation 4.7 where c_i are the contrast coefficients from Table 4.13 and μ_i are the results for the response factors from Table 4.14. Results for the calculated contrasts are shown in Table 4.15.

Table 4.15 - Contrasts

Contrast	Void volume fraction V_v (%)	Fibre volume fraction V_f (%)	In-plane thermal conductivity k_{cip} (W/mK)	Through-thickness thermal conductivity k_{ctt} (W/mK)
A	0.5	1.7	0.3	0.114
B	-5.4	1.8	0.1	0.078
C	1.5	2.6	0.1	-0.165
D	3.5	8.4	0.8	0.075
AC	2.9	-11.3	0.3	0.100
AD	-2.3	6.5	-0.1	0.000
BC	2.8	-9.8	0.5	0.042
BD	-3.2	1.6	0.1	-0.008
CD	-4.1	-2.0	-0.1	-0.047

Contrasts that are far from zero are said to be significant while those that are close to zero are said to be non-significant; a significant contrast means that said contrast has a definitive impact on the response factor. This distinction between significant and non-significant contrasts depends upon the relative magnitudes of the sum of squares $SS(\mathrm{C})$ between the contrasts. The sum of squares for each contrast was calculated using Equation 4.8 and presented in Table 4.16. Then the sum of squares values for each response factor were plotted in descending order, representing the order of importance of the various contrasts, with points connected to form the profile of a cliff; this is referred to as a scree plot

for the response factor. A scree plot provides a graphic tool for analysing the sum of squares values towards determining which contrasts are significant. Points that are at the bottom of the cliff represent background noise and are referred to as the rubble while the height of any cliff above the rubble indicates whether contrasts are significant. For example, in the scree plot for porosity, the rubble consists of all contrasts except B while contrast B is clearly above the rubble, Figure 4.27; in this case, contrast B is referred to as significant and the addition of MWCNTs is deemed to have a definitive impact on the porosity of the plate. However, in some cases where the point belonging to a contrast is not so obviously above the rubble, such as contrasts D and AD in Figure 4.28, the significance of such contrasts is not definitive and more testing should be performed to gather response values. If after further data collection, the point becomes a part of the rubble, then the contrast which the point belongs to is not significant. If the said point still stands above the rubble, then the contrast which the point belongs to is significant; however, this would mean that the said contrast has a minor impact on the response factor. Scree plots for the 4 response factors are shown in Figures 4.27 to 4.30. Results and implications are discussed in Section 4.2.6.

$$SS(C) = \frac{C^2}{\sum_{i=1}^{j} c_i^{\,2}} \tag{4.8}$$

Table 4.16 - Sum of squares

Contrast	Sum of squares			
	Void volume fraction V_v (%)	Fibre volume fraction V_f (%)	In-plane thermal conductivity k_{cip} (W/mK)	Through-thickness thermal conductivity k_{ctt} (W/mK)
A	0.031	0.361	0.0094	0.0016
B	3.645	0.405	0.0007	0.0008
C	0.188	3.000	0.0003	0.0023
D	1.021	0.270	0.0495	0.0005
AC	1.051	15.96	0.0102	0.0010
AD	0.661	5.281	0.0008	0.0002
BC	0.980	12.01	0.0277	0.0002
BD	1.280	0.320	0.0005	0.0000
CD	1.401	0.563	0.0007	0.0002

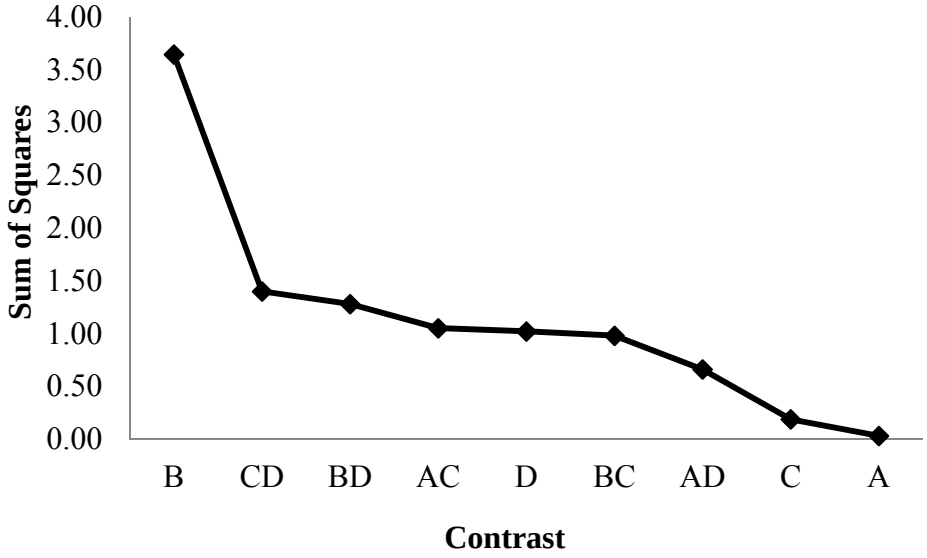

Figure 4.27 - Scree plot for porosity V_v

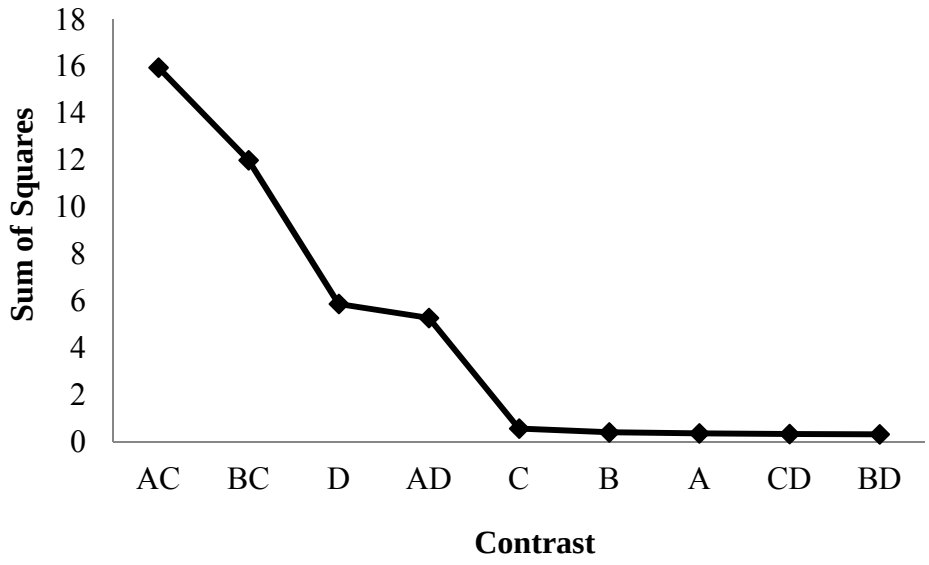

Figure 4.28 - Scree plot for fibre volume fraction V_f

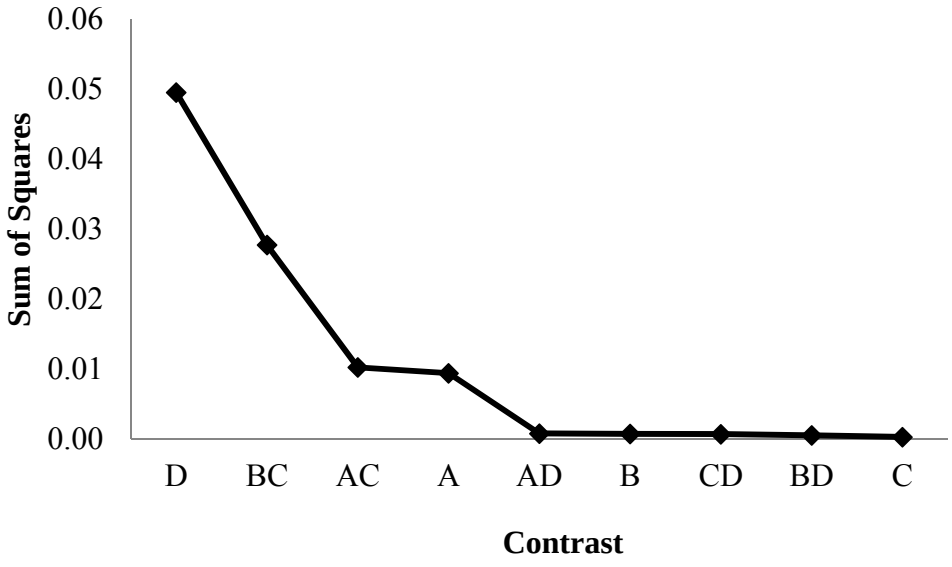

Figure 4.29 - Scree plot for in-plane thermal conductivity k_{cip}

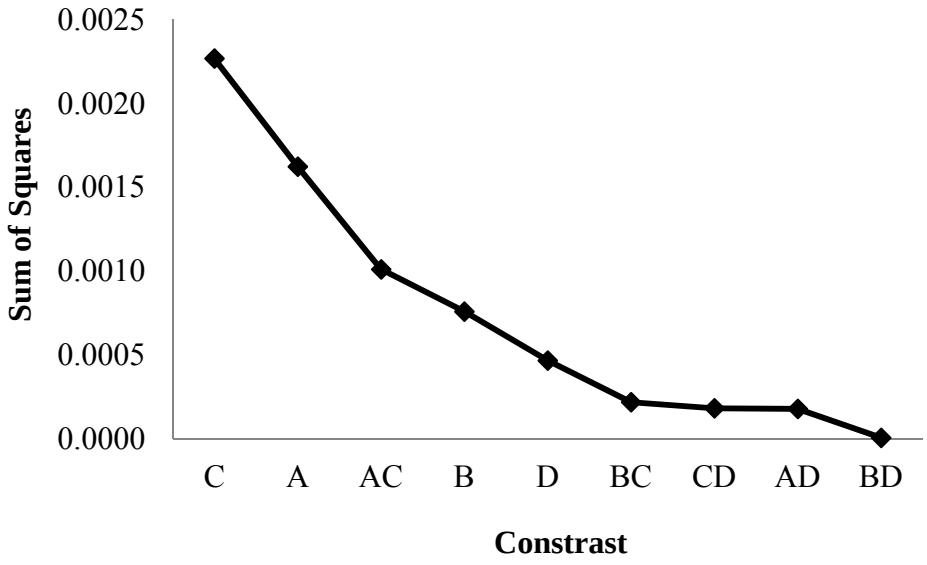

Figure 4.30 - Scree plot for through-thickness thermal conductivity k_{ctt}

Thermal conductivities of the HTS40 carbon fibres, of fabrics consisting of the aforementioned fibres at approximately 55% V_f presented in Chapter 3, and of composites consisting of the aforementioned fabrics at similar V_f values presented in Chapter 4 are summarized and compared in Table 4.17.

Table 4.17 - Summary of thermal conductivities of carbon fibres, fabrics and composites

	In-plane/axial thermal conductivity (W/mK)	Through-thickness/transverse thermal conductivity (W/mK)
Fibre	k_{fa} : 7.95	k_{ft} : 1.36
Fabric	k_{rip} : ≈2.5	k_{rtt} : ≈0.25
Composite	k_{cip} : 2 to 3	k_{ctt} : 0.5 to 0.6

4.2.6 Discussion

The effect of loading MWCNTs on the porosity of composite plates was reported previously in Section 4.2.4.3, where plates P10 (a) and P18 (a) as well as plates P10 (c) and P18 (b) had the same manufacturing parameters except that plate P10 used neat LEO 2376 resin while plate P18 used MWCNT-reinforced resin LEO 2377. Porosity values for plates P18 (a) and (b) were much lower at 1.2% and 0.0% respectively compared with those for plates P10 (a) and (c) at 4.0% and 5.4% respectively, Figures 4.24 and 4.25. This effect was confirmed by the scree plot for porosity, Figure 4.27, where contrast B associated with MWCNT addition was shown to be significant. The multi-scale composites had lower porosities than the neat composites; loading MWCNTs into LEO 2376 and LEO 2396 resins decreased the average porosity of the plates from 2.0% to 0.7%.

This can be explained by the resin bleed during manufacturing. Loading MWCNTs into an epoxy resin increases its viscosity and in turn it affects resin flow during cure; resin bleed is reduced, leaving fewer dry regions. Resin LEO 2396 has a lower viscosity profile than resin LEO 2376, hence it was expected that composite plates manufactured using resin LEO 2396 would yield higher V_v values than those manufactured using resin LEO 2376. Results from plates P12 (a) to (d) fulfilled this expectation: P12 (b) and (d) showed higher porosity values compared with P12 (a) and (c), respectively. Similarly, plates P10 (b) and (d) also showed higher porosity values compared with P10 (a) and (c), respectively.

Contrasts AC and BC represent the joint effect of resin base and fabric architecture and the joint effect of MWCNT addition and fabric architecture respectively on V_f and were shown to be significant, Figure 4.28; hence the effects of resin base and MWCNT addition on V_f depend on the fabric architecture. For non-crimp fabrics, using the 239x resin base and

loading MWCNTs lowers V_f while for twill fabrics, these increase V_f. Hence resin LEO 2376 should be used with fabrics of the non-crimp architecture resin while resin LEO 2397 should be used with fabrics of the twill architecture. No physical explanation can be given for these results at this point, and more plates should be manufactured and characterised to investigate further contrasts AC and BC as well as contrasts D and AD; contrasts D and AD were not shown obviously to be significant by the scree plot for V_f, Figure 4.28, but they could have a minor impact on V_f depending on results from further testing as discussed in Section 4.2.5.

Contrast D was shown to be significant by the scree plot for k_{cip}, Figure 4.29, while the scree plot for k_{ctt}, Figure 4.30 showed that none of the contrasts affected the through-thickness thermal conductivity. Contrast D shows that using fabrics with higher surface densities results in higher in-plane thermal conductivity. This can be explained by the increase in V_f achieved by using fabrics with higher surface densities as shown by contrast D in the scree plot for V_f, Figure 4.28. Similar to contrasts D and AD in Figure 4.28, the significance of contrast BC is also not definitive and more plates should be manufactured and characterised to investigate this contrast further.

Results from Section 4.1 showed that nanocomposites reinforced with MWCNTs at 0.3% by weight demonstrated thermal isotropy and their thermal conductivities were 1% higher than those of the neat epoxy resins, Table 4.5. Results from the Plackett-Burman plates from Section 4.2.5 showed that thermal conductivities of the multi-scale composites manufactured using the same MWCNT-reinforced resins from Section 4.1 were not significantly different from thermal conductivities of the neat composites; the average

thermal conductivity of multi-scale composites was 3% higher than that of the neat composites. Hence the effect of loading MWCNTs at 0.3% by weight is negligible in terms of thermal conductivity enhancements. This generally agrees with studies from the literature, which reported a drop in thermal conductivity of 1% of the carbon fibre-epoxy composite upon a similar MWCNT loading of 0.5% [28].

However, loading MWCNTs may be justifiable through enhancements in mechanical and electrical properties. These aspects are being investigated by other students working on the same CRIAQ COMP 510 project. Also, the average porosity of the multi-scale composites was 68% lower than that of the neat composites; hence loading MWCNTs reduced the porosity of the composite plates significantly. This can improve the mechanical properties of the plates such as tensile strength, impact toughness, inter-laminar shear strength and flexural strength [137], [138].

Table 4.17 shows that thermal conductivities of carbon fibre HTS40 are approximately 5 times higher in the axial and transverse direction compared with the in-plane and through-thickness thermal conductivities of dry carbon fabrics using these fibres, respectively. The in-plane thermal conductivity of dry carbon fabrics and composites manufactured using these fabrics are comparable at similar fibre volume fractions, but the through-thickness thermal conductivities of such composites are 2 to 3 times higher than those of the dry fabrics. Anisotropy ratios for thermal conductivities of the fibre and composites are approximately 5 while the thermal conductivity anisotropy ratio of the dry fabrics is approximately 10. The difference in anisotropy ratios between dry fabrics and composites constituting the same fibres is likely due to the heat diffusion phenomenon in these materials. In dry fabrics, heat diffusion occurs along the fibres in the in-plane direction

and through contact points between adjacent fibres in the through-thickness direction, as shown by results from Chapter 3 of this thesis; hence the thermal anisotropic behaviour of the carbon fibres is amplified in dry fabrics. However, in composites, the presence of the thermally isotropic epoxy between adjacent fibres helps to bridge paths for heat flow; hence the thermal anisotropy behaviour of composites is affected to a lesser extent by that of the constituent fibres compared with dry fabrics.

5 Heat transfer simulations

Thick laminates are increasingly used in aerospace, marine and civil applications. Large curing exotherms in the resin caused by conventional cure cycles combined with the low thermal conductivity of the resin, limiting heat dissipation, may result in a temperature overshoot at the centre of laminate, causing residual thermal stresses and matrix degradation in the most severe cases. Hence modelling heat transfer and cure kinetics is especially important towards ensuring that their temperature distribution remains controlled during manufacturing; knowledge gained from heat transfer simulations provide useful tools for optimisation of the cure cycle towards avoiding the aforementioned issues. Modelling heat transfer is also useful for studying resin infusion during the RFI process, where knowledge of resin viscosity which controls flow requires temperature profiles through the laminate at all times during manufacturing, as obtained from the heat transfer simulations.

Heat transfer models of the RFI process coupled with cure kinetics were found in the literature. However, some of these models were not validated experimentally [30] while others provided temperature predictions only for the top and bottom surfaces of the laminate but not at any location inside [32]. Some of these models [31] investigated the effects of manufacturing parameters such as the convective heat transfer coefficient of the autoclave or oven and heating rates of the cure cycle. However, none of these models investigated specifically the effect of the thermal conductivity of the laminate, or the effect of using a CNT-reinforced resin compared with its neat counterpart on the temperature profiles in the laminate.

Three-dimensional transient heat transfer simulations were performed using FLUENT ANSYS 13.0, a finite volume package through ANSYS Workbench. The model geometry, input parameters and simulation setup in FLUENT are presented in Sections 5.1, 5.2 and 5.3, respectively. The model was validated experimentally and the effects of the laminate thickness, heat transfer coefficient, laminate thermal conductivity, cure kinetics and CNT addition into the resin on the temperature profiles at the top, centre and bottom of the laminate were investigated systematically, Section 5.4. This chapter ends with a discussion of the model and the effects of the various parameters, Section 5.5.

5.1 Model geometry

The geometry of the heat transfer model was taken to be that of the bleed control configuration, Figure 4.12 (b) as simulation results were compared with temperature profiles recorded during manufacturing of PB plates using this configuration. The geometry of the bleed control configuration was simplified to that shown in Figure 5.1. The components were created using DesignModeller in ANSYS Workbench 13.0, Figure 5.2 and dimensions of these parts are shown in Table 5.1 except that for the laminate, which varies between different cases as discussed in detail in the following pages. The ancillary materials covering the side walls of the laminate and components were not present in the geometry of the model; these materials were incorporated with a specified thickness within the boundary conditions of the side walls of the components. For simplicity, certain ancillary layers were combined and created as a single component, namely components 2, 4 and 6 in Figure 5.1. For component 6 which consists of a layer of release film, a layer of perforated release film and 2

layers of bleeders, the effective density and specific heat were calculated using the rule of mixture from those of the individual materials while the effective thermal conductivity was calculated using equivalent thermal circuit analysis.

The asymmetry of the assembly is a result of the physical bleed control configuration and although the tool plate and the release films were created as single components, their faces needed to be split into multiple parts (Figure 5.2) in order for software FLUENT to recognize those faces when importing the geometry, due to the differences in in-plane dimensions between these components and components 3 to 7, Figure 5.1. Studies from the literature showed that the effect of contact resistances on the resulting temperature profiles in similar vacuum bag configurations is negligible [31]; hence contact resistances between components were neglected in this thesis. Temperature profiles at locations L1, L2, L3 and L4 were recorded during simulations, Figure 5.1. Temperature profiles at the bottom surface, centre and top surface of the laminate, indicated by locations L1, L2 and L3 respectively, are especially important for investigating the temperature distribution in the laminate.

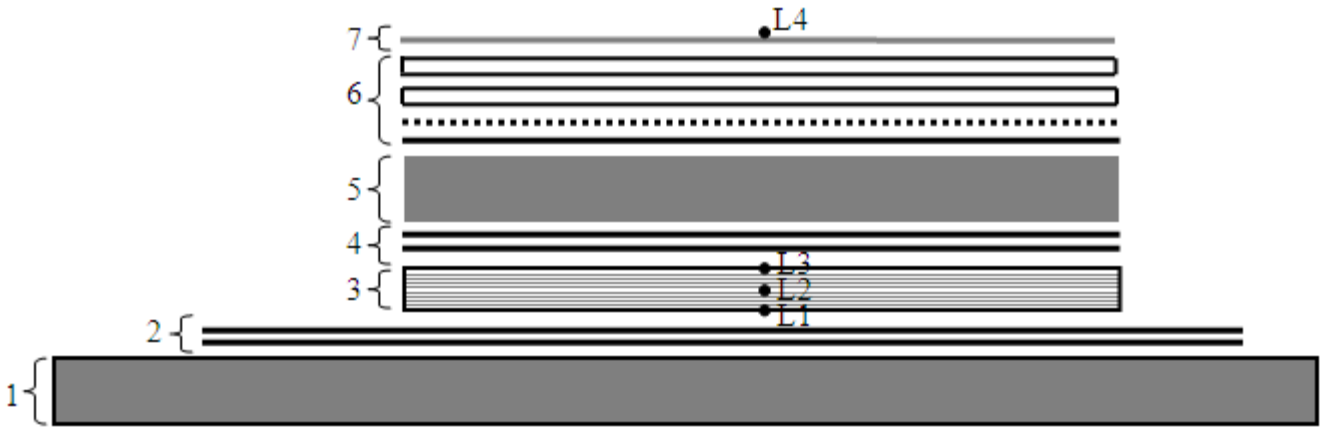

1) Tool plate
2) Release films
3) Fabric and resin laminate
4) Release films
5) Caul plate
6) Perforated release film, release film and bleeders
7) Vacuum bag

Figure 5.1- Simplified geometry of the bleed control configuration

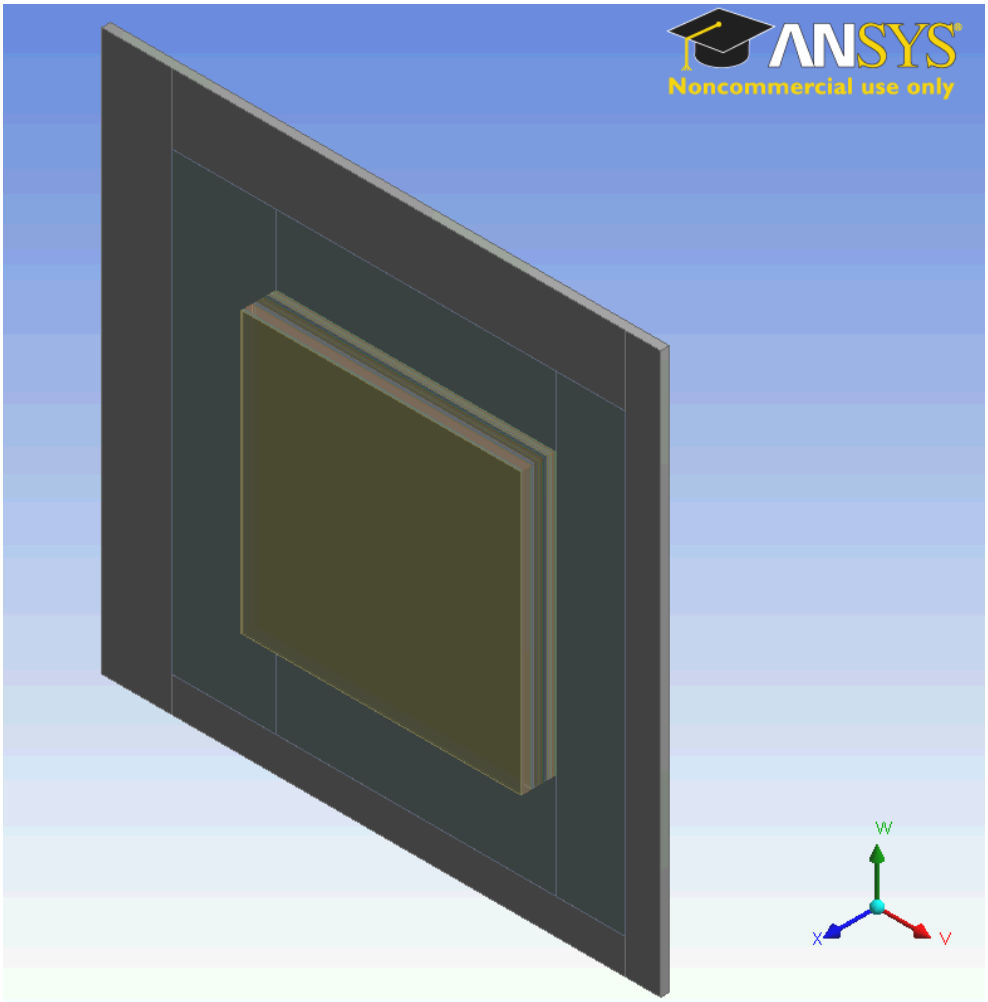

Figure 5.2 - Geometry of model in FLUENT ANSYS

Table 5.1 - Dimensions of model components

Component	Description	Length by width (mm)	Thickness (mm)
1	Tool plate	400x400	6.35
2	2 Release film	330x330	0.05
4	2 Release films	200x200	0.05
5	Caul plate	200x200	6.35
6	Perforated release film + release film + 2 bleeders	200x200	1.35
7	Vacuum bag	200x200	0.05

*Detailed dimensions of the laminate, component 3 are discussed on the following pages.

Simulations were run with two different laminate thicknesses for investigating the effect of laminate thickness on the temperature profiles at locations L1 to L4 during manufacturing; the thicknesses were 4.4 mm and 17.6 mm. The layup sequence for the 4.4 mm laminate is shown in Figure 5.3, corresponding to plate PB11 presented in Section 4.2. Then a laminate 17.6 mm thick, referred to as plate VD, was manufactured for validating the model for thick laminates. Its layup sequence is shown in Figure 5.4. The experimental procedure and manufacturing parameters used for plate VD were the same as those for plate PB11 presented in Section 4.2. Both plates were manufactured with the same LEO 2396 resin and non-crimp fabric F2.

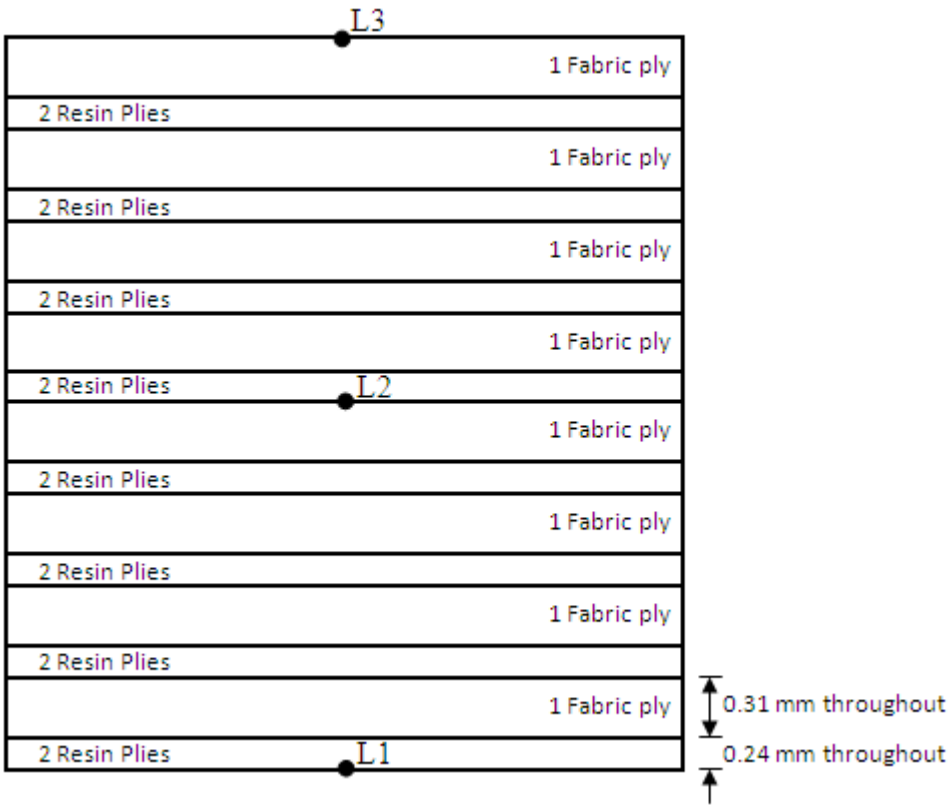

Figure 5.3 - Layup sequence for 4.4 mm laminate: plate PB11

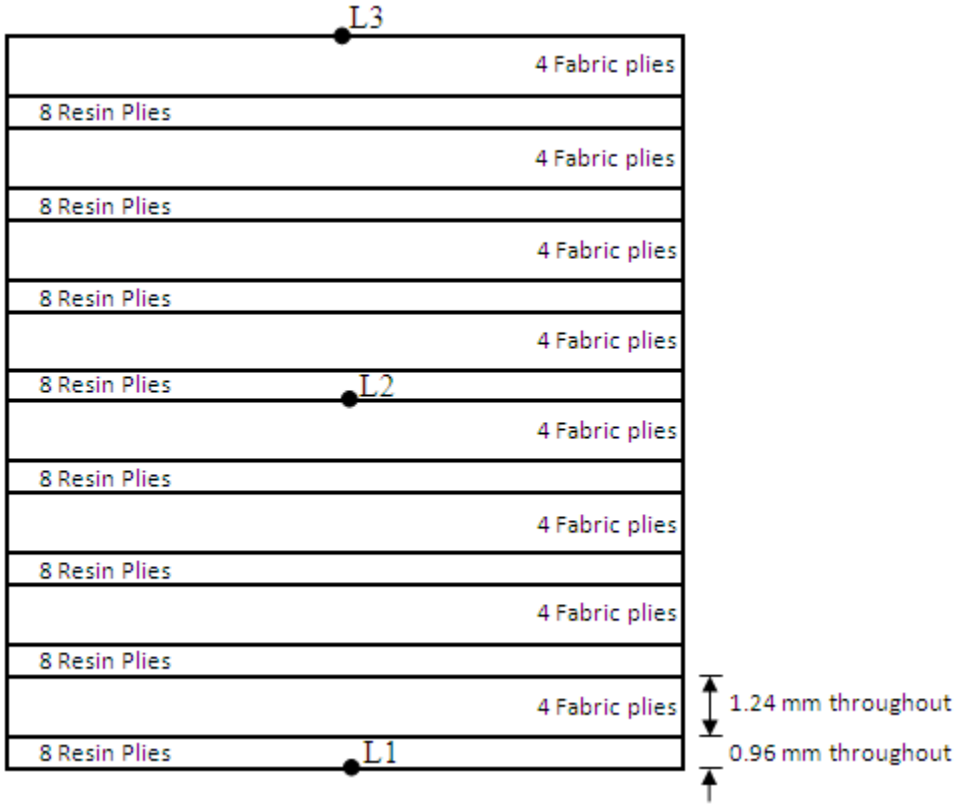

Figure 5.4 - Layup sequence for 17.6 mm laminate: plate VD

In the RFI process, modelling heat transfer and cure kinetics is not separate from modelling resin flow. The cure kinetics model requires temperatures from the heat transfer model while the heat transfer model requires heat generation due to the curing exotherm from the cure kinetics model, as well as changes in geometry during consolidation from the flow model. However, the main focus of this thesis within project CRIAQ COMP 510 project is to investigate the thermal aspects of carbon fibre fabrics and composites, and to develop heat transfer simulations coupled with cure kinetics during the cure cycle; a fluid flow model is currently being developed by Simon Baril-Gosselin, a candidate for the PhD studying infusion in the project. Hence no changes in the geometry of the laminate occur at any point during the simulations presented in this thesis; a constant laminate thickness was used

throughout each simulation. The initial thickness of the vacuum bagged laminate under 0.02 bars of vacuum before consolidation was measured to be 21 mm for plate VD compared with 17.6 mm for the final thickness of the consolidated and cured plate. The final thickness of the laminate was used in all simulations as opposed to the initial thickness; resin flow and consolidation occur during the initial stages of the cure cycle; hence, for most of the cure cycle the laminate thickness is its final thickness after consolidation. Also, cure kinetics are slow during the initial stages of the cure cycle and begin to accelerate at the start of the first dwell, after consolidation has occurred; this further justifies using the final laminate thickness.

Each layer consisting of fabric plies and resin plies seen in Figures 5.3 and 5.4 was created as a separate component in DesignModeller, although they were collectively referred to as component 3 in the previous pages. Dimensions of resin and fabric components are shown in Table 5.2. The geometry was then imported into the Meshing Application in ANSYS Workbench 13.0. The mesh of the entire vacuumed bag assembly consisted of 6820 elements, Figure 5.5 and the element size for each part was 12.5 mm by 12.5 mm by the thickness of the part; the thickest parts were the conductive aluminium caul and tool plates at 6.25 mm while the thinnest part was 0.05 mm, hence one element through the thickness of each part was sufficient. The mesh generated for the ancillary material components consisted of elements with large aspect ratios up to 250; however, temperature profiles were solved from the conservation of energy, which is a second order linear problem and hence should not be affected significantly by aspect ratios of the elements [139]. Also, studies performed for second order elliptical problems [140] and similar second order linear problems such as the advection-diffusion equation [141] showed that the effect of using aspect ratios up to

1000 on solution accuracy was negligible. Type T thermocouples insulated in braided glass were used for recording temperature profiles which were 0.321 mm in diameter. Thermocouples were placed at the same locations L1 to L4 as shown in Figure 5.1 for recording temperature profiles during manufacturing, where the exact locations L1, L2 and L3 in the fabric and resin layup are seen in Figures 5.3 and 5.4 for the 4.4 mm and 17.6 mm laminates, respectively.

Table 5.2 - Dimensions of fabric and resin layers in 4.4 mm and 17.6 mm laminates

Laminate thickness (mm)	Component	Length by width (mm)	Thickness (mm)
4.4	each fabric layer, 1 ply	200x200	0.31
4.4	each resin layer, 2 plies	200x200	0.24
17.6	each fabric layer, 4 plies	200x200	1.24
17.6	each resin layer, 8 plies	200x200	0.96

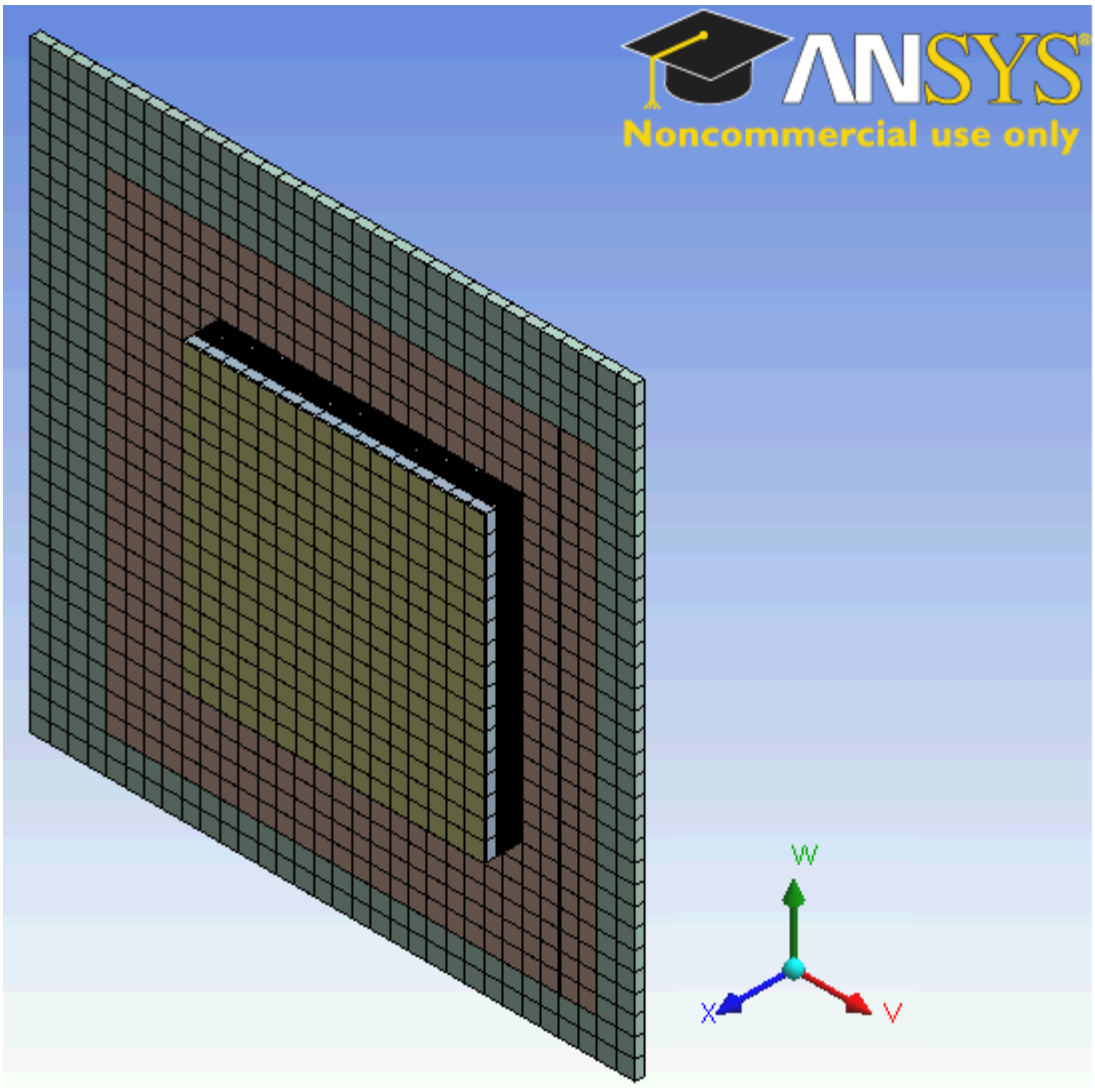

Figure 5.5 - Mesh in FLUENT ANSYS

5.2 Material properties and input parameters

The viscosity profile specified in the LEO resin datasheets showed a window spanning approximately 30 minutes, starting around 30 minutes into the cure cycle, during which the viscosity of the resin is low enough to allow infusion [142]. Hence flow is possible between 30 minutes and 60 minutes into the cure cycle. However, as the simulations do not model flow or changes in geometry as mentioned previously, consolidation was assumed to occur instantaneously for the purposes of heat transfer, which is fairly reasonable when comparing the 30 minute window with the five and half hour cure cycle duration. As the exact nature of flow was not the focus of this thesis and is being studied by others in the project, the exact time at which infusion is complete during the 30 minute window is not known; hence consolidation was assumed to occur at the end of said window where flow is known to have ceased, at 60 minutes into the cure cycle.

Before consolidation occurs, the laminate consists of intercalated layers of fabric and resin, Figure 5.6 (a). As the assembly is heated under the application of vacuum, the viscosity of the resin is reduced and the resin infuses into the fabric. The empty spaces present in the fabric layers before consolidation are then replaced with resin, and the laminate becomes a composite consisting of carbon fibres and resin, as shown by an equivalent representation in Figure 5.6 (b). However, since simulations do not account for flow and hence must maintain the same geometry of the intercalated laminate throughout the simulation, material properties must be assigned to the fabric and resin layers before and after consolidation in a manner as to account for this change in geometry; material properties change at 60 minutes into the cure cycle. Material properties of the fabric and resin layers before consolidation as well as those of the fibre and resin layers after consolidation are discussed in detail in the following pages

for modelling heat transfer during the manufacturing of plate PB11 at a thickness of 4.4 mm. Properties used for modelling heat transfer during the manufacturing of plate VD at a thickness of 17.6 mm were assumed to be the same as those for the 4.4 mm laminate as it was simply a repeat of PB11 at 4 times the thickness. Properties of the aluminium tool and caul plates were taken from the ANSYS material library whilst those of the ancillary materials were taken from their material datasheets [134], [135], [143].

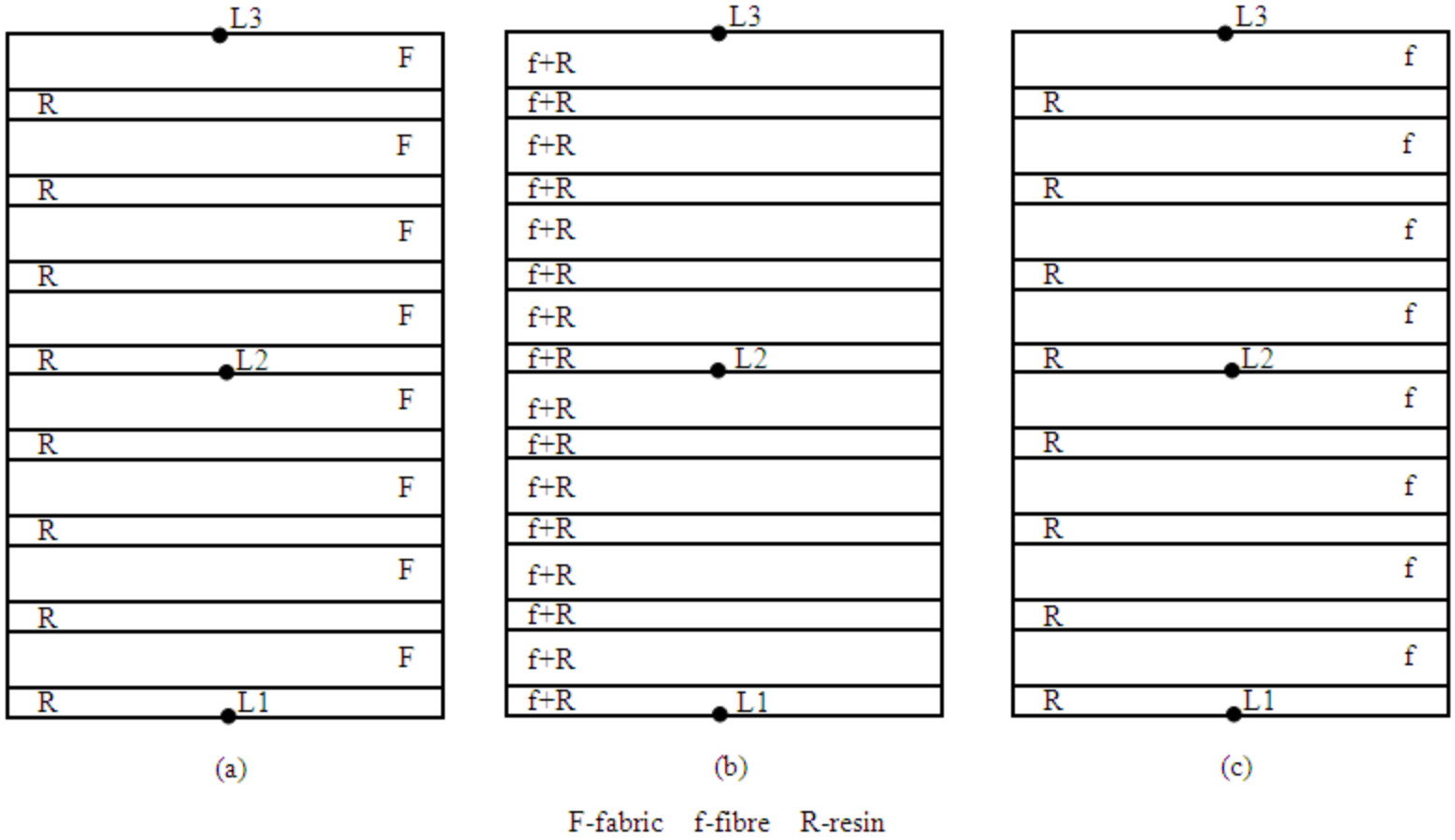

Figure 5.6 - (a) Laminate before consolidation (b) laminate after consolidation and (c) equivalent representation of laminate after consolidation in terms of density and specific heat

Before consolidation, material properties of the dry fabric layers in the laminate were taken to be those of the dry carbon fibre fabric F2. Thermal conductivity of the dry fabric was taken from measured values presented in Chapter 3 at a V_f of 57% based on the V_f of plate PB11, Section 4.2. Values for the density and specific heat of the fabric were taken to be 57% of the values for the HTS40 carbon fibre [52].

Material properties of the resin were taken to be those of resin LEO 2396, where the density and thermal conductivity measured and presented in Section 4.1 were used. The heat generation term in the law of conservation of energy, Equation 2.32, was obtained from the Kamal-Sourour cure kinetics model, Equations 2.27 to 2.29. Nicholas Krumenacker, a candidate for the PhD at McGill University and colleague in this project, was responsible for studying resin cure kinetics; parameter fittings for the Kamal-Sourour model were performed by Nicholas. Parameters are provided as raw values as supplied by McGill in Table 5.3.

Isothermal DSC tests on the LEO 2396 and LEO 2397 resins were conducted at 130°C, 150°C, 170°C, 180°C and 200°C followed by a heat ramp of 2°C. The degree of the cure and temperature were plotted as a function of time, leading to curves for LEO 2396 and LEO 2397 resins that were not remarkably different, Figure 5.7. Results in the literature [113] showed that loading MWCNTs at 1% by weight only induced a slight acceleration of cure; hence resin LEO 2397, which consists of resin LEO 2396 loaded with MWCNTs at 0.3% showed only a slightly higher degree of cure compared with the neat LEO 2396 resin at a given time.

Table 5.3 – Raw values for fitted parameters for Kamal-Sourour model

Parameter	LEO 2396	LEO 2397
A_1 (1/s)	410033	350168
E_1 (J/mol)	77793	127454
m_1	0.00	0.00
n_1	18.87	61.86
A_2 (1/s)	264148	108105
E_2 (J/mol)	67520	66000
m_2	0.51	0.26
n_2	2.71	2.10
a	8.19	10.7
b	-1.19	-1.09
c (1/K)	0.005	0.005
Q_{RT} (J/g)	432.7	409.3

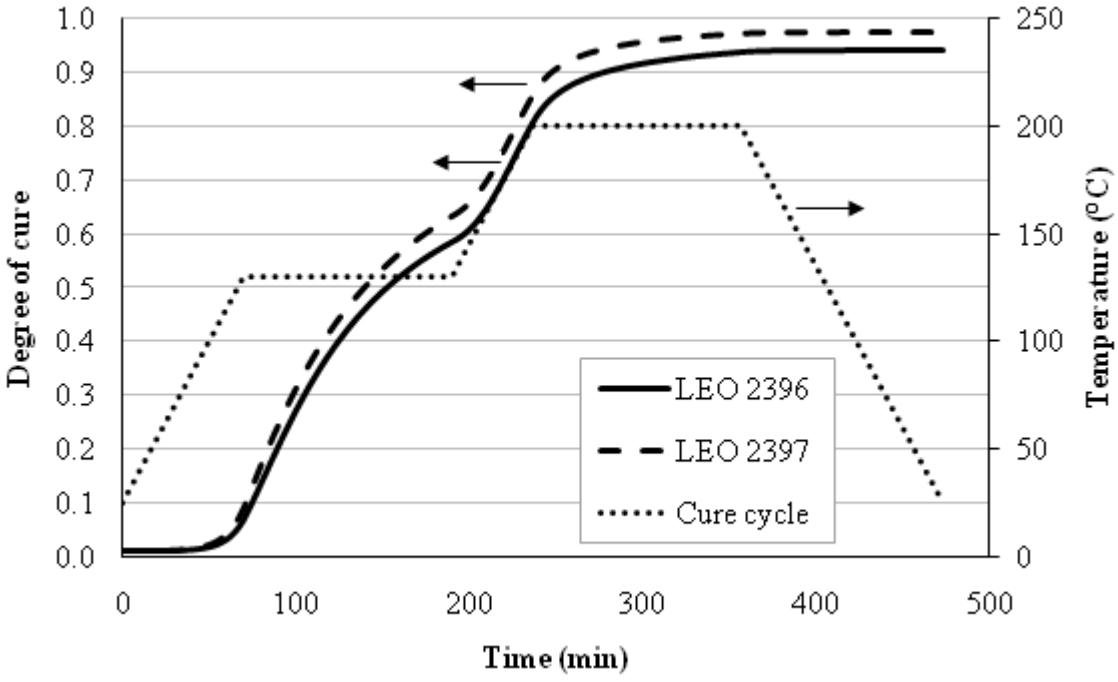

Figure 5.7 - Degree of cure and temperature as a function of time

The specific heat of the resin as a function of temperature was obtained through MDSC analysis. Samples were sent to the Canadian Construction Materials Centre at the National Research Council (NRC), Ottawa. MDSC was conducted with a modulation amplitude and frequency of 0.5°C and 80 seconds respectively on a 7.75 mg sample of uncured LEO 2396 resin film. The sample was subjected to the standard Axson cure cycle: ramp at 2°C/min up to 130°C, isothermal hold for two hours then another ramp at 2°C/min up to 200°C followed by an isothermal hold for two hours. Results showed that the specific heat varied linearly as a function of temperature, Figure 5.8; values were extrapolated over the temperature range from 25°C to 200°C, at 2200 J/kgK and 2600 J/kgK respectively, and inputted as material properties of the resin for simulations.

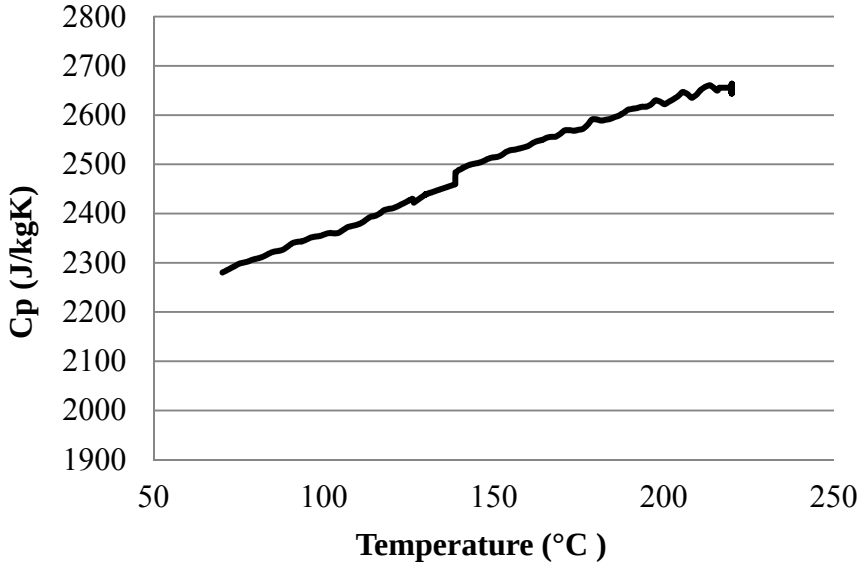

Figure 5.8 - Specific heat of resin LEO 2396 as a function of temperature

After consolidation has occurred, the composite laminate can be represented by an equivalent arrangement as shown in Figure 5.6 (b). The spaces present in the fabric layers

before consolidation are replaced with resin, and the laminate becomes a composite consisting of carbon fibres and resin. Hence material properties of the composite should be assigned to all layers in the geometry, Figure 5.6 (b). Thermal conductivity for all layers in the model were assigned as that measured for the composite plate PB11, which had a V_f value of 57%. Density ρ and specific heat C_p values for all layers should ideally have been assigned as those of the composite, calculated using the rule of mixture at 57% V_f. However, this could not be done due to software limitations in FLUENT; FLUENT allows for density and specific heat assignments as a function of time through a user-defined function (UDF) for one material only, hence values of ρ and C_p could not be assigned as mentioned above for both the fabric and the resin layers in Figure 5.6 (a) after consolidation.

Therefore, rather than assigning ρ and C_p values as those of the composite, the geometry was kept as separate fibre and resin layers with their respective ρ and C_p values, Figure 5.6 (c). This arrangement is equivalent to Figure 5.6 (b) for the purposes of monitoring temperatures at locations L1, L2 and L3 as indicated in Figures 5.3 and 5.4, as the density and specific heat of a composite material are the weighted average of densities and specific heat capacities of its constituents regardless of their physical arrangement. This arrangement poses a limitation on the simulations: temperatures can be monitored at interfaces between fibre and resin layers as shown in Figure 5.9 but temperatures at locations inside fibre and resin layers cannot be predicted accurately by the simulations. However, as previously mentioned, the most important locations for studying temperature distribution in the laminate are the top, centre and bottom of the laminate. This is supported by simulations and heat transfer models found in the literature, Section 2.4 which monitor temperatures at

said locations only, hence this limitation is of little importance for studying the temperature distribution in the laminate. Material properties for all components are summarised and presented in Table 5.4.

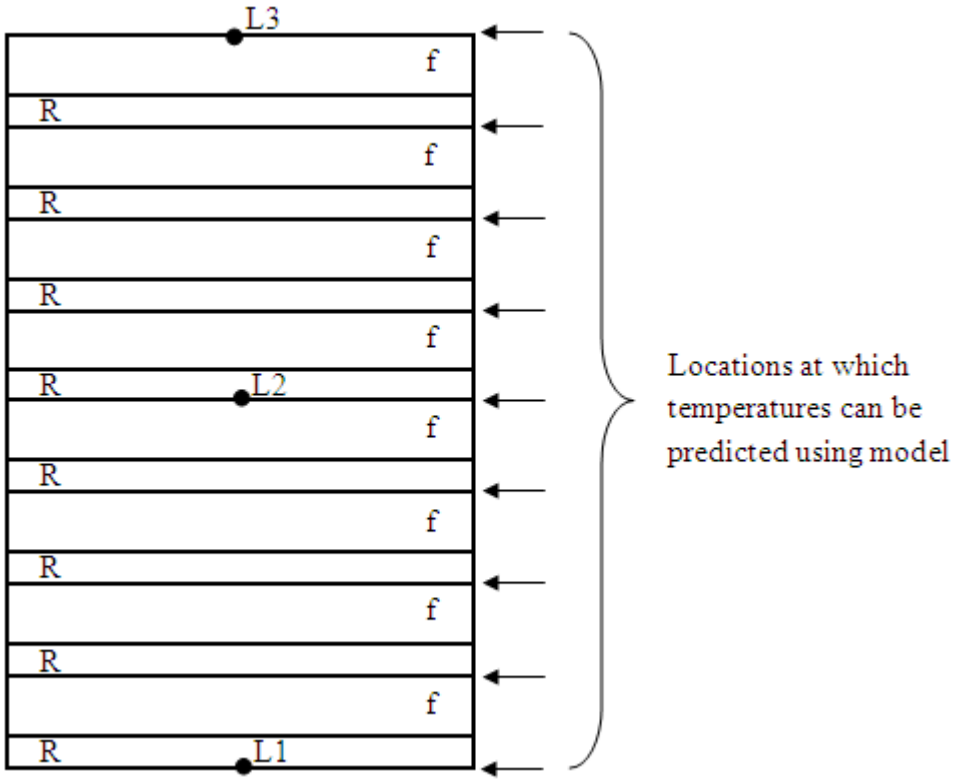

Figure 5.9 – Locations at which temperatures can be predicted using model

Table 5.4- Material properties

Component	Description	Density (kg/m^3)	Specific heat (J/kgK)	In-plane/through-thickness thermal conductivity (W/mK)
1	Tool plate	2719	871	202
2	2 Release films	1730	1900	0.25
3	Fabric (before consolidation)	971	391	2.188/0.182
3	Fibre (after consolidation)	710	1770	2.188/0.5
3	Resin (before consolidation)	1150	2200-2600*	0.2
3	Resin (after consolidation)	1150	2200-2600*	0.5
4	2 Release films	1730	1900	0.25
5	Caul plate	2719	871	202
6	Perforated release film + release film + 2 bleeders	314.4	626-745*	0.0104
7	Vacuum bag	1130	1500-2400*	0.24

*Specific heat capacities vary linearly as a function of temperature from 25°C to 200°

The heat transfer coefficient h in the convection oven was obtained by matching simulation results to experimental temperature profiles of a single aluminium plate. The tool plate used for manufacturing composites was placed in the oven and subjected to the standard Axson cure cycle. Temperatures were recorded by two thermocouples taped to the centre of the plate, one on the top surface and one on the bottom surface. Temperature profiles were monitored in LabView for several minutes to ensure adequate contact between the thermocouples and the aluminium. Simulations were run in FLUENT where the geometry consisted of the tool plate; an initial h value of 20 W/m^2K was estimated and set for the convective boundary conditions for all surfaces of the plate. Temperature profiles at the locations of the thermocouples were predicted and were found to be higher than experimental values. An h value of 15 W/m^2K was then used and model predictions matched the measured temperature profiles. Hence the heat transfer coefficient for all simulations was set as 15 W/m^2K unless otherwise specified. A constant h value was assumed for the simulations; in reality, it is a complex distribution inside the autoclave or oven.

5.3 Simulation setup

Three-dimensional transient heat transfer simulations were performed using FLUENT ANSYS 13.0. The solver was set to transient mode and the meshed geometry was imported from the ANSYS Meshing Application. All walls shared between two neighbouring parts were imported as a coupled wall with the same temperatures. Convective boundary conditions with a heat transfer coefficient of 15 W/m^2K were set for all surfaces of the assembly exposed to air in the oven. The temperature in the oven was monitored by a single thermocouple in the air at the lower corner of the oven which provided feedback control for the temperature profile of the oven following the standard Axson cure cycle specified in Section 5.2 was followed; the temperature as a function of time was coded in C and imported into FLUENT as a profile user-defined function (UDF), Appendix D. Material properties of the fabric and resin layers were set to values presented in Table 5.4 as a function of time using UDFs, Appendix D.

The quadratic upwind differencing scheme was used for the solver. Temperature monitors were set at locations L1 to L4 as shown in Figures 5.1, 5.3 and 5.4 in the simulations and temperature profiles predicted at each location were recorded at four minute intervals during the cure cycle; recording temperatures every four minutes provided enough points for plotting temperature profiles during a five and half hour cure cycle whilst writing temperature values into an output file at more frequent intervals would lengthen the computational time. All temperatures were initialized to 25°C and a fixed time step of 1 second was used for simulations unless otherwise specified for a total of 19650 time steps during the cure cycle. Convergence was monitored using the default scaled energy residual of 10^{-6}. Cure kinetics of the resin were imported into FLUENT as a source term through a UDF,

Appendix D. The heat generation was calculated using the Kamal-Sourour model and the cumulative heat of reaction was incremented at the end of each time step using a UDF, Appendix D. Cure kinetics can be switched off in the setup by disabling the source term under the cell zone conditions. The solution procedure is shown in Figure 5.10.

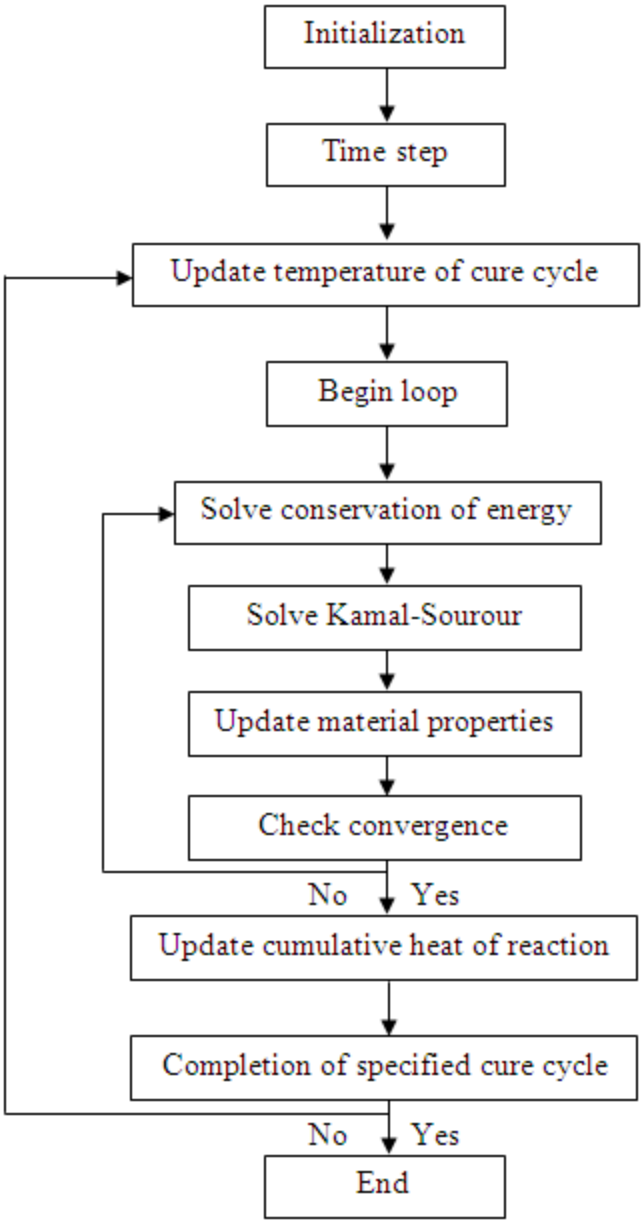

Figure 5.10- Solution procedure in FLUENT ANSYS

5.4 Results, experimental validation and discussion

Eleven heat transfer simulations (SimHT) were run, Table 5.5. The laminate thickness, convective heat transfer coefficient, laminate thermal conductivity and cure kinetics were changed between cases for determining the effects of these parameters on temperature profiles at locations L1 to L4, Figure 5.1 and comparisons were made between various cases, Table 5.6. Results from cases SimHT1, Figure 5.11 and SimHT2, Figure 5.12 were used for validating the model for laminate thicknesses of 4.4 mm and 17.6 mm, respectively. Results from SimHT1 and SimHT2 were compared with temperatures at locations L1, L2, L3 and L4 measured during the manufacturing of plate PB11, Figures 5.13 to 5.16 and plate VD, Figures 5.17 to 5.20, respectively. The temperatures measured experimentally were taken at 20 second intervals using data acquisition through LabView; hence the measured data was shown in the form of a continuous line as opposed to discrete data points for reading. Results and comparisons made between different cases are shown in Figures 5.21 to 5.56. Thermal conductivities of the laminate before and after consolidation for cases SimHT1 to SimHT5, SimHT10 and SimHT11 were used as specified in Table 5.4, referred to as the original parameters (OP) while thermal conductivities for cases SimHT6 to SimHT9 were constant with time.

Table 5.5 - Summary of simulations

Case	Laminate thickness (mm)	Heat transfer coefficient (W/m^2K)	Thermal conductivities of laminate (W/mK)	Cure	Resin
SimHT1	4.4	15	OP	enabled	LEO 2396
SimHT2	17.6	15	OP	enabled	LEO 2396
SimHT3	4.4	15	OP	disabled	LEO 2396
SimHT4	17.6	15	OP	disabled	LEO 2396
SimHT5	17.6	15	OP	enabled	LEO 2397
SimHT6	4.4	15	0.2	enabled	LEO 2396
SimHT7	4.4	15	0.1	enabled	LEO 2396
SimHT8	17.6	15	0.2	enabled	LEO 2396
SimHT9	17.6	15	0.1	enabled	LEO 2396
SimHT10	4.4	5	OP	enabled	LEO 2396
SimHT11	17.6	5	OP	enabled	LEO 2396

Table 5.6 - Comparisons between simulations

Comparison	Comparison between cases	Effect
C1	SimHT1 and SimHT2	laminate thickness
C2	SimHT1 and SimHT3	cure
C3	SimHT2 and SimHT4	cure
C4	SimHT2 and SimHT5	MWCNT addition in resin
C5	SimHT6 and SimHT7	laminate thermal conductivity
C6	SimHT8 and SimHT9	laminate thermal conductivity
C7	SimHT1 and SimHT10	heat transfer coefficient
C8	SimHT2 and SimHT11	heat transfer coefficient

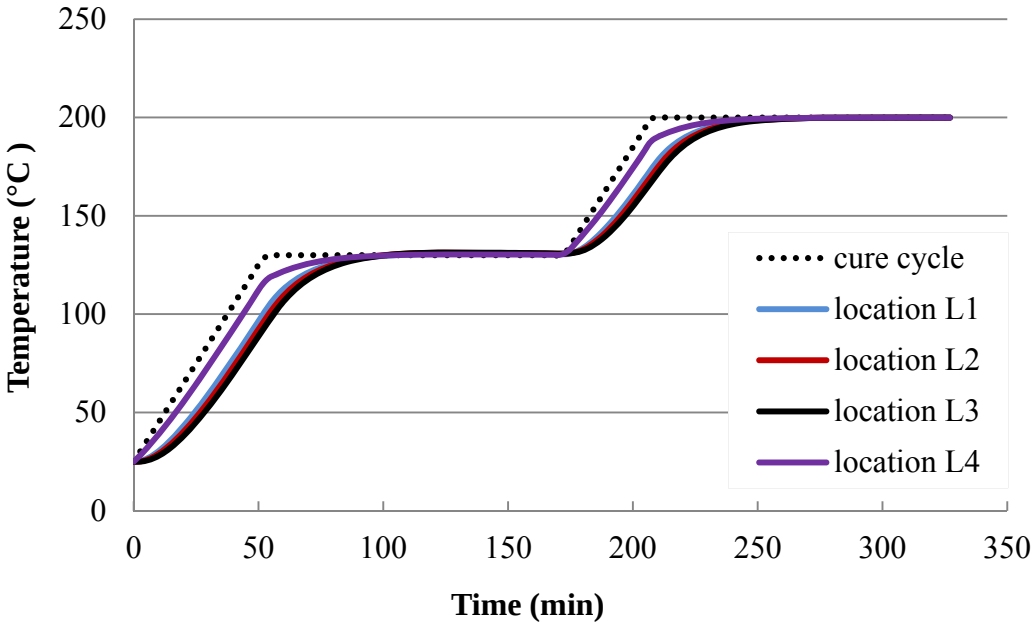

Figure 5.11 - Temperature profiles from SimHT1

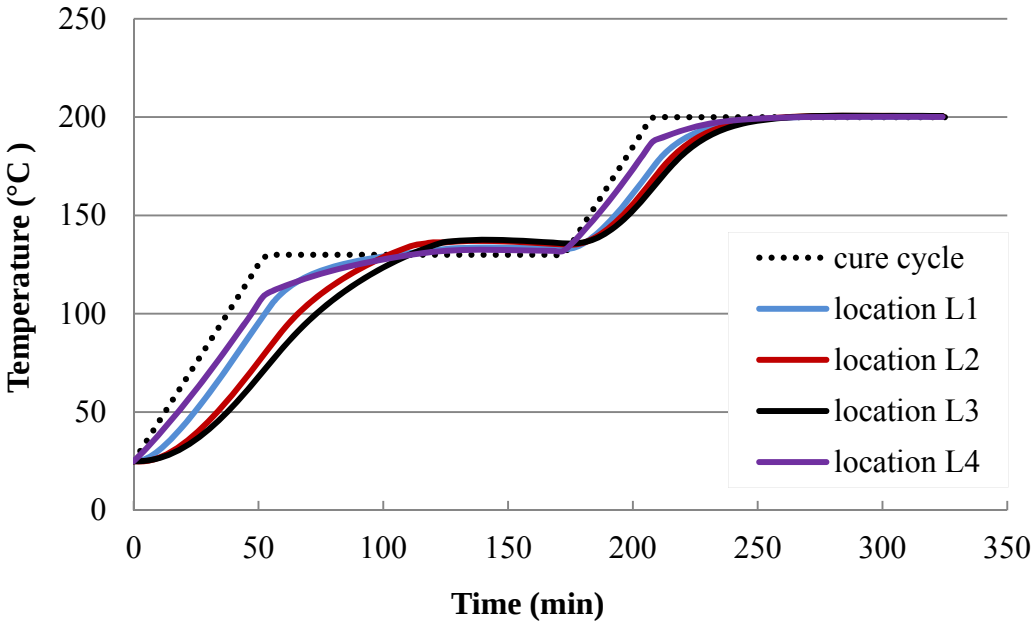

Figure 5.12 - Temperature profiles from SimHT2

Simulation temperature profiles for the 4.4 mm and 17.6 mm thick laminates showed that the thermal lag of temperature profiles at all locations compared with the cure cycle increased during the first heating ramp, Figures 5.11 and 5.12. Thermal lag continued for another 50 minutes into the first dwell, during which temperatures of all components approached the specified temperature plateau of the cure cycle at 130°C. Then for the rest of the first dwell from 100 minutes to 180 minutes, temperature profiles for the 4.4 mm laminate at all locations were maintained at 130°C. However, for the 17.6 mm laminate, temperatures at the centre of the laminate reached 137°C for the rest of the first dwell, which can be explained by the exotherm released due to resin cure. This difference in behaviour between the 4.4 mm and 17.6 mm laminates suggests that the effect of cure kinetics on the temperature profiles at the centre of the laminate varies with laminate thickness. The maximum temperature differences were 8°C and 28°C for SimHT1 and SimHT2, respectively. Temperatures during the second ramp and dwell behaved in a similar manner as those during the first ramp and dwell described above.

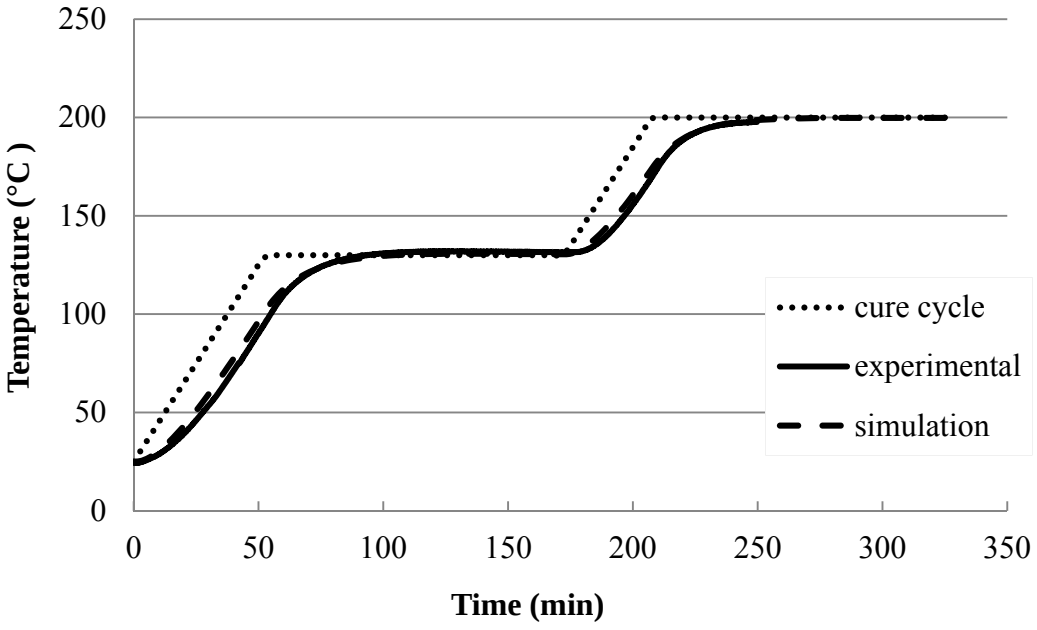

Figure 5.13 - Experimental validation of SimHT1: location L1

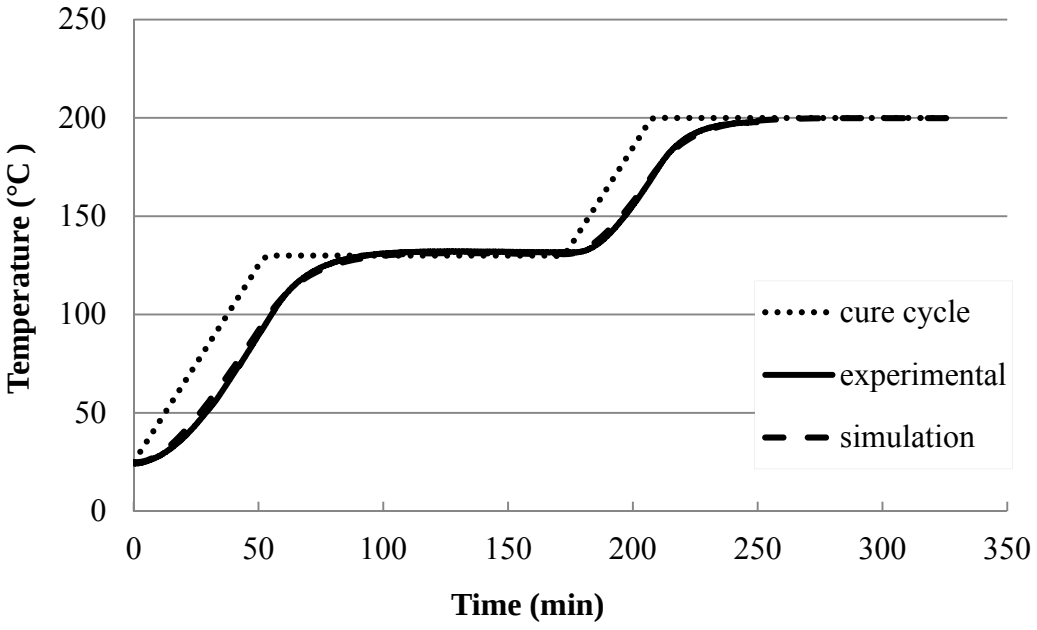

Figure 5.14 - Experimental validation of SimHT1: location L2

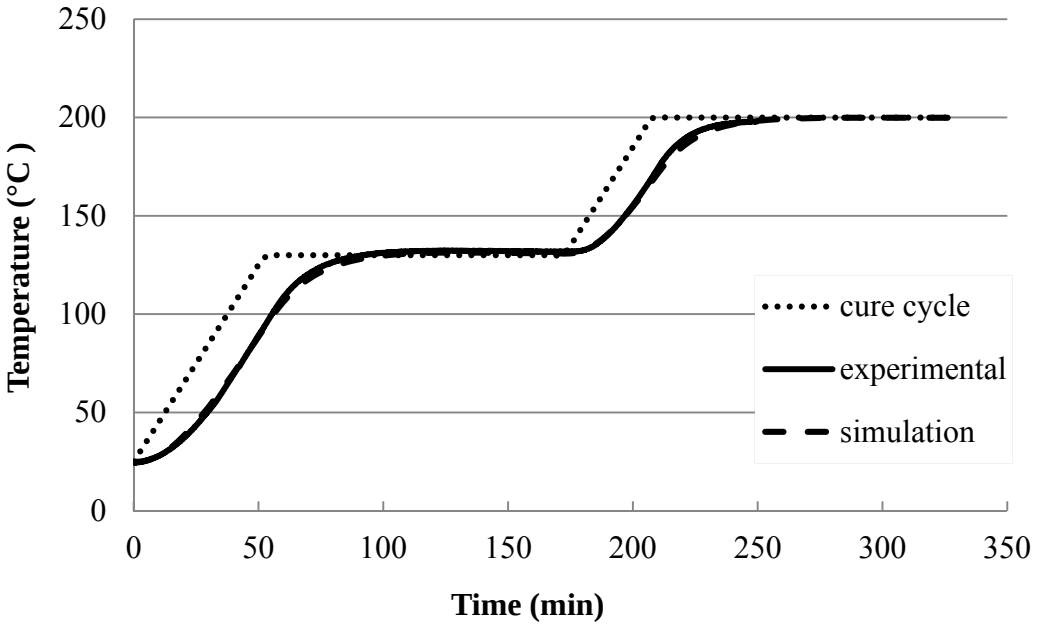

Figure 5.15 - Experimental validation of SimHT1: location L3

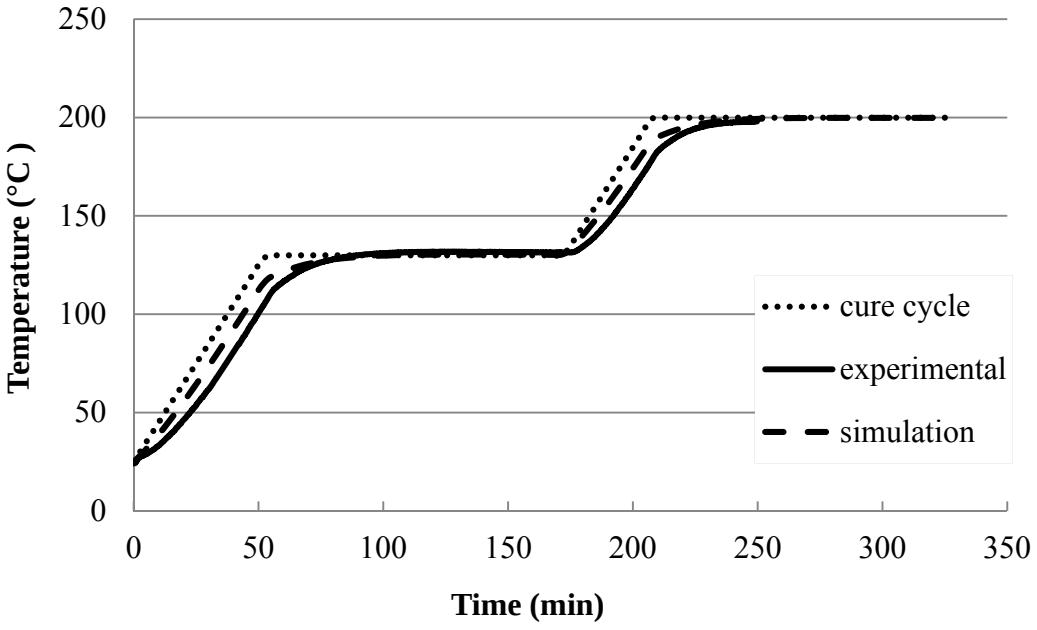

Figure 5.16 - Experimental validation of SimHT1: location L4

The model was validated experimentally for the 4.4 mm thick laminate; temperature profiles at locations L1 to L4 predicted by simulations were generally in very good agreement with temperatures measured during the manufacturing of plate PB11, Figures 5.13 to 5.16. Measured temperatures at locations L2 and L3 matched those predicted by SimHT1 whilst measured temperatures at locations L1 and L4 were slightly lower than those predicted by SimHT1; experimental curves lag behind temperature curves predicted by simulations at locations L1 and L4. As temperatures near the surfaces of the vacuum bag assembly are influenced primarily by conditions of the ambient air in the oven and less significantly by properties or characteristics of the laminate, this indicates a slight mismatch of the oven air conditions between experiment and simulations, such as the temperature profile of the cure cycle or the convective heat transfer coefficient of the oven h. A possible source of error could be that the temperature profile of the cure cycle inside the oven lagged behind that specified in the simulations due to the slow heating during the initial warm-up of the oven. Also, the distribution of the heat transfer coefficient inside an autoclave or a convection oven is complex and not constant with location [144]. For instance, heat is forced into the oven by a fan located above the vacuum bag assembly, hence h of the air under the vacuum bag assembly is likely lower than that of the air above the assembly even though convection occurs from all directions. However, in the simulations, h was assumed to be constant at all locations inside the oven and a value of 15 W/m^2K was assigned for all convective boundary conditions. This accounts for the higher temperature profile at location L4 predicted by the simulation compared with the measured temperature profile. Another possible source of error is that the thermocouples were taped down to locations L1 to L4 for measurements using a thick, high temperature tape which may lower experimental temperature readings.

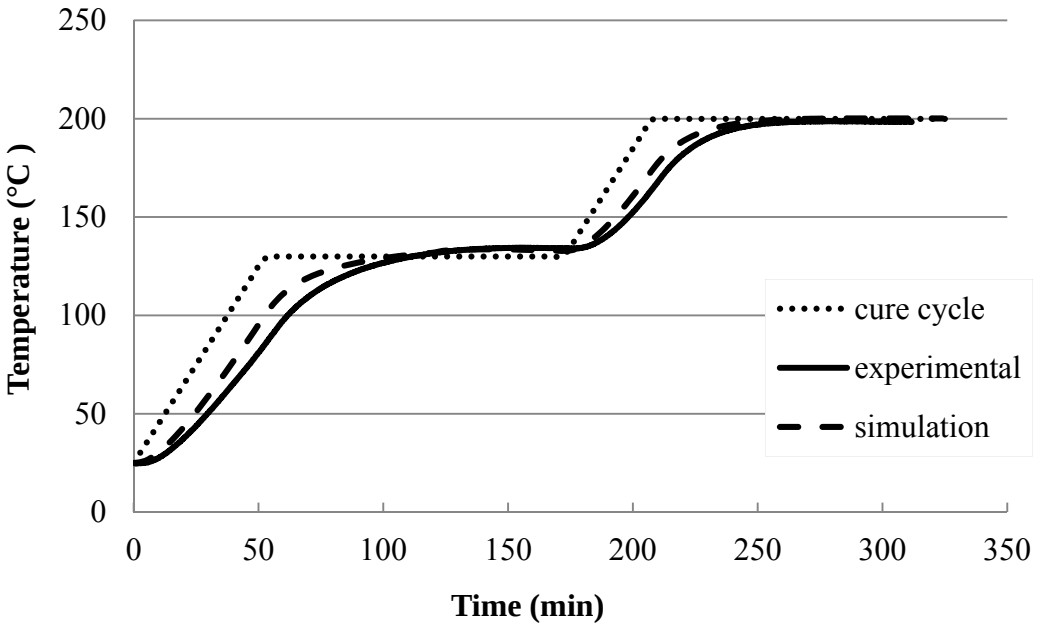

Figure 5.17 - Experimental validation of SimHT2: location L1

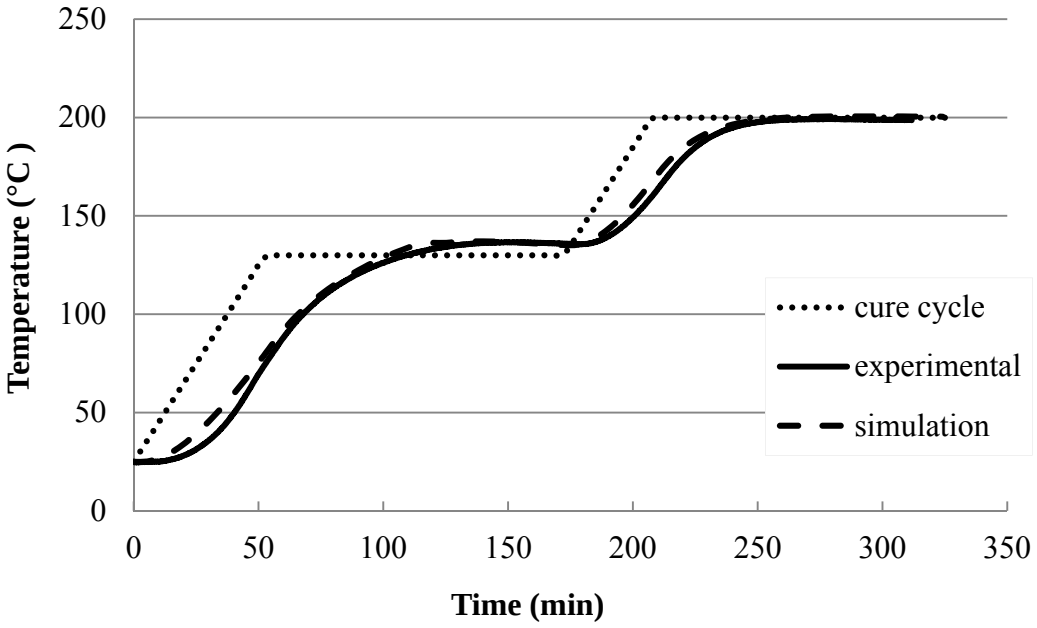

Figure 5.18 - Experimental validation of SimHT2: location L2

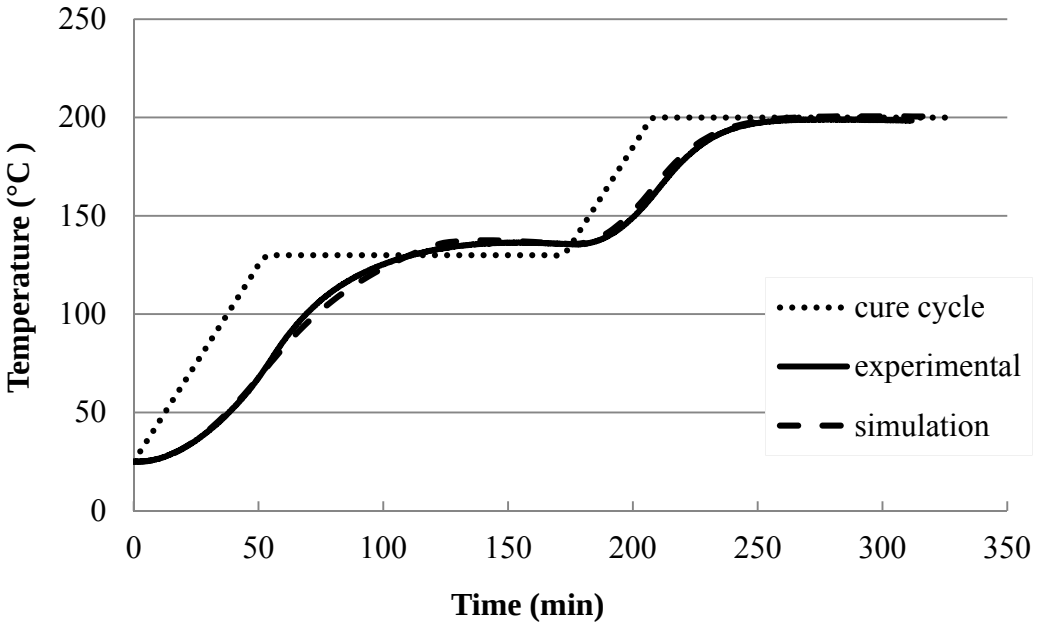

Figure 5.19 - Experimental validation of SimHT2: location L3

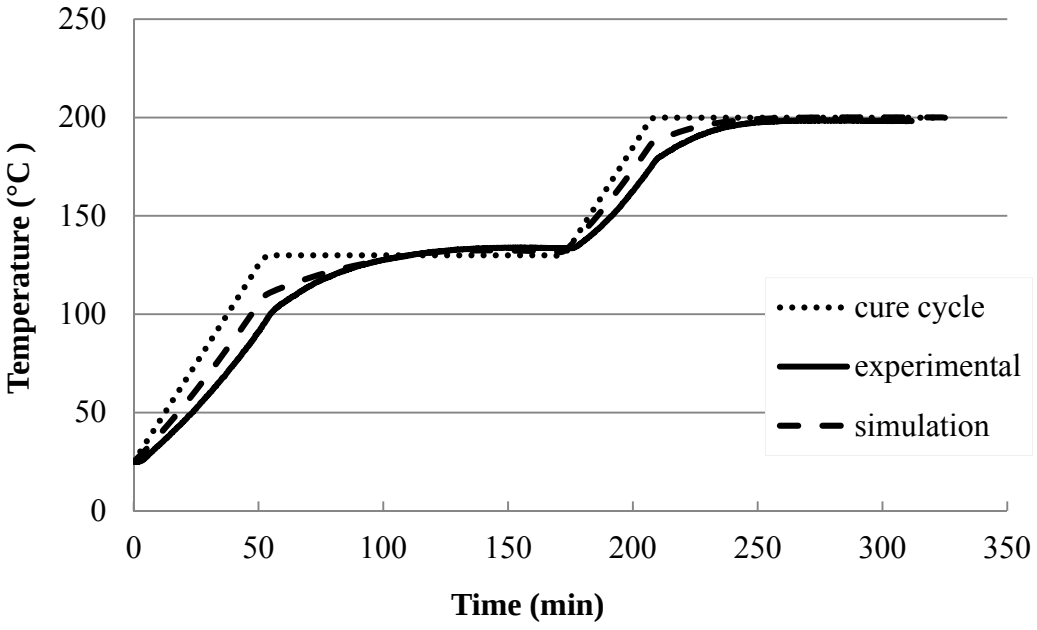

Figure 5.20 - Experimental validation of SimHT2: location L4

The model was also validated experimentally for the 17.6 mm thick laminate; temperature profiles at locations L1 to L4 predicted by simulations were generally in good agreement with temperatures measured during the manufacturing of plate VD, Figures 5.17 to 5.20. Similar to Figures 5.13 to 5.16, experimental temperatures measured at locations L2 and L3 matched those predicted by SimHT2 closely whilst experimental temperatures measured at locations L1 and L4 were slightly lower than those predicted by SimHT2; experimental curves lagged behind temperature curves predicted by simulations at locations L1 and L4 with possible sources of error as mentioned previously. Overall, Figures 5.13 to 5.20 showed that the heat transfer and resin cure phenomena during RFI manufacturing can be predicted successfully using the model developed in thesis.

Convergence was tested by repeating SimHT2 using time steps of 0.5 seconds and 0.25 seconds. These chosen time steps were not smaller than the original 1 second time step by orders of magnitude, due to the computational power and time required; one simulation with a fixed time step of 0.25 seconds takes approximately 10 hours to run. Results showed scant differences between SimHT2 using the 3 time steps, Figures 5.21 to 5.24. Hence a time step of 1 second was used for all simulations reported in this chapter.

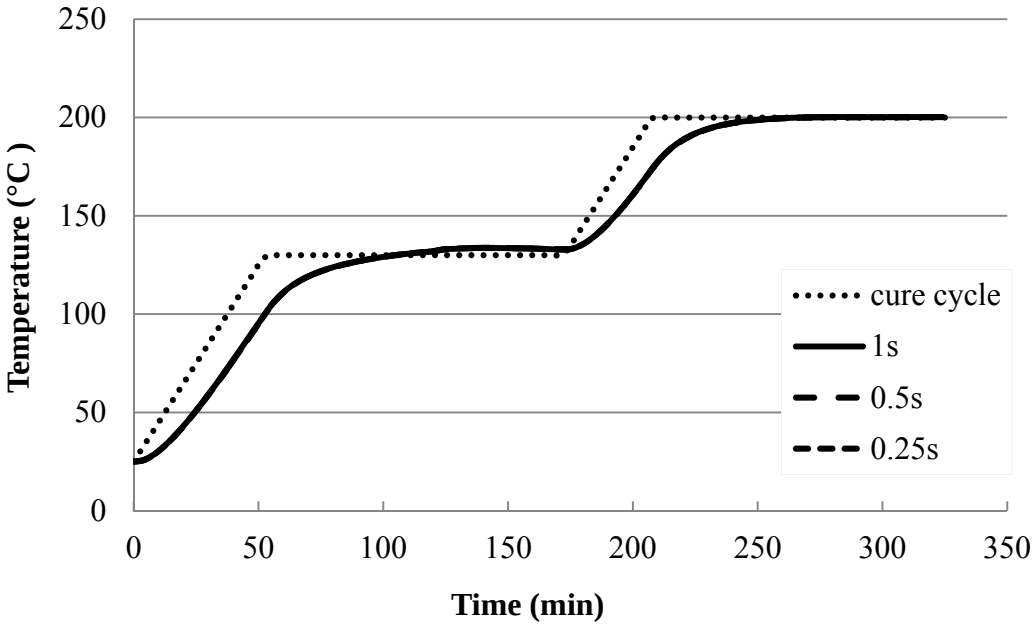

Figure 5.21 - Convergence of SimHT2: location L1

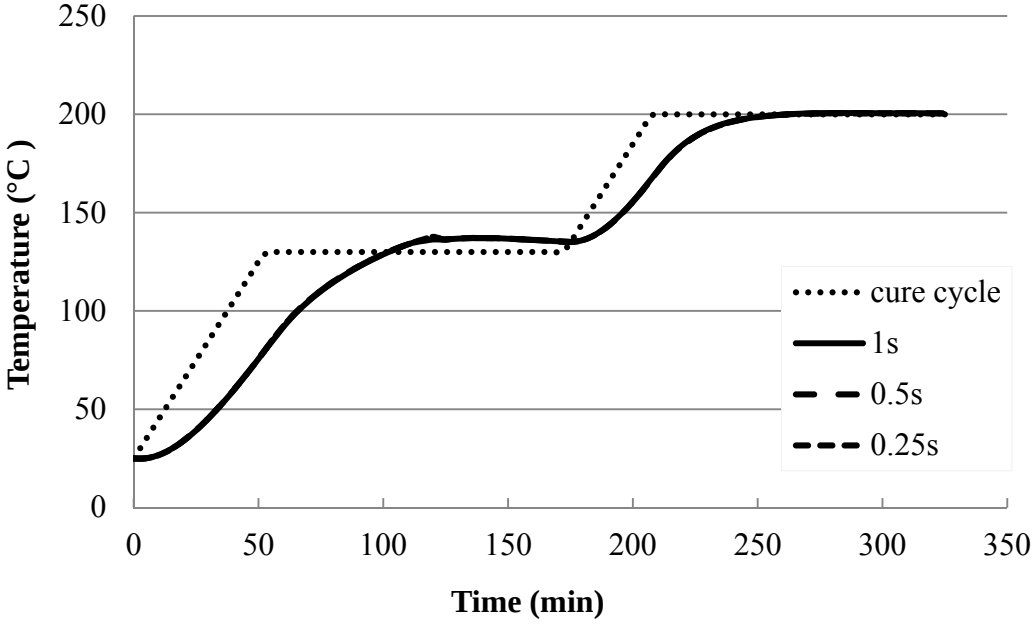

Figure 5.22 - Convergence of SimHT2: location L2

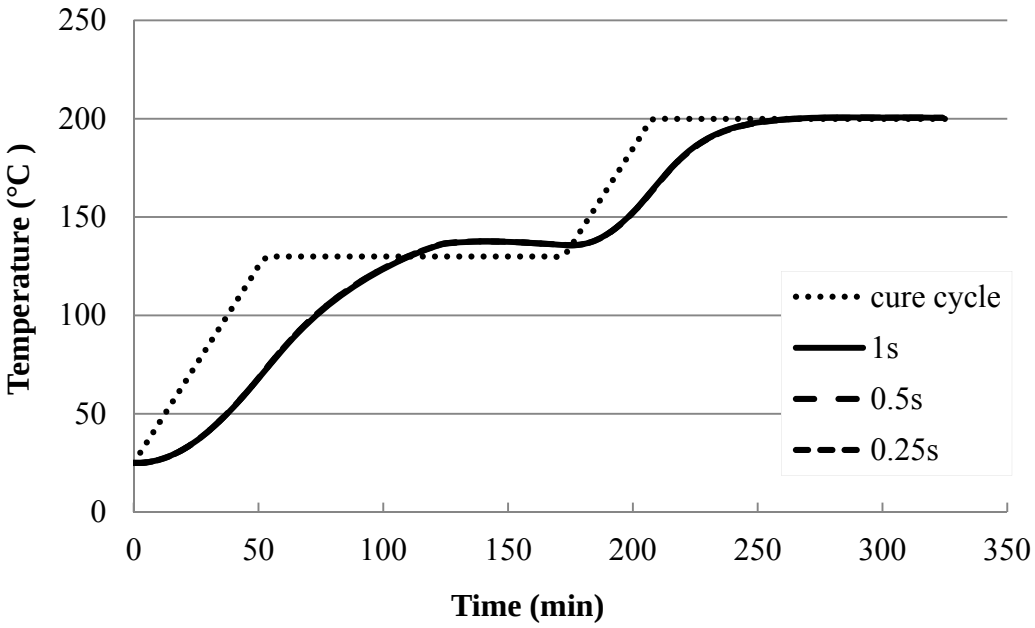

Figure 5.23 – Convergence of SimHT2: location L3

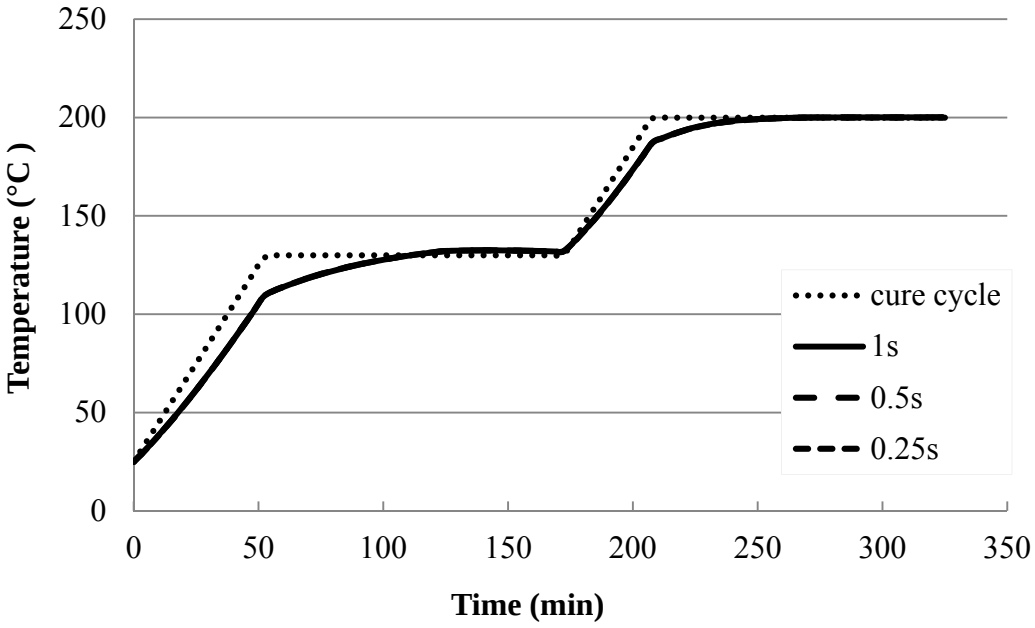

Figure 5.24 – Convergence of SimHT2: location L4

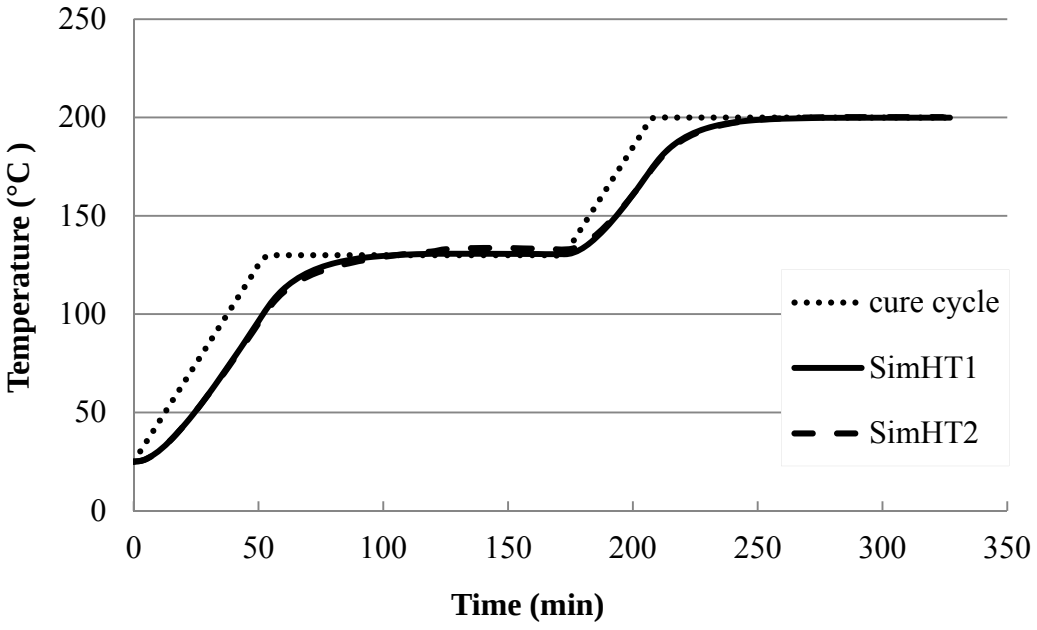

Figure 5.25 - Comparison C1: location L1

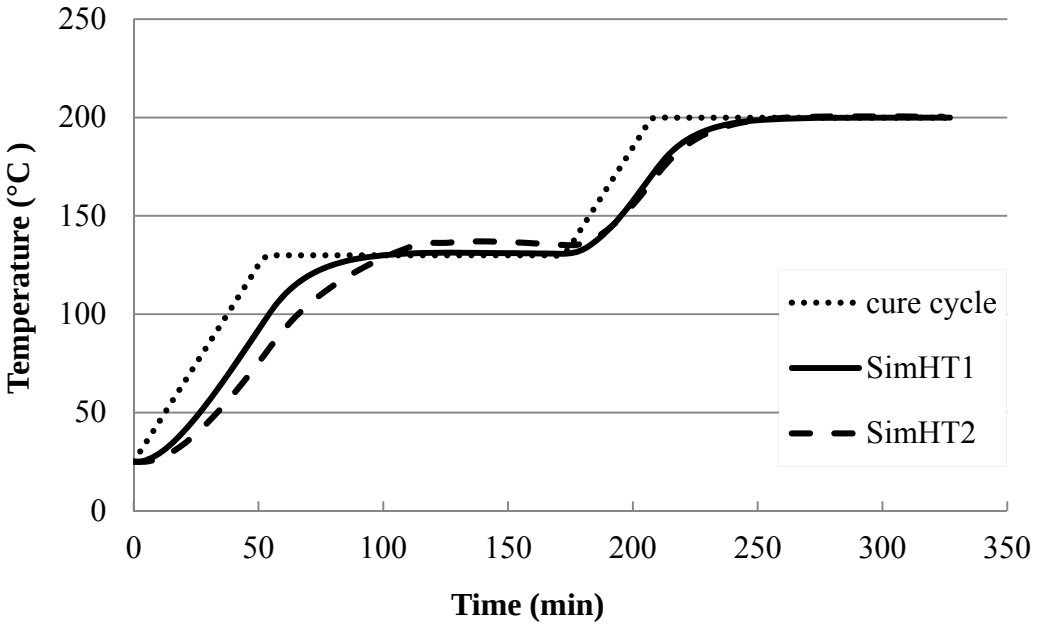

Figure 5.26 - Comparison C1: location L2

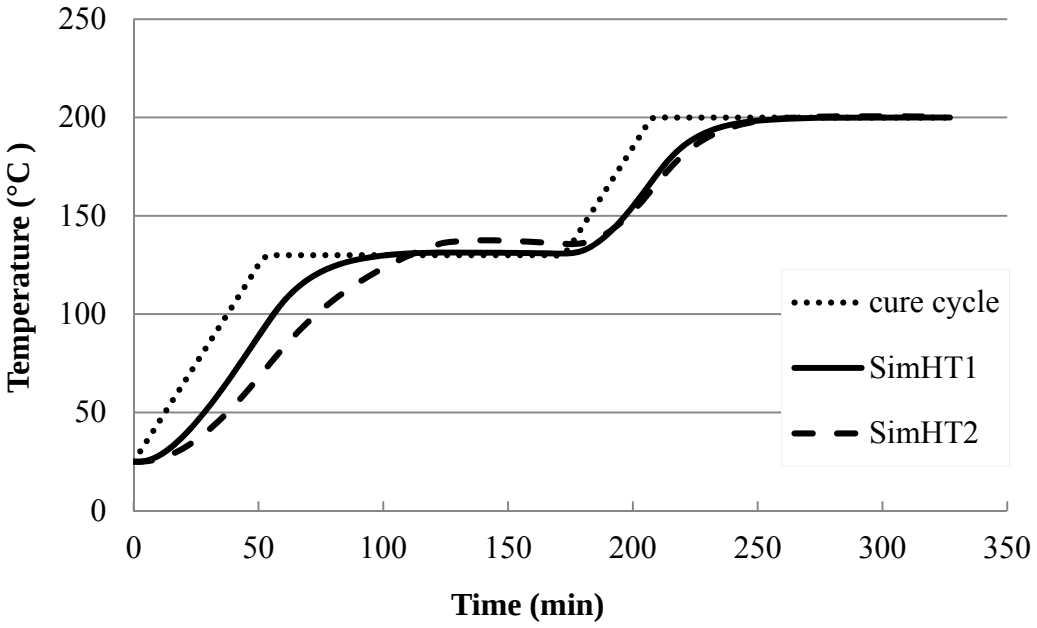

Figure 5.27 - Comparison C1: location L3

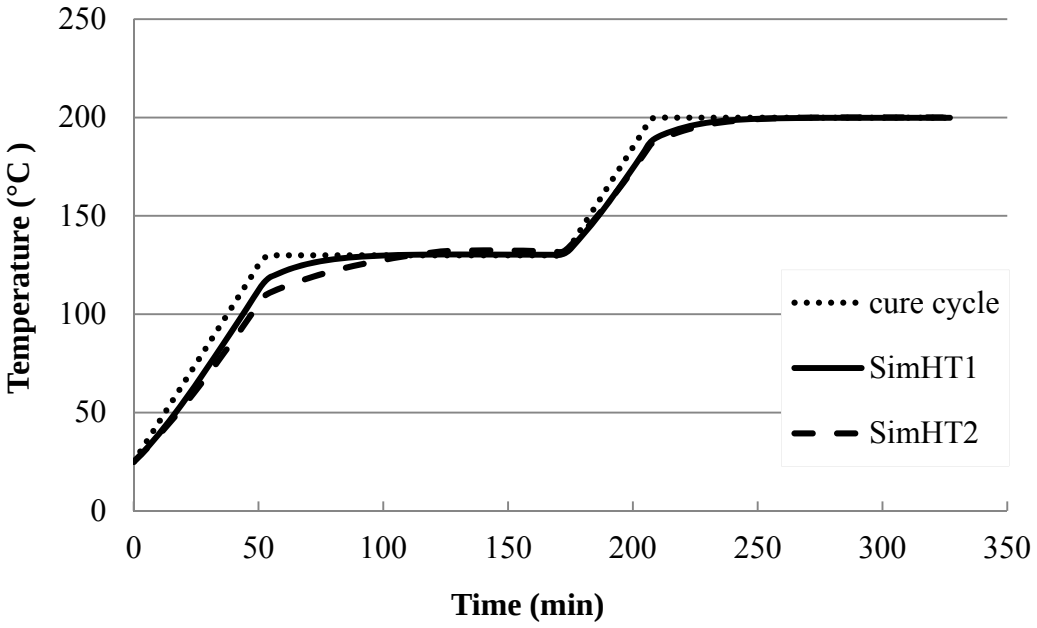

Figure 5.28 - Comparison C1: location L4

The effect of laminate thickness was seen in comparison C1 between SimHT1 and SimHT2. Temperatures at locations L1 and L4 showed scant differences between the two cases (Figures 5.25 and 5.28) as temperatures near the surfaces of the vacuum bag assembly are influenced primarily by conditions of the ambient air in the oven and less significantly by properties or characteristics of the laminate. Temperatures at locations L2 and L3 inside the vacuum bag assembly were lower for the 17.6 mm laminate compared with the 4.4 mm laminate during heating ramps, as a thicker laminate results in poor conduction of heat from the ambient air towards the centre of the laminate and causes lower temperatures at the centre. However, temperatures at the centre of the laminate were higher for the 17.6 mm laminate compared with the 4.4 mm laminate during the first dwell as a thicker laminate results in poor dissipation of the more pronounced curing exotherm generated at the centre of the laminate.

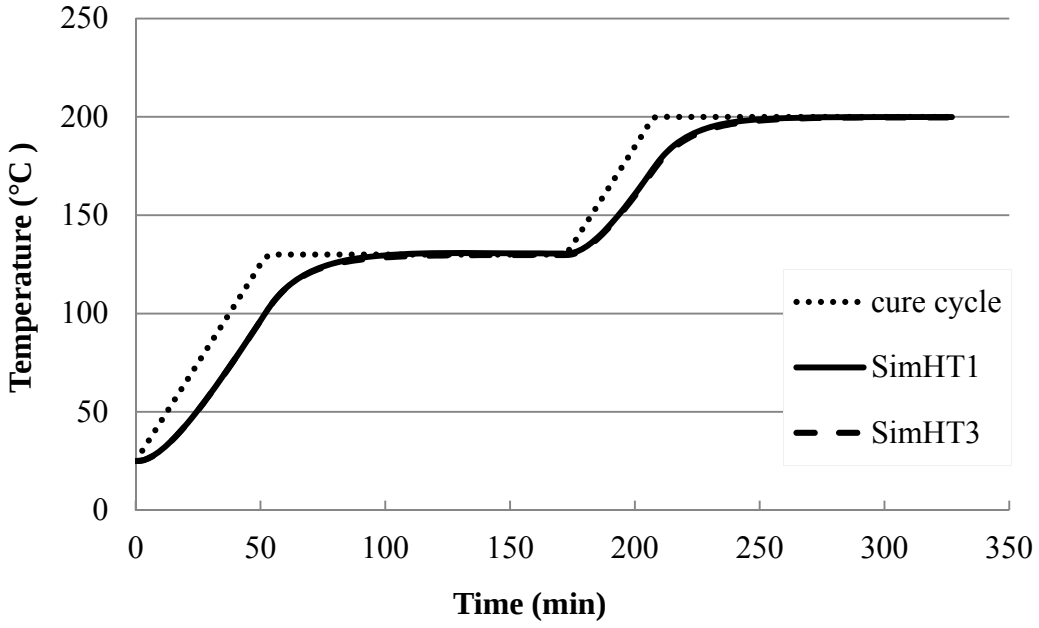

Figure 5.29 - Comparison C2: location L1

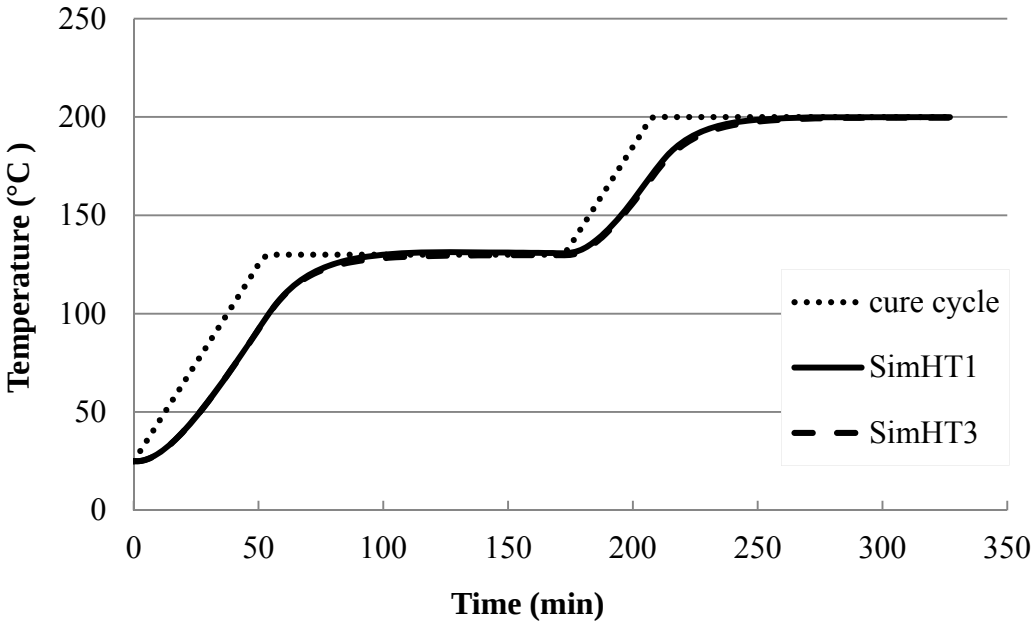

Figure 5.30 - Comparison C2: location L2

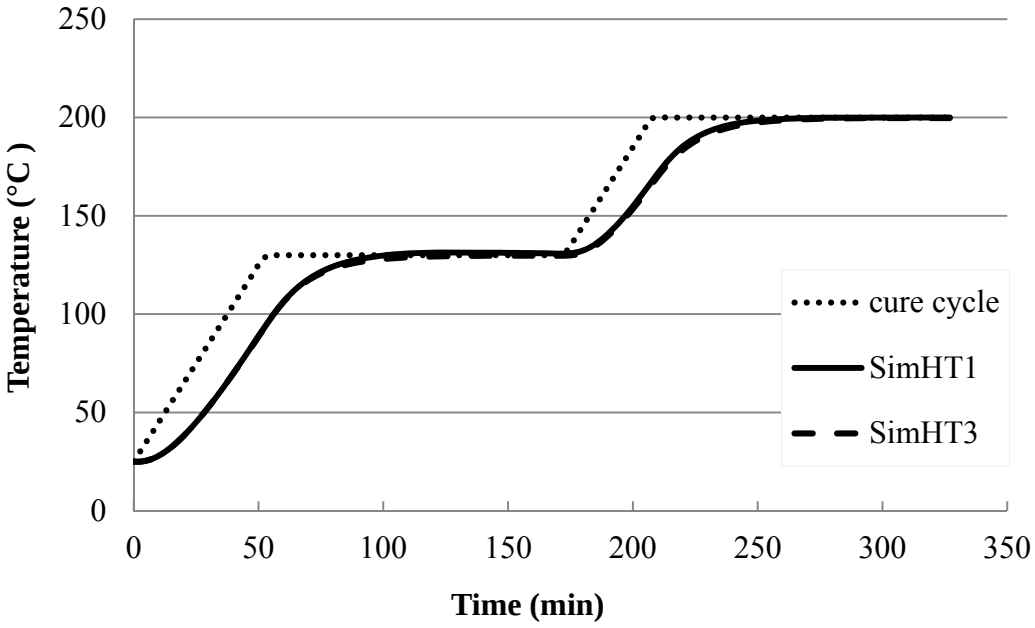

Figure 5.31 - Comparison C2: location L3

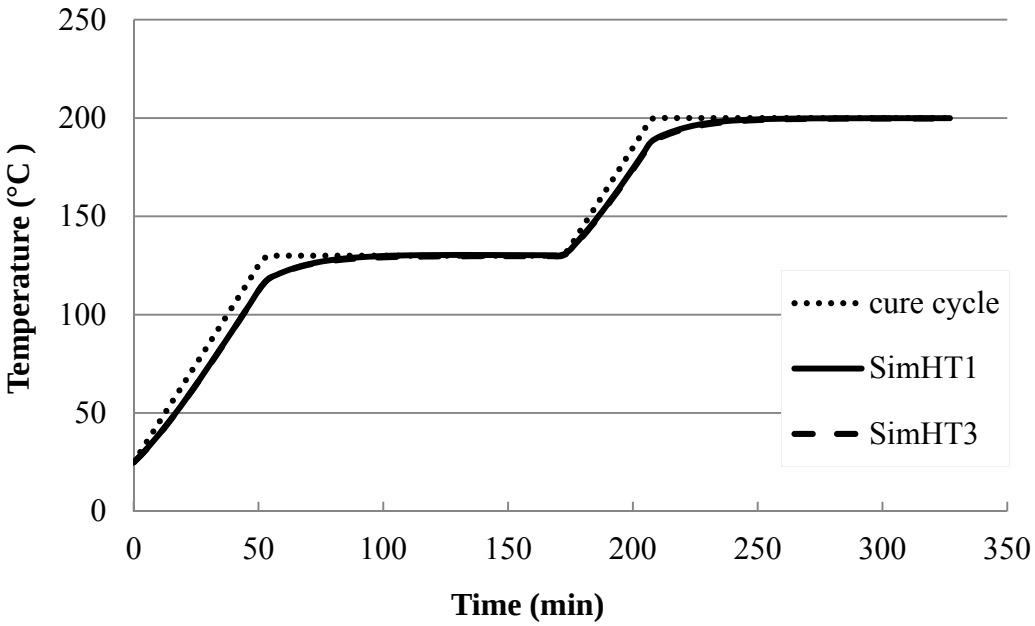

Figure 5.32 - Comparison C2: location L4

Comparison C2 shows that the effect of cure was negligible at a laminate thickness of 4.4 mm, Figures 5.29 to 5.32; the maximum temperature difference between SimHT1 and SimHT3 was only 1°C. This was to be expected, as the curing exotherm released during the cure cycle for a thin laminate can be dissipated easily from the centre of the laminate outwards into the air.

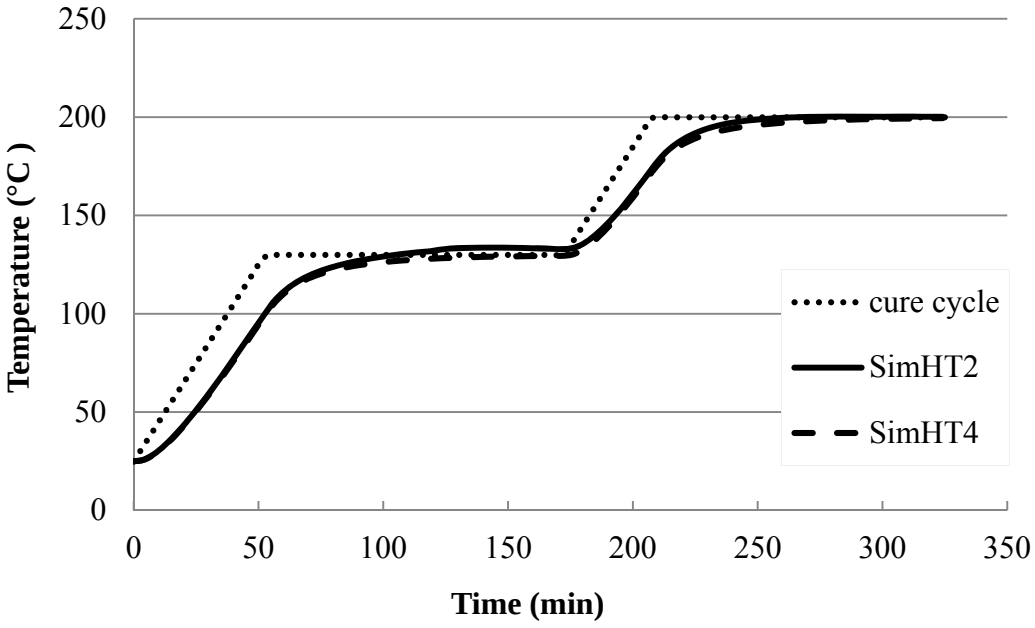

Figure 5.33 - Comparison C3: location L1

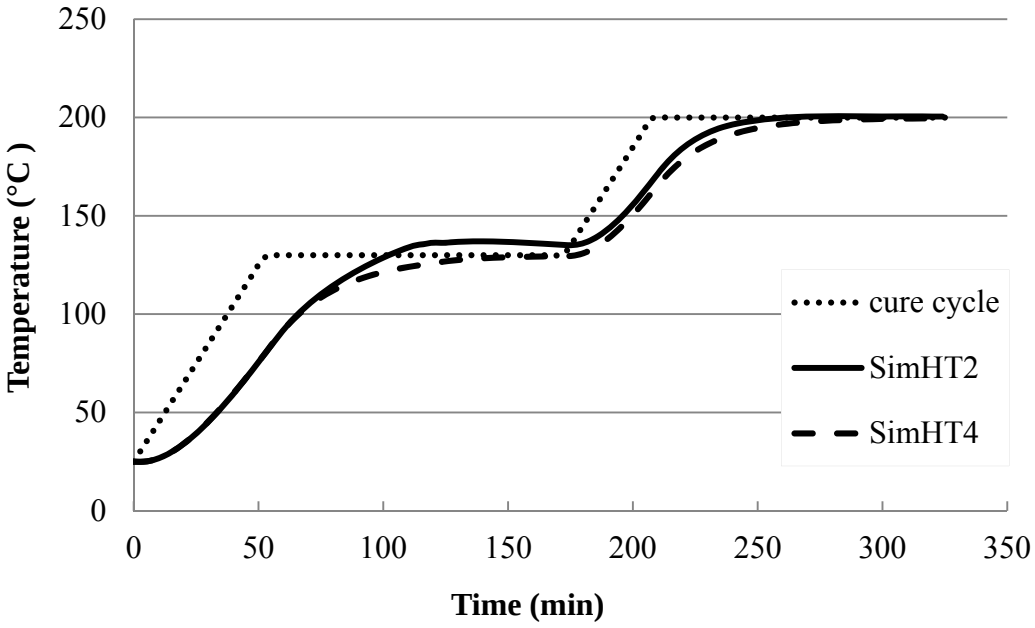

Figure 5.34 - Comparison C3: location L2

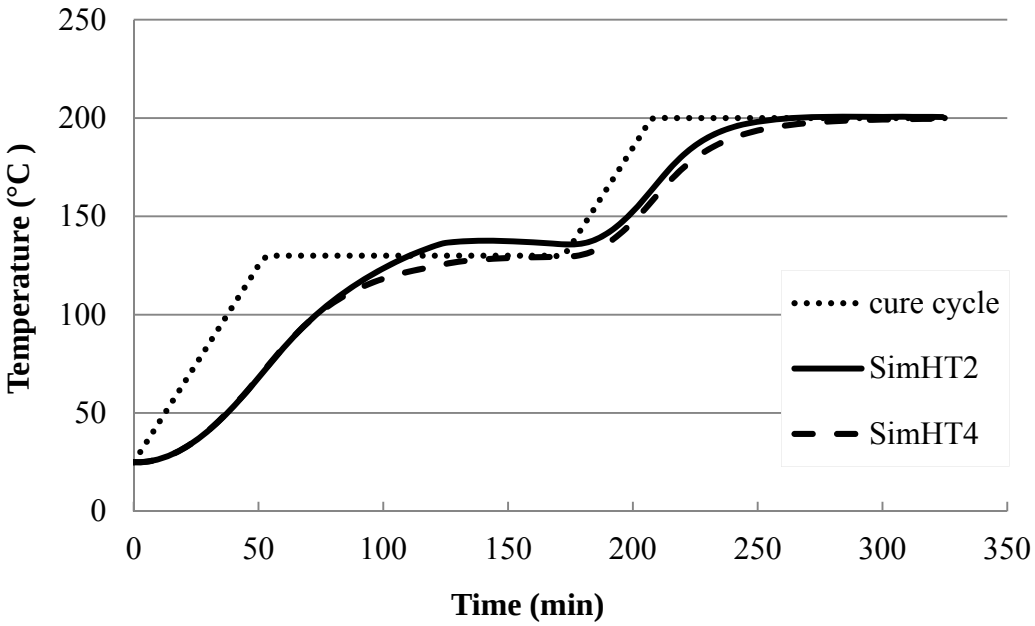

Figure 5.35 - Comparison C3: location L3

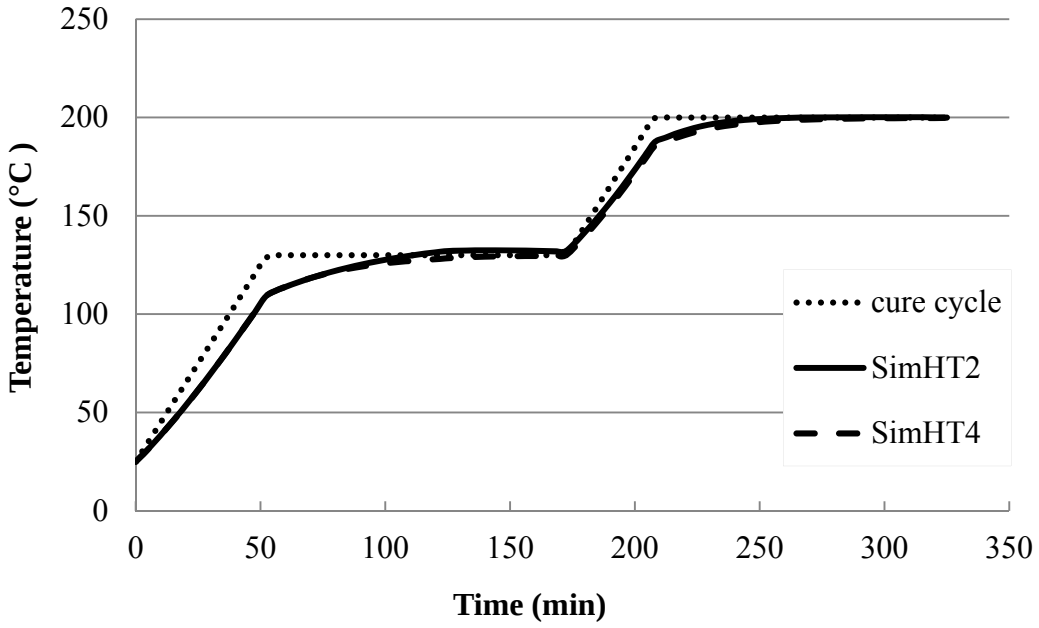

Figure 5.36 - Comparison C3: location L4

Similar to comparison C2, temperatures at locations L1 and L4 in comparison C3 showed scant differences between SimHT2 which included the effect of cure and SimHT4 in which cure was disabled, Figures 5.33 and 5.36; temperatures at locations near the surfaces of the vacuum bag assembly are influenced primarily by conditions of the ambient air in the oven and less significantly by properties or characteristics of the laminate. However, unlike comparison C2, comparison C3 shows that the effect of cure is detectable at locations L2 and L3 inside the laminate for a thickness of 17.6 mm; curing of the resin resulted in higher temperature profiles and the maximum temperature difference between cases SimHT2 and SimHT4 was 10°C. Hence comparisons C2 and C3 demonstrate that the effect of cure kinetics varies with laminate thickness and is more significant in thicker laminates. However, the effect of resin cure kinetics is relatively small as shown by Figures 5.33 to 5.36 given the drastic change in laminate thickness from 4.4 mm to 17.6 mm. This suggests that resin LEO

2396 used in this project is a slow-curing epoxy where the total heat of reaction of the resin is released over a relatively long period of time. This is seen in DSC results for resin LEO 2396 shown in Figure 5.7, where the resin cures over the entire duration of the cure cycle and approaches a degree of cure of 1 towards the end of the second dwell. This indicates the importance of the post-cure segment specified in the Axson cure cycle in achieving a fully cured composite. As the exotherm was released over the course of a few hours, no large overshoot in temperature occurred during the manufacturing of the 17.6 mm thick laminate using resin LEO 2396, unlike those manufactured using typical epoxies where overshoots up to 40°C can be seen at the centre of laminate [3]. This in turn suggests that resin LEO 2396 combined with the cure cycle specified by the manufacturer is well-suited for manufacturing laminates with typical thicknesses of 4 mm to 5 mm as well as thick laminates of 15 mm to 20 mm, without causing thermal degradation of the matrix or major residual stresses.

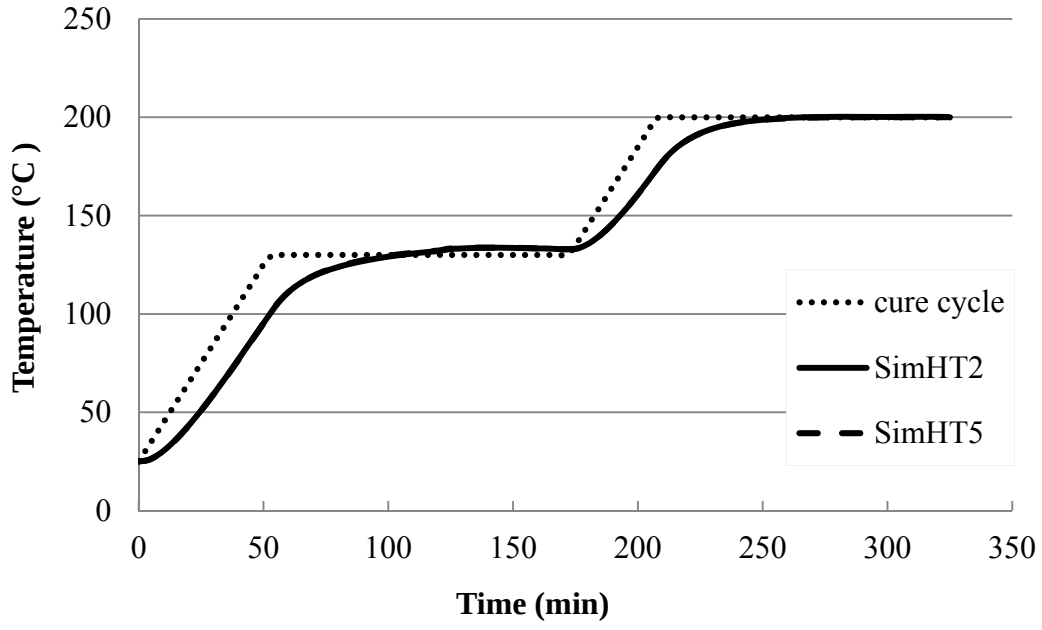

Figure 5.37 - Comparison C4: location L1

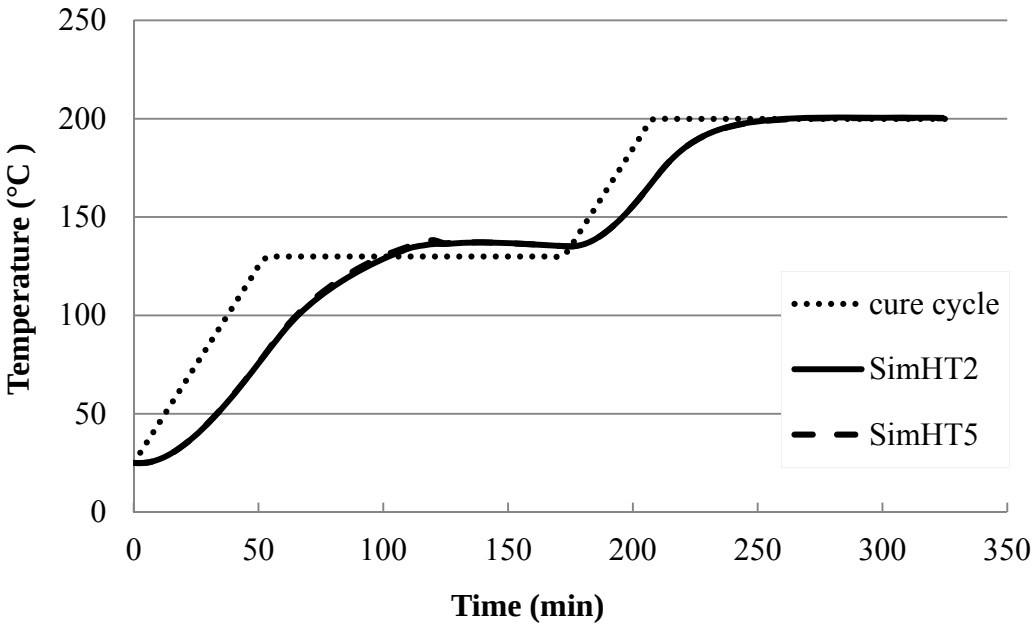

Figure 5.38 - Comparison C4: location L2

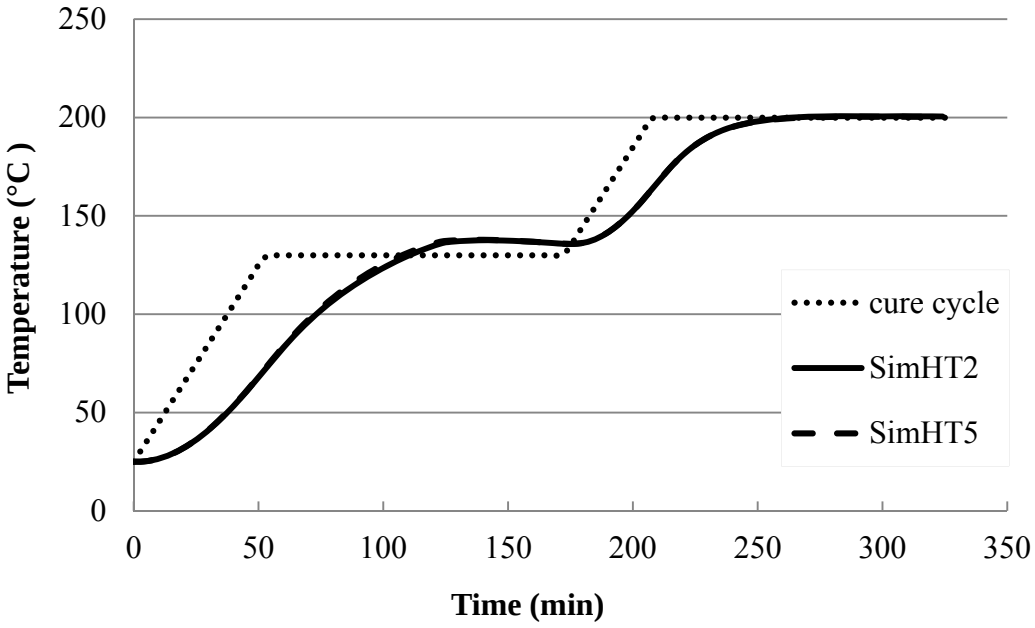

Figure 5.39 - Comparison C4: location L3

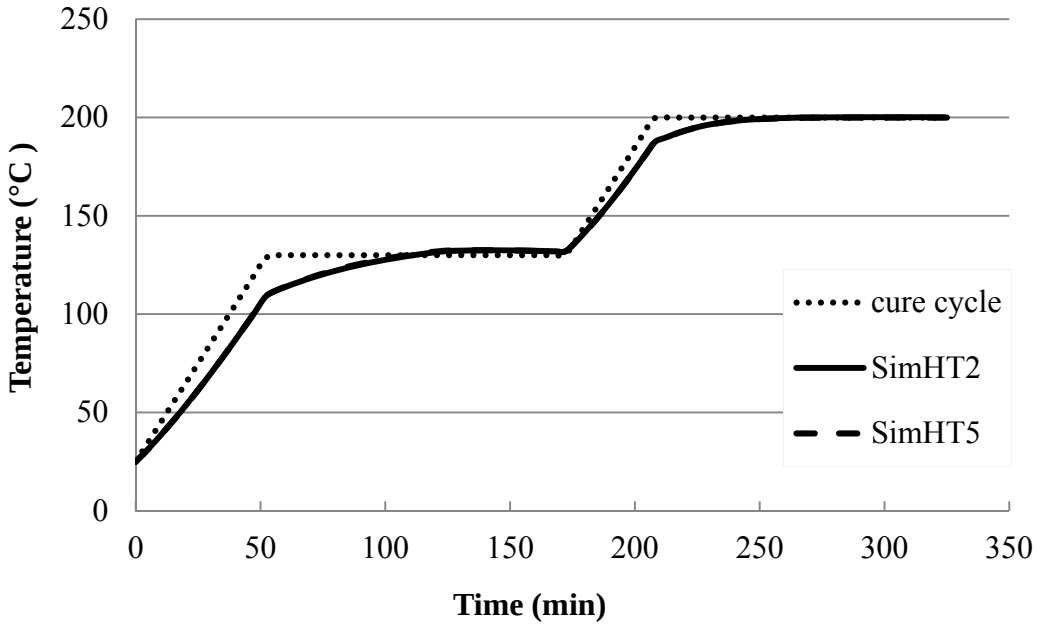

Figure 5.40 - Comparison C4: location L4

Comparison C4 shows that the effect of MWCNT addition into resin LEO 2396 was negligible even for a thick laminate of 17.6 mm, Figures 5.37 to 5.40. Loading MWCNTs was expected to increase the temperature profile at the centre of the laminate; however the maximum temperature difference between cases SimHT2 and SimHT5 was only 1°C. This can be explained by the lower heat of reaction of MWCNT-reinforced resin LEO 2397 at 409.3 J/g compared with that of resin LEO 2396 at 432.7 J/g, negating the already small difference in cure kinetics of resin LEO 2397 compared with resin LEO 2396 observed the DSC results for said resins, Figure 5.7.

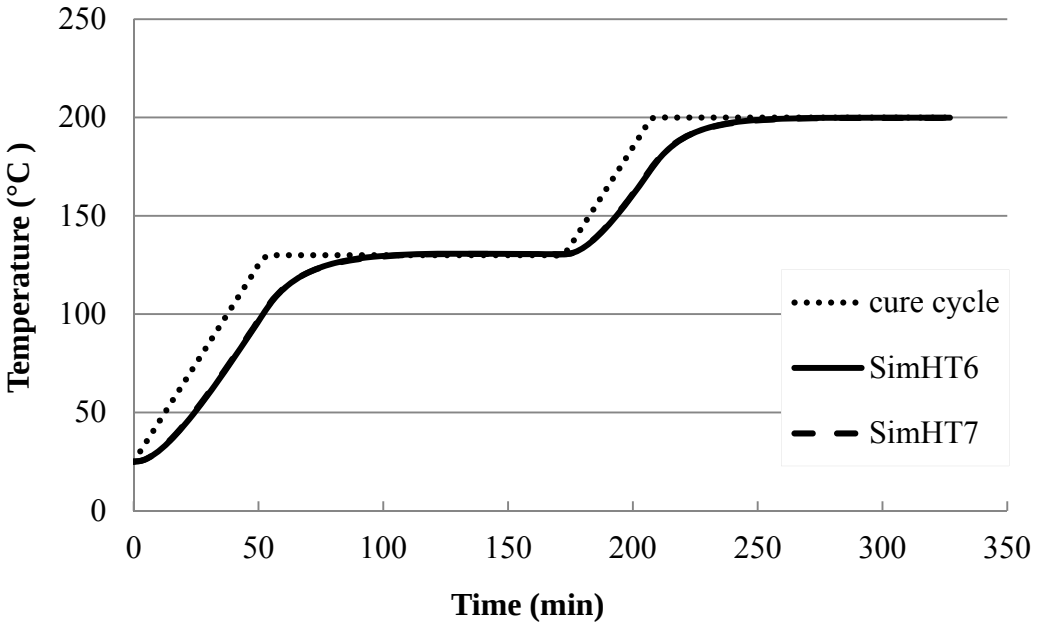

Figure 5.41 - Comparison C5: location L1

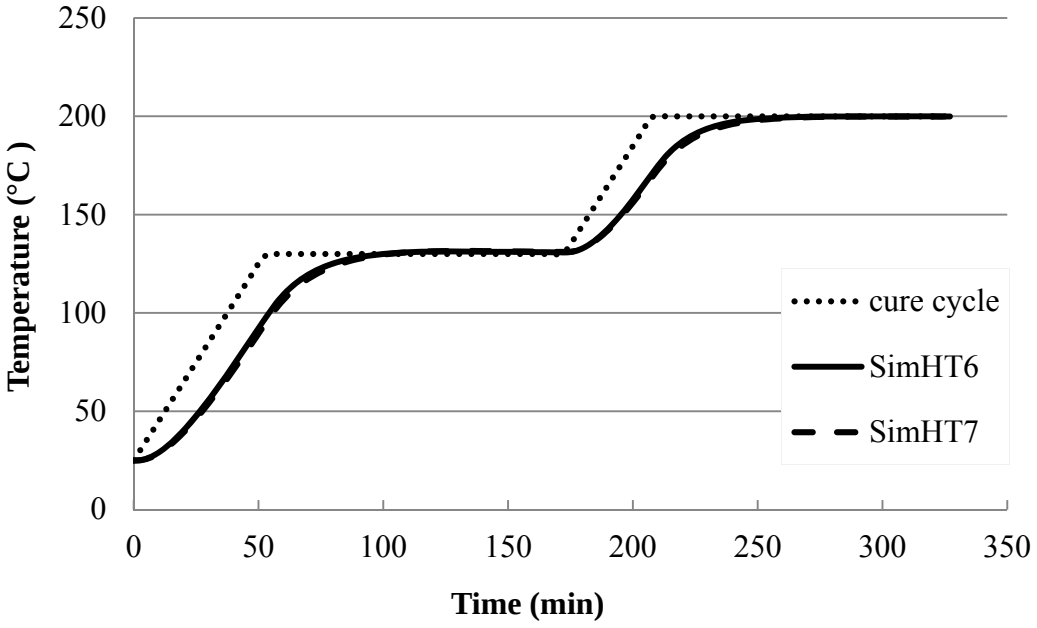

Figure 5.42 - Comparison C5: location L2

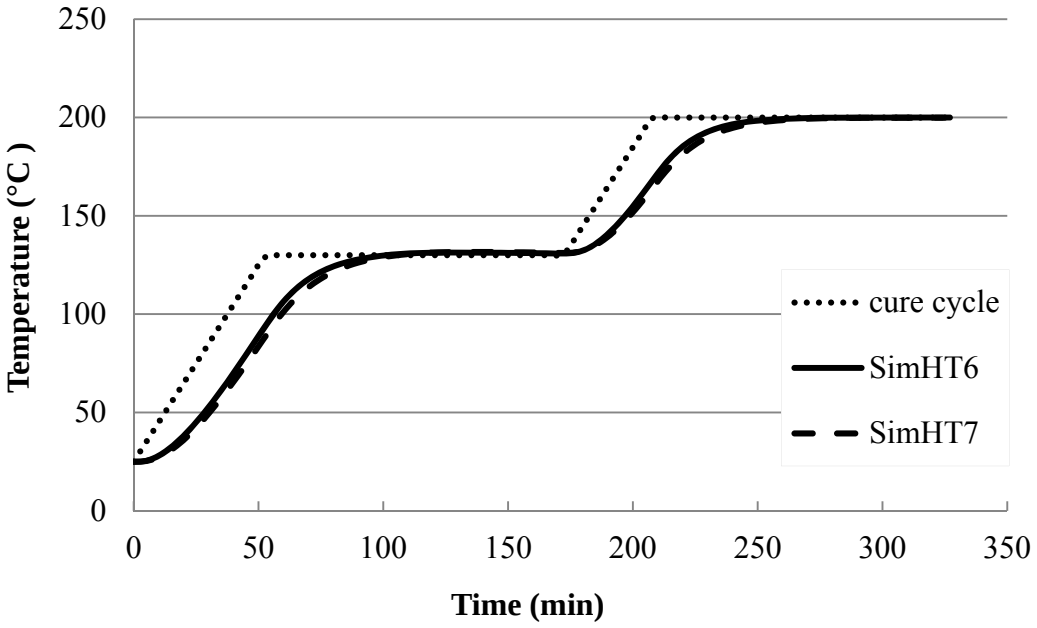

Figure 5.43 - Comparison C5: location L3

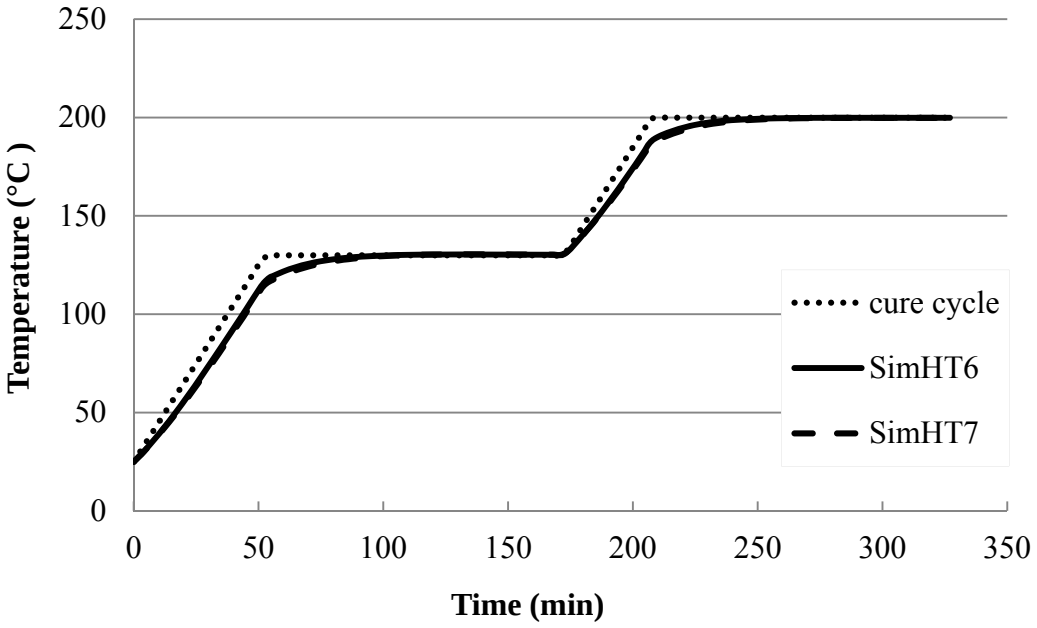

Figure 5.44 - Comparison C5: location L4

Comparison C5 shows that the effect of thermal conductivity of the laminate is negligible for a laminate thickness of 4.4 mm (Figures 5.41 to 5.44); the maximum temperature difference between SimHT6 and SimHT7 was only 2°C. This was to be expected, as the conduction of heat into the centre of the laminate and the dissipation of heat from the centre of laminate should not be hindered significantly for small laminate thicknesses.

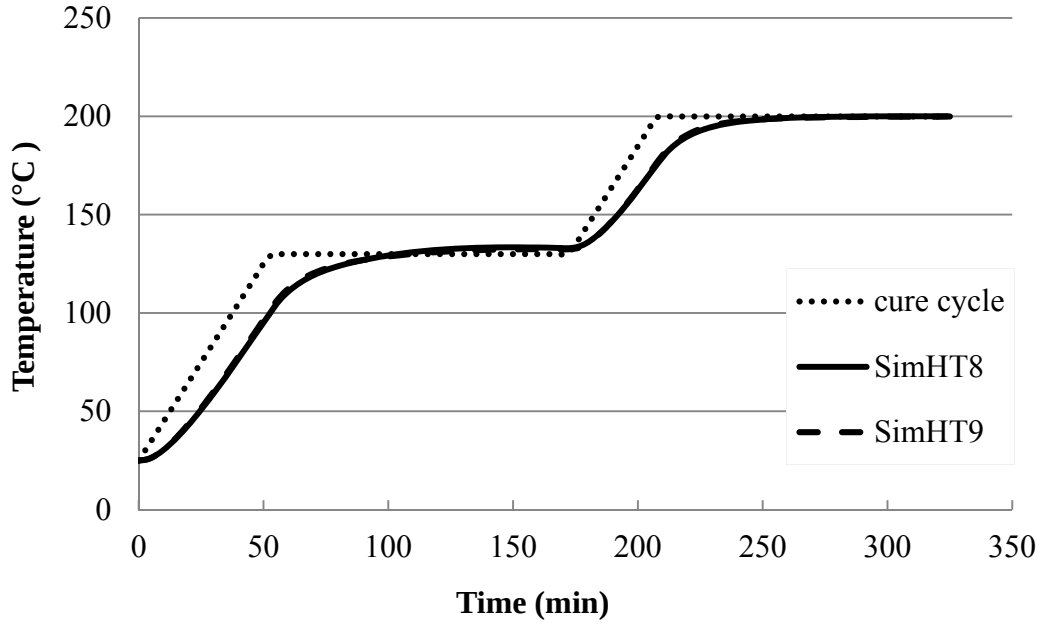

Figure 5.45 - Comparison C6: location L1

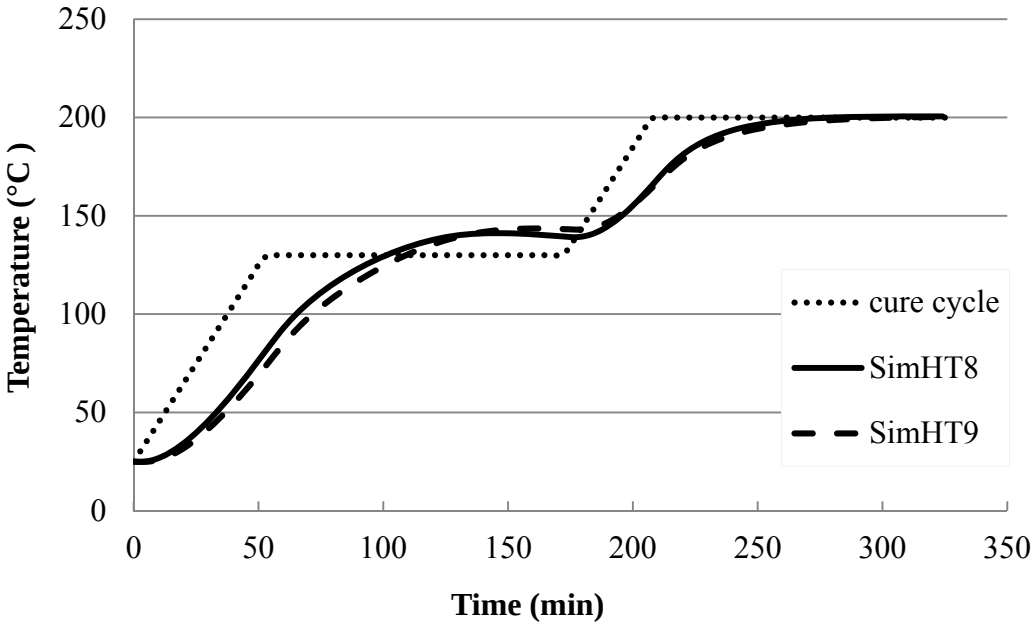

Figure 5.46 - Comparison C6: location L2

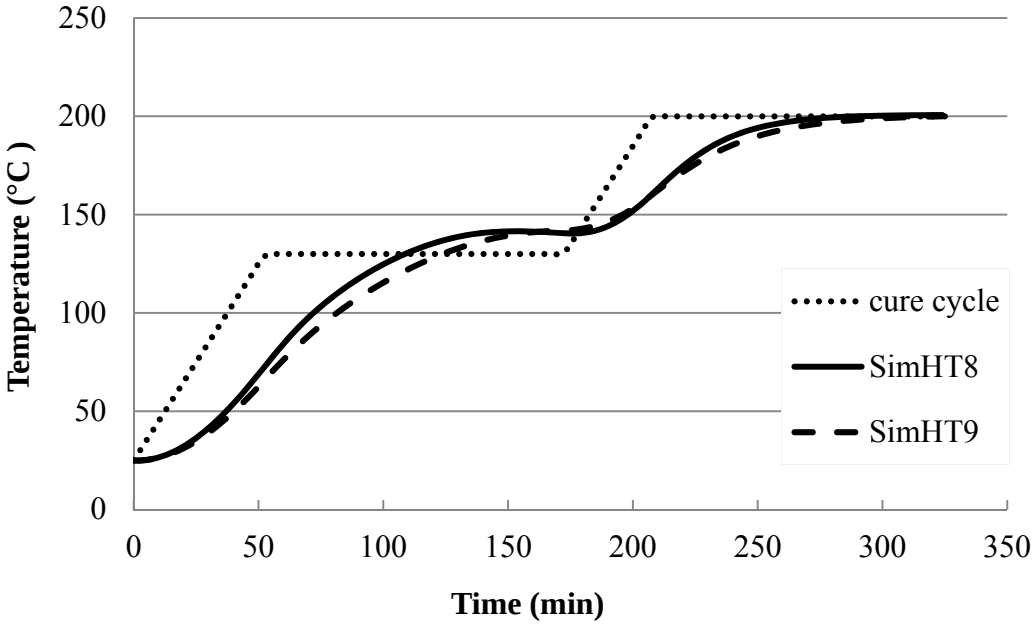

Figure 5.47 - Comparison C6: location L3

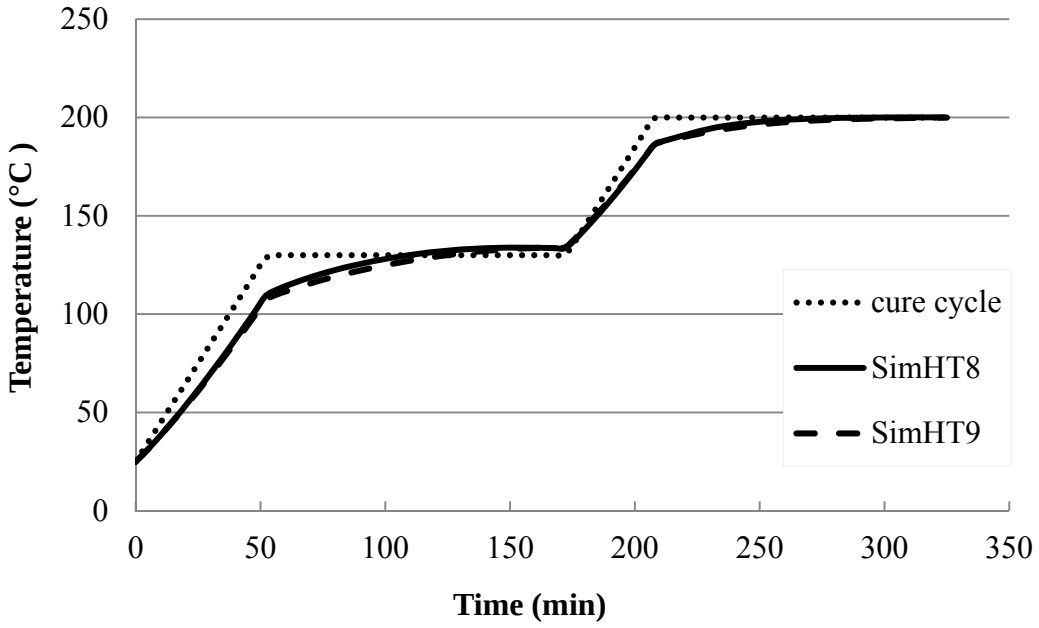

Figure 5.48 - Comparison C6: location L4

Similar to comparisons C1 and C3, temperatures at locations L1 and L4 in comparison C6 showed scant differences between cases SimHT6 and SimHT7 with different laminate thermal conductivities, Figures 5.45 and 5.48. However, comparison C6 shows that the effect of thermal conductivity of the laminate is significant for locations L2 and L3 inside the laminate for a laminate thickness of 17.6 mm, Figures 5.46 and 5.47; the maximum temperature difference between SimHT8 and SimHT9 was 12°C. During heating ramps, a lower thermal conductivity of the laminate results in poor conduction of heat from the ambient air towards the centre of the laminate and causes lower temperatures at the centre. Then towards the end of a dwell, a lower thermal conductivity of the laminate results in poor dissipation of heat from the centre of the laminate towards the outer surfaces of the assembly and causes higher temperatures at the centre. Similar to the effect of cure, comparisons C5

and C6 show that the effect of thermal conductivity of the laminate varies with laminate thickness and is more significant in thicker laminates.

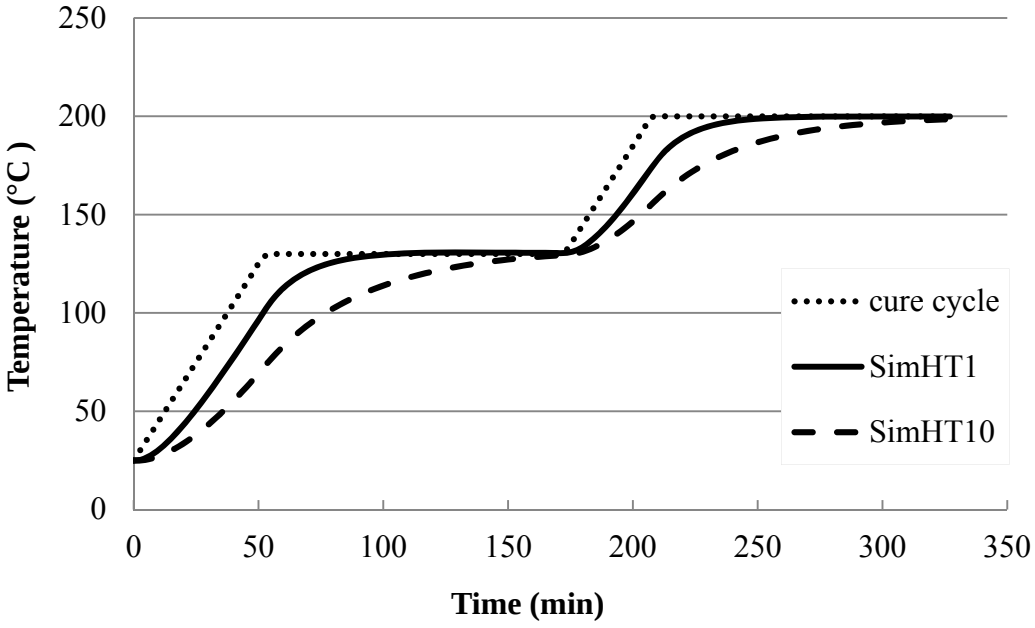

Figure 5.49 - Comparison C7: location L1

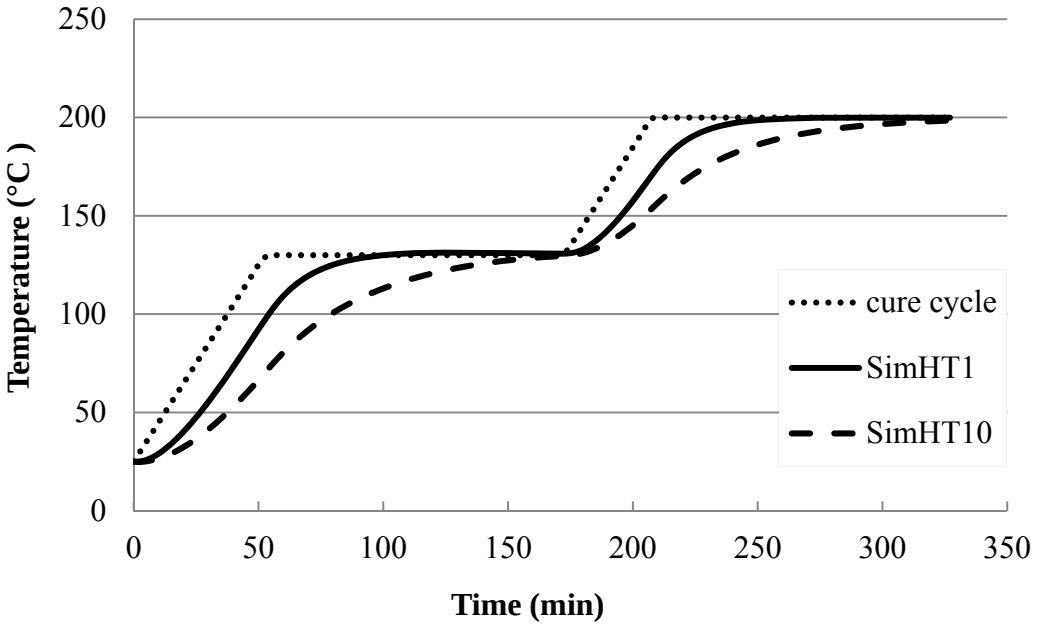

Figure 5.50 - Comparison C7: location L2

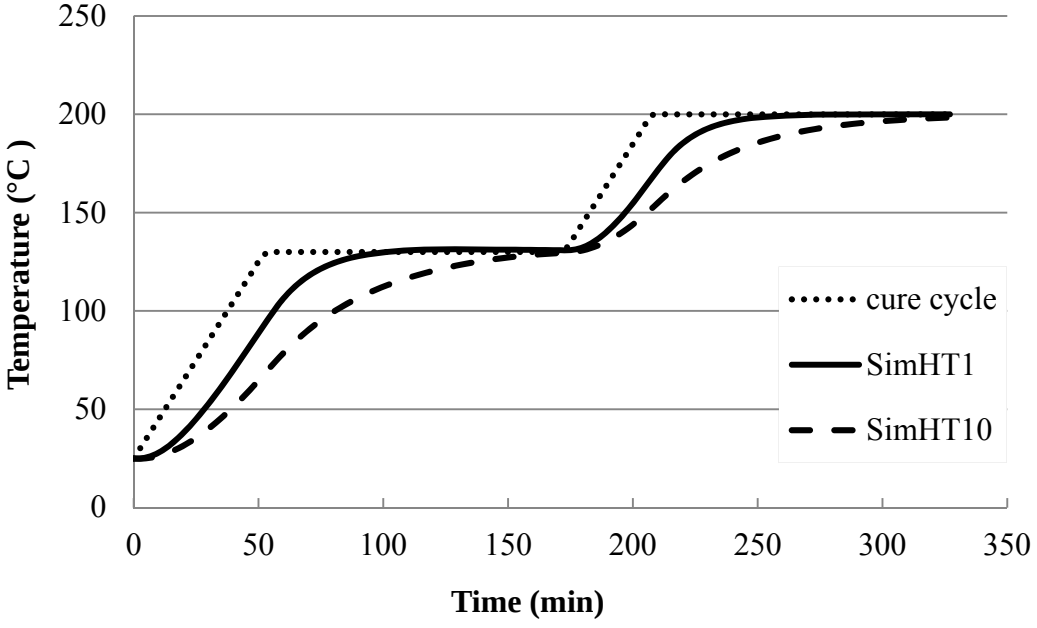

Figure 5.51 - Comparison C7: location L3

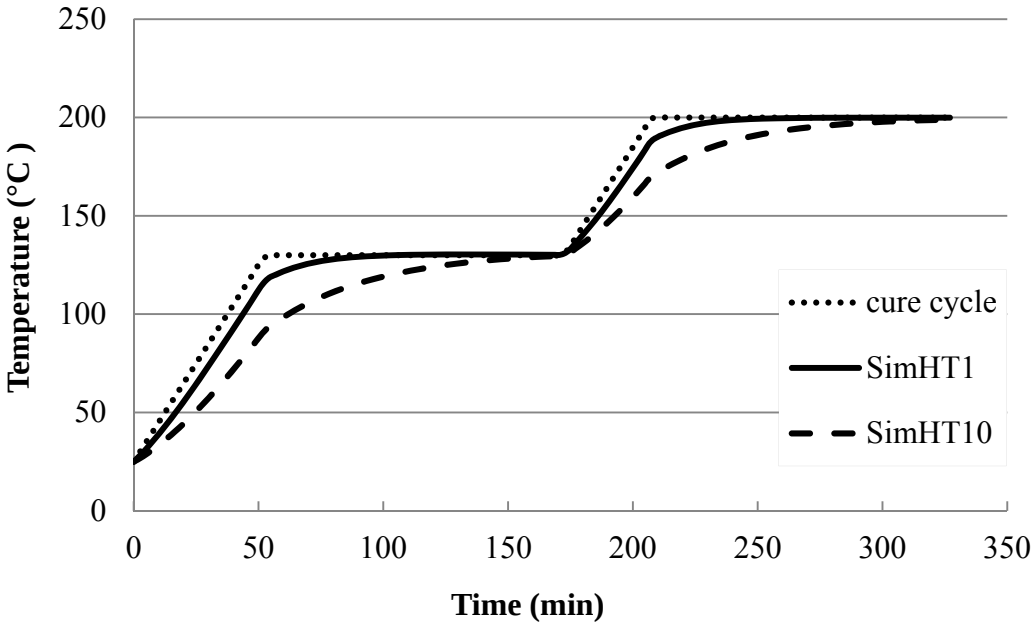

Figure 5.52 - Comparison C7: location L4

Comparison C7 shows that the convective heat transfer coefficient of the oven affects temperature profiles at locations L1 to L4 within the vacuum bag assembly equally, Figures 5.49 to 5.52. The effect of the heat transfer coefficient was most significant at the beginning of the first dwell at 80 minutes into the cure cycle; temperatures at all locations were observed to be approximately 30°C higher for the 4.4 mm thick laminate when using a value of 15 W/m^{2}K compared with 5 W/m^{2}K. A higher h value also enables the temperature profiles at all locations to follow that of the specified cure cycle more closely; the temperature plateau at 130°C for the first dwell was achieved at the centre of the laminate 95 minutes into the cure cycle for an h value of 15 W/m^{2}K compared with 160 minutes into the cure cycle for an h value of 5 W/m^{2}K.

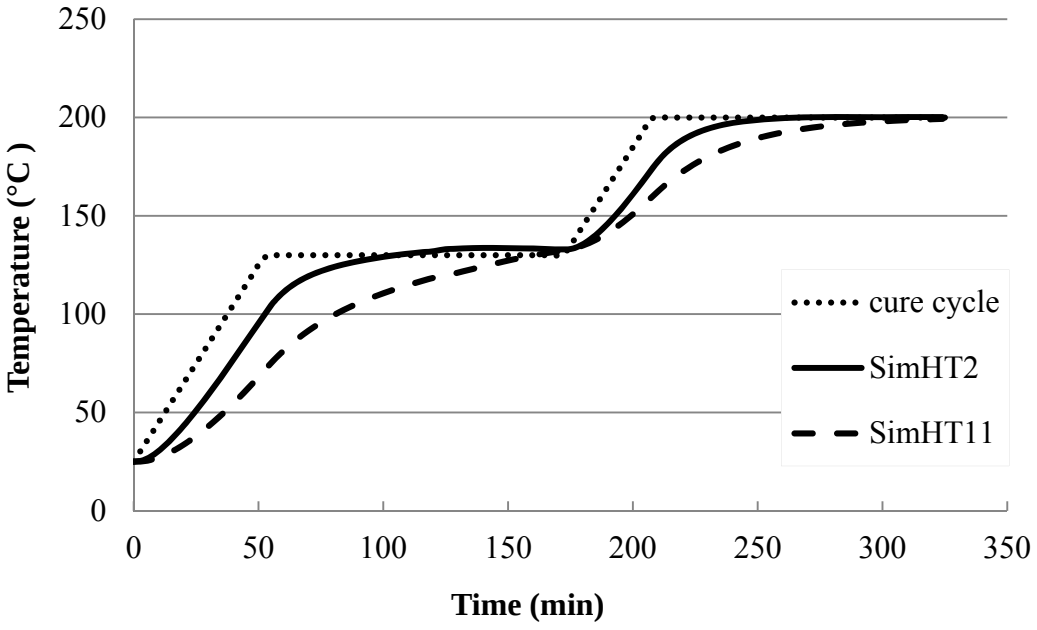

Figure 5.53 - Comparison C8: location L1

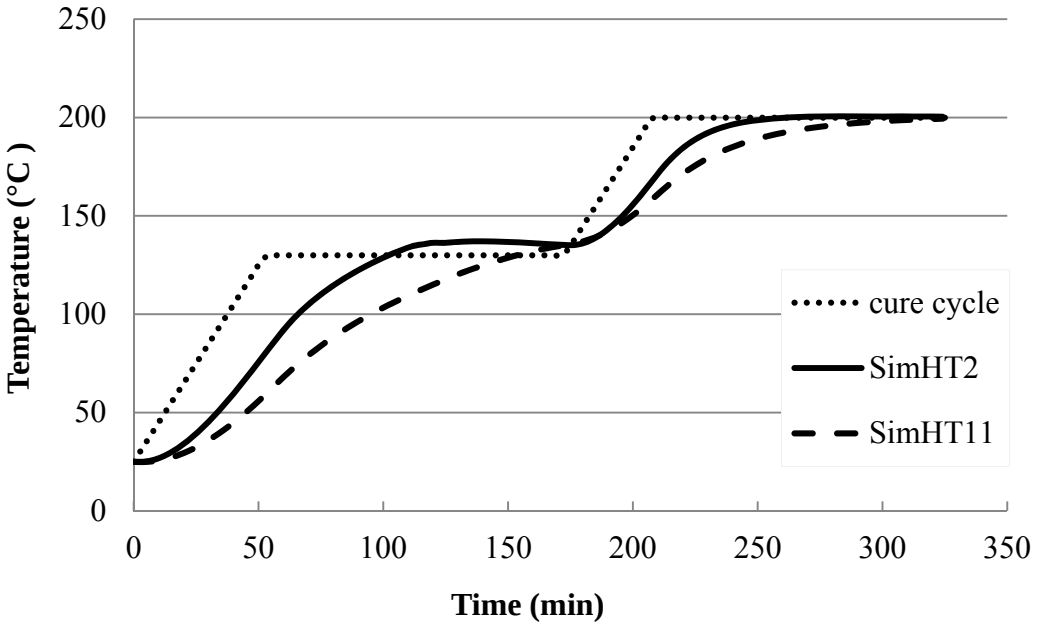

Figure 5.54 - Comparison C8: location L2

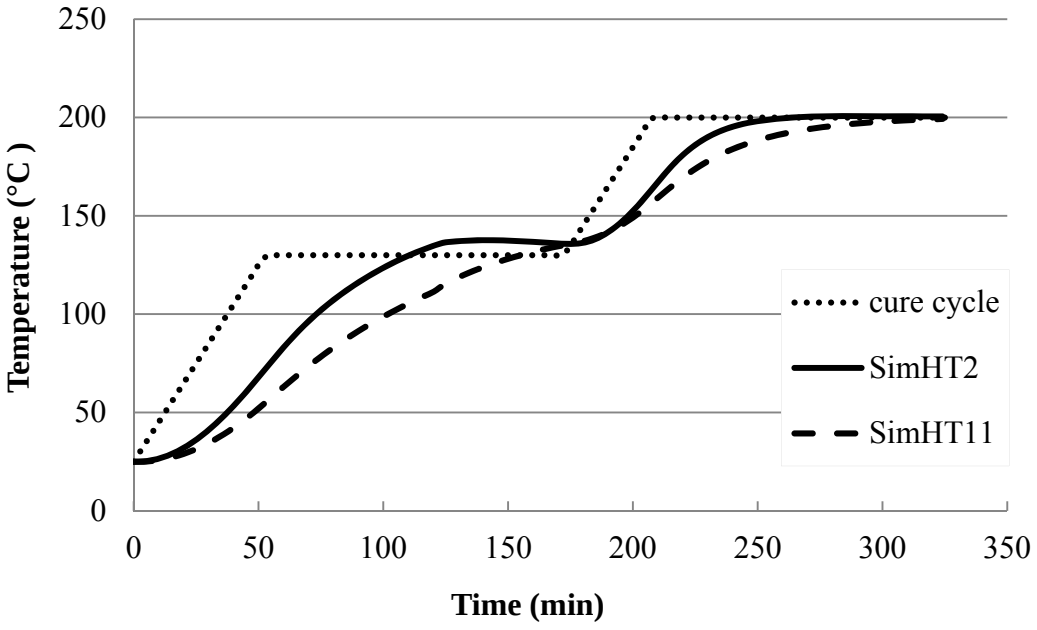

Figure 5.55 - Comparison C8: location L3

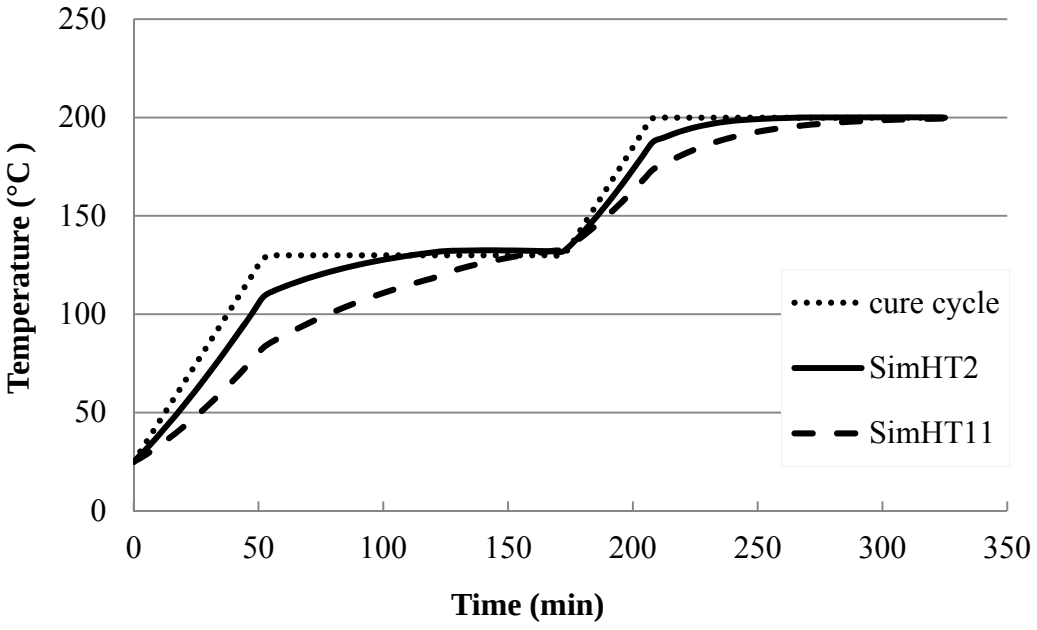

Figure 5.56 - Comparison C8: location L4

Similar to comparison C7, comparison C8 also shows that the convective heat transfer coefficient of the oven affects temperature profiles at locations L1 to L4 within the vacuum bag assembly equally, Figures 5.53 to 5.56. Similar to C7, the effect of h was most significant during the first dwell at 110 minutes into the cure cycle; temperatures at all locations were observed to be approximately 30°C higher for the 17.6 mm thick laminate when using a value of 15 W/m^{2}K compared with 5 W/m^{2}K. Also similar to C7, a higher h value also enables the temperature profiles at all locations to follow that of the specified cure cycle more closely; the temperature plateau at 130°C for the first dwell was achieved at the centre of the laminate with an h value of 15 W/m^{2}K around 100 minutes into the cure cycle compared with 160 minutes into the cure cycle for an h value of 5 W/m^{2}K. Comparisons C7 and C8 show that unlike the effects of the laminate thickness, resin cure and thermal conductivity of the laminate, the effect of the convective heat transfer coefficient does not depend on laminate thickness.

6 Conclusions

The overall goals of the thesis were to measure and model thermal conductivities of dry carbon fibre fabrics, CNT-reinforced epoxies and multi-scale composites made from these fabrics and epoxies, as well as modelling heat transfer in laminates during manufacturing. All objectives listed in Section 1.2 were achieved:

- k_{rip} and k_{rtt} of two dry carbon fibre fabrics were measured at various V_f values and modelled using analytical models and FLUENT simulations
- Neat and MWCNT-reinforced resin plates were manufactured and the effect of MWCNT addition on the thermal conductivity of the resins was investigated
- A procedure was developed for manufacturing composite plates using the RFI process
- The effects of various manufacturing parameters on V_f and V_v of composite plates were investigated
- V_f , V_v , k_{cip} and k_{ctt} of the composite plates were characterised
- Influential material parameters including MWCNT addition on V_f , V_v , k_{cip} and k_{ctt} were identified using the Plackett-Burman design of experiment methodology
- Simulations were developed in FLUENT to model heat transfer coupled with resin cure kinetics of the laminate during manufacturing, and were validated experimentally
- The effects of various parameters on the temperature profiles of the laminate were investigated using the simulations

Measured k_{rip} and k_{rtt} data for two carbon fibre fabrics as a function of V_f were presented. Well-defined trends were observed for the in-plane and through-thickness directions; k_{rip} varied linearly from 1.303 W/mK to 2.249 W/mK whilst k_{rtt} varied from 0.112 W/mK to 0.219 W/mK in an exponential recovery trend as a function of V_f. k_{rip} values for the non-crimp fabric were slightly higher than those for the twill fabric at the same V_f, which can be explained by the crimped fibres in the woven twill architecture. However, values of k_{rip} and k_{rtt} for the two fabrics were generally in the same range, which suggests that thermal conductivity does not depend heavily on architecture for non-crimp and woven fabrics. This suggests that little difference should be expected between architectures such as plain weave, twill weaves and satin weaves. k_{rip} values were predicted successfully by the CLT and in-plane thermal conductivities between dry fabrics and composites made using the same fabrics were similar, which demonstrates that the in-plane thermal conductivity depends primarily on the axial fibre thermal conductivity. Measured data for k_{rtt} were 2 to 3 times lower than k_{ctt} which demonstrates that the through-thickness thermal conductivity depends heavily on the surrounding material. Published models, such as the Clayton analytical model yield accurate predictions for k_{ctt} but largely underestimate k_{rtt} values. Simulations developed in FLUENT which accounted for fibre-fibre contacts yielded successful predictions for k_{rtt}. The simulations showed that k_{rtt} depends on the evolution of heat paths in the through-thickness direction as a result of improvements in the fibre contact network during compaction, and provided a simplified illustration to the fibre-fibre contacts that will be investigated more formally in future work.

Neat and MWCNT-reinforced epoxy plates using two base resins were manufactured and all plates demonstrated thermal isotropy. Thermal conductivities of plates made using the 239x base with and without 0.3% MWCNTs compared with those made using the 237x base were 4.1% and 3.5% higher, respectively. The effective medium approach combined with the Maxwell equation accounting for V_v yielded accurate predictions for thermal conductivities of MWCNT-reinforced plates with a maximum error of 3.4%. Results from the model showed that the effect of loading MWCNTs at less than 2% was negligible; loading MWCNTs at 0.3% increased the thermal conductivity of epoxy by only 1%. This generally agreed with studies in the literature loading MWCNTs at 0.3%, where thermal conductivity increased by 4% [17] to 6% [23]. However, loading MWCNTs at more than 2% presents challenging issues for composite processing that would need to be investigated. Hence further work should be pursued for investigating different parameters of the CNTs that may increase the thermal conductivity of epoxy, such as functionalising the CNTs or using CNTs with a different aspect ratio [87]. Also, the effect of loading graphene nanoplatelets (GNP) or other thermally conductive reinforcements along with CNTs can be investigated, Figure 6.1; recent research [145] showed a synergetic effect on the thermal conductivity enhancement due to combined loading of SWCNTs and GNPs to be more effective than the enhancement due to each reinforcement alone.

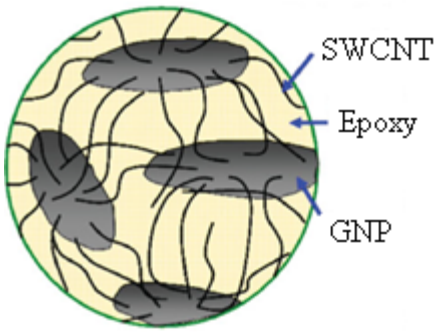

Figure 6.1 - Schematic of SWCNTs-GNPs network in epoxy matrix

A procedure was developed for manufacturing composite plates using the RFI process. A set of 19 preliminary composite plates were manufactured for investigating the effects of various manufacturing parameters such as heating rate, curing temperature, vacuum bag configuration, application of vacuum, pre-compaction and layup sequence on V_f and V_v of the plates. From these results, the best parameters were chosen for manufacturing a set of 12 composite plates using the Plackett-Burman design of experiment methodology for investigating the effects of fabric architecture, surface density, resin base and MWCNT addition on the V_f, V_v, k_{cip} and k_{ctt} of the plates. Loading MWCNTs at 0.3% reduced the average V_v of the composite significantly from 2.0% to 0.7% due to a reduction in resin bleed. Results also showed that resin LEO 2376 should be used with non-crimp fabrics for maximising V_f while resin LEO 2397 should be used with twill fabrics. However, no physical explanation can be given for these results at this point, and more plates should be manufactured and characterised to investigate these effects further. Results also showed that using fabrics with higher surface density resulted in a slight increase in k_{cip} from 2.520 W/mK to 2.649 W/mK while k_{ctt} was not affected by any material parameter investigated.

The effect of loading MWCNTs at 0.3% on thermal conductivity of composites was negligible. This generally agrees with studies in the literature which reported a decrease in thermal conductivity of carbon fibre-epoxy composites of 1% upon loading MWCNTs at 0.5% [28].

Three-dimensional transient heat transfer simulations were developed in FLUENT for modelling heat transfer coupled with resin cure kinetics during RFI laminate manufacturing. Temperature profiles at the top, centre and bottom of the laminate were monitored and the model was validated experimentally for two laminate thicknesses: 4.4 mm and 17.6 mm. Increasing the laminate thickness from 4.4 mm to 17.6 mm lowered the temperature profile in the laminate centre significantly and increased the maximum temperature difference between the surface and the centre from 8°C to 28°C. The effect of the heat transfer coefficient was significant for both laminate thicknesses: a decrease of approximately 30°C at all locations of the laminate was observed when the heat transfer coefficient was decreased from 15 W/m^2K to 5 W/m^2K. The effect of MWCNT addition into the resin was negligible at both laminate thicknesses; the maximum increase observed in the temperature profiles when using the MWCNT-reinforced resin compared with the neat counterpart was only 1°C. This can be explained by the small difference in the cure kinetics of resin LEO 2396 compared with resin LEO 2397. The effect of cure and laminate thermal conductivity depended on the laminate thickness: their effects were negligible for the 4.4 mm laminate whilst disabling resin cure and decreasing thermal conductivity of the laminate from 0.2 W/mK to 0.1 W/mK for the 17.6 mm laminate resulted in temperature increases up to 10°C and 12°C respectively at the laminate centre. However, the relatively small effect of the cure given the drastic change in laminate thickness suggest that the epoxies used in this project are slow-curing

resins. This in turn suggests that these resins combined with the cure cycle recommended by the manufacturer are well-suited for manufacturing laminates with typical thicknesses of 4 mm to 5 mm as well as thick laminates of 15 mm to 20 mm; no large exotherm occurred during the manufacturing of the thick laminate to cause thermal degradation of the matrix or residual stresses.

References

[1] P. Hubert, “Development of nanochemicals filled epoxy systems for aerospace applications - CRIAQ 510 proposal.” 2011.

[2] D. Qian, E. C. Dickey, R. Andrews, and T. Rantell, “Load transfer and deformation mechanisms in carbon nanotube-polystyrene composites,” *Appl. Phys. Lett.*, vol. 76, no. 20, p. 2868, 2000.

[3] M. Cadek, J. N. Coleman, V. Barron, K. Hedicke, and W. J. Blau, “Morphological and mechanical properties of carbon-nanotube-reinforced semicrystalline and amorphous polymer composites,” *Appl. Phys. Lett.*, vol. 81, no. 27, p. 5123, 2002.

[4] M. J. Biercuk, M. C. Llaguno, M. Radosavljevic, J. K. Hyun, a. T. Johnson, and J. E. Fischer, “Carbon nanotube composites for thermal management,” *Appl. Phys. Lett.*, vol. 80, no. 15, p. 2767, 2002.

[5] N. Hu, Z. Masuda, C. Yan, G. Yamamoto, H. Fukunaga, and T. Hashida, “The electrical properties of polymer nanocomposites with carbon nanotube fillers,” *Nanotechnology*, vol. 19, no. 21, pp. 57–66, May 2008.

[6] NetComposites, “Resin film infusion,” 2013. [Online]. Available: http://www.netcomposites.com/guide/resin-film-infusion/61. [Accessed: 15-Aug-2013].

[7] S. Xiaogang, L. Jihong, and L. Sa, “Research on heat conduction performance of carbon-fibre fabric based on infrared thermal imaging technology,” *2008 IEEE Int. Symp. Knowl. Acquis. Model. Work.*, vol. 4, no. 1, pp. 40–43, Dec. 2008.

[8] F.-L. Zhu and K.-J. Li, “Fractal analysis of effective thermal conductivity for woven fabrics used in fire fighters’ protective clothing,” *J. Fire Sci.*, vol. 29, no. 1, pp. 3–20, May 2010.

[9] Y. Yamashita, H. Yamada, and H. Miyake, “Effective thermal conductivity of plain weave fabric and its composite material made from high strength fibers,” *J. Text. Eng.*, vol. 54, no. 4, pp. 111–119, 2008.

[10] S. Berber, Y. Kwon, and D. Tomanek, “Unusually high thermal conductivity of carbon nanotubes,” *Phys. Rev. Lett.*, vol. 84, no. 20, pp. 4613–6, May 2000.

[11] W. Kowbel, W. Champion, J. C. Withers, and W. Shih, “Low cost, high thermal conductivity composite heat spreaders for power electronics,” *Sixt. Annu. IEEE Semicond. Therm. Meas. Manag. Symp.*, pp. 195–200.

[12] Z. Antar, H. Noel, J. F. Feller, P. Glouannec, and K. Elleuch, "Thermophysical and fadiative properties of conductive biopolymer composite," *Mater. Sci. Forum*, vol. 714, pp. 115–122, Mar. 2012.

[13] M. B. Bryning, D. E. Milkie, M. F. Islam, J. M. Kikkawa, and a. G. Yodh, "Thermal conductivity and interfacial resistance in single-wall carbon nanotube epoxy composites," *Appl. Phys. Lett.*, vol. 87, no. 16, pp. 19–21, 2005.

[14] E. S. Choi, J. S. Brooks, D. L. Eaton, M. S. Al-Haik, M. Y. Hussaini, H. Garmestani, D. Li, and K. Dahmen, "Enhancement of thermal and electrical properties of carbon nanotube polymer composites by magnetic field processing," *J. Appl. Phys.*, vol. 94, no. 9, p. 6034, 2003.

[15] T. C. Clancy and T. S. Gates, "Modeling of interfacial modification effects on thermal conductivity of carbon nanotube composites," *Polymer (Guildf).*, vol. 47, no. 16, pp. 5990–5996, Jul. 2006.

[16] L. Ekstrand, H. Kristiansen, and J. Liu, "Characterization of thermally conductive epoxy nanocomposites," *28th Int. Spring Semin. Electron. Technol. Meet. Challenges Electron. Technol. Progress, 2005*, no. 3, pp. 35–39, 2005.

[17] F. H. Gojny, M. H. G. Wichmann, B. Fiedler, I. a. Kinloch, W. Bauhofer, A. H. Windle, and K. Schulte, "Evaluation and identification of electrical and thermal conduction mechanisms in carbon nanotube-epoxy composites," *Polymer (Guildf).*, vol. 47, no. 6, pp. 2036–2045, Mar. 2006.

[18] C. Guthy, F. Du, S. Brand, K. I. Winey, and J. E. Fischer, "Thermal conductivity of single-walled carbon nanotube-PMMA nanocomposites," *J. Heat Transfer*, vol. 129, no. 8, p. 1096, 2007.

[19] R. A. Hauser, "Synergistic Effects and Modeling of Thermally Conductive Resins for Fuel Cell Bipolar Plate Applications-PhD," ProQuest, 2011.

[20] S. T. Huxtable, D. G. Cahill, S. Shenogin, L. Xue, R. Ozisik, P. Barone, M. Usrey, M. S. Strano, G. Siddons, M. Shim, and P. Keblinski, "Interfacial heat flow in carbon nanotube suspensions," *Nat. Mater.*, vol. 2, no. 11, pp. 731–4, Nov. 2003.

[21] E. Lizundia, A. Oleaga, A. Salazar, and J. R. Sarasua, "Nano and microstructural effects on thermal properties of poly (l-lactide)/multi-wall carbon nanotube composites," *Polymer (Guildf).*, vol. 53, no. 12, pp. 2412–2421, May 2012.

[22] M. Martin-Gallego, R. Verdejo, M. Khayet, J. M. O. de Zarate, M. Essalhi, and M. A. Lopez-Manchado, "Thermal conductivity of carbon nanotubes and graphene in epoxy nanofluids and nanocomposites," *Nanoscale Res. Lett.*, vol. 6, no. 1, p. 610, Jan. 2011.

[23] a Moisala, Q. Li, I. Kinloch, and A. Windle, “Thermal and electrical conductivity of single and multi-walled carbon nanotube-epoxy composites,” *Compos. Sci. Technol.*, vol. 66, no. 10, pp. 1285–1288, Aug. 2006.

[24] S. Han and D. D. L. Chung, “Increasing the through-thickness thermal conductivity of carbon fiber polymer–matrix composite by curing pressure increase and filler incorporation,” *Compos. Sci. Technol.*, vol. 71, no. 16, pp. 1944–1952, Nov. 2011.

[25] Y. a. Kim, S. Kamio, T. Tajiri, T. Hayashi, S. M. Song, M. Endo, M. Terrones, and M. S. Dresselhaus, “Enhanced thermal conductivity of carbon fiber-phenolic resin composites by the introduction of carbon nanotubes,” *Appl. Phys. Lett.*, vol. 90, no. 9, p. 093125, 2007.

[26] S. Tzeng and Y. Lin, “Thermal conductivity of carbon fiber fabric-phenolic resin composites with CNT or CNF addition,” in *Annual World Conference on Carbon, Clemson US*, 2010, pp. 188–189.

[27] S. Wang and J. Qiu, “Enhancing thermal conductivity of glass fiber-polymer composites through carbon nanotubes incorporation,” *Compos. Part B Eng.*, vol. 41, no. 7, pp. 533–536, Oct. 2010.

[28] M. Zimmer, Q. Cheng, S. Li, J. Brooks, R. Liang, B. Wang, and C. Zhang, “Comparative characterization of multiscale carbon fiber composite with long and short MWCNTs at higher weight fractions,” *J. Nanomater.*, vol. 2012, pp. 1–9, 2012.

[29] B. Ashrafi, A. M. Díez-Pascual, L. Johnson, M. Genest, S. Hind, Y. Martinez-Rubi, J. M. González-Domínguez, M. Teresa Martínez, B. Simard, M. a. Gómez-Fatou, and A. Johnston, “Processing and properties of PEEK/glass fiber laminates: Effect of addition of single-walled carbon nanotubes,” *Compos. Part A Appl. Sci. Manuf.*, vol. 43, no. 8, pp. 1267–1279, Aug. 2012.

[30] D. C. Blest, S. McKee, A. K. Zulkifle, and P. Marshall, “Curing simulation by autoclave resin infusion,” *Compos. Sci. Technol.*, vol. 59, pp. 2297–2313, 1999.

[31] J. H. Oh and D. G. Lee, “Cure cycle for thick glass-epoxy composite laminates,” *J. Compos. Mater.*, vol. 36, no. 1, pp. 19–45, 2002.

[32] A. C. Caba, D. Rattazzi, R. Batra, and A. C. Loos, “Verification of a simulation model for RFI of complex shaped composite structures,” *J. Reinf. Plast. Compos.*, vol. 18, no. 16, pp. 1465–1478, 1999.

[33] Y. Yang, F. Robitaille, and S. Hind, “Thermal conductivity of carbon fiber fabrics,” in *19th International Conference on Composite Materials, Montreal Canada*, 2013, pp. 1–10.

[34] X. Huang, “Fabrication and properties of carbon fibers,” *Materials (Basel).*, vol. 2, pp. 2369–2403, Dec. 2009.

[35] S. W. Beckwith, “Composites reinforcement fibers : III - The carbon and graphite families (Part B),” in *SAMPE 49th International Symposium and Exhibition*, 2011, vol. 47, no. 3, pp. 44–45.

[36] A. Mortensen, *Concise Encyclopedia of Composite Materials*. Netherlands: Elsevier, 2007, pp. 93–95.

[37] C. Zweben, “Emerging high-volume applications for advanced thermally conductive materials,” in *49th International Symposium and Exhibition, California US*, 2004, pp. 1–12.

[38] D. Chung, *Carbon Fiber Composites*. Massachusetts: Butterworth-Heinemann, 1994, pp. 9–10.

[39] M. S. Dresselhaus, G. Dresselhaus, and P. Avouris, *Carbon Nanotubes: Synthesis, Structure, Properties and Applications*. Berlin, Germany: Springer-Verlag, 2001, pp. 21–23.

[40] Missile Defense Agency-National Technology Transfer Center, “Vapor grown carbon fibers,” 2008. .

[41] F. W. J. Van Hattum, “Report: A study of the mechanical properties of vapour grown carbon fibres and carbon fibre-thermoplastic composites,” *Univ. Minho, Spain*, 1999.

[42] J. Hou, X. Wang, and L. Zhang, “Thermal characterization of submicron polyacrylonitrile fibers based on optical heating and electrical thermal sensing,” *Appl. Phys. Lett.*, vol. 89, no. 15, 2006.

[43] J. X. Wei, “Report: Carbon fiber thermal conductivity measurement and analysis,” *Beijing Institue Mater. Sci. Technol. Div.*, 1989.

[44] Toray, “T300 DATA SHEET CARBON,” pp. 6–7.

[45] H. A. Katzman, P. M. Adams, T. D. Le, and C. S. Hemminger, “Characterization of low thermal conductivity pan-based carbon fibers,” *Carbon N. Y.*, vol. 32, no. 3, pp. 379–391, Jan. 1994.

[46] L. Qiu, X. H. Zheng, J. Zhu, G. P. Su, and D. W. Tang, “The effect of grain size on the lattice thermal conductivity of an individual polyacrylonitrile-based carbon fiber,” *Carbon N. Y.*, vol. 51, pp. 265–273, Jan. 2013.

[47] T. Yamane, S. Katayama, M. Todoki, and I. Hatta, “The measurments of thermal conductivity of carbon fibres,” *J. Wide Bandgap Mater.*, vol. 7, no. 4, pp. 294–305, Apr. 2000.

[48] Hexcel, “IM10 carbon fiber product datasheet,” 2010.

[49] Hexcel, “IM7 carbon fiber product datasheet,” 2010.

[50] Hexcel, “AS4 carbon fiber product datasheet,” 2010.

[51] S. Hind, “Predicting and measuring thermal conductivity in carbon-epoxy unidirectional tape and textile reinforced composites-MASc,” University of Ottawa, 2008.

[52] T. Tenax, “Tenax HTS carbon fiber product datasheet,” 2011.

[53] BP Amoco Chemicals, “Thornel carbon fibers product datasheet,” 2012.

[54] S. Hind and F. Robitaille, “Measurement , modeling , and variability of thermal conductivity for structural polymer composites,” *Polym. Compos.*, vol. 31, no. 5, pp. 847–857, 2010.

[55] R. C. Wetherhold and J. Wang, “Difficulties in the theories for predicting transverse thermal conductivity of continuous fiber composites,” *J. Compos. Mater.*, vol. 28, no. 15, pp. 1491–1498, Sep. 1994.

[56] Cytec, “Thornel 50 carbon fibre properties,” 2013.

[57] H. J. Lee and R. E. Taylor, “Thermophysical properties of carbon/graphite fibers and MOD-3 fiber-reinforced graphite,” *Carbon N. Y.*, vol. 13, no. 6, pp. 521–527, Jan. 1975.

[58] M. Matusiak, “Investigation of the thermal insulation properties of multilayer textiles,” *J. Fibres Text.*, vol. 14, no. 5, pp. 98–102, 2006.

[59] M. Uzun, “Ultrasonic washing effect on thermo physiological properties of natural based fabrics,” *J. Eng. Fibres Fabr.*, vol. 8, no. 1, pp. 39–51, 2013.

[60] E. Onofrei, A. M. Rocha, and A. Catarino, “The influence of knitted fabrics’ structure on the thermal and moisture management properties,” *J. Eng. Fibres Fabr.*, vol. 6, no. 4, pp. 10–22, 2011.

[61] M. Matusiak and K. Sikorski, “Influence of the structure of woven babrics on their thermal insulation properties,” *J. Fibres Text.*, vol. 19, no. 5, pp. 46–53, 2011.

[62] M. Ziaei and M. Ghane, “Thermal insulation property of spacer fabrics integrated by ceramic powder impregnated fabrics,” *J. Ind. Text.*, vol. 43, no. 1, pp. 20–33, May 2013.

[63] I. Cerkez, H. B. Kocer, and R. M. Broughton, “A practical cost model for selecting nonwoven insulation materials,” *J. Eng. Fibres Fabr.*, vol. 7, no. 1, pp. 1–9, 2012.

[64] N. V Bol’shakova, O. M. Kostenok, A. M. Il’in, and V. I. Kostyukhin, “Thermal conductivity of carbon-graphite fibres and fabrics,” *J. Therm. Eng.*, no. 9, pp. 524–527, 1991.

[65] Cytec, “Thornel VCB-20 carbon fibre cloth datasheet,” 2012.

[66] Z. Han and A. Fina, “Thermal conductivity of carbon nanotubes and their polymer nanocomposites: A review,” *Polym. Sci.*, vol. 36, no. 7, pp. 914–944, Jul. 2011.

[67] G. S. Springer and S. W. Tsai, “Thermal conductivities of unidirectional materials,” *J. Compos. Mater.*, vol. 1, no. 2, pp. 166–173, Jan. 1967.

[68] W. A. Clayton, “Report: Thermal conductivity of phenolic-carbon chars,” *Boeing Co.*, pp. 1–181, 1969.

[69] A. Dasgupta and R. K. Agarwal, “Orthotropic thermal conductivity of plain-weave fabric composites using a homogenization technique,” *J. Compos. Mater.*, vol. 26, no. 18, pp. 2736–2758, Jan. 1992.

[70] R. C. Progelhof, J. L. Throne, and R. Ruetsch, “Methods for predicting the thermal conductivity of composite systems: a review,” *Polym. Eng. Sci.*, vol. 76, no. 9, pp. 615–625, 1976.

[71] R. Pal, “On the Lewis-Nielsen model for thermal and electrical conductivity of composites,” *Compos. Part A Appl. Sci. Manuf.*, vol. 39, no. 5, pp. 718–726, May 2008.

[72] S. W. Tsai and H. Hahn, *Introduction to Composite Materials*. Pennsylvania, USA: Technomic Publishing, 1980.

[73] M. W. Pilling, B. Yates, M. a. Black, and P. Tattersall, “The thermal conductivity of carbon fibre-reinforced composites,” *J. Mater. Sci.*, vol. 14, no. 6, pp. 1326–1338, Jun. 1979.

[74] A. F. Kregers, I. A. Repelis, and A. M. Tolks, “Heat conductivity of a fibre-reinforced composite and of its components,” *Mech. Compos. Mater.*, no. 4, pp. 407–412, 1988.

[75] D. J. Radcliffe and H. M. Rosenberg, “The thermal conductivity of glass-fibre and carbon-fibre/epoxy composites from 2 to 80 K,” *Cryogenics (Guildf).*, vol. 22, no. 5, pp. 245–249, 1982.

[76] B. Nysten and J.-P. Issi, “Composites based on thermally hyperconductive carbon fibres,” *Composites*, vol. 21, no. 4, pp. 339–343, Jul. 1990.

[77] Y. Gowayed and J. C. Hwang, “Thermal conductivity of composite materials made from plain weaves and 3D weaves,” *Compos. Eng.*, vol. 5, no. 9, pp. 1177–1186, 1995.

[78] A. F. Kregers and Y. G. Melbardis, “Calculation of the deformability of a three-dimensionally reinforced composite with an elastoplastic matrix,” *Mech. Compos. Mater.*, vol. 18, no. 4, pp. 408–413, 1982.

[79] Q. G. Ning and T. W. Chou, “A general anaytical model for predicting the transverse effective thermal conductivities of woven fabric composites,” *Compos. Part A Appl. Sci. Manuf.*, pp. 315–322, 1998.

[80] A. Dasgupta, R. K. Agarwal, and M. Bhandarkar, “Three dimensional modeling of woven fabric composites for effective thermo-mechanical and thermal properties,” *Compos. Sci. Technol.*, vol. 56, pp. 209–223, 1996.

[81] N. S. Goo and K. Woo, “Measurement and prediction of effective thermal conductivity for woven fabric composites,” *Int. J. Mod. Phys. B*, vol. 17, no. 8, pp. 1808–1813, 2003.

[82] L. Ci, J. Suhr, V. Pushparaj, X. Zhang, and P. M. Ajayan, “Continuous carbon nanotube reinforced composites.,” *Nano Lett.*, vol. 8, no. 9, pp. 2762–6, Sep. 2008.

[83] Q. Li, C. Liu, X. Wang, and S. Fan, “Measuring the thermal conductivity of individual carbon nanotubes by the Raman shift method,” *Nanotechnology*, vol. 20, no. 14, pp. 57–61, Apr. 2009.

[84] E. Pop, D. Mann, Q. Wang, K. Goodson, and H. Dai, “Thermal conductance of an individual single-wall carbon nanotube above room temperature,” *Nano Lett.*, vol. 6, no. 1, pp. 96–100, Jan. 2006.

[85] Y. Gu and Y. Chen, “Thermal conductivities of single-walled carbon nanotubes calculated from the complete phonon dispersion relations,” *Phys. Rev. B*, vol. 76, no. 13, pp. 41–48, Oct. 2007.

[86] J. R. Lukes and H. Zhong, “Thermal Conductivity of Individual Single-Wall Carbon Nanotubes,” *J. Heat Transfer*, vol. 129, no. 6, p. 705, 2007.

[87] A. Cao and J. Qu, "Size dependent thermal conductivity of single-walled carbon nanotubes," *J. Appl. Phys.*, vol. 112, no. 1, pp. 35–43, 2012.

[88] P. Kim, L. Shi, A. Majumdar, and P. McEuen, "Thermal transport measurements of individual multiwalled nanotubes," *Phys. Rev. Lett.*, vol. 87, no. 21, pp. 55–58, Oct. 2001.

[89] T.-Y. Choi, D. Poulikakos, J. Tharian, and U. Sennhauser, "Measurement of the thermal conductivity of individual carbon nanotubes by the four-point three-omega method.," *Nano Lett.*, vol. 6, no. 8, pp. 1589–93, Aug. 2006.

[90] D. De Koninck, "Thermal Conductivity Measurements Using the 3-Omega Technique: Application to Power Harvesting Microsystems-MASc," McGill University, 2008.

[91] M. Fujii, X. Zhang, H. Xie, H. Ago, K. Takahashi, T. Ikuta, H. Abe, and T. Shimizu, "Measuring the thermal conductivity of a single carbon nanotube," *Phys. Rev. Lett.*, vol. 95, no. 6, pp. 55–58, Aug. 2005.

[92] B. MaterialScience, "Baytubes C150P product datasheet," 2006.

[93] Nanocyl, "Multi-Wall Carbon Nanotubes," 2009. [Online]. Available: http://www.nanocyl.com/CNT-Expertise-Centre/Carbon-Nanotubes/Multi-wall-Nanotubes-MWNT. [Accessed: 14-Jun-2013].

[94] CheapTubesInc, "Pricing of SWCNTs and MWCNTs Cheap Tubes Inc.," 2009. [Online]. Available: http://www.cheaptubesinc.com/carbon-nanotubes-prices.htm#Single_Walled_Nanotubes_Prices. [Accessed: 14-Jun-2013].

[95] Nanothinx, "Pricing of MWCNTs Nanothinx," Rio Patras, Greece, 2013.

[96] NanoLab, "Pricing of SWCNTs and MWCNTs," 2011. [Online]. Available: http://www.nano-lab.com/nanotubes-industrialgrade.html. [Accessed: 14-Jun-2013].

[97] HelixMaterialSolutions, "Pricing of SWCNTs and MWCNTs," 2012. [Online]. Available: http://www.helixmaterial.com/Ordering.html. [Accessed: 14-Jun-2013].

[98] S. Shenogin, a. Bodapati, L. Xue, R. Ozisik, and P. Keblinski, "Effect of chemical functionalization on thermal transport of carbon nanotube composites," *Appl. Phys. Lett.*, vol. 85, no. 12, p. 2229, 2004.

[99] Z. Spitalsky, L. Matejka, M. Slouf, E. N. Kunyoshento, J. Korvarova, J. Zemek, and J. Kotek, "Modification of carbon nanotubes and its effect on properties of carbon nanotube-epoxy nanocomposites," *Polym. Compos.*, vol. 30, pp. 1378–1387, 2009.

[100] C.-W. Nan, G. Liu, Y. Lin, and M. Li, "Interface effect on thermal conductivity of carbon nanotube composites," *Appl. Phys. Lett.*, vol. 85, no. 16, p. 3549, 2004.

[101] Y. Xu, G. Ray, and B. Abdel-Magid, "Thermal behavior of single-walled carbon nanotube polymer–matrix composites," *Compos. Part A Appl. Sci. Manuf.*, vol. 37, no. 1, pp. 114–121, Jan. 2006.

[102] G. a Niklasson, C. G. Granqvist, and O. Hunderi, "Effective medium models for the optical properties of inhomogeneous materials.," *Appl. Opt.*, vol. 20, no. 1, pp. 26–30, Jan. 1981.

[103] C. Nan, T. Physik, U. Saarlandes, and D.- Saarbrucken, "Inverse problem for composites with imperfect interface: determination of interfacial thermal resistance, thermal conductivity of constituents and microstructural parameters," *Am. Ceram. Soc.*, vol. 83, no. 4, pp. 848–854, 2000.

[104] P. Nihar, "Thermal conductivity of nanowires, nanotubes and polymer-nanotube composites," Worcester Polytechnic Institute, 2010.

[105] J. G. Park, Q. Cheng, J. Lu, J. Bao, S. Li, Y. Tian, Z. Liang, C. Zhang, and B. Wang, "Thermal conductivity of MWCNT-epoxy composites: the effects of length, alignment and functionalization," *Carbon N. Y.*, vol. 50, no. 6, pp. 2083–2090, May 2012.

[106] H. Sinaei and S. V Hoa, "Improvement of thermal conductivity of epoxy resin for the manufacturing of thick composites," in *25th American Society for Composites Conference*, 2010, pp. 1139–1148.

[107] K. Yang, M. Gu, Y. Guo, X. Pan, and G. Mu, "Effects of carbon nanotube functionalization on the mechanical and thermal properties of epoxy composites," *Carbon N. Y.*, vol. 47, no. 7, pp. 1723–1737, Jun. 2009.

[108] M. Nadler, T. Mahrholz, U. Riedel, C. Schilde, and A. Kwade, "Preparation of colloidal carbon nanotube dispersions and their characterisation using a disc centrifuge," *Carbon N. Y.*, vol. 46, no. 11, pp. 1384–1392, Sep. 2008.

[109] TAInstruments, "Thermal analysis: an introduction."

[110] M. R. Kamal and S. Sourour, "Kinetics and thermal characterization of thermoset cure," *Polym. Eng. Sci.*, vol. 13, no. 1, pp. 59–64, Jan. 1973.

[111] Z.-S. Guo, S. Du, and B. Zhang, "Temperature distribution of thick thermoset composites," *Model. Simul. Mater. Sci. Eng.*, vol. 12, no. 3, pp. 443–452, May 2004.

[112] H. Xie, B. Liu, Q. Sun, Z. Yuan, J. Shen, and R. Cheng, "Cure kinetic study of carbon nanofibers-epoxy composites by isothermal DSC," *J. Appl. Polym. Sci.*, vol. 96, no. 2, pp. 329–335, Apr. 2005.

[113] H. Xie, B. Liu, Z. Yuan, J. Shen, and R. Cheng, "Cure kinetics of carbon nanotube-tetrafunctional epoxy nanocomposites by isothermal differential scanning

calorimetry," *J. Polym. Sci. Part B Polym. Phys.*, vol. 42, no. 20, pp. 3701–3712, Oct. 2004.

[114] M. R. Kamal, "Thermoset characterization for moldability analysis," *Polym. Eng. Sci.*, vol. 14, no. 3, pp. 231–239, 1974.

[115] K. C. Cole, "A new approach to modeling the cure kinetics of epoxy-amine thermosetting resins-mathematical development," *Macromolecules*, vol. 24, no. 11, pp. 3093–3097, May 1991.

[116] M. Chapartegui, S. Florez, C. Elizetxea, M. Fernandez, and A. Santamaria, "Carbon nanotubes accelerate epoxy resin curing," *Society of Plastics Engineers*, Jul-2011. [Online]. Available: http://linkinghub.elsevier.com/retrieve/pii/S0032386108004011. [Accessed: 23-May-2013].

[117] I. El Sawi, P. A. Olivier, P. Demont, and H. Bougherara, "Investigation of the effect of double-walled carbon nanotubes on the curing reaction kinetics and shear flow of an epoxy resin," *J. Appl. Polym. Sci.*, vol. 126, pp. 358–366, 2012.

[118] A. Allaoui and N. Bounia, "How carbon nanotubes affect the cure kinetics and glass transition temperature of their epoxy composites – a review," *Express Polym. Lett.*, vol. 3, no. 9, pp. 588–594, Aug. 2009.

[119] Incropera, DeWitt, Bergman, and Lavine, *Fundamentals of Heat and Mass Transfer*, 6th ed. Denvers, USA: John Wiley and Sons, 2007.

[120] S. C. Joshi, X. L. Liu, and Y. C. Lam, "A numerical approach to the modeling of polymer curing in fibre-reinforced composites," *Compos. Sci. Technol.*, vol. 59, pp. 1003–1013, 1999.

[121] I. L. Lee, A. C. Loos, and G. S. Springer, "Heat of reaction, degree of cure and viscosity of Hercules 3501-6 resin," *J. Compos. Mater.*, vol. 16, pp. 510–520, 1982.

[122] C. Chamis, "Simplified composite micromechanics equations for hygral, thermal and mechanical properties," in *38th Annual Conference of the Society of Plastics Industry*, 1983, pp. 1–9.

[123] Hukseflux, "Hukseflux thermal conductivity measurement systems," 2013. [Online]. Available: http://www.hukseflux.com/product_group/thermal-conductivity. [Accessed: 30-Jul-2013].

[124] Hukseflux, "THISYS device manual," vol. 0817. .

[125] Hukseflux, "THASYS device manual," vol. 0801. Netherlands.

[126] Airtech, "Datasheet for Dahlar release film 125," no. 714. 2004.

[127] EngineeringToolbox, “Properties of air,” 2013. [Online]. Available: http://www.engineeringtoolbox.com/air-properties-d_156.html. [Accessed: 29-Jul-2013].

[128] Axson, “Datasheet for LEO 2376 epoxy resin.” 2011.

[129] BayerMaterialScience, “Datasheet for Baytubes C150P.” 2008.

[130] CheapTubesInc, “Specifications for MWCNTS from CheapTubes.” 2009.

[131] Axson, “Material Safety Data Sheet for 2376 epoxy resin.” 2009.

[132] V. Choudhary and A. Gupta, “Report: Polymer-carbon nanotube nanocomposites,” 2001.

[133] Airtech, “Datasheet for Dahlar 125 release film,” no. 714. 2004.

[134] Airtech, “Datasheet for Securlon L1000 v.” 2010.

[135] Airtech, “Datasheet for WL5200 release films,” vol. 8100, no. 714. 2005.

[136] D. Wheeler, *Understanding Industrial Experimentation*, 2nd ed. Tennessee, USA: SPC Press, 1990.

[137] H. Huang and R. Talreja, “Effects of void geometry on elastic properties of unidirectional fiber reinforced composites,” *Compos. Sci. Technol.*, vol. 65, no. 13, pp. 1964–1981, Oct. 2005.

[138] S. Ghiorse, “Effect of void content on the mechanical properties of carbon fibre-epoxy laminates,” *SAMPE*, vol. 24, no. 2, 1993.

[139] J. R. Shewchuk, “What is a good linear finite element: interpolation, conditioning, anisotropy and quality measures,” in *11th International Meshing Roundtable, New York US*, 2002.

[140] J. R. Rice, “Report: The aspect ratio significant for finite element problems,” *Purdue Univ.*, 1985.

[141] T. E. Tezduyar and Y. Osawa, “Finite element stabilization parameters computed from element matrices and vectors,” *Comput. Methods Appl. Mech. Eng.*, vol. 190, no. 3–4, pp. 411–430, Oct. 2000.

[142] Axson, “Datasheet for AKD 2396 epoxy.” 2000.

[143] Airtech, “Datasheet for UltraWeave 606,” no. 714. 2005.

[144] N. Slesinger, T. Shimizu, A. Arafath, and PoursartipA, “Heat transfer coefficient distribution inside an autoclave,” in *17th International Conference for Composite Materials*, 2009.

[145] A. Yu, P. Ramesh, X. Sun, E. Bekyarova, M. E. Itkis, and R. C. Haddon, “Enhanced Thermal Conductivity in a Hybrid Graphite Nanoplatelet - Carbon Nanotube Filler for Epoxy Composites,” *Adv. Mater.*, vol. 20, no. 24, pp. 4740–4744, Dec. 2008.

Appendix A – Dimensional Measurements of Resin and Composite Plates

Dimensional measurements of resin plates

Plate #	Plate	Length			Width			Thickness			Length	Width	Thickness
1	1	109.87	109.86	109.94	69.02	69.33	70.23	3.77	3.67	3.84	109.89	69.53	3.76
	2	109.60	109.38	109.25	69.53	69.20	68.62	3.73	3.81	3.70	109.41	69.11	3.75
2	1	108.43	108.71	108.68	68.78	69.09	69.10	2.04	2.06	2.14	108.61	108.71	2.08
	2	108.57	108.37	108.80	68.64	68.61	68.62	2.02	1.99	2.10	108.58	68.62	2.04
3	1	106.40	106.75	106.27	68.84	68.74	68.56	1.74	1.85	1.94	106.47	68.71	1.84
4	1	114.20	114.18	114.22	65.05	65.05	65.07	2.15	2.29	2.31	114.2	65.06	2.25
	2	114.28	114.25	114.21	66.56	66.56	66.57	2.21	2.10	2.27	114.25	66.56	2.19
5	1	107.84	107.57	107.85	67.21	67.77	68.57	2.43	2.57	2.37	107.75	67.85	2.46
	2	107.36	106.92	107.58	68.17	68.86	69.03	2.55	2.61	2.54	107.29	68.69	2.57
6	1	107.58	107.42	107.11	68.44	67.95	67.95	5.52	5.47	5.35	107.37	68.11	5.45
	2	107.81	108.51	108.74	69.40	69.35	69.08	5.43	5.38	5.44	108.35	69.28	5.42

Dimensional measurements of Plackett-Burman composite plates

Plate #	Plate	Length			Width			Thickness			Length	Width	Thickness
1	3	98.96	98.75	98.52	69.79	70.39	71.14	4.01	4.04	4.05	98.74	70.44	4.03
	4	96.84	96.68	96.87	69.10	69.51	69.88	4.01	4.07	4.11	96.8	69.50	4.06
2	3	95.79	96.15	96.64	67.65	67.90	68.11	4.11	4.10	4.08	96.19	67.89	4.10
	4	94.63	94.63	94.73	68.20	68.37	68.62	4.01	4.07	4.10	94.66	68.40	4.06
3	4	100.44	100.80	101.24	71.66	70.78	69.85	4.54	4.47	4.51	100.83	70.76	4.51
	6	100.53	101.15	101.37	68.49	68.33	69.03	4.52	4.45	4.52	101.02	68.62	4.50
4	1	98.32	97.86	97.23	70.68	70.99	71.27	4.47	4.47	4.45	97.80	70.98	4.46
	2	98.60	98.37	98.14	70.41	70.36	70.30	4.49	4.47	4.45	98.37	70.36	4.47
5	3	95.74	95.84	95.91	70.46	70.10	69.88	4.16	4.21	4.23	70.15	70.15	4.20
	6	96.11	96.15	95.89	68.33	68.84	69.10	4.16	4.16	4.17	68.76	68.76	4.16
6	3	98.60	98.75	98.50	68.89	68.81	68.77	4.21	4.25	4.25	68.82	98.62	4.24
	4	97.42	97.36	97.39	70.01	69.79	69.73	4.13	4.15	4.22	69.84	97.39	4.17
7	1	95.17	95.28	95.18	69.89	69.83	69.81	4.24	4.18	4.29	95.21	69.84	4.24
	2	94.44	94.39	94.56	69.62	69.74	69.32	4.32	4.28	4.23	94.46	69.56	4.28
8	3	95.40	95.93	95.15	68.39	68.37	68.65	4.40	4.41	4.39	95.49	68.47	4.40
	6	93.45	93.81	94.20	68.37	68.37	68.46	4.34	4.41	4.27	93.82	68.40	4.34
9	4	100.49	100.67	101.08	67.87	67.67	67.40	3.90	3.89	3.89	100.75	67.65	3.89
	6	100.92	100.97	100.79	70.07	69.76	69.64	4.00	3.99	3.99	100.89	69.82	3.99
10	1	100.62	100.71	100.87	72.46	72.51	72.32	4.15	4.20	4.22	100.73	72.43	4.19
	6	97.00	97.01	96.94	71.58	71.41	71.34	4.23	4.24	4.21	96.98	71.44	4.23
11	3	100.12	99.66	99.34	68.83	68.70	68.43	4.40	4.44	4.36	99.71	68.65	4.40
	4	98.00	97.86	97.76	68.48	68.20	68.04	4.35	4.35	4.53	99.87	68.24	4.41
12	4	98.66	98.79	98.90	71.12	70.91	70.43	4.49	4.46	4.41	98.78	70.82	4.45
	6	98.60	98.53	98.38	72.13	71.88	71.93	4.46	4.47	4.41	98.50	71.98	4.45

Appendix B – Resin Datasheets

Gurit SA70 epoxy resin

SA 70

Epoxy Adhesive Film

- Low temperature cure
- Designed for bonding prepreg skins to honeycomb and certain foam cores
- Compatible with SE 70 prepregs
- Toughened for impact resistance and peel strength
- Controlled flow for maximum bond integrity

Introduction

SA 70 adhesive film is a toughened epoxy film on a glass carrier with excellent tack and drape characteristics. It offers many advantages over traditional wet lay-up techniques for bonding of composite skins to cores, including: consistent bond-line thickness and weight, high strain to failure, high toughness, handling convenience, controlled flow and a 4 week outlife at ambient temperature (21°C).

Instructions For Use

Core bonding

Various core materials can be used with the adhesive film system, including certain foams (provided that special procedures are followed) and honeycombs.

The system is fully compatible with all SE and ST prepreg and SPRINT® systems and also Ampreg 22, Ampreg 26 and Ampreg Pregel liquid epoxy systems.

Nomex or Aluminium honeycomb cores

1. Core to First Skin

For bonding honeycomb into place onto a cured laminate, a minimum of a 250g/m² film should be used, with extra resin film used where there are any steps, wrinkles or unevenness in the laminate. Apply the film over the laminate with the paper side uppermost then remove the release paper. Bed in the honeycomb core to the film and splice the core segments with a wrap of at least two layers of film applied to each honeycomb edge. After positioning all the core pieces, vacuum the core in place using at least 80% vacuum and cure the adhesive film for a minimum of 8 hours at 70-75°C. The full cure required will be achieved when the outer skin is cured and bonded into place, using one of the cure cycles below.

2. Second Skin to Core

One procedure is to co-cure the outer skin together with the core bond. For this, a single layer of 250g adhesive film should be rolled over the honeycomb surface, and bedded well into the cells. In this way it should be possible to reposition misplaced prepreg plies, without disturbing the adhesive layer. With a controlled flow system such as SE 70, care should be taken to ensure that excess resin is not removed from the adhesive interface, by using a fine microporous release film. **It is also critical when using this process that adequate precautions are taken to perforate the SE70/SA70 skin to allow air removal from the Nomex prior to gelation. Failure to do so will result in skin blow off** (contact Gurit Technical Services or see SE 70 / SA 70 Processing Notes).

Foam Cores

SAN based polymer foams (**Core**cell) can be processed with SA 70 without the need for any special treatment on the foam. A layer of 250gms glue film should be used for both the first and second skin as a minimum. Usually the lower density needs higher film weight to fill the more open cell structure (PVC foams). Care must be taken if processing temperatures exceed 80°C, as **Core**cell foam can be dimensionally unstable above these temperatures. SA 70 is not compatible with untreated PVC foams. Contact Gurit Technical Services.

Properties

Uncured Resin Properties			
Adhesive Film Weight (standard products)	150gm²	250gm²	400gm²
Glass Carrier Weight	25gm²	25gm²	25gm²
Total Film Weight	175gm²	275gm²	425gm²
Resin Colour	Turquoise blue		
Stability @ 21°C	4 weeks		
Stability @ -18°C	1 year		
Hazard definiton	Xi, N		

B.2 Nanoledge LEO/AKD 2376 epoxy resin

NANOLEDGE

High Performance | Nanoparticles | Eco-friendly

LEO 2376 - DATASHEET

Introduction

LEO 2376 is a 100% semi-solid resin film. It is designed for RFI process to manufacture composite parts with carbon or glass fabrics or UD tapes.

LEO 2376 semi-solid resin film is the top quality solution to:
- EASILY MANUFACTURE COMPOSITE by fast stacking of RESIN FILM onto fibers
- AVOID HEAVY CLEANING of production equipments
- COMPLY WITH ENVIRONMENTAL CONCERNS by limiting waste disposal.

LEO 2376 is specially designed to meet Aerospace requirements in terms of performance and process. It provides temperature resistance up to 170°C (338°F).

Typical handling properties

Property	*Unit*	*Value*
Film density	g/m²	40 to 400
Color		Transparent
Physical form		Semi-solid
Tack @ 25°C (77°C)		Low

Typical physical properties

Property	*Unit*	*Value*
Viscosity @ 60°C (140°F)	mPa.s	190 000
Glass transition Tg	°C (°F)	160 (320)
Glass transition after autoclave curing	°C (°F)	180 (356)

Property[1]	*Unit*	*Value*
G_IC Initiation (Mode I)	J/m²	172
G_IC Propagation (Mode I)	J/m²	425

1. Data on 8 layers carbon fabric composite cured in autoclave

Packaging and Storage

LEO 2376 semi-solid resin film is available in 60 cm width rollers. Rollers length varies from 50 to 200 m depending on the film density.

LEO 2376 system must be stored at low temperature (-18°C / 0°F) in a dry place (humidity < 75%).

LEO 2376 system shelf-life: 6 months at -18°C (0°F).

For more information on packaging and storage, consult Nanoledge.

RFI processing instructions

LEO 2376 semi-solid resin film has a good drapeability and a very low tack at 25°C. It is thereby very easy to use for composite part manufacturing.

Please refer to following instructions for making composite parts by RFI:

1. Cut the LEO 2376 semi-solid resin film and fabrics or UD tapes to reach the optimal design.
2. Remove the release paper and stack strongly the LEO 2376 semi-solid resin film onto the fabric or UD tape. It is advised to perform the stacking at room temperature (23-27°C / 73-80°F). If the LEO 2376 semi-solid resin film temperature is under 25°C (77°F), do not hesitate to gently heat the film while stacking the film.
   Then remove the support paper.
3. To ensure the impregnation of resin into the fabric or UD tape, it is advised to alternate resin and fiber layers.

Infusion vacuum pressure advised is 14 bars (200psi).
Typical curing cycle is 130°C (266°F) during 2 hours and 200°C (392°F) during 2 hours.
The heating rate is around 1.5-2°C/min (3°F/min).

B.3 Nanoledge LEO/AKD 2396 epoxy resin

NANOLEDGE

High Performance I Nanoparticles I Eco-friendly

AKD 2396 – Datasheet

AKD 2396 is a high performance epoxy system for prepreg manufacturing. AKD 2396 semi-solid resin ensures:

- High temperature resistance up to 355°F
- Low viscosity during process for optimal fabric wetting and complex shape part manufacturing

AKD 2396 is also available as semi solid resin film (LEO 2396) for an easiest way to manufacture composites.

Typical handling properties

Property	AKD 2396
Color	Light yellow
Physical form	Semi-solid
Tack @ 77°F (25°C)	Low

Typical rheological properties

Property	Unit	AKD 2396
Viscosity @ 140°F (60°C)	mPa.s	61,000
Viscosity @ 158°F (70°C)	mPa.s	18,500
Viscosity @ 176°F (80°C)	mPa.s	8,600

Processing

AKD 2396 semi-solid resin reaches a suitable viscosity for fabric wetting at a temperature ranging from 140 to 167°F (60 to 75°C).

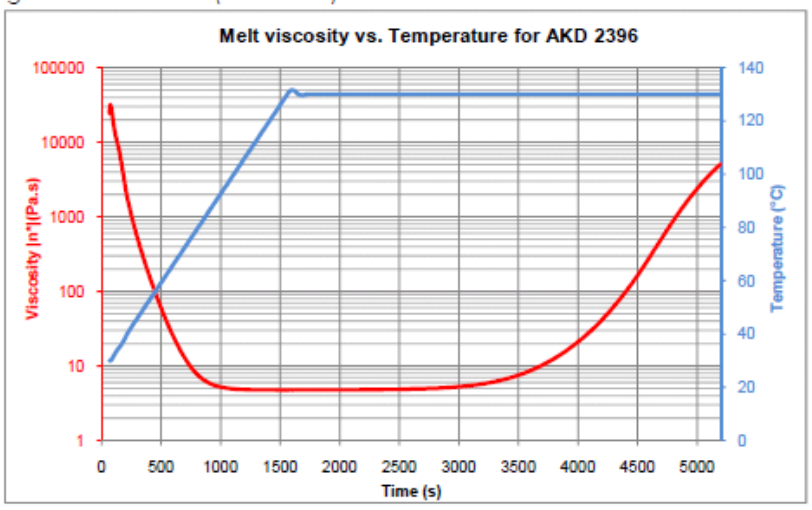

NANOLEDGE

High Performance | Nanoparticles | Eco-friendly

Curing cycle

Full performance of the AKD 2396 semi-solid resin will be reached after a post-cure of:

2 hours at 266°F (130°C) + 2 hours at 392°F (200°C)

Heating ramp of 3 °F (around 1.5-2°C) is recommended to optimize the impregnation of the resin system into the fabric.

Typical thermal properties

Method	*Unit*	*Glass transition temperatures*
DMA- Storage Modulus	°F (°C)	**350 (176)**
DMA- Loss Modulus peak		**356 (180)**
DMA- tan δ		**390 (199)**
DSC		**356 (180)**

DMA Analysis for AKD 2396

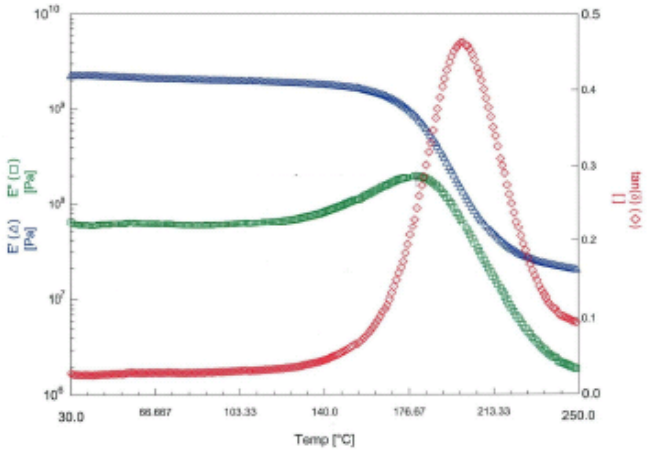

Storage

AKD 2396 system must be stored at low temperature (0°F /-18°C). In those conditions, shelf-life is 6 months.

B.4 Bayer Material Science Baytubes C150P

Bayer MaterialScience

baytubes® C 150 P

Agglomerate of Multi-Wall Carbon Nanotubes

Preliminary Data Sheet for Product Development

Baytubes® are agglomerates of multi-wall carbon nanotubes with low outer diameter, narrow diameter distribution and an ultra-high aspect ratio (length-to-diameter ratio). Baytubes® show excellent tensile strength and E-modulus, as well as exceptional thermal and electrical conductivity.

Properties of Multi-Wall Carbon Nanotubes (MWNT)

Tensile strength	> 10 GPa
E-modulus	> 1 TPa
Thermal conductivity	> 2000 W/mK
Electrical conductivity	> 10^4 S/cm

Baytubes® are produced in a high-yield catalytic process based on chemical vapor deposition. The process yields easy to handle agglomerates with low apparent density. The optimized process results in a high degree of purity (low concentration of free residual catalyst and absence of free amorphous carbon).

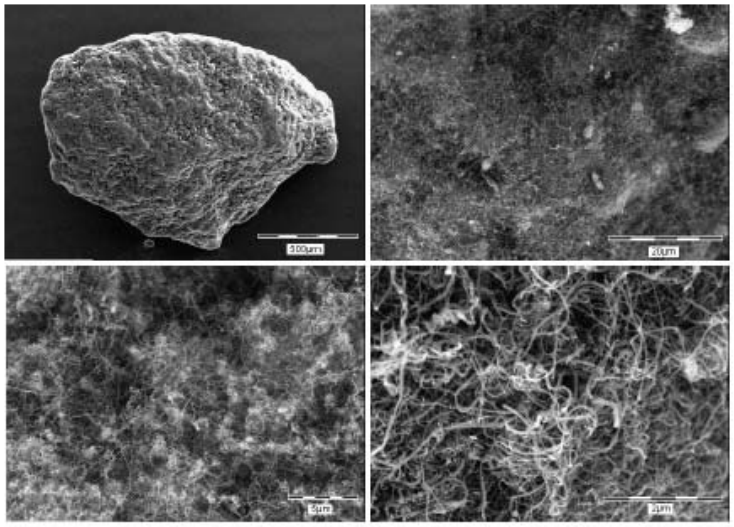

BAYTUBES® C 150 P

Typical values

Property	Value	Unit	Method
C-Purity	≥95	wt%	Calculated or ashing
Free amorphous carbon	Not detectable	wt%	TEM
Outer mean diameter	~13	nm	TEM
Inner mean diameter	~4	nm	TEM
Length	>1	µm	SEM
Bulk density	130-150	kg/m³	EN ISO 60
Loose agglomerate size (>90wt%)	0.1-1	mm	PSD

Length of Baytubes C150P after Dispersion:
Depending on the polymer matrix and the dispersion employed the length of Baytubes C 150 P varies between 0,2 – 1µm (TEM analysis)

For specification see the Product Data Sheet www.baytubes.com
www.bayercoatings.com

Disclaimer

Disclaimer for Development Products

This is a development product. Further information, including amended or supplementary data on hazards associated with its use, may be compiled in the future. For this reason no assurances are given as to type, conformity, processability, long-term performance, characteristics, or other production or application parameters. Therefore, the purchaser/user uses the product entirely at his own risk without having been given any warranty or guarantee, and agrees that the supplier shall not be liable for any damages, of whatever nature, arising out of such use. Commercialization and continued supply of this material are not assured. Its supply may be discontinued at any time.

Test Values

Unless specified to the contrary, the values given have been established to our best knowledge based on current production samples. The figures should be regarded as guide values only and not as binding minimum or maximum values. Under certain conditions, the properties can be affected to a considerable extent by further processing.

Processing Note

For incorporation of Baytubes® into polymers or other materials, the appropriate processing conditions of the corresponding polymers or materials have to be observed. Addition of Baytubes® into viscous materials may affect the viscosity. To preclude any risk to the health and well-being of people involved in the handling and processing of Baytubes®, tolerance limits for the work environment must be ensured by provision of efficient exhaust ventilation and fresh air at the workplace in accordance with the Baytubes® Safety Data Sheet. Application, use and processing of our products and the products manufactured by you on the basis of our technical advice are beyond our control and, therefore, entirely your own responsibility.

Editor:
Bayer MaterialScience AG,
D-51368 Leverkusen,

www.bayermaterialscience.com

Contact:
Tel. +49 214 30 21055
Fax +49 214 30 9621055

info@baytubes.com
www.baytubes.com

Appendix C – Polishing Procedure

1) Polish by hand on Silicone Carbide Waterproof Paper 240

2) Grind on machine with Piano 110
   Under Single Samples
   Med
   Wear
   1) Sic-Pap

   Put water over disk first then grind for 2 minutes. Repeat on other side

3) Grind on machine with Piano 220
   Under Single Samples
   Med
   Wear
   2) Sic-Pap

   Put water over disk first then grind for 2 minutes on the proper side. Repeat until grinding has gone through epoxy casting

4) Clean disk with brush and clean sample holder and samples. To clean grinding disk:
   Under Manual Prep
   160rpm
   Water ON
   Move outwards with brush

5) Put samples into beaker filled with water into ultrasonic machine for 5 minutes.

6) Put green LARGO disk on
   Check that there is ample 9µm fluid
   Refill with 50% 9 µm solution and 50% distilled water if needed
   Shake bottle well

7) Polish:
   First put 9µm fluid all over disk
   Under Sim Cu
   LARGO
   Polish for 2 minutes. Repeat until most large scratches are gone

8) Clean samples, head, disk with brush

9) Put white MOL disk on
   Check that there is ample 3µm fluid
   Refill with 50% 3 µm solution and 50% distilled water if needed

Shake bottle well

10) Polish:
    First put fluid all over disk before starting
    Sim Incl
    DAC
    Polish for 2 minutes. Repeat until most scratches are gone

11) Clean samples, head, disk with card

12) Get black CHEM disk
    Check that there is ample OPS fluid in large blue bottle
    Refill with 50% OPS solution and 50% distilled water if needed
    Shake bottle well

13) Polish:
    First put fluid on disk first
    Sim Cu
    Chem
    Polish for 1 minute
    Turn on water until OPS fluid flows out
    Then automatically polishing for another minute will start with water instead of the fluid
    Repeat CHEM until almost all scratches are gone

14) Clean samples, head, disk with a cleaning card

15) Clean out all the tubing that have been used:
    Take tubing out of bottle and put it in a cup filled with clean water
    Select the tube to clean and press F1 to start cleaning. Repeat for all tubes used

Appendix D - User-Defined Functions

```
#include "udf.h"

//global variables
double source=0;
//initialize alpha to 0.05%
double total_heat=0.0005*(432.7*1100000);
double timestep=1;
double K1=0;
double K2=0;
double alpha=0;
double alpha_over_t=0;
double term_two_num=0;
double term_two_denom=0;


DEFINE_PROFILE(bc_temp, t, i)
{
        face_t f ;

        real flow_time = RP_Get_Real("flow-time");

        if (flow_time <= 3150 )
        {

        begin_f_loop(f,t)
        {
        F_PROFILE(f,t,i) = 25+2*(flow_time/60)+273;  //ramp to 130C at 2C/min

        }
        end_f_loop(f,t)
        }

        if (flow_time > 3150 && flow_time < 10350)
        {

        begin_f_loop(f,t)
        {
        F_PROFILE(f,t,i) = 130+273;  //dwell at 130C for 2h
        }
        end_f_loop(f,t)
         }
```

```
        if (flow_time >= 10350 && flow_time <= 12450)
        {

         begin_f_loop(f,t)
        {
        F_PROFILE(f,t,i) = 130+2*((flow_time/60)-172.5)+273;  //ramp from 130 to 200C at
                                                                2C/min
        }
         end_f_loop(f,t)
        }

        if (flow_time > 12450 && flow_time < 19650)
        {

        begin_f_loop(f,t)
        {
        F_PROFILE(f,t,i) = 200+273;  //dwell at 200C for 2h
        }
        end_f_loop(f,t)
        }

}


//Computes heat generation term for resin
//432.7 J/g or 432.7*1100000 J/m3 total heat of reaction
DEFINE_SOURCE(heat_gen, c, t, dS, eqn)
{

        K1=410033*exp(-1*77793/8.3145/C_T(c,t));
        K2=264148*exp(-1*67520/8.3145/C_T(c,t));
        alpha=total_heat/(432.7*1100000);

        term_two_num=K2*pow(alpha,0.51)*pow((1-alpha),2.71);
        term_two_denom=1+exp(8.19*alpha+8.19*1.19-8.19*0.005*C_T(c,t));
        alpha_over_t=K1*pow((1-alpha),18.87)+term_two_num/term_two_denom;

        source=alpha_over_t*(432.7*1100000);

        return source;

}


//Specifies specific heat of fabric
DEFINE_SPECIFIC_HEAT(cell_cp, T, Tref, h, yi)
```

```
{

        //local variables
        real cp;
                        real temp = T;
        real flow_time = RP_Get_Real("flow-time");

        if (flow_time <= 3600 )
        cp = 390;

        if (flow_time > 3600 )
        cp = 710;

        return cp;

}


//Specifies density of fabric
DEFINE_PROPERTY(cell_density, c, t)
{

         //local variables
        real rho;
        real flow_time = RP_Get_Real("flow-time");

        if (flow_time <= 3600 )
        rho = 974;

        if (flow_time > 3600 )
        rho = 1770;

        return rho;

}


//Specifies thermal conductivity of fabric
DEFINE_PROPERTY(cell_cond_fabric, cell, thread)
{

        //local variables
        real therm_cond;
        real flow_time = RP_Get_Real("flow-time");
```

```
        if (flow_time <= 3600 )
        therm_cond =0.182;

        if (flow_time > 3600 )
        therm_cond = 0.5;

        return therm_cond;

}


//Specifies thermal conductivity of resin
DEFINE_PROPERTY(cell_cond_resin, cell, thread)
{

        //local variables
        real therm_cond;
        real flow_time = RP_Get_Real("flow-time");

        if (flow_time <= 3600 )
        therm_cond =0.2;

        if (flow_time > 3600 )
        therm_cond = 0.5;

        return therm_cond;

}


//Tracks cumulative heat of reaction of resin
DEFINE_EXECUTE_AT_END(cumulative)
{

        total_heat = total_heat+source*timestep;

}
```